

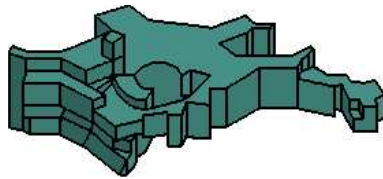
Dissertation zum Erlangen des akademischen Grades *Doktor der Naturwissenschaften*
der Fakultät für Physik der Ludwig-Maximilians-Universität München

Max-Planck-Institut für Astrophysik

Methods for detecting and characterising clusters of galaxies

vorgelegt von Björn Malte Schäfer aus Zweibrücken

München, 26.Jan.2005



Dissertation der Fakultät für Physik der
Ludwig-Maximilians-Universität München

Björn Malte Schäfer:

Methods for detecting and characterising clusters of galaxies

Dissertation der Fakultät für Physik der Ludwig-Maximilians-Universität München
ausgeführt am Max-Planck-Institut für Astrophysik

Vorsitzende:	Prof. Dr. Dorothee Schaile
1. Gutachter:	Prof. Dr. Matthias Bartelmann
2. Gutachter:	Prof. Dr. Simon D.M. White
Beisitzer:	Dr. Hans Böhringer

Tag der mündlichen Prüfung: 06.Jun.2005

Robert Frost:

On Looking Up By Chance At The Constellations

You'll wait a long, long time for anything much
To happen in heaven beyond the floats of cloud
And the Northern Lights that run like tingling nerves.
The sun and moon get crossed, but they never touch,
Nor strike out fire from each other nor crash out loud.
The planets seem to interfere in their curves
But nothing ever happens, no harm is done.
We may as well go patiently on with our life,
And look elsewhere than to stars and moon and sun
For the shocks and changes we need to keep us sane.
It is true the longest drought will end in rain,
The longest peace in China will end in strife.
Still it wouldn't reward the watcher to stay awake
In hopes of seeing the calm of heaven break
On his particular time and personal sight.
That calm seems certainly safe to last to-night.

Contents

1. Abstract	1
2. Introduction and motivation	3
3. Cosmology and cosmic structure formation	5
3.1. Friedmann-Lemaître cosmological models	5
3.1.1. Cosmological principles and the Robertson-Walker metric	5
3.1.2. Cosmometry	6
3.1.3. Cosmic microwave background	8
3.2. Structure formation	10
3.2.1. Growth of density perturbations in cold dark matter models	10
3.2.2. Numerical simulations of cosmic structure formation	13
3.3. Physics of clusters of galaxies	13
3.3.1. Formation of clusters of galaxies	13
3.3.2. Observational properties of clusters	14
4. PLANCK-surveyor	21
4.1. Introduction to the PLANCK-surveyor	21
4.2. PLANCK mission objectives	21
4.3. Instrument description	22
5. Construction of all-sky thermal and kinetic Sunyaev-Zel'dovich maps	23
5.1. Introduction	23
5.2. Sunyaev-Zel'dovich definitions	24
5.3. Simulations	25
5.3.1. Hubble-volume simulation	25
5.3.2. Small scale SPH cluster simulations	26
5.4. Sunyaev-Zel'dovich map construction	26
5.4.1. SZ-template map preparation	26
5.4.2. Cluster selection and scaling relations	28
5.4.3. Projection onto the celestial sphere	29
5.4.4. Completeness of the all-sky SZ-maps	29
5.5. Results	31
5.5.1. Sky views	32
5.5.2. Distribution of angular sizes	35
5.5.3. Distribution of the integrated thermal and kinetic Comptonisation	36
5.5.4. Distribution of Comptonisation per pixel	38
5.5.5. Angular power spectra of the thermal and kinetic SZ-effects	39
5.5.6. Source counts at PLANCK frequencies	40
5.6. Summary	43
6. Microwave emission components of the Milky Way and the Solar system	45
6.1. Introduction	45
6.2. Sunyaev-Zel'dovich definitions	46
6.3. Submillimetric observations with PLANCK	46

6.3.1.	Beam shapes	46
6.3.2.	Scanning strategy and noise-equivalent maps	48
6.4.	Foreground emission components	49
6.4.1.	Galactic dust emission	50
6.4.2.	Galactic synchrotron emission	51
6.4.3.	Galactic free-free emission	51
6.4.4.	CO-lines from giant molecular clouds	52
6.4.5.	Planetary submillimetric emission	54
6.4.6.	Submillimetric emission from asteroids	55
6.4.7.	Future work concerning PLANCK's foregrounds	56
6.5.	Simulating SZ-observations by PLANCK	57
6.5.1.	SZ-map preparation	58
6.5.2.	CMB-map generation	58
6.5.3.	Preparation of simulation data sets	58
6.5.4.	PLANCK-channel correlation properties	61
6.6.	Summary and conclusion	62
7.	Matched and scale-adaptive multifiltering	65
7.1.	Introduction: multi-frequency optimised filtering	65
7.1.1.	Assumptions and definitions	66
7.1.2.	Concepts in filter construction	67
7.1.3.	Matched filter	68
7.1.4.	Scale-adaptive filter on the sphere	68
7.1.5.	Detection level and gain	69
7.2.	Optimised SZ-filters for PLANCK	69
7.2.1.	Numerical derivation of filter kernels	69
7.2.2.	Discussion of filter kernels	69
7.2.3.	Filter renormalisation and synthesis of likelihood maps	76
7.3.	Summary and conclusion	79
8.	Properties of PLANCK's SZ-cluster sample	81
8.1.	Simulation setup and peak extraction	81
8.1.1.	Filter construction and synthesis of likelihood maps	81
8.1.2.	Morphology of SZ-clusters in filtered sky-maps	81
8.1.3.	Peak extraction and cluster identification	82
8.2.	Noise properties and peak statistics	82
8.2.1.	Noise in the filtered and co-added maps	82
8.2.2.	Detection significances	83
8.3.	Cluster detectability as a function of filter parameters	85
8.4.	Cluster properties of the recovered SZ-sample	85
8.4.1.	Cluster population in the mass-redshift plane	85
8.4.2.	Position accuracy of PLANCK's SZ-clusters	90
8.5.	Spatial homogeneity of PLANCK's SZ-cluster sample	93
8.6.	Distribution of peculiar velocities	95
8.7.	Summary and conclusion	95
9.	A Peano-Hilbert partition for HEALPix tessellated spheres	99
9.1.	Motivation	99
9.2.	HEALPix tessellation	99
9.3.	Peano-Hilbert curves for HEALPix	100
9.4.	Properties of the Peano-Hilbert ordering	102
9.5.	Summary	104
10.	Redshift estimation of clusters by wavelet decomposition of their SZ-morphology	105

10.1. Introduction	105
10.2. Sunyaev-Zel'dovich definitions	106
10.3. Wavelets	107
10.3.1. Wavelet definitions	107
10.3.2. Application of wavelets to a cluster profile	107
10.3.3. Analogy to power spectra in Fourier analysis	110
10.4. Simulations	110
10.4.1. SPH cluster simulations	111
10.4.2. SZ-map preparation	111
10.4.3. Cluster selection	111
10.4.4. CMB map generation	113
10.4.5. Simulated single-frequency SZ-observations	114
10.5. Analysis	114
10.5.1. Wavelet basis functions	115
10.5.2. Measurement of wavelet quantities	115
10.5.3. Wavelet spectrum of SZ-cluster maps	116
10.5.4. Correlations with physical quantities	117
10.5.5. Measurement principle	120
10.5.6. Principal component analysis	120
10.5.7. Redshift dependence of the wavelet parameters	121
10.5.8. Noise contributions and their suppression	123
10.5.9. Redshift estimation	126
10.6. Systematics	128
10.6.1. Influence of tilted scaling relations	128
10.6.2. Cool cores of clusters	129
10.6.3. Wavelet analysis of unselected clusters	130
10.7. Redshift estimation in a nutshell	131
10.8. Summary	131
11. Coded mask imaging of extended sources with Gaussian random fields	135
11.1. Introduction	135
11.2. Coded mask imaging	136
11.3. Gaussian random fields	136
11.3.1. Definitions	136
11.3.2. Algorithm	137
11.3.3. Choice of the PSF	137
11.3.4. Scaling applied to the Gaussian random fields	138
11.3.5. Gaussian random fields for circular apertures	138
11.4. Results	139
11.4.1. Visual impression	139
11.4.2. Reproducibility of the PSF	139
11.4.3. Pixel-to-pixel variance	142
11.4.4. Distribution of the pixel amplitudes	142
11.4.5. Partial shadowing	143
11.4.6. Thresholded realisations	143
11.5. Ray-tracing simulations including finite photon statistics	145
11.5.1. Simulation setup	146
11.5.2. Point source sensitivity of a set of Gaussian random fields	147
11.5.3. Sensitivity in observations of extended sources	147
11.5.4. Field-of-view in the observation of point sources	148
11.6. Summary and outlook	149
12. Gravitational Lensing	151
12.1. Introduction	151

12.2. Gravitational light deflection	151
12.2.1. Light deflection from Fermat's principle	151
12.2.2. Cosmological weak lensing	152
12.2.3. Applications of weak lensing in cosmology	153
12.3. Ray-tracing simulations on the large-scale structure	153
12.3.1. A ray-tracing code for cosmological n -body simulations: <code>leica.c</code>	154
12.3.2. Features	155
12.4. Summary and conclusion	155
13. Gravitomagnetic lensing and the integrated Sachs-Wolfe/Rees-Sciama effect	157
13.1. Introduction	157
13.2. Key formulae	158
13.2.1. Structure formation	158
13.2.2. Dark matter currents	159
13.2.3. Limber's equation for vector fields	159
13.3. Gravitomagnetic lensing	161
13.3.1. Definitions	161
13.3.2. Gravitomagnetic lensing by the large-scale structure	162
13.3.3. Perturbative treatment	163
13.3.4. Corrections to the power spectrum	165
13.3.5. Projected lensing power spectra	165
13.4. Integrated Sachs-Wolfe effect	166
13.4.1. Definitions	167
13.4.2. Connection to the gravitomagnetic potentials	167
13.4.3. Putting the Sachs-Wolfe effect in a cosmological context	168
13.4.4. Perturbative treatment	169
13.4.5. Power spectrum of dark matter currents	169
13.4.6. integrated Sachs-Wolfe angular power spectrum	170
13.5. Summary	171
14. Summary and outlook	173
A. Numerical evaluation of SPH-projections	177
B. Derivation of spherical matched and scale-adaptive filter kernels	181
B.1. Assumptions and definitions	181
B.2. Convolution theorem on the sphere	181
B.3. Concepts of optimised filtering on the sphere	182
B.3.1. Matched filter	183
B.3.2. Scale-adaptive filter	183
C. Integration of Legendre-P_ℓ weighted functions	185
D. Integration of Bessel-J_ℓ weighted functions	187
D.1. Approximation formulae	187
D.2. Numerical integration	187
E. Decomposition of mixed 3-point correlators of density and velocity fields	189
F. Propagation of photons through gravitomagnetic fields	191
Bibliography	193

1. Abstract

Methods for detecting and characterising clusters of galaxies

The main theme of this PhD-thesis is the observation of clusters of galaxies at submillimetric wavelengths. The Sunyaev-Zel'dovich (SZ) effect due to interaction of cosmic microwave background (CMB) photons with electrons of the hot intra-cluster medium causes a distinct modulation in the spectrum of the CMB and is a very promising tool for detecting clusters out to very large distances. Especially the European PLANCK-mission, a satellite dedicated to the mapping of CMB anisotropies, will be the first experiment to routinely detect clusters of galaxies by their SZ-signature. This thesis presents an extensive simulation of PLANCK's SZ-capabilities, that combines all-sky maps of the SZ-effect with a realisation of the fluctuating CMB and submillimetric emission components of the Milky Way and of the Solar system, and takes instrumental issues such as the satellite's point-spread function, the frequency response, scan paths and detector noise of the receivers into account.

For isolating the weak SZ-signal in the presence of overwhelming spurious components with complicated correlation properties across PLANCK's channels, multifrequency filters based on matched and scale-adaptive filtering have been extended to spherical topologies and applied to simulated data. These filters were shown to efficiently amplify and extract the SZ-signal by combining spatial band-filtering and linear combination of observations at different frequencies, where the filter shapes and the linear combination coefficients follow from the cross- and autocorrelation properties of the sky maps, the anticipated profile of SZ clusters and the known SZ spectral dependence. The characterisation of the resulting SZ-sample yielded a total number of 6×10^3 detections above a statistical significance of 3σ and the distribution of detected clusters in mass, redshift, and position on the sky.

In a related project, a method of constructing morphological distance estimators for resolved SZ cluster images is proposed. This method measures a cluster's SZ-morphology by wavelet decomposition. It was shown that the spectrum of wavelet moments can be modeled by elementary functions and has characteristic properties that are non-degenerate and indicative of cluster distance. Distance accuracies following from a maximum likelihood approach yielded values as good as 5% for the relative deviation, and deteriorate only slightly when noise components such as instrumental noise or CMB fluctuations were added. Other complications like cool cores of clusters and finite instrumental resolution were shown not to affect the wavelet distance estimation method significantly.

Another line of research is the Rees-Sciama (RS) effect, which is due to gravitational interaction of CMB photons with non-stationary potential wells. This effect was shown to be a second order gravitational lensing effect arising in the post-Newtonian expansion of general relativity and measures the divergence of gravitomagnetic potentials integrated along the line-of-sight. The spatial autocorrelation function of the Rees-Sciama effect was derived in perturbation theory and projected to yield the angular autocorrelation function while taking care of the differing time evolution of the various terms emerging in the perturbation expansion. The RS-effect was shown to be detectable by PLANCK as a correction to the primordial CMB power spectrum at low multipoles. Within the same perturbative formalism, the gravitomagnetic corrections to the autocorrelation function of weak gravitational lensing observables such as cosmic shear could be determined. It was shown that those corrections are most important on the largest scales beyond 1 Gpc, which are difficult to access observationally. For contemporary weak lensing surveys, gravitomagnetic corrections were confirmed not play a significant role.

A byproduct of the simulation of CMB fluctuations on the basis of Gaussian random fields was a new way of generating coded mask patterns for X-ray and γ -ray imaging. Coded mask cameras observe a source by recording the shadow cast by a mask onto a position-sensitive detector. The distribution of sources can be reconstructed from this shadowgram by correlation techniques. By using Gaussian random fields, coded mask patterns can be specifically tailored for a predefined point-spread function which yields significant advantages with respect to sensitivity in the observation of extended sources while providing a moderate performance compared to traditional mask generation schemes in the observation of point sources. Coded mask patterns encoding Gaussian point-spread functions have been subjected to extensive ray-tracing studies where their performance has been evaluated.

Methoden zum Aufspüren und Charakterisieren von Galaxienhaufen

Das zentrale Thema dieser Dissertation ist die Beobachtung von Galaxienhaufen bei Millimeter-Wellenlängen. Der Sunyaev-Zel'dovich (SZ) Effekt, der durch die Wechselwirkung der Photonen des kosmischen Mikrowellenhintergrundes (CMB) mit Elektronen des heißen intra-Cluster Mediums im Zentrum von Galaxienhaufen hervorgerufen wird, verursacht eine Modulation des CMB-Spektrums und ist eine sehr vielversprechende Technik, Galaxienhaufen bis zu sehr großen Abständen zu entdecken. Vor allem der europäische PLANCK-Satellit, der die Kartographie der CMB-Anisotropien zur Aufgabe hat, wird das erste Observatorium sein, das routinemäßig Galaxienhaufen durch ihre SZ-Signatur aufspürt. In dieser Dissertation wird eine detaillierte Simulation der SZ-Beobachtungen mit PLANCK beschrieben, die Himmelskarten des SZ-Effekts mit Fluktuationen des Mikrowellenhintergrundes und Vordergrundemissionen der Milchstraße und des Sonnensystems verbindet. Instrumentelle Komplikationen wie die Ortsauflösung der Optik, die Frequenzfenster der Radioempfänger, das Scan-Muster und das Detektorrauschen wurden berücksichtigt.

Um das schwache SZ-Signal zu isolieren, das durch die um ein Vielfaches stärkeren Vordergrunde überdeckt ist, wurden Multifrequenz-Filter basierend auf dem *matched filter*- und dem *scale-adaptive filter*-Algorithmus auf sphärische Topologien erweitert und auf die simulierten Daten angewendet. Es wurde gezeigt, dass diese Filter das SZ-Signal effizient verstärken und extrahieren können, was durch die Kombination von räumlichen Filtern und Linearkombination verschiedener Karten geschieht. Die Filterformen und Koeffizienten der Linearkombination folgen aus den Kreuz- und Autokorrelationseigenschaften der Himmelskarten, dem erwarteten SZ-Profil der Galaxienhaufen und dem bekannten spektralen Verlauf des SZ-Effekts. Der resultierende SZ-Katalog, der 4×10^3 Einträge mit Signifikanzen größer als 3σ umfasst, wurde in Bezug auf die Verteilung der detektierten Galaxienhaufen in Masse, Rotverschiebung und Position untersucht.

In einem verwandten Projekt stelle ich eine Methode vor, mittels derer der Abstand eines SZ-Galaxienhaufens durch seine Morphologie abgeschätzt werden kann. In dieser Methode wird die Morphologie eines Galaxienhaufens durch Wavelets analysiert. Es konnte gezeigt werden, dass das Spektrum der Wavelet-Momente durch elementare Funktionen beschrieben werden kann und charakteristische Eigenschaften hat, die nicht-entartet sind und Indikatoren für den Abstand des Galaxienhaufens sind. Die Genauigkeit der Abstandsmessung, die wahrscheinlichkeits-theoretisch bestimmt wurde, ergibt Werte von 5% für die relative Abweichung, wobei sich diese Zahl nur marginal verschlechtert, wenn Rauschkomponenten wie instrumentelles Rauschen oder CMB-Fluktuationen berücksichtigt werden. Es konnte gezeigt werden, dass andere Komplikationen, wie abgekühlte Kerne von Galaxienhaufen oder die endliche Ortsauflösung der Detektoren, diese Methode nicht stark beeinflussen.

Ein anderes Forschungsgebiet ist der Rees-Sciama (RS) Effekt, der durch gravitative Wechselwirkung der CMB-Photonen mit zeitlich veränderlichen Gravitationsfeldern verursacht wird. Dieser Effekt konnte auf einen Gravitationslinseneffekt zweiter Ordnung zurückgeführt werden, der in der post-Newtonschen Entwicklung der Formeln der allgemeinen Relativitätstheorie erscheint. In dieser Darstellung misst der RS-Effekt die Divergenz der gravitomagnetischen Potentiale entlang der Sichtlinie. In dieser Beschreibung wurde die Autokorrelationsfunktion des RS-Effekts in Störungsrechnung hergeleitet und projiziert, um die Winkel-Autokorrelationsfunktion zu erhalten, während die verschiedenen Zeitentwicklungen der Terme in der Störungsreihe berücksichtigt wurden. Der RS-Effekt sollte von PLANCK als Korrektur zur Autokorrelationsfunktion des primordialen CMB auf grossen Winkelskalen detektierbar sein. Innerhalb des gleichen Formalismus habe ich gravitomagnetische Korrekturen zu der Autokorrelationsfunktion beliebiger Gravitationslinsengrößen bestimmt, die auf den größten Skalen jenseits von 1 Gpc wichtig werden sollten, allerdings Experimenten nur schwer zugänglich sind. Auf Skalen, die durch laufende Durchmusterungen untersucht werden, spielen gravitomagnetische Korrekturen nur eine untergeordnete Rolle.

Ein Nebenprodukt der Simulationen von CMB-Fluktuationen basierend auf Gaußschen Zufallfeldern ist eine neue Methode, Masken für kodierte Aperturen in abbildenden Röntgen- und γ -Kameras zu erzeugen. Bei kodierten Aperturen wird eine Quelle durch den Schattenwurf einer Zufallsmaske auf einen ortsauflösenden Detektor beobachtet. Die Verteilung der Quellen kann durch Korrelationstechniken aus dem Schattenmuster rekonstruiert werden. Unter Verwendung von Gaußschen Zufallfeldern können kodierte Aperturen für jede gewünschte point-spread Funktion erzeugt werden, was einen bedeutenden Vorteil in Bezug auf Sensitivität in der Beobachtung von ausgedehnten Quellen darstellt, während ihre Leistungsfähigkeit in der Beobachtung von Punktquellen hinter etablierten Techniken zur Erzeugung von Aperturen zurückbleibt. Diese Ergebnisse folgen aus aufwändigen numerischen Simulationen, in denen die Gaußschen Zufallfelder auf ihre Leistungsfähigkeit im Vergleich zu anderen Aperturmustern untersucht wurde.

2. Introduction and motivation

The last couple of decades has witnessed the evolution of cosmology from a philosophical to a sound scientific discipline. The first observational fact was E. Hubble's discovery of the recession velocity of galaxies, which he found to be proportional to their distance. This suggested that space itself is expanding and not static. World models in the framework of general relativity based on solutions of Friedmann's equations were found by A. Einstein and W. de Sitter which explain the universal expansion. R. Alpher, H. Bethe and G. Gamov investigated the thermal history of an expanding Universe and realised that the early Universe was hot and dense enough to allow thermonuclear synthesis of light elements. Their theory was supported by measurements of the cosmic abundance of light elements, in particular of deuterium. A further prediction of their work was the cosmic background radiation, which was successively detected by A. A. Penzias and R. W. Wilson.

Today, the parameters describing the homogeneous dynamics of the Universe are known on the percent level and cosmology turned to answering the question of structure formation. Fluctuations in the sky temperature of the cosmic microwave background suggested that the structures such as galaxies and clusters of galaxies form by gravitational amplification from these tiny primordial seed fluctuations which was suggested by I. Novikov and Y. B. Zel'dovich. J. Peebles proposed that most of the matter was not electromagnetically interacting (dark matter) and that the structure formed by gravitational aggregation of this newly introduced fluid, which mended a number of problems baryonic models of structure growth were unable to overcome. It was then proposed by J. P. Ostriker, M. Rees and S. D. M. White that luminous objects like galaxies form inside dark matter structures by condensation and cooling of baryons. In this thesis, Chapter 3 provides a summary of the key results of cosmology, structure formation and cluster physics.

Theories of cosmic structure formation can be tested in a number of ways. In modern cosmology the statistical properties of the dark matter field or any tracer of it like the spatial distribution of baryons or galaxies as tracer particles are described in terms of its n -point correlation function. The correlation functions are observationally accessible by various experiments. Classically, the large-scale distribution of galaxies was the first to be investigated and continues to be a very interesting technique. In particular, it yields information about the clustering of dark matter on small scales and the transition from linear to nonlinear structure formation, where perturbation theory ceases to be applicable. Another observational channel is the X-ray band: Clusters of galaxies are powerful emitters of X-ray radiation and X-ray surveys are able to determine the fluctuations of the density field by investigating its peak statistics on the cluster separation scale. Furthermore, X-rays probe the distribution of baryons inside dark matter halos and investigate processes like radiative cooling, feedback and metal enrichment which strongly influences the baryonic morphology of a cluster.

All these observations are aiming at the determination of cosmological parameters related to structure formation to a level of accuracy comparable to the parameters governing the homogeneous dynamics of the Universe. Observations of the dynamics of the large-scale structure are complemented by numerical computer simulations of structure growth. In these models, the equations of structure formation (the equation of continuity, Euler's equation and Laplace's equation) are solved for a discretised density field. Despite the fact that these simulations are very challenging from the algorithmic and computational point of view, they yield valuable insight into dark matter dynamics in the nonlinear stages of structure evolution, halo formation and baryonic physics in the centres of galaxies and clusters of galaxies. The core theme of this thesis is the derivation of observational properties of the large-scale structure from numerical simulations. Of special interest to this thesis is the simulation of clusters of galaxies in a new observational window: The thermal Sunyaev-Zel'dovich effect predicts that clusters of galaxies leave a trace in the spectrum of the cosmic microwave background radiation by Compton interaction of the electrons of the hot-intra cluster medium with photons of the microwave background. Recent advances in submillimetric receiver technology made the detection of this small effect possible.

The major part of this thesis is dedicated to a detailed simulation of Sunyaev-Zel'dovich (SZ) observations for the PLANCK-surveyor satellite. A short description of the instrument and an overview of PLANCK's mission

objectives is given in Chapter 4. PLANCK will be the first observatory to routinely detect clusters of galaxies by their SZ-signature. The SZ-effect is a particularly promising tool for investigating clusters of galaxies because clusters can be detected out to very large distances, possibly out to redshifts of unity as analytic estimates suggest. Chapters 5 through 8 describe a very detailed simulation of PLANCK's SZ-capabilities which includes many aspects of cluster formation and distribution, baryonic physics and asymmetric SZ-morphologies, Galactic and ecliptic foregrounds and many instrumental imperfections such as receiver noise, frequency response and resolution of the optical system. The weak SZ-signal is amplified and extracted by matched and scale-adaptive filtering, which has been extended to spherical topologies and multi-frequency observations.

In Chapter 10, I propose a method of constructing morphological distance estimators for resolved SZ cluster images. This method measures a cluster's SZ-morphology by wavelet decomposition. It is shown that the spectrum of wavelet moments can be modeled by elementary functions and has characteristic properties that are non-degenerate and indicative of cluster distance. Distance accuracies following from a maximum likelihood approach yielded values as good as 5% for the relative deviation, and deteriorate only slightly when noise components such as instrumental noise or CMB fluctuations were added. Other complications like cool cores of clusters and finite instrumental resolution were shown not to affect the wavelet distance estimation method significantly. This method will be of particular use in future dedicated high-yield SZ-surveys in order to select targets for optical or X-ray follow-up observations.

Chapter 9 is more technical in nature. A central quantity in CMB data analysis tasks is the pairwise pixel covariance matrix, which contains information about non-isotropic and non-Gaussian noise components and is a key quantity in map reconstruction, component separation and foreground subtraction. For usual pixel numberings in the HEALPix tessellation of the sphere, which is commonly used in CMB data analysis, the covariance matrix has a very complicated shape. I propose to number the pixels along a fractal, self-similar Peano-Hilbert curve that can be constructed for all HEALPix resolutions. Using this numbering, the covariance matrix assumes a band-diagonal shape which makes the computation of the determinant and matrix inversion possible.

A byproduct of the simulation of CMB fluctuations on the basis of Gaussian random fields was a new way of generating coded mask patterns for X-ray and γ -ray imaging, which is described in Chapter 11. Coded mask cameras observe a source by recording the shadow cast by a mask onto a position-sensitive detector. The distribution of sources can be reconstructed from this shadowgram by correlation techniques. By using Gaussian random fields, coded mask patterns can be specifically tailored for a predefined point-spread function which yields significant advantages with respect to sensitivity in the observation of extended sources while providing a moderate performance compared to traditional mask generation schemes in the observation of point sources. Coded mask patterns encoding Gaussian point-spread functions have been subjected to extensive ray-tracing studies where their performance has been evaluated.

Another experimental tool for investigating the correlation properties of the cosmic density field is gravitational lensing. Gravitational interaction of photons with the large-scale structure induces tiny distortions in the images of background galaxies which can nowadays be measured reliably. There exist mathematical tools that link the angular correlation properties of the distorted galaxy images to the spatial correlation properties of the dark matter density field, in particular the amplitude of the correlation function. In Chapter 12 I describe a ray-tracing code for computing lensed photon geodesics on density fields following from cosmological simulations of structure formation. This code covers many aspects of gravitational lensing and is able to derive lensing data from cosmological simulation at a high level of authenticity.

So far, gravitational lensing has only been considered for stationary matter distributions, but the post-Newtonian expansion of the geodesic equation to second order shows that matter streams influence photon geodesics by the gravitomagnetic potentials they generate. The growth of structure and the formation of objects requires large coherent matter streams so that it seemed natural to extend the theory of gravitational light deflection to non-stationary situations. In Chapter 13, I investigate gravitomagnetic corrections to weak gravitational lensing by streams in the large-scale structure in perturbation theory. Detailed analysis of the geodesic equation showed that the Rees-Sciama effect, which describes the frequency shift of photons introduced by time-varying gravitational potentials can be consistently treated in the gravitomagnetic framework. Applying perturbation theory yielded the Rees-Sciama autocorrelation function, which should be detectable as a correction to the autocorrelation function of CMB temperature fluctuations on large angular scales. The core results of this thesis are summarised in Chapter 14 together with a compilation of key techniques in Appendices A through F.

3. Cosmology and cosmic structure formation

Abstract

This chapter provides an introduction to the theory of cosmic structure formation, and the key concepts of modern cosmology as relevant for this work. After summarising Friedmann-Lemaître cosmological models in Sect. 3.1, the theory of cosmological structure formation and the description of the statistical properties of the large-scale structure by means of correlation functions is presented in Sect. 3.2. Various aspects of the physics of clusters of galaxies, e.g. their formation and their properties in different observational channels are discussed in Sect. 3.3.

3.1. Friedmann-Lemaître cosmological models

3.1.1. Cosmological principles and the Robertson-Walker metric

3.1.1.1. Relativistic world models

In general relativistic world models, events are described by their world coordinates, a 4-tuple containing the time coordinate and three spatial coordinates. The infinitesimal distance ds between two events differing in coordinates by dx^μ can be computed with the metric tensor $g_{\mu\nu}$, $ds^2 = g_{\mu\nu}dx^\mu dx^\nu$. In general relativity, the metric $g_{\mu\nu}$ is a dynamical field, which is determined by Einstein's field equation (Landau & Lifshitz 1975),

$$R_{\mu\nu} - \frac{R}{2}g_{\mu\nu} \equiv G_{\mu\nu} = \frac{8\pi G}{c^4}T_{\mu\nu} + \Lambda g_{\mu\nu}, \quad \text{with} \quad T_{\mu\nu} = \left(\rho + \frac{p}{c^2}\right)v_\mu v_\nu - pg_{\mu\nu}, \quad (3.1)$$

where the energy momentum tensor composed of the density ρ and pressure p of the cosmological fluids moving with 4-velocities v_μ acts as a source term. The Einstein-tensor $G_{\mu\nu}$ is formed from the Ricci tensor $R_{\mu\nu}$ and the Ricci scalar R , which are contractions of the Riemann tensor $R_{\kappa\lambda\mu\nu}$, i.e. of the second derivatives of the metric $g_{\mu\nu}$. Hence, formula 3.1 is a generalised Poisson equation. In eqn. 3.1, Λ denotes the cosmological constant.

3.1.1.2. Cosmological principle

In order to make an ansatz for the metric tensor $g_{\mu\nu}$ and to find a spherically symmetric solution of Einstein's field equation 3.1 that describes the expansion dynamics of the Universe, the cosmological principle was introduced. This principle requires isotropy and homogeneity:

- When averaged over sufficiently large scales, there exists a mean motion of matter and radiation in the Universe. From a frame of reference comoving with this mean motion, all averaged observables appear to be isotropic.
- All (imaginary) observers who follow this mean motion experience the same history of the Universe and measure the same values for all averaged observables.

3.1.1.3. Robertson-Walker line element

The spatial coordinates of an observer at rest in the comoving frame, from which the mean motion of radiation and matter appears isotropic, are constant, $dx^i = 0$ and hence $ds^2 = g_{00}dt^2$. It follows from the postulate of isotropy that clocks can be synchronised in a way that space-time components of the metric tensor g_{0i} vanish. The line element satisfying the cosmological postulates can be written:

$$ds^2 = c^2 dt^2 + g_{ij} dx^i dx^j, \quad (3.2)$$

where g_{ij} are the spatial components of the metric tensor. In order to conserve homogeneity the spatial part of the metric is only allowed to scale with a function $a(t)$ depending on cosmic time t , giving:

$$ds^2 = c^2 dt^2 - a^2(t) d\mathbf{r}^2, \quad (3.3)$$

where $d\mathbf{r}$ is the line element on spatial hypersurfaces. Introducing spherical coordinates $\mathbf{r} = (w, \theta, \phi)$ gives the Robertson-Walker line element for homogeneous and isotropic spaces:

$$ds^2 = c^2 dt^2 - a^2(t) \left[dw^2 + f_K^2(w) (d\theta^2 + \sin^2 \theta d\phi^2) \right]. \quad (3.4)$$

Homogeneity requires, that the function $f_K(w)$ is either trigonometric for positive values of the curvature K , linear for vanishing K or hyperbolic for negative K :

$$f_K(w) = \begin{cases} \frac{1}{\sqrt{K}} \sin(\sqrt{K}w) & , K > 0, \text{ spherical,} \\ w & , K = 0, \text{ flat,} \\ \frac{1}{\sqrt{|K|}} \sinh(\sqrt{|K|}w) & , K < 0, \text{ hyperbolic.} \end{cases} \quad (3.5)$$

3.1.1.4. Redshift

Due to the expansion of the Universe, photons are redshifted during their propagation from their source to the observer. In general, the redshift z of an object is the fractional Doppler shift of its light resulting from radial motion with velocity v :

$$z \equiv \frac{\lambda_o}{\lambda_s} - 1 \longrightarrow 1 + z = \sqrt{\frac{1 + v/c}{1 - v/c}}, \quad (3.6)$$

where λ_s is the wavelength of the emitted and λ_o of the observed radiation. In cosmology, the Doppler shift is due to emitter's recession with the Hubble flow and thus related to the ratio of scale factors a at the times of emission and absorption: $1 + z = \frac{a_o}{a_s}$. For an observer at $z_o = 0$ and source $z_s = z$, the formula becomes $a = 1/(1+z) \leftrightarrow z = 1/a - 1$.

3.1.2. Cosmometry

3.1.2.1. Friedmann's equations and the adiabatic equation

Solving Einstein's field equation 3.1 with the Robertson-Walker metric 3.4 as an ansatz for $g_{\mu\nu}$ for a homogeneous perfect fluid leads to Friedmann's equations (Friedmann 1922, 1924):

$$\frac{\dot{a}}{a} = \sqrt{\frac{8\pi G}{3} \rho - K \frac{c^2}{a^2} + \frac{\Lambda}{3}} \quad \text{and} \quad \frac{\ddot{a}}{a} = -\frac{4\pi G}{3} \left(\rho + \frac{3p}{c^2} \right) + \frac{\Lambda}{3}, \quad (3.7)$$

which describe the time evolution of the scale factor $a(t)$ depending on the properties of the cosmological fluids. The two Friedmann equations can be combined to form the adiabatic equation,

$$\frac{d}{dt} \left[a^3(t) c^2 \rho(t) \right] + p(t) \frac{d}{dt} a^3(t) = 0, \quad (3.8)$$

which describes the time evolution of the energy content of a volume that is expanding with the Hubble flow. The change in internal energy $d(a^3 c^2 \rho)$ in a volume is equal to the $p dV$ -work, i.e. the pressure times the change in proper volume. For that reason, the adiabatic equation corresponds to the first law of thermodynamics applied to the cosmological expansion. The Hubble function $H(t)$ is defined as the logarithmic derivative of $a(t)$:

$$H(t) \equiv \frac{d}{dt} \ln(a) = \frac{\dot{a}}{a} \longrightarrow H^2(t) = H_0^2 \left[\frac{\Omega_R}{a^4(t)} + \frac{\Omega_M}{a^3(t)} + \frac{\Omega_K}{a^2(t)} + \Omega_\Lambda \right]. \quad (3.9)$$

The value of H_0 is one of the least accurately known cosmological parameters, but measurements of CMB anisotropies (Spergel et al. 2003) and from Cepheid variable stars in distant galaxies (the Hubble key project, Freedman et al. 2001) seem to converge to a value of $H_0 = 100 h \text{ kms}^{-1} \text{ Mpc}^{-1}$ with $h \simeq 0.7$. The combination

$$\frac{3H_0^2}{8\pi G} \equiv \rho_{\text{crit}} \quad (3.10)$$

is the critical density of the Universe. If in a cosmological model all densities add up to ρ_{crit} , spatial hypersurfaces are flat and the curvature K vanishes. The energy density of all cosmological fluids (radiation $3p/c^2$, matter ρ , curvature K and the cosmological constant Λ) can be expressed in units of ρ_{crit} to yield:

$$\Omega_R = \frac{8\pi G p}{c^2 H_0^2}, \quad \Omega_M = \frac{\rho}{\rho_{\text{crit}}}, \quad \Omega_K = \frac{K c^2}{H_0^2}, \quad \Omega_\Lambda = \frac{\Lambda}{3H_0^2}, \quad \text{etc.} \quad (3.11)$$

For filling in the suspiciously looking gap in the Hubble function H for the $a^{-1}(t)$ term, a new field ϕ_Q referred to as quintessence with the density Ω_Q has been invented (Wetterich 1988, Ratra & Peebles 1988, Wetterich 1995, Doran & Wetterich 2003) and generalised by using a specific choice of the self-interaction potential $V(\phi_Q)$ to mimic arbitrary dependences on the scale factor a . Today's most accurate measurements of the density parameters have been carried out by the WMAP satellite (Spergel et al. 2003). Reference values are matter density $\Omega_M = 0.27 \pm 0.04$, baryonic density $\Omega_B = 0.044 \pm 0.004$, curvature $\Omega_K = 0.02 \pm 0.02$ and cosmological constant $\Omega_\Lambda = 0.73 \pm 0.04$. The radiation density Ω_R does not play a role in cosmic dynamics after decoupling due to its fast decrease with a .

3.1.2.2. Distances in cosmology

In curved and non-stationary space-time, distances are no longer unique and different distance measurement prescriptions lead to different distance measures. In general relativity, distance measures relate the positions of two events on two separate geodesic lines, which intersect a common light cone centered on an observer (Bartelmann & Schneider 2001, Hogg 1999). The proper time $d_P(z_s, z_o)$ is defined to be the light travel time of a signal emitted by a source at redshift z_s to an observer at $z_o < z_s$: $dd_P = -cdt$. Inserting the Hubble function yields $dd_P = -cda/(aH)$ and finally:

$$d_P(z_o, z_s) = \frac{c}{H_0} \int_{a(z_s)}^{a(z_o)} da \left[a^{-1}\Omega_M + \Omega_K + a^2\Omega_\Lambda \right]^{-\frac{1}{2}}. \quad (3.12)$$

The comoving distance, which is a very important distance measure in gravitational lensing and simulations of structure formation, is defined to be the distance on the spatial hyper-surface at time t between the world lines of source and observer comoving with the Hubble flow. Light travels along the geodesic, $ds = 0$, hence $cdt = -add_C$. Replacing dt as before by inserting the Hubble function H gives $dd_C = -cdt/a = -cda/(a^2H)$:

$$d_C(z_o, z_s) = \frac{c}{H_0} \int_{a(z_s)}^{a(z_o)} da \left[a\Omega_M + a^2\Omega_K + a^4\Omega_\Lambda \right]^{-\frac{1}{2}}. \quad (3.13)$$

The comoving distance with the observer at $z = 0$ is referred to as $w(z) \equiv d_C(z_o, z_s)$. Yet another distance measure is the angular diameter distance $d_A(z_s, z_o)$, which relates the physical size ΔL of an object at redshift z_s to its angular size $\Delta\alpha$ as seen from an observer at redshift z_o , $\Delta\alpha d_A = \Delta L$. The angular size of a yardstick placed at z_s should decrease proportional to $a(z_s)f_K(w(z_s))$, where $f_K(w(z_s))$ is the radial coordinate distance between observer and object, and $a(z_s)$ is the scale factor at the time of light emission, which gives:

$$d_A(z_o, z_s) = a(z_s)f_K [d_C(z_o, z_s)]. \quad (3.14)$$

Due to the factor $a(z_s)$, the angular diameter distance is not additive. The luminosity distance $d_L(z_s, z_o)$ relates the luminosity of a source at z_s to the flux received by an observer at z_o .

$$d_L(z_o, z_s) = \left(\frac{a(z_o)}{a(z_s)} \right)^2 d_A(z_s, z_o) = \frac{a(z_o)^2}{a(z_s)} f_K [d_C(z_o, z_s)]. \quad (3.15)$$

The luminosity distance is proportional to the angular diameter distance, which relates the physical area of a source at z_s to its apparent solid angle, as seen from the observer at z_o . The energy flux is further diminished, because the photons are redshifted by a_o/z_s and the difference in arrival times of two photons is stretched by a_o/z_s , giving the final formula. The various distance measures as a function of redshift z are compared in Fig. 3.1.

From these distance measures, only d_P , d_C and d_L are monotonic in a and z . Furthermore, only $d_C(z)$ and $d_P(z)$ are additive, which follows from the relation $\int_{z_1}^{z_3} da d_i(a) = \int_{z_1}^{z_2} da d_i(a) + \int_{z_2}^{z_3} da d_i(a)$. Yet another distance measure that finds application in gravitational lensing studies is the parallax distance $d_X(z)$ (Weinberg 1972, Schneider et al. 1992).

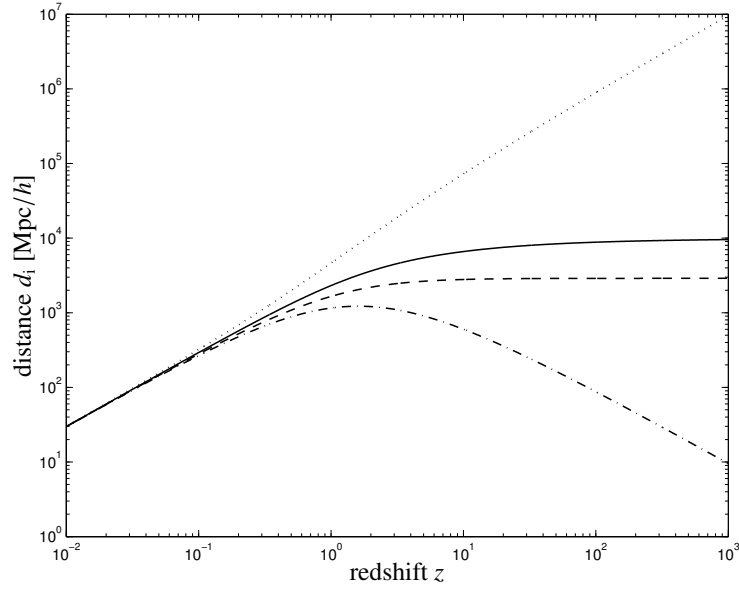


Figure 3.1.: Distance measures in cosmology: The comoving distance $d_C(z) = w(z)$ (solid line), the proper distance $d_p(z)$ (dashed line), the angular diameter distance $d_A(z)$ (dash-dotted line) and the luminosity distance $d_L(z)$ (dotted line).

3.1.3. Cosmic microwave background

3.1.3.1. Cosmic microwave background radiation

The cosmic microwave background (CMB) originated in the early hot phase of the Universe, when photons were created in thermal equilibrium with electromagnetically interacting particles (Dicke et al. 1965). With the Hubble expansion, the Universe cooled adiabatically. The adiabatic index of relativistic particles is $\gamma = 4/3$ (Shapiro & Teukolsky 1983), which yields for the adiabatic expansion $T \propto V^{1-\gamma} \propto a$. During the expansion, photons remained in thermal equilibrium until the temperature was sufficiently low for the electrons to combine with protons and α -particles to form hydrogen and helium. The photons decoupled from the matter constituents due to the rapidly decreasing abundance of charged particles. In this way, the Universe became transparent for radiation at a redshift of $z \approx 10^3$. The photons retained their Planckian spectrum they had acquired while they were in thermal equilibrium with the electron-positron plasma, and the temperature decreased in proportion with the scale factor. The relic radiation was detected by Penzias & Wilson (1965) and is nowadays proved to have a black body spectrum with $T_{\text{CMB}} = 2.725$ K (Fixsen et al. 1996) to very high accuracy.

The CMB shows tiny temperature anisotropies ($\Delta T/T \approx 10^{-5}$) imprinted by density perturbations present at the time of decoupling through various mechanisms (Hu 1995, Giovannini 2004). The physics governing the behaviour of a volume element of electron-proton plasma coupled to a radiation field is an interplay between gravity and radiation pressure. Photons released in overdense regions are redshifted because they have to climb out potential wells and hence they are cooler than the average CMB temperature. This effect, first examined by Sachs & Wolfe (1967), probes the potential fluctuations (and hence the density fluctuations) on the surface of last scattering. On scales smaller than the sound horizon, radiation pressure is able to provide a restoring force against the pull of gravity. The plasma-photon fluid is thus carrying out oscillations, which are excited when the size of the perturbation is equal to the horizon. At fixed physical scale, these oscillations are coherent, giving rise to distinct peaks in the CMB power spectrum. On the smallest scales, density perturbations can be destroyed if the radiation pressure exceeds the self-gravity.

Apart from these primordial CMB fluctuations, the growth of cosmic structure imprints a wealth of secondary anisotropies, either by interaction of CMB photons with electrons (Sunyaev-Zel'dovich effects, Ostriker-Vishniac effect) or by gravitational interaction (integrated Sachs-Wolfe effect, Rees-Sciama effect, gravitational lensing). The study of these effects and their detectability with next-generation CMB observatories such as PLANCK is the

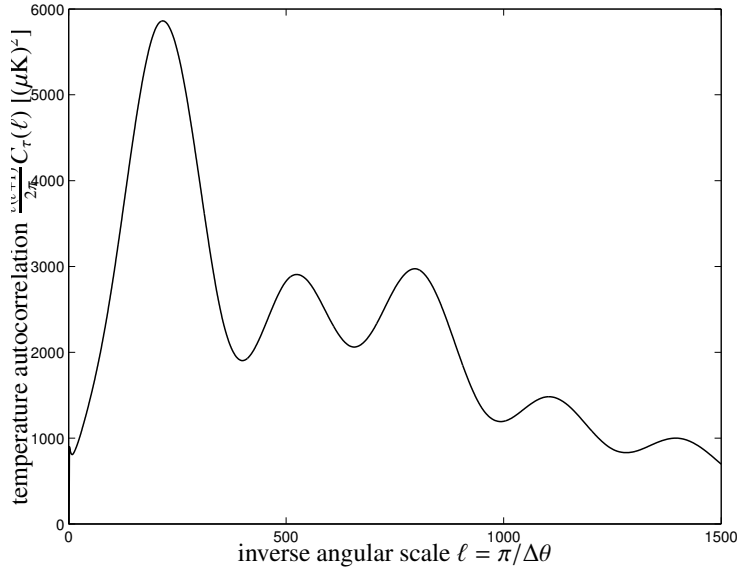


Figure 3.2.: The angular power spectrum $C_\tau(\ell)$ of the fluctuations in the cosmic microwave background $\tau(\theta)$, for the Λ CDM model, with $\Omega_M = 0.3$, $\Omega_B = 0.04$ and $\Omega_\Lambda = 0.7$.

primary subject of this thesis.

3.1.3.2. Statistical description of the CMB: Gaussian random fields

Due to their Gaussianity, the CMB temperature fluctuations $\tau(\theta)$ can be decomposed into spherical harmonics $Y_{\ell m}(\theta, \varphi)$, which form a harmonic system of functions, because they are solutions to Laplace's equation in spherical coordinates:

$$\tau_{\ell m} = \int_{4\pi} d\Omega \tau(\theta) Y_{\ell m}^*(\theta) \leftrightarrow \tau(\theta) = \sum_{\ell=0}^{\infty} \sum_{m=-\ell}^{+\ell} \tau_{\ell m} Y_{\ell m}(\theta) \text{ with } Y_{\ell m} = \sqrt{\frac{2\ell+1}{4\pi}} \sqrt{\frac{(\ell-|m|)!}{(\ell+|m|)!}} P_{\ell m}(\cos\theta) e^{im\varphi}. \quad (3.16)$$

From the $\tau_{\ell m}$ -coefficients, the angular power spectrum $C_\tau(\ell)$ can be obtained by averaging over all $2\ell + 1$ values of m at given multipole order ℓ , i.e. at fixed angular scale $\Delta\theta \simeq \pi/\ell$:

$$C_\tau(\ell) \equiv \frac{1}{2\ell+1} \sum_{m=-\ell}^{+\ell} \tau_{\ell m} \tau_{\ell m}^*. \quad (3.17)$$

Provided that the CMB fluctuations are indeed a Gaussian random field, all statistical information is contained in $C_\tau(\ell)$. Current CMB data is subjected to a plethora of techniques aiming at the amplification and detection of non-Gaussian features. Most of the analyses find the CMB to be consistent with Gaussianity (Komatsu et al. 2003), but interesting non-Gaussian features should be present, the most notable being gravitational lensing of the CMB (Hu 2000b, Hamana et al. 2004).

The angular power spectrum $C_\tau(\ell)$ as a function of inverse angular scale $\ell \simeq \pi/\Delta\theta$ of the CMB fluctuations $\tau(\theta)$ is depicted in Fig. 3.2 for a Λ CDM model. By using cosmological Boltzmann codes (Seljak & Zaldarriaga 1996, Lewis et al. 2000, Hu 2000a), the power spectrum $C_\tau(\ell)$ can be computed for a given set of cosmological parameters. By inversion, measurements of $C_\tau(\ell)$ are powerful probes of the cosmology, especially the geometry of the universe in terms of the curvature Ω_K . Furthermore, $C_\tau(\ell)$ provides important information about the statistics of fluctuations in the matter field δ at early times, when the fluctuations are still linear, $\delta \ll 1$.

3.1.3.3. Cosmic neutrino background

In analogy to the CMB, there is a background of relic neutrinos from the era of nucleosynthesis in the early universe at redshifts of $z \simeq 10^{10}$, that decoupled at temperatures of $k_B T \simeq 1$ MeV, because at this stage, the time scale of leptonic interactions became larger than the expansion time scale of the Universe. The neutrinos from this cosmic neutrino background are expected to have Fermi-Dirac spectrum with an equilibrium temperature of $T_{\text{CNB}} = 1.95\text{K}$.

3.2. Structure formation

3.2.1. Growth of density perturbations in cold dark matter models

3.2.1.1. Properties of dark matter

The current models of structure formation require the majority of matter not to couple to photons and to interact only by gravity. The most stringent observation which requires the matter to be dark, i.e. not interacting electromagnetically is the formation of structure since the emergence of the CMB, apart from rotation curves of spiral galaxies, gravitational microlensing or discrepancies of mass estimates of clusters of galaxies by application of the virial theorem compared to sum of masses of the cluster's member galaxies and the intra-cluster medium.

Dark matter is believed to be a yet undiscovered gravitationally interacting elementary particle, that neither carries electromagnetic, nor strong charges, but possibly interacts by the weak nuclear force. There is a large industry of experiments aiming at a direct detection of dark matter particles (CDMS¹, DAMA², GENIUS³, EDELWEISS⁴), but it is doubtful whether their sensitivity is sufficiently high. Dark matter interacts solely by gravity and is thought to have a vanishing cross section for collisions with other dark matter particles, which impacts on the central structure of gravitationally bound objects. Self-interacting dark matter influences the core structure of dark matter haloes (Yoshida et al. 2000) or could be detected by its annihilation signal (Stöhr et al. 2003). At the time of their decoupling from weak interactions, the dark matter particles were non-relativistic, i.e. cold, which has important implications on structure formation. The standard model of cosmological structure formation assumes the existence of initial seed fluctuations in the dark-matter distribution, which grew by gravitational attraction. A possible mechanism for producing these seed fluctuation are quantum fluctuations in the early universe, which were stretched to cosmological size by inflation.

3.2.1.2. Linear growth

Perturbations in the dark matter density field $\rho(\mathbf{x}, t)$ are described by the density contrast $\delta(\mathbf{x}, a)$:

$$\delta(\mathbf{x}, a) = \frac{\rho(\mathbf{x}, a) - \langle \rho(a) \rangle}{\langle \rho(a) \rangle}, \quad (3.18)$$

with the average cosmic density $\langle \rho(a) \rangle = \Omega_M \rho_{\text{crit}} a^{-3}$. By using (relativistic) perturbation theory, it can be shown that in the linear regime $|\delta| \ll 1$ perturbations grow differently with a , depending which fluid dominates the cosmological dynamics, as long as the Einstein-de Sitter limit is fulfilled, i.e. $\Omega_M(a) \simeq 1$:

$$\delta(a) \propto \begin{cases} a^2 & , a < a_{\text{eq}}, \text{ radiation dominated era,} \\ a & , a > a_{\text{eq}}, \text{ matter dominated era.} \end{cases} \quad (3.19)$$

At late times, when either the matter density Ω_M has decreased sufficiently or the cosmological Ω_Λ has started dominating the Hubble expansion, the linear growth depends on time a according to:

$$\frac{\delta(a)}{\delta(1)} = a \frac{g'(a)}{g'(1)} \equiv D_+(a). \quad (3.20)$$

¹<http://cdms.berkeley.edu/>

²<http://www.lngs.infn.it/lngs/htexts/dama/welcome.html>

³<http://www.mpi-hd.mpg.de/nonacc/genius.html>

⁴<http://edelweiss.in2p3.fr/indexedwe.html>

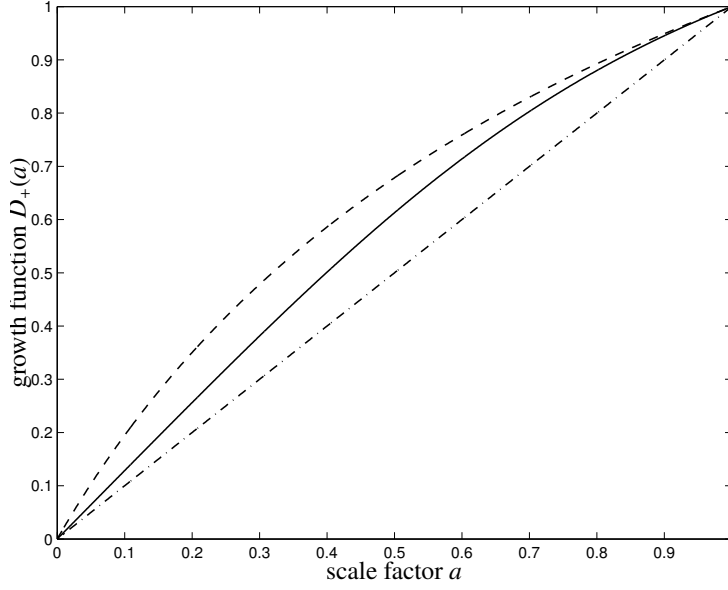


Figure 3.3.: The growth function $D_+(a)$ for the Λ CDM model (solid line), the SCDM model (dash-dotted line) and a low-density model with $\Omega_M = 0.3$ and vanishing cosmological constant $\Omega_\Lambda = 0.0$ (dashed line).

A phenomenological fit to $g'(a)$ for the Ω_M -dominated phase of structure growth is provided by [Carroll et al. \(1992\)](#):

$$g'(a) = \frac{5}{2} \Omega_M(a) \left[\Omega_M^{4/7}(a) - \Omega_\Lambda(a) + \left(1 + \frac{1}{2} \Omega_M(a) \right) \left(1 + \frac{1}{70} \Omega_\Lambda(a) \right) \right]^{-1}. \quad (3.21)$$

The growth function $D_+(a)$ as a function of scale factor a of the Λ CDM model, the SCDM model and a low density model without cosmological constant Λ is depicted in Fig. 3.3.

3.2.1.3. 2-point statistics, initial conditions and the shape of $P_\delta(k)$

The density fluctuations $\delta(\mathbf{x})$ are assumed to be Gaussian, and can be completely characterised by their power spectrum $P_\delta(k)$, which is defined by:

$$\langle \delta(\mathbf{k}) \delta^*(\mathbf{k}') \rangle = (2\pi)^3 \delta_D(\mathbf{k} - \mathbf{k}') P_\delta(k), \quad (3.22)$$

with the Fourier transform $\delta(\mathbf{k}) = \int d^3x \delta(\mathbf{x}) \exp(-i\mathbf{k}\mathbf{x})$. In linear perturbation theory, the density field grows homogeneously, hence individual Fourier components evolve independently:

$$\delta(\mathbf{x}, a) = D_+(a) \delta(\mathbf{x}) \longrightarrow \delta(\mathbf{k}, a) = D_+(a) \delta(\mathbf{k}), \quad (3.23)$$

as long as the wavelength of the perturbation is small compared to the comoving horizon size. $d_H = c/[aH(a)]$, i.e. the distance which a photon can cover since the big bang.

It is commonly assumed that the power spectrum $P_\delta(k)$ is scale invariant on large scales, $P_\delta(k) \propto k^{n_s}$ with $n_s \simeq 1$ ([Harrison 1970](#), [Peebles & Yu 1970](#), [Zeldovich 1972](#)). On small scales, the growth of structure is suppressed by the fast radiation driven expansion at early times. A perturbation in δ , which has the wavelength $\lambda = 2\pi/k$ can start growing at the cosmic epoch a_{start} if λ is smaller than the horizon size at that epoch, $\lambda < d_H(a_{\text{start}})$. But at early times, the expansion time scale t_{Hubble} is smaller than the collapse time scale t_{DM} :

$$t_{\text{Hubble}} \propto \frac{1}{\sqrt{G\rho_R}} < \frac{1}{\sqrt{G\rho_M}} \propto t_{\text{DM}}, \quad (3.24)$$

due to $\rho_R > \rho_M$ and the growth of the perturbation stalls. This suppression is effective from a_{start} until the epoch of matter-radiation equality a_{eq} , defined by $\rho_R(a_{\text{eq}}) = \rho_M(a_{\text{eq}})$, which takes place at a redshift of $z \simeq 24500$. In total,

fluctuations with $\lambda < d_H(a_{\text{eq}})$ are suppressed by $(a_{\text{start}}/a_{\text{eq}})^2$. Now, the time a_{start} is a function of the wavelength of the fluctuation, by $\lambda = d_H(a_{\text{start}})$. In the Einstein-de Sitter regime, $d_H(a)$ is approximated by $c/(aH(a)) \simeq a$, which gives a suppression proportional to λ^2 on scales smaller than the horizon size at the epoch of matter-radiation equality a_{eq} , the numerical value of which is $0.025/(\Omega_M h)$ Hubble radii.

With the suppression of growth $\propto \lambda^2 = (2\pi/k)^2 \propto k^{-2}$, one obtains for the asymptotic behaviour of $P_\delta(k) \propto k^{n_s-4} \simeq k^{-3}$ on small scales. Fitting functions, that link these two asymptotic regimes in a smooth way are obtained by applying Boltzmann solvers to the equations of cosmic structure formation. A particularly accurate fit is provided by [Bardeen et al. \(1986\)](#):

$$P(k) \propto k^{n_s} \cdot T^2(k) \quad \text{with the transfer function} \quad (3.25)$$

$$T(q) = \frac{\ln(1 + 2.34q)}{2.34q} \left[1 + 3.89q + (16.1q)^2 + (5.46q)^3 + (6.71q)^4 \right]^{-\frac{1}{4}} \quad (3.26)$$

The wave vector k is commonly divided by the shape parameter Γ introduced by [Efstathiou et al. \(1992\)](#) for CDM models and extended to models with $\Omega \neq 1$ by [Sugiyama \(1995\)](#):

$$q = \frac{k/\text{Mpc}^{-1}h}{\Gamma} \quad \text{with } \Gamma = \Omega_M h \exp\left(-\Omega_B \cdot \left[1 + \frac{\sqrt{2h}}{\Omega_M}\right]\right). \quad (3.27)$$

The normalisation of the power spectrum $P(k)$ is given by the parameter σ_8 , with is defined as the variance of the density fluctuations δ on scales of $R = 8$ Mpc:

$$\sigma_R^2 = \frac{1}{2\pi^2} \int_0^\infty dk k^2 W^2(kR) P(k). \quad (3.28)$$

Here, $W(r)$ is a window function of top-hat shape, the Fourier-transform of which is given by:

$$W(x) = \frac{3}{x^3} [\sin(x) - x \cos(x)] = \frac{3}{x} J_1(x). \quad (3.29)$$

The dark matter power spectrum $P_\delta(k)$ of the overdensity field $\delta(\mathbf{x})$ in the adiabatic Λ CDM model is shown in Fig. 3.4 for $\sigma_8 = 0.9$ and $n_s = 1$, which are used in all simulations in this thesis. The values measured by WMAP are $\sigma_8 = 0.84 \pm 0.04$ and $n_s = 0.93 \pm 0.03$ ([Spergel et al. 2003](#)).

3.2.1.4. Velocities in the large-scale structure

The equation of continuity $\dot{\rho} + \text{div} \mathbf{j}$ requires the existence of large-scale matter flows $\mathbf{j} = \rho \mathbf{v}$ due to the formation of objects ($\dot{\rho} > 0$). Assuming linear perturbations in density, $\rho = \rho_0 + \delta\rho$, and velocity, $\mathbf{v} = \delta\mathbf{v}$, the continuity equation reads $\dot{\delta} = -\text{div}(\delta\mathbf{v})$. For a harmonic perturbation with wave vector \mathbf{k} , the velocity perturbation $\delta\mathbf{v}$ is parallel to \mathbf{k} :

$$\delta\mathbf{v}(\mathbf{k}) = -ia \frac{\mathbf{k}}{k^2} \dot{\delta}(\mathbf{k}) \quad (3.30)$$

The time evolution of the density field δ is homogeneous in the linear regime, hence $\delta(\mathbf{k}) = D_+(a)\delta(\mathbf{k})$, yielding with the definition of the Hubble function $\dot{a} = aH(a)$ and the normalisation of the growth function:

$$\delta\mathbf{v}(\mathbf{k}) = -iaH(a)f(\Omega) \frac{\mathbf{k}}{k^2} \delta(\mathbf{k}) \quad (3.31)$$

The function f describes the dependence of the equation of continuity on cosmic time and mainly depends on the mass density Ω_M ([Peebles 1980](#), [Lahav et al. 1991](#))

$$f(\Omega) = \frac{d \ln \delta}{d \ln a} = \frac{d \ln D(a)}{d \ln a} \simeq \Omega_M(a)^{0.6} \quad (3.32)$$

The investigation of peculiar velocities in the local universe is a very interesting topic. Reconstructions of the cosmic velocity field as carried out e.g. with the POTENT algorithm proposed by [Bertschinger & Dekel \(1989, 1991\)](#) and [Dekel & Bertschinger \(1991\)](#) are used to test whether cosmic flows are irrotational and can be derived from a velocity potential, and yield important dynamical estimates of Ω_M and σ_8 .

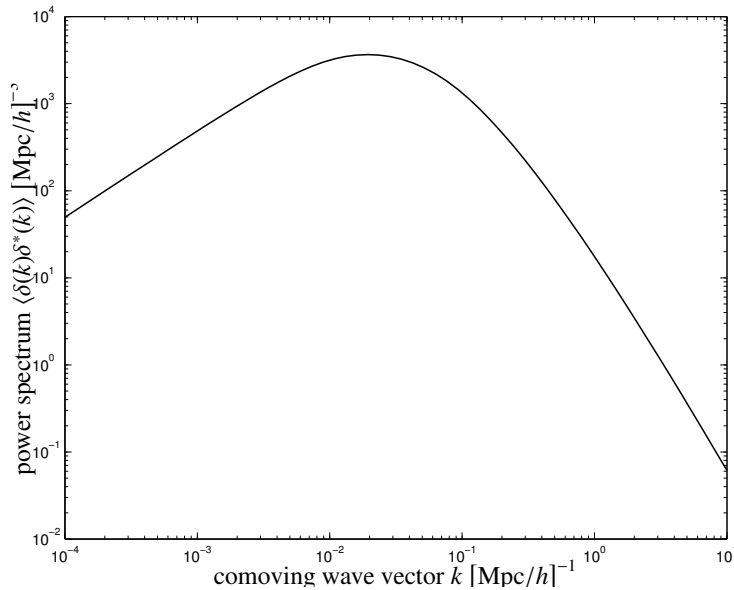


Figure 3.4.: The linear power spectrum $P_\delta(k)$ of the overdensity $\delta(\mathbf{x})$ in an adiabatic cold dark matter (CDM) model.

3.2.2. Numerical simulations of cosmic structure formation

In the course of the structure formation, objects with high values in the overdensity field δ are formed, e.g. galaxies ($\delta \simeq 10^6$), clusters of galaxies ($\delta \simeq 100$) and superclusters ($\delta \simeq 10$). Clearly, perturbation theory is not applicable for describing the dynamics of these objects. Furthermore, the structure formation proceeds heterogeneously, i.e. the relation $\delta(\mathbf{x}, a) = D_+(a)\delta(\mathbf{x})$ is violated, which leads to a coupling of modes $\delta(\mathbf{k})$ in Fourier space. This can easily be understood because the growth function acquires a dependency on the spatial coordinates apart from the time variable: $D_+(\mathbf{x}, a)$. The Fourier transform of $D_+(\mathbf{x}, a)\delta(\mathbf{x})$, being a product of two functions, is a convolution, which links modes in Fourier space with different wave vectors \mathbf{k} . Thirdly, non-linear processes give rise to non-Gaussian features. This is simply due to the fact that the density fluctuation field is bounded to small values $\delta > -1$, but an upper bound does not exist. Hence, the distribution of δ necessarily develops a non-vanishing skewness in the course of structure formation, and the statistical description of the properties of δ based on 2-point correlation functions and power spectra $P_\delta(k)$ fails.

In order to investigate cosmic structure formation in the non-linear regime, numerical simulations are carried out. These codes, the most notable of which is GADGET (Springel et al. 2001, Springel & Hernquist 2002), numerically solve the equations of cosmic structure formation,

$$\dot{\rho} + \text{div}(\rho\mathbf{v}) = 0, \quad \dot{\mathbf{v}} + (\mathbf{v}\nabla)\mathbf{v} = -\frac{1}{\rho}\nabla p - \nabla\Phi, \quad \Delta\Phi = 4\pi G\rho, \quad (3.33)$$

by introducing particles in order to discretise the density field ρ and the velocity field \mathbf{v} . Extensions to GADGET include baryonic dynamics, magnetic fields and cosmic rays. Simulations carried out with GADGET are a key tool of this thesis.

3.3. Physics of clusters of galaxies

3.3.1. Formation of clusters of galaxies

3.3.1.1. Spherical collapse

A key concept in the CDM model of cosmic structure formation by the hierarchical build-up of structure from small scales to large scales is the formation of dark matter haloes. These are long-lived quasi-equilibrium systems

of dark matter particles which were formed by gravitational collapse (White & Narayan 1987). As a model, one considers a spherically symmetric density perturbation which evolves under the influence of gravity embedded in an expanding background. In a matter dominated universe, the radius r of the perturbation evolves with time t according to a cycloidal solution of $\ddot{r} = -GM/r^2$ (Longair 1998, Peacock 1999):

$$r = A(1 - \cos \theta) \quad (3.34)$$

$$t = B(\theta - \sin \theta) \quad (3.35)$$

with $A^3 = GMB^2$ and the phase angle θ . The spherical perturbation will break away from the Hubble expansion and reach a maximal radius at $\theta = \pi$, $t = \pi B$. Following the time evolution further, the sphere will collapse to a point at $\theta = 2\pi$. Extrapolating linear theory to this time yields $\delta = \delta_c \equiv 1.69$. In reality, dissipation sets in and converts the kinetic energy of the collapse, or, equivalently, the gravitational binding energy released by the collapse to random motion of the particles. At this stage, the overdensity of the sphere at virialisation has reached a value of $\delta \simeq 200$.

The exact profile of a virialised density perturbation after gravitational collapse is governed by the dissipative processes which cause dark matter systems to relax, e.g. two-body relaxation, dynamical friction and violent relaxation. From numerical n -body simulations it is found that the profiles of dark matter haloes are described by a universal law (Navarro et al. 1996):

$$\frac{\rho(r)}{\rho_{\text{crit}}} = \frac{\delta_c}{x(1+x)^2} \quad \text{with} \quad x = \frac{r}{r_s}, \quad (3.36)$$

with $r_s = r_{\text{vir}}/c$. r_{vir} is defined that the mean density inside a sphere of that radius is 200 times the critical density. c is called concentration parameter:

$$\delta_c = \frac{200}{3} \frac{c^3}{\ln(1+c) - \frac{c}{1+c}}. \quad (3.37)$$

Luminous objects like galaxies are thought to form by cooling and condensation inside CDM haloes (White & Rees 1978).

3.3.1.2. Press-Schechter theory

According to the derivation of Press & Schechter (1974), the number density $n(M, z)dM$ of haloes of mass M per unit comoving volume as a function of redshift z is given by:

$$n(M, z)dM = \sqrt{\frac{2}{\pi}} \frac{\bar{\rho}_0}{M} \frac{dv}{dM} \exp\left(-\frac{v^2}{2}\right) dM \quad \text{with} \quad v \equiv \frac{\delta_c}{D_+(z)\sigma(M)}, \quad (3.38)$$

and the critical overdensity $\delta_c = 1.69$, which only weakly depends on cosmology. Press-Schechter theory has been put onto a solid mathematical foundation by Bond et al. (1991): A massive object will form by gravitational collapse, if the average overdensity in a volume containing that mass exceeds some threshold value δ_c , independent of substructure. The location, properties and number densities of these bound objects can be estimated by smoothing the initial linear density field with a filter of characteristic length R_f . Peaks in the filtered density field can be assigned a mass $M \sim \frac{4}{3}\pi\rho_0 R_f^3$.

In order to link the number of objects of mass M to the peak statistics of a Gaussian random field smoothed on the scale R_f , Bond et al. (1991) proceed by considering the random trajectory of δ at a fixed point in space when varying R_f with the initial conditions $R_f = \infty$ and $\delta = 0$. The filtered field starts to develop fluctuations of increasing amplitude as the smoothing radius R_f is decreased. If the filtered field δ first exceeds the threshold value δ_c set by spherical collapse theory, an object of mass $M(R_f)$ will form. This analysis is most easily performed using a sharp truncation in k -space as a filter. Decreasing R_f corresponds to broadening the k -space filter which adds new k -space shells, all of which are independent for a Gaussian random field. The trajectory $\delta(R_f)$ is then a random walk. The probability that a random walk starting at $\delta = 0$ exceeds the threshold δ_c is then given by $\text{erfc}\left[\frac{\delta_c}{\sqrt{2}\sigma(M)}\right]$, where $\sigma(M)$ is the variance of the top-hat filtered field δ . From this result, eqn. (3.38) follows by differentiation.

As summarised in Mo & White (2002), the number density of haloes of mass M depends of course on the shape of the power spectrum and its normalisation σ_8 . The increase of $D_+(z)$ with cosmic time causes the threshold value δ to decrease such that massive objects form at late times. Hence, low-mass objects form early in the cosmic mass hierarchy from strong fluctuations in contrast to massive objects, that form at late times from weak fluctuations.

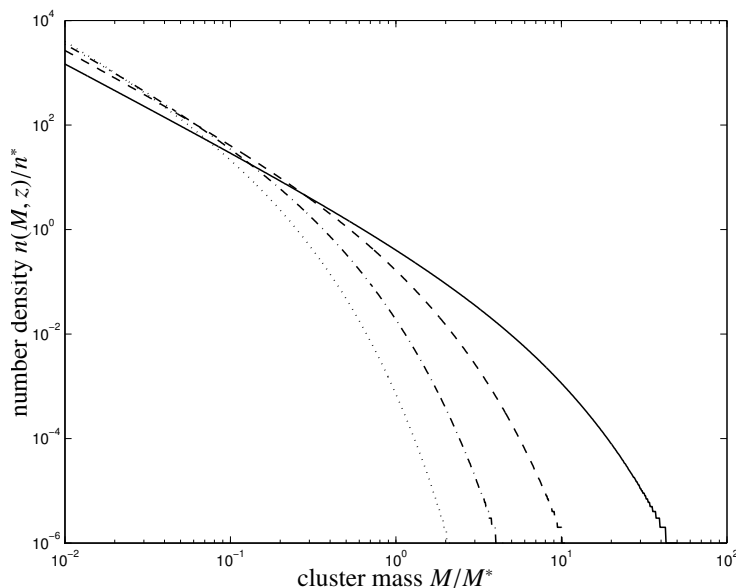


Figure 3.5.: The Press-Schechter mass function $n(M, z)dM$ for redshifts $z = 0$ (solid), $z = 1$ (dashed line), $z = 2$ (dash-dotted line) and $z = 3$ (dotted line), for the Λ CDM cosmology.

The formalism has been extended by [Sheth & Tormen \(1999\)](#) to non-spherical ellipsoidal collapse to yield a slightly modified mass function $n(M, z)dM$. The Press-Schechter function $n(M, z)dM$ at four different redshifts z is given in Fig. 3.5. The increase of the mass scale M_* at which the power law breaks with decreasing redshift z can easily be seen, indicating the growth of massive objects by merging of smaller objects with time. A typical value for the number density of clusters n^* is ≈ 100 clusters at $z = 0$ in a comoving volume of $(100 \text{ Mpc}/h)^3$, with masses $M > 5 \times 10^{13} M_\odot/h$.

3.3.2. Observational properties of clusters

Galaxies form associations ranging from pairs of galaxies to small groups with tens of member galaxies to large clusters containing as many as a few thousand members. Clusters of galaxies are the largest and most massive gravitationally bound systems in the Universe. The most massive clusters reach masses of up to $10^{15} M_\odot$, which makes them massive enough to cause distortions in the images of background galaxies due to gravitational lensing. Mass estimates with the virial theorem applied to the motion of galaxies inside the cluster yields large discrepancies with the mass obtained by adding up the masses of the individual galaxies and the mass of the intra-cluster medium. This leads to the conclusion that clusters largely consist of dark matter, in fact, they are large enough to be representative samples of the universal mass composition. In the cores of clusters of galaxies, hot intergalactic gas has been detected, both by its X-ray emission and by its interaction with the CMB radiation. Clusters of galaxies are laboratories for studying the non-linear phases of structure evolution, the interplay between dark matter dynamics and gas physics, and the evolution of galaxies in the cluster environment and the interaction of active galaxies with the intra-cluster medium.

In this section, the observational properties of clusters of galaxies as relevant to this work are summarised. Clusters of galaxies appear vastly different in differing observational channels. Fig. 3.6 might give a first impression: The figure compares the column density of baryons (in units of g/cm^2) with the thermal Sunyaev-Zel'dovich map (the dimensionless thermal Comptonisation y) and the X-ray map (in units of erg/cm^2 in the energy range $0.1 \text{ keV} \dots 10 \text{ keV}$) of a simulated massive cluster ($M = 2.25 \times 10^{15} M_\odot/h$) at redshift $z = 0$. The baryon distribution and the thermal Comptonisation are very similar in size, but the baryon distribution shows a great amount of substructure, whereas the Comptonisation map appears to be smooth. This is due to the fact that the Comptonisation measures pressure, which is a smooth quantity because the substructure is in pressure equilibrium with the ambient gas. The X-ray emission is concentrated to the central region of the cluster, because the X-ray emissivity

is proportional to the density squared.

3.3.2.1. Gravitational lensing

Due to their large masses, clusters of galaxies distort the shapes of background galaxies by gravitational lensing. They are the only cosmological objects massive enough to give rise to lensing effects that can be seen by eye. Background galaxies appear to be stretched into impressive giant luminous arcs and arclets, which can be used for reconstructing the mass distribution (Broadhurst et al. 2004). These reconstructions are in agreement with expectations from n -body simulations (Navarro et al. 1996, 2004). The theory of gravitational lensing and numerical methods for ray-tracing studies on cosmological n -body simulations of the large-scale structure and individual clusters of galaxies will be developed in detail in Chapter 12.

3.3.2.2. Optical properties of clusters of galaxies

Historically clusters were found as overdensities in the galaxy number density by visual inspection of optical sky survey plates. In this way, Abell et al. (1989) have compiled the classic Abell catalogue comprising 4073 entries. They required that clusters had more than 30 member galaxies within the magnitude range m_3 to $m_3 + 2$ (m_3 being the apparent magnitude of the third brightest cluster member) and with a nominal redshift $z \leq 0.2$. The total number of galaxies belonging to a cluster is difficult to assess, but clusters with as many as a few thousand member galaxies have been found. A very interesting point is the density-morphology relation, which states that inside clusters of galaxies the ratio of the numbers of elliptical to spiral galaxies is inverted relative to the field (Dressler 1980, 2004). This means that the galaxies interact heavily with the cluster.

The distribution $\Phi(L)$ of the luminosities L of the cluster member galaxies are described by the Schechter function (Schechter 1976),

$$\Phi(x)dx = \Phi^* x^\alpha \exp(-x)dx \quad \text{with} \quad x = \frac{L}{L^*}, \quad (3.39)$$

with a characteristic luminosity L^* , or, equivalently, a characteristic absolute magnitude M^* . Parameter values are $\alpha = 5/4$, $\Phi^* = 0.012h^3/\text{Mpc}^3$ and $M_B^* = -20.6$. Dividing the integrated luminosity function by the integrated mass function yields the mass-to-light ratio of clusters of galaxies. A typical value for M/L is $250 M_\odot/L_\odot$. At low masses and luminosities, the Press-Schechter mass function and the Schechter luminosity function are not related by a fixed mass-to-light ratio M/L . This is interpreted in a way that in low-mass haloes a mechanism is active that keeps those systems from forming stars. Although a number of possible mechanisms has been proposed, it is still unclear what exactly causes these low-mass systems to be devoid of stars.

3.3.2.3. X-ray emission by clusters of galaxies

Clusters of galaxies are strong emitters of X-ray radiation, which is produced as thermal bremsstrahlung by a hot ($T \simeq 10^7 \text{ K} \dots 10^8 \text{ K}$) and dilute ($n = 10^2 \text{ m}^{-3} \dots 10^3 \text{ m}^{-3}$) plasma situated in the core of the cluster. X-ray luminosities reach values of up to $L_X = 10^{45} \text{ erg/s}$. Apart from thermal bremsstrahlung, X-ray observatories have detected atomic lines of highly ionised metals such as Fe^{26+} . In a relaxed cluster, the hot plasma is in dynamic equilibrium with the dark matter, i.e. the ratio β of the specific kinetic energy $\sigma_{\text{vel}}^2/2$ stored in the random motion of the dark matter particles (or, equivalently, the galaxies which act as tracer particles), which is characterised by the velocity dispersion $\sigma_{\text{vel}}^2 = \langle v_{\text{pec}}^2 \rangle$ and the thermal energy of the gas $3k_B T/(2\mu m_H)$,

$$\beta = \frac{\mu m_H \sigma_{\text{vel}}^2}{3k_B T}, \quad (3.40)$$

is of order unity. Hence, $\sigma_{\text{vel}} = 10^6 \text{ m/s}$ corresponds to a temperature of $T \simeq 10^8 \text{ K}$. In eqn. (3.40), $\mu \simeq 0.6$ is the mean atomic weight of the gas and m_H denotes the mass of a hydrogen atom. If the hot plasma is in pressure equilibrium, a determination of the mass $M(< r)$ inside the radius r is possible (Fabricant et al. 1980):

$$\frac{GM(< r)}{r} = -\frac{k_B T}{\mu m_H} \left(\frac{d \ln \rho}{d \ln r} + \frac{d \ln T}{d \ln r} \right) \quad (3.41)$$

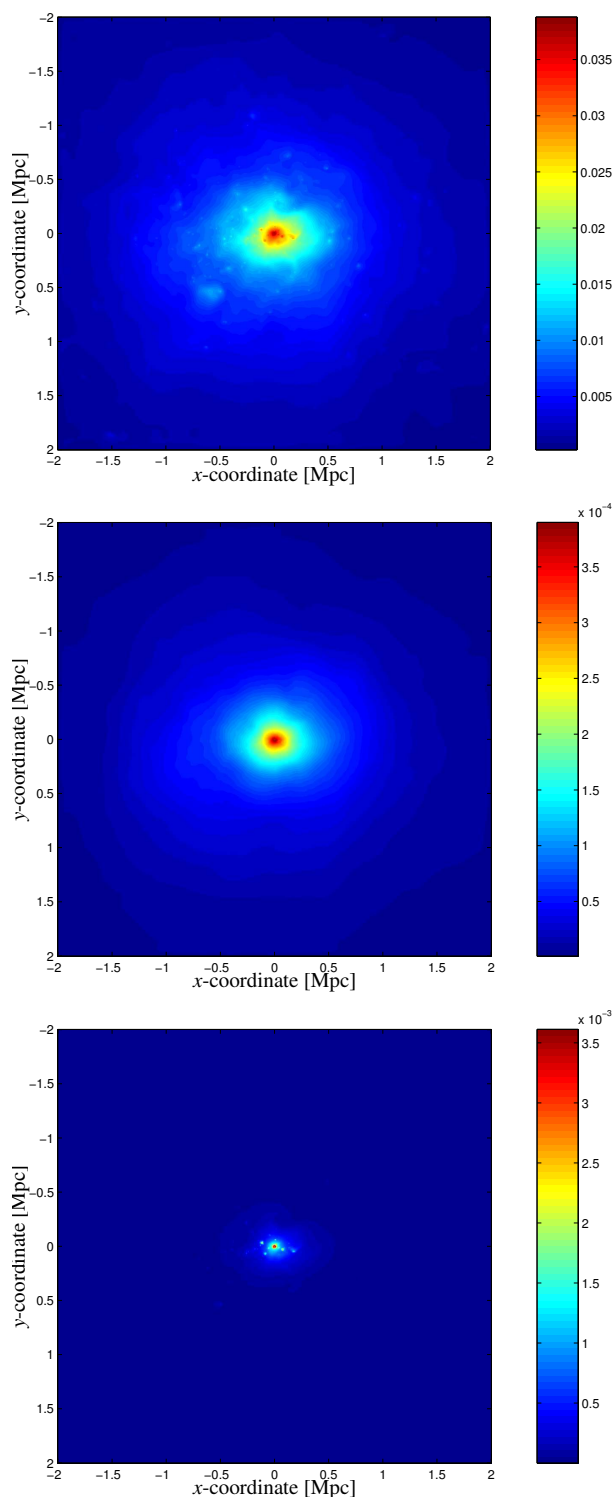


Figure 3.6.: A GADGET simulated cluster of galaxies of mass $M = 2.25 \times 10^{15} M_{\odot}/h$ at redshift $z = 0$. The top panel shows the projected baryonic matter distribution $\int \rho_B dz$ in units of g/cm^2 , the centre panel the thermal Comptonisation $y = \int n_e T_e dz$, and the bottom panel the distribution of thermal X-rays $S_X = \int n_e^2 \sqrt{T_e} dz$ in units of erg/cm^2 (The photon energies were restricted to the range 0.1 keV ... 10 keV). The (mass weighted) X-ray temperature of this cluster is $T_X = 9.17$ eV. Data has been kindly provided by K. Dolag.

The temperature T can be determined by spectroscopy, and the mass density profile $\rho(r)$ by analysing the X-ray surface brightness map $S_X(r)$,

$$S_X(r) = \frac{1}{2\pi} \int_r^\infty dr' \frac{r'}{\sqrt{r'^2 - r^2}} \kappa(r'), \quad (3.42)$$

with the emissivity $\kappa(r) \propto n_e^2 \sqrt{T}$. By assuming primordial element composition and a value for the ratio of baryonic and dark matter density, the surface brightness map, being an Abel integral, can be inverted to find the density $\rho(r)$ (Cavaliere 1980). With the King-profile as an approximate description for the dark matter profile, by assuming constant temperature T and a relation between gas density ρ_g and dark matter density ρ , one obtains the β -profile (Cavaliere & Fusco-Femiano 1978), which is a reasonable fit to X-ray observations (e.g. Abell 1413, Pratt & Arnaud 2002):

$$\frac{\rho_g}{\rho_g^{(0)}} = \left(\frac{\rho}{\rho^{(0)}} \right)^\beta \quad \longrightarrow \quad \rho_g(r) = \rho_g^{(0)} \left(1 + \left(\frac{r}{r_c} \right)^2 \right)^{\frac{3\beta}{2}}. \quad (3.43)$$

Eqn. (3.43) is a very useful model and will be frequently used in this thesis in analytic estimates concerning the Sunyaev-Zel'dovich effect. For relaxed clusters, simple relations between mass M , temperature T and X-ray luminosity L_X hold (Kaiser 1986, Bryan & Norman 1998). The mass-temperature relation has been confirmed by many X-ray observations and numerical simulations (Navarro et al. 1995). In spherical collapse, the velocity dispersion is a function of mass. Assuming isothermality yields:

$$k_B T = \frac{GM^{2/3} \mu m_H}{2\beta} \left(\frac{H^2(z) \Delta_c}{2G} \right)^{1/3} \quad \longrightarrow \quad T \propto M^{2/3}, \quad (3.44)$$

with the (cosmology-dependent) overdensity $\Delta_c = 18\pi^2$ of a spherical top-hat perturbation that has just virialised (Peebles 1980). The bolometric X-ray luminosity L_X can be obtained by integration:

$$L_X = 6.8 \times 10^{44} \left(\frac{k_B T}{1.0 \text{ keV}} \right)^2 \sqrt{\Delta_c} H^2(z) \left(\frac{\Omega_B}{\Omega_M} \right)^2 \text{ erg/s} \quad \longrightarrow \quad L_X \propto T^2. \quad (3.45)$$

In reality, clusters are rarely in a relaxed state but exhibit a wealth of X-ray features such as cool cores, cold fronts and X-ray cavities (Sarazin 1986). Scaling relations linking the X-ray observables as derived above are equally well applicable and very useful in estimations of Sunyaev-Zel'dovich properties of clusters of galaxies.

3.3.2.4. Thermal and kinetic Sunyaev-Zel'dovich effect

Another observational channel which is sensitive to the distribution of baryons inside clusters of galaxies is the Sunyaev-Zel'dovich effect. CMB photons passing through a cluster will experience Compton collisions with electrons of the hot ionised intra-cluster medium, causing distortions in the spectrum of the emergent radiation. This Comptonisation of CMB photons on electrons of the ICM is referred to as the thermal Sunyaev-Zel'dovich (SZ) effect (Sunyaev & Zel'dovich 1972, 1980). In the easiest interpretation, Compton scattering couples the hot reservoir of thermal energy stored inside the ICM to the cold CMB. According to the laws of thermodynamics, there will be a transfer of thermal energy from the hot to the cold reservoir. Because the ICM is very dilute and the Compton interaction only weak, the relaxation time for the two reservoirs to reach the same equilibrium temperature is long, much longer than the Hubble time. In fact, the CMB is not thermalised, but one observes only a tiny variation in the CMB spectrum in the direction of the cluster (being of the order 10^{-4}), because the direction dependence of the Compton interaction removes low-energetic photons from the line-of-sight, and scatters photons with higher energies into the line-of-sight, giving rise to the peculiar spectral signature of the SZ-effect.

In order to analyse these distortions quantitatively, the transport equation governing the effect of Compton scattering on the photon spectrum needs to be derived. The change in the photon phase space occupation number $n(\omega)$ as a function of photon energy $\hbar\omega \equiv h\nu$ can be derived with the Kompaneets equation, which is a quantum mechanical extension to the Fokker-Planck equation (Peacock 1999):

$$\dot{n} = \left(\frac{\sigma_T n_e \hbar}{m_e c} \right) \frac{1}{\omega^2} \frac{\partial}{\partial \omega} \left\{ \omega^4 \left[n(n+1) + \frac{k_B T_e}{\hbar} \frac{\partial n}{\partial \omega} \right] \right\}. \quad (3.46)$$

The optical depth of the ICM in clusters is very low so that photons can be considered to scatter once at most. In this case, the Kompaneets equation yields a linear change in the phase space occupation number $n(\omega)$,

$$\Delta n = y \frac{1}{v^2} \frac{\partial}{\partial v} \left(v^4 \frac{\partial n}{\partial v} \right) \quad \text{with} \quad y \equiv \frac{\sigma_T k_B}{m_e c^2} \int dz n_e T_e. \quad (3.47)$$

The quantity y is the thermal Comptonisation, which measures the product of electron density n_e and temperature T_e , i.e. the ICM pressure along the line-of-sight. Inserting a Planckian spectral distribution for the CMB $S(x) = S_0 x^3 / (\exp(x) - 1)$ with the flux density $S_0 = 22.9 \text{ Jy/arcmin}^2$ yields the flux change $S_{\mathcal{Y}}/S_0 = \Delta n/n$:

$$S_{\mathcal{Y}}(x) = y S_0 \frac{x^4 \exp(x)}{(\exp(x) - 1)^2} \left[x \frac{\exp(x) + 1}{\exp(x) - 1} - 4 \right]. \quad (3.48)$$

Consequently, photons are redistributed in energy from the Rayleigh-Jeans part of the Planckian curve to the Wien regime. The SZ-effect vanishes at a frequency of $x = 3.83 \rightarrow \nu = 217 \text{ GHz}$, which is an important tool in SZ-observations. A very elegant approach to the spectral redistribution has been found independently (and almost simultaneously) by [Enßlin & Kaiser \(2000\)](#) and [Sazonov & Sunyaev \(2000\)](#), who describe the spectral redistribution in terms of a convolution kernel. In this formalism, the SZ effect can be extended to relativistic electrons.

Apart from the unordered thermal motion of the ICM electrons, CMB photons may interact with the bulk motion of baryonic matter streams inside a cluster or of the motion of the cluster as a whole relative to the CMB. The isotropic CMB appears to have a dipolar structure from a frame of reference comoving with a baryonic flow, and the direction dependence of the Compton scattering causes a transfer of kinetic energy of the cluster to the CMB spectral distribution. This is known as the kinetic Sunyaev-Zel'dovich effect. The flux change $S_{\mathcal{W}}$ is given by:

$$S_{\mathcal{W}} = w S_0 \frac{x^4 \exp(x)}{(\exp(x) - 1)^2} \quad \text{with} \quad w = \frac{\sigma_T}{c} \int dz n_e v_r. \quad (3.49)$$

In this formula, v_r is the radial component of the cluster's velocity in the CMB frame. The frequency dependence of the thermal and kinetic SZ-effects in comparison to the Planckian CMB spectrum is given in Fig. 3.7. Important SZ-quantities are the Comptonisations integrated over the cluster face,

$$\mathcal{Y} = \int d\Omega y \quad \text{and} \quad \mathcal{W} = \int d\Omega w, \quad (3.50)$$

which determine the signal strength in an SZ-observation. The SZ-effects are valuable tools to search for clusters in CMB data. Because no photons are lost in the scattering process, and the Comptonisations \mathcal{Y} and \mathcal{W} decrease only slowly with redshift z , they are likely to yield detections out to large distances. Applied to individual objects, the thermal SZ-effect measures pressure differences inside the ICM and may be a powerful diagnostic of plasma dynamics.

3.3.2.5. integrated Sachs-Wolfe/Rees-Sciama effect

The growth of structure imprints additional anisotropies on the cosmic microwave background (CMB) by the time variation of the gravitational potentials along the propagation path of a CMB photon. When transversing time-varying potentials, the energy gains and losses a CMB photon experiences in entering and leaving potential wells do not cancel exactly. In this way, one expects a net blueshift of CMB photons in forming voids and a net redshift in matter-accreting clusters of galaxies. This effect is called the integrated Sachs-Wolfe (iSW) effect in the regime of linear structure formation ([Sachs & Wolfe 1967](#)) and Rees-Sciama (RS) effect ([Rees & Sciama 1968](#)) if the density perturbations grow nonlinearly. The perturbations ΔT of the CMB sky temperature T_{CMB} can be written as:

$$\tau \equiv \frac{\Delta T}{T_{\text{CMB}}} = -\frac{2}{c^3} \int dw \frac{\partial \Phi}{\partial \eta}, \quad (3.51)$$

where $\partial \Phi / \partial \eta$ is the derivative of the gravitational potentials with respect to conformal time η .

The iSW/RS effect is of particular interest, since it measures the dynamics of structure formation independent of the type and state of matter. The iSW/RS effect has been studied theoretically in individual objects ([Martínez-González et al. 1990](#)) and could be used for the investigation of cluster mergers ([Rubiño-Martín et al. 2004](#)). More

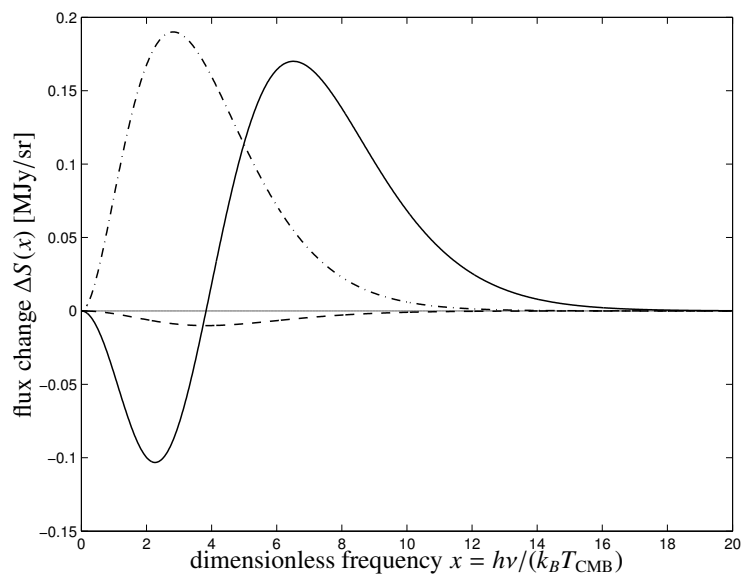


Figure 3.7.: The frequency dependence of the Sunyaev-Zeldovich flux change $\Delta S(x)$ as a function of dimensionless frequency $x = h\nu/(k_B T_{\text{CMB}})$, for a cluster with electron temperature $T_e = 10$ keV, thermal Comptonisation $y = 10^{-4}$, and velocity $v_{\text{pec}} = 500$ km/s. The plot shows the frequency dependence of the thermal SZ-effect (solid line), the kinetic SZ-effect (dashed line) and the CMB black body spectrum (dash-dotted line) scaled by 5×10^{-4} for comparison.

importantly, it is sensitive to mapping the large-scale structure as it highlights the sites of active structure formation (Kaiser 1982, Martínez-González & Sanz 1990, Martínez-González et al. 1992, 1994, Seljak 1996b).

In conclusion, the various observational channels are powerful diagnostics of the cluster's dynamics, in the baryonic as well as in the dark matter sector. Clusters of galaxies are by far more complicated objects than mere gravitationally interacting swarms of galaxies: Future experiments will open up the SZ-window which complements X-ray observations in important respects and directly investigates the pressure distribution and deviations from hydrostatic equilibrium of the ICM. Gravitational lensing and the RS-effect shed light on dark matter distribution and dark matter dynamics, whereas the kinetic SZ-effect is sensitive to baryonic streams inside clusters.

4. PLANCK-surveyor

4.1. Introduction to the PLANCK-surveyor

The PLANCK-surveyor^{1,2,3} (Tauber 2000) is a European space mission dedicated to the mapping of the CMB anisotropies. It is scheduled for launch in 2007 and will be the fourth CMB observatory in a line of successful space missions: RELIKT (Strukov et al. 1992a,b), COBE (Hauser et al. 1998, Wright et al. 1996) and WMAP (Hinshaw et al. 2003). A core component of my thesis is the simulation of Sunyaev-Zel'dovich observations to be carried out with PLANCK (Chapters 5, 6, 7 and 8), apart from the prediction of the observability of the integrated Sachs-Wolfe effect (Chapter 13).

4.2. PLANCK mission objectives

PLANCK will carry out a polarisation sensitive survey of the entire microwave sky in 9 frequency bands ranging from 30 GHz up to 857 GHz with unprecedented angular resolution of up to 5'0. Its scientific objectives are:

- **CMB studies:** PLANCK will map the CMB sky up to multipole moments exceeding $\ell = 2000$, well beyond the third acoustic peak into the Silk damping regime. Its cartography of the microwave sky and the estimation of the CMB power spectrum enable the determination of cosmological parameters (matter density Ω_M , cosmological constant Ω_Λ , baryon density Ω_B , the spectral index of the dark matter power spectrum n_s at large scales and Hubble's constant H_0) with an accuracy better than 1% (Bond et al. 1997, Zaldarriaga et al. 1997). It will yield insights into the initial conditions of structure formation (White et al. 1994), shed light on the origin of primordial fluctuations along with a determination of inflation scenarios (Bond et al. 1996, Steinhardt 1996), where the Gaussianity of the primordial fluctuations is an important issue, and will test for topological defects (Kibble 1976, Coulson et al. 1994). Further areas of interest in primary CMB fluctuations include constraints on properties of dark matter and dark energy (Dodelson et al. 1996) and the production of chemical elements after reionisation (Basu et al. 2004).
- **CMB polarisation:** The detection of polarised CMB radiation along with the determination of power spectra of the polarised components will yield important constraints on cosmic reionisation scenarios. Another important reason for measuring the power spectra of polarised components is their power to break degeneracies of parameter constellations that result from the measurement of the temperature autocorrelation function alone (Efstathiou & Bond 1999).
- **thermal Sunyaev-Zel'dovich effect:** PLANCK is expected to detect about 10^4 clusters of galaxies from their thermal SZ-signature. This cluster catalogue will reach out to very large redshifts and surpasses the classic Abell catalogues and all X-ray catalogues by the number of entries. This catalogue will yield insights into the cosmic evolution of clusters of galaxies which is closely linked to the parameters σ_8 and Ω_M and the dark-energy density Ω_Ω and the equation of state parameter w . It is doubtful whether PLANCK's sensitivity will be sufficient to determine velocities of clusters by the kinetic Sunyaev-Zel'dovich effect (Aghanim et al. 2001).

¹<http://planck.mpa-garching.mpg.de>

²<http://sci.esa.int/planck>

³<http://astro.estec.esa.int/Planck>

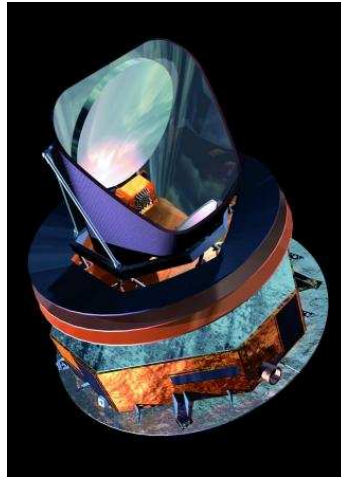


Figure 4.1.: The PLANCK-surveyor satellite

- **gravitational lensing:** The sensitivity and angular resolution of PLANCK will enable to detect deviations from the primordial CMB power spectrum due to gravitational lensing of the CMB by the large-scale structure. Another lensing effect is the integrated Sachs-Wolfe or Rees-Sciama effect, which should be strong enough to be detectable as a correction to the CMB power spectrum on large angular scales. Gravitational lensing has been the subject of many investigations, for instance by [Seljak \(1994, 1996a\)](#), [Cole & Efstathiou \(1989\)](#), [Bartelmann & Schneider \(2001\)](#).
- **extragalactic point sources:** PLANCK will yield an extensive catalogue of extragalactic point sources and will be able to give a crude determination of their spectral properties. Possible types of point sources include infrared ([Franceschini & Andreani 1995](#)) and radio galaxies, AGNs, QSOs and blazars and inverted spectra radio sources. PLANCK will complement precursing infrared observatories in studying the cosmic far infrared background ([Puget 1998a,b](#)).
- **Galactic studies:** PLANCK's channels above 353 GHz will be, due to their supreme angular resolution, especially suited to study Galactic foregrounds. PLANCK will determine the properties and temperatures of Galactic dust, and will examine the cloud and cirrus morphology ([Boulanger 1990](#)). In the field of Galactic synchrotron emission, it will determine spectral indices at high frequencies, will constrain the Galactic cosmic ray distribution and map the Galactic magnetic field ([Falgarone et al. 1992](#), [Tagger et al. 1995](#)).
- **Solar system studies:** PLANCK is expected to detect about 100-150 asteroids and comets ([Cremonese et al. 2002](#)), and will help to determine their thermal properties at low frequencies. Another sub-millimetric emission component of the Solar system to be investigated is the zodiacal light ([Reach et al. 2003a](#)).

4.3. Instrument description

The PLANCK-surveyor satellite is depicted in Fig. 4.1. Its optical system consists of two aluminium coated carbon fiber mirrors arranged in an off-axis tilted Gregorian configuration that guides the radiation to a detector array. The primary mirror is an off-axis mounted paraboloid with a diameter of 1.3 m and a focal length of 72 cm. The secondary mirror is a hyperboloid with 80 cm diameter and a focal length of 50 cm. The total wavefront error will be smaller than $40 \mu\text{m}$.

There will be two types of receivers onboard: The low-frequency instrument (LFI), which operates at frequencies of 30 GHz, 44 GHz and 70 GHz, and the high-frequency instrument (HFI), for observations at frequencies between 100 GHz and 857 GHz. The LFI uses high electron mobility transistors as receivers, cooled to a temperature of 20 K. The HFI is an array of bolometers, which are cooled to a temperature of 0.1 K. Some of the HFI-channels are equipped with polarisation filters. The sensitivity of PLANCK will suffice to record fluctuations of $2 \mu\text{K}$ on angular

scales below 10° . PLANCK will carry out its survey from the second Lagrangian point $L2$ in the Earth-Sun system at a distance of approximately 1.5×10^6 km from Earth.

5. Construction of all-sky thermal and kinetic Sunyaev-Zel'dovich maps

Abstract

All-sky thermal and kinetic Sunyaev-Zel'dovich (SZ) maps are presented for assessing how well the PLANCK mission can find and characterise clusters of galaxies, especially in the presence of primary anisotropies of the cosmic microwave background (CMB) and various galactic and ecliptic foregrounds. The maps have been constructed from numerical simulations of structure formation in a standard Λ CDM cosmology and contain all clusters out to redshifts of $z = 1.46$ with masses exceeding $5 \times 10^{13} M_{\odot}/h$. By construction, the maps properly account for the evolution of cosmic structure, the halo-halo correlation function, the evolving mass function, halo substructure and adiabatic gas physics. The velocities in the kinetic map correspond to the actual density environment at the cluster positions. I characterise the SZ-cluster sample by measuring the distribution of angular sizes, the integrated thermal and kinetic Comptonisations, the source counts in the three relevant PLANCK-channels, and give the angular power-spectra of the SZ-sky. While my results are broadly consistent with simple estimates based on scaling relations and spherically symmetric cluster models, some significant differences are seen which may affect the number of cluster detectable by PLANCK.

5.1. Introduction

The Sunyaev-Zel'dovich (SZ) effects (Sunyaev & Zel'dovich 1972, 1980, Birkinshaw 1999, Rephaeli 1995) have evolved from physical peculiarities to valuable and sound observational tools in cosmology. The thermal SZ-effect arises because photons of the cosmic microwave background (CMB) experience Compton-collisions with electrons of the hot plasma inside clusters of galaxies and are spectrally redistributed. The amplitude of the modulation of the Planckian CMB spectrum is a measure of the cluster electron column density and temperature. Alternatively, CMB photons may gain energy by elastic Compton collisions with electrons of the intra-cluster medium (ICM) due to the peculiar motion of the cluster relative to the CMB. This so-called kinetic SZ-effect is proportional to the peculiar velocity weighted electron column density and directly measures the cluster's velocity component parallel to the line-of-sight relative to the comoving CMB frame.

The advancement in sensitivity and angular resolution of sub-millimeter and microwave receivers have allowed high quality interferometric imaging of more than fifty clusters of galaxies by ground based telescopes (Carlstrom et al. 2002) out to redshifts of ~ 0.8 , despite incomplete coverage of the Fourier plane. Apart from its primary scientific objective, namely the cartography of the CMB with angular resolutions close to $5'$, the upcoming PLANCK mission (Mandolesi et al. 1995, Tauber 2000) will be a unique tool for observing clusters of galaxies by their SZ-signature. PLANCK is expected to yield a cluster catalogue that is surpassing the classic optical Abell catalogues or any existing X-ray catalogue in numbers as well as in depth and sky coverage.

The capability of PLANCK to detect SZ-clusters has been the subject of many recent works, pursuing analytical (Aghanim et al. 1997, Delabrouille et al. 2002, Bartelmann 2001, Moscardini et al. 2002) as well as semianalytical (Kay et al. 2001, Hobson & McLachlan 2003) and numerical approaches (Herranz et al. 2002, White 2003). Their consensus is an expected total number of a few times 10^4 clusters and the detectability of (sufficiently massive) clusters out to redshifts of $z \lesssim 1$. The authors differ mainly in the expected distribution of the detectable clusters in redshift z . Where addressed, the authors remain sceptic about the detectability of the kinetic SZ-effect.

As a result of various approximations made, there are clearly limitations in these studies: Concerning the SZ profiles of isolated clusters, simplifying assumptions like spherical symmetry, complete ionisation and isothermality have usually been made. Analytical treatments mostly rely on β -profiles for modeling the spatial variation of the Compton- y parameter. Temperature models mostly make use of scaling laws derived from spherical collapse theory

or are taken from X-ray observations. Naturally, the halo-halo correlation function is not taken account of, neither do the velocities correspond to the actual density environment, they are commonly drawn from a (Gaussian) velocity distribution.

The primary application of the all-sky SZ-maps would lie in the assessment of the extent to which cluster substructure and deviations from spherical symmetry, the halo-halo clustering and deviations from the scaling-laws alter the predictions made based on analytic methods.

Additionally, the investigations mentioned above lack the inclusion of galactic foregrounds (for a comprehensive review of foregrounds concerning PLANCK, see [Bouchet & Gispert 1999](#)), the thermal emission from planets and minor celestial bodies of the solar system, beam patterns and spatially non-uniform instrumental noise. In order to quantify the extent to which the galactic and ecliptic foregrounds impede the SZ-observations by PLANCK, i.e. down to which galactic latitudes clusters will be detectable, a detailed simulation is necessary. Furthermore, the noise patterns will be highly non-uniform due to PLANCK's scanning strategy. For investigating this issue, all-sky maps of the thermal and kinetic SZ-effects are essential.

In my map construction, I use two numerical simulations of cosmic structure formation: The Hubble-volume simulation, that provided a well-sampled cluster catalogue covering a large volume and secondly, a set of template clusters resulting from a gas-dynamical simulation on much smaller scales, allowing us to extract template clusters. For all clusters of the Hubble-volume simulation, a suitable template was chosen and after having performed a scaling operation to improve the match it is projected onto the celestial sphere at the position requested by the Hubble-volume catalogue. By construction, the resulting all-sky SZ-maps show halo-halo correlation even on large angular scales, incorporate the evolution of the mass function and have the correct size distribution. In the kinetic SZ-map, it is ensured that the cluster peculiar velocities correspond to the ambient cosmological density field. Furthermore, the template clusters do exhibit realistic levels of substructure and departures from isothermality, and their ensemble properties also account for scatter around the idealised scaling laws. Therefore, most of the imperfections of traditional approaches will be remedied by my map construction process. However, there are impediments that could not be disposed of: They include gas physics beyond adiabaticity, e.g. radiative cooling and supernova feedback, that significantly alter the baryon distribution and temperature profiles of the ICM and hence the SZ-amplitude, incomplete ionisation, inclusion of filamentary structures and uncollapsed objects or diffuse gas. Another process influencing the thermal history of the ICM is reionisation, which also had to be excluded. Yet another complication are non-thermal particle populations in clusters of galaxies that give rise to the relativistic SZ-effect ([Wright 1979](#), [Sazonov & Sunyaev 1998](#), [Enßlin & Kaiser 2000](#), [Sazonov & Sunyaev 2000](#)).

This chapter is structured as follows: After the definition of the basic SZ quantities in Sect. 5.2, the simulations are outlined in Sect. 5.3. The construction of the maps is described in detail in Sect. 5.4 and the properties of the resulting maps are compiled in Sect. 5.5. Finally, the conclusions are presented in Sect. 5.6.

5.2. Sunyaev-Zel'dovich definitions

Compton interactions of CMB photons with electrons of the ionised ICM give rise to the thermal and kinetic Sunyaev-Zel'dovich effects and induce surface brightness fluctuations in the CMB sky, either because of the thermal motion of the ICM electrons (thermal SZ) or because of the bulk motion of the cluster itself (kinetic SZ).

The relative change $\Delta T/T$ in thermodynamic CMB temperature at position θ as a function of dimensionless frequency $x = h\nu/(k_B T_{\text{CMB}})$ due to the thermal SZ-effect is given by eqn. (5.1):

$$\frac{\Delta T}{T}(\theta) = y(\theta) \left(x \frac{e^x + 1}{e^x - 1} - 4 \right) \quad \text{with} \quad (5.1)$$

$$y(\theta) = \frac{\sigma_T k_B}{m_e c^2} \int dl n_e(\theta, l) T_e(\theta, l), \quad (5.2)$$

where the amplitude y of the thermal SZ-effect is commonly known as the thermal Comptonisation parameter. It is proportional to the line-of-sight integral of the temperature weighted thermal electron density (c.f. eqn. (5.2)). m_e , c , k_B and σ_T denote electron mass, speed of light, Boltzmann's constant and the Thompson cross section, respectively. The kinetic SZ-effect arises due to the motion of the cluster relative to the CMB rest frame parallel to the line of sight. The respective temperature change is given by:

$$\frac{\Delta T}{T}(\theta) = -w(\theta) \quad \text{with} \quad w(\theta) = \frac{\sigma_T}{c} \int dl n_e(\theta, l) v_r(\theta, l). \quad (5.3)$$

data set	z range	Ω/sr	N_{halo}	shape
MS	$0.0 \leq z \leq 0.58$	4π	564818	sphere
NO	$0.58 < z \leq 1.46$	$\pi/2$	182551	northern octant shell
PO	$0.58 < z \leq 1.46$	$\pi/2$	185209	southern octant shell

Table 5.1.: Basic characteristics of the light-cone outputs used for compiling a cluster catalogue. The columns denote the label of the data set, the range in redshift z , the solid angle Ω covered, the number of objects N_{halo} retrieved, and the geometrical shape.

Here, v_r is the radial component of the cluster velocity, i.e. the velocity component parallel to the line-of-sight. The convention is such that the CMB temperature is increased, if the cluster is moving towards the observer, i.e. if $v_r < 0$. In analogy to y , the quantity w is referred to as the kinetic Comptonisation parameter.

5.3. Simulations

Due to the SZ-clusters being detectable out to very large redshifts, due to their clustering properties on very large angular scales, and due to the requirement of reducing cosmic variance when simulating all-sky observations as will be performed by PLANCK, there is the need for very large simulation boxes, encompassing look-back distances to redshifts of order $z \approx 1$ which corresponds to comoving scales exceeding 2 Gpc. Unfortunately, a simulation incorporating dark matter and gas dynamics that covers cosmological scales of that size down to cluster scales and possibly resolving cluster substructure is presently beyond computational feasibility.

For that reason, a hybrid approach is pursued by combining results from two simulations: The Hubble-volume simulation (Jenkins et al. 2001, Colberg et al. 2000), and a smaller scale simulation including (adiabatic) gas physics (White et al. 2002). The analysis undertaken by Bartelmann (2001) gives expected mass and redshift ranges for detectable thermal SZ-clusters, which are covered completely by the all-sky SZ-map presented here.

The assumed cosmological model is the standard Λ CDM cosmology, which has recently been supported by observations of the WMAP satellite (Spergel et al. 2003). Parameter values have been chosen as $\Omega_M = 0.3$, $\Omega_\Lambda = 0.7$, $H_0 = 100 h \text{ km s}^{-1} \text{ Mpc}^{-1}$ with $h = 0.7$, $\Omega_B = 0.04$, $n_s = 1$ and $\sigma_8 = 0.9$.

5.3.1. Hubble-volume simulation

The Hubble-volume simulation is one of the largest simulations of cosmic structure formation carried out to date. The simulation domain is a box of comoving side length 3 Gpc/ h (for the standard Λ CDM cosmology) and comprises 10^9 dark matter particles. The simulations used were carried out by the Virgo Supercomputing Consortium using computers based at the Computing Centre of the Max-Planck-Society in Garching and at the Edinburgh parallel Computing Centre. The data are publicly available for download¹.

The light-cone output of the Hubble-volume simulation (Evrard et al. 2002) was used for compiling a cluster catalogue. This ensures, that the abundance of clusters at any given redshift z corresponds to the level of advancement in structure formation up to this cosmic epoch. The minimal mass was set to $5 \times 10^{13} M_\odot/h$, which roughly corresponds to the transition mass between a rich group of galaxies and a cluster. In order to cover redshifts out to the anticipated limit for PLANCK, light-cone outputs of differing geometry were combined: First, a sphere covering the full solid angle of 4π was used for redshift radii of $z = 0$ to $z = 0.58$. For redshifts exceeding $z = 0.58$, the northern and southern octant data sets were added. The octant data sets span a solid angle of $\pi/2$ and were replicated by rotation in order to cover the full sphere. Table 5.1 summarises the properties of the different output geometries. In this way, a cluster catalogue with cluster mass M , position on the sky θ , redshift z and peculiar velocity v_r projected onto the line-of-sight was compiled, comprising a total number of 2035858 clusters. For the sky-map construction, the positions θ were interpreted as ecliptic coordinates, the default coordinate system for PLANCK.

Here, it should be mentioned that the combination of different outputs gives rise to boundary discontinuities, at the surface of the central sphere as well as on the faces of the octant shells. These discontinuities do not only show up in

¹<http://www.mpa-garching.mpg.de/galform/virgo/hubble>

the spatial halo distribution, but also in the velocities of clusters close to simulation box boundaries. Furthermore, the cluster catalogues exhibit small completeness deficiencies close to the edges of the simulation domain.

5.3.2. Small scale SPH cluster simulations

A hydrodynamical simulation of cosmological structure formation (White et al. 2002) constitutes the basis of the SZ-template map construction. The simulation was performed with the GADGET code² (Springel et al. 2001) using the ‘entropy-conserving’ formulation of SPH (Springel & Hernquist 2002). The simulation, first analysed in White et al. (2002), followed 216^3 dark matter particles as well as 216^3 gas particles in a cubical box of comoving side length $100 \text{ Mpc}/h$ with periodic boundary conditions. Purely adiabatic gas physics and shock heating were included, but radiative cooling and star formation were ignored, which however does not result in significant differences in SZ morphology, as shown by White et al. (2002), but would impact on the scaling relations as demonstrated by da Silva et al. (2001). I analyse 30 output redshifts ranging from $z = 0$ out to $z = 1.458$. The comoving spacing along the line-of-sight of two subsequent outputs is $100 \text{ Mpc}/h$. Halos were identified using a friends-of-friends algorithm with linking length $b = 0.164$, which yields all member particles of cluster-sized groups. Then I employed a spherical overdensity code to estimate the virial mass and radius of each cluster. I computed the mass M_{vir} inside a sphere of radius r_{vir} , interior to which the average density was 200 times the critical density $\rho_{\text{crit}} = 3H(z)^2/(8\pi G)$. A lower mass threshold of $M_{\text{vir}} \geq 5 \times 10^{13} M_{\odot}/h$ was imposed in order to match the lower mass limit adopted for the Hubble-volume cluster catalogue.

5.4. Sunyaev-Zel'dovich map construction

The construction of the all-sky SZ-map proceeds in three steps: First, a set of template cluster maps was derived based on cluster data from a gas-dynamical simulation (Sect. 5.4.1). Then, for each of the clusters in the cluster catalogue obtained from the Hubble-volume simulation, a suitable hydrodynamical cluster template has been selected, scaled in mass and temperature in order to better fit the cluster from the Hubble-volume catalogue (Sect. 5.4.2), and, for the kinetic sky map, boosted to the radial peculiar velocity required by the Hubble-volume simulation. The last step is the projection onto a spherical celestial map (Sect. 5.4.3). In the subsequent paragraph (Sect. 5.4.4), the completeness of the resulting SZ-maps is investigated analytically.

5.4.1. SZ-template map preparation

Square maps of the Compton- y parameter of the selected clusters were generated by SPH projection of all friends-of-friends identified member gas particles onto a Cartesian grid with 128^2 mesh points. The (comoving) side length s of the map was adapted to the cluster size, such that the comoving resolution $g = s/128$ of the grid is specific to a given map.

If the particle p at position $\mathbf{r}_p = (x_p, y_p, z_p)$ has a smoothing length h_p , an SPH electron number density n_p , and an SPH electron temperature T_p , the Compton- y parameter for the pixel at position \mathbf{x} is given by:

$$y(\mathbf{x}) = \frac{\sigma_T k_B}{m_e c^2} \frac{h_p^3}{g^2} \sum_p \left[\int_{x-g/2}^{x+g/2} dx_p \int_{y-g/2}^{y+g/2} dy_p \int_{-h_p}^{h_p} dz_p \mathcal{K}\left(\frac{r}{h_p}\right) n_p T_p \right] \quad (5.4)$$

$$\text{with } r = \sqrt{(x_p - x)^2 + (y_p - y)^2 + z_p^2}. \quad (5.5)$$

Here, I assume complete ionisation and primordial element composition of the ICM for the determination of electron number density and temperature. In this way, I produce projections along each of the three coordinate axes. The function \mathcal{K} is the spherically symmetric cubic spline kernel suggested by Monaghan & Lattanzio (1985), which was also used in the SPH simulation:

$$\mathcal{K}(u) = \frac{8}{\pi} \times \begin{cases} 1 - 6u^2 + 6u^3, & 0 \leq u \leq 1/2 \\ 2(1 - u)^3, & 1/2 < u \leq 1 \\ 0, & u > 1 \end{cases} \quad \text{with } u = r/h_p. \quad (5.6)$$

²<http://www.mpa-garching.mpg.de/galform/gadget/index.shtml>

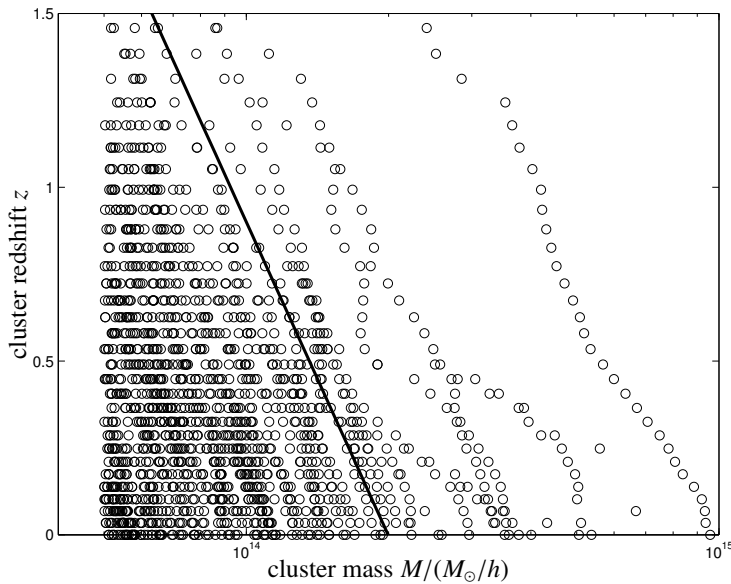


Figure 5.1.: The population of the template clusters in the mass-redshift plane. The line separates the sparsely sampled region from the region in which a sufficient number of template clusters is available.

The fact that the kernel \mathcal{K} has a compact support $u \in [0 \dots 1]$ greatly reduces the computational effort. Details of the SPH projection are summarised in Appendix A.

The kinetic maps were treated in complete analogy: Maps of the Thomson optical depth τ were derived by means of eqn. (5.7):

$$\tau(\mathbf{x}) = \sigma_T \frac{h_p^3}{g^2} \sum_P \left[\int_{x-g/2}^{x+g/2} dx_p \int_{y-g/2}^{y+g/2} dy_p \int_{-h_p}^{h_p} dz_p \mathcal{K}\left(\frac{r}{h_p}\right) n_p \right]. \quad (5.7)$$

In eqn. (5.7), the influence of velocity differences inside the clusters was omitted. At the stage of projecting the template clusters onto the spherical map, the τ -map obtained is boosted with the peculiar line-of-sight velocity v_r in units of the speed of light c required by the entry in the Hubble-volume catalogue in order to yield a Compton- w amplitude.

Neglecting velocity differences inside the clusters does not seriously affect the measurement of cluster peculiar velocities with the kinetic SZ-effect shown by Nagai et al. (2003), the scatter in the velocity estimates increases only little (50 – 100 km/s) when considering a rather narrow beam ($\Delta\theta = 1'.0$ FWHM), while the kinetic SZ-amplitude remains an unbiased estimator of the peculiar velocity. For my application purpose, the situation is even less troublesome because of PLANCK's wide beams ($\gtrsim 5'.0$ (FWHM)).

In this way, a sample of 1518 individual template clusters was obtained, and maps for projections along all three coordinate axes were derived, yielding a total of 4554 template maps for each of the two SZ-effects. Fig. 5.1 shows the distribution of clusters in the mass-redshift plane. Especially at high masses, the smooth growth of clusters by accretion can be clearly seen. Sudden jumps to larger masses are caused by the merging of low-mass clusters.

A limitation to my SZ-map construction is immediately apparent: The 4554 cluster template maps derived from the hydro-simulation are not strictly independent, but merely show the same clusters at different redshift. Thus, the morphological variety remains limited, but even though there is of course some variation in morphology due to accretion and merging events. This, however, may not be a severe restriction, keeping the wide PLANCK-beams in mind, that are unlikely to resolve cluster substructure for a large fraction of detectable clusters. In this case, the simulation will pick up mismatches in Comptonisation relative to the value expected from the spherical collapse model in conjunction with the Press-Schechter distribution of halo masses.

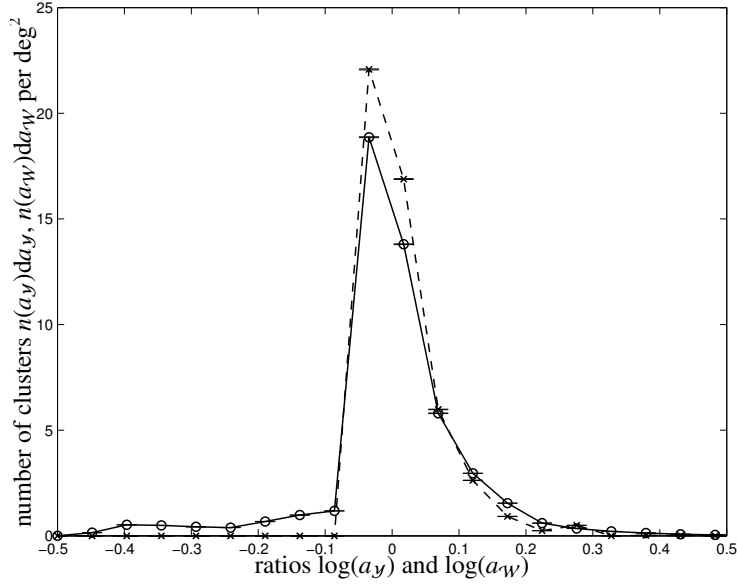


Figure 5.2.: Distribution of the ratios a_Y (circles, solid line) and a_W (crosses, dashed line) that describes the impact of the mismatch between friends-of-friends masses and virial masses on the Comptonisations \mathcal{Y} and \mathcal{W} .

5.4.2. Cluster selection and scaling relations

In order to select a template map for projection, the closest template cluster in the $\log(M)$ - z -plane for a given cluster from the Hubble-volume simulation was chosen. For the sparsely sampled region of the M - z -plane to the right of the line in Fig. 5.1, a cluster from a pool containing the most massive clusters to the right of this line in the redshift bin under consideration was drawn.

The template clusters are scaled in mass, temperature and spatial extent in order to yield a better match to the cluster from the Hubble-volume simulation according to formulae 5.8-5.10. The scaling is parameterised by the masses of the cluster of the Hubble-volume simulation $M_{\text{vir}}^{(\text{Hubble})}$ and the template cluster $M_{\text{vir}}^{(\text{template})}$:

$$q_M = \frac{M_{\text{vir}}^{(\text{Hubble})}}{M_{\text{vir}}^{(\text{template})}} \quad (5.8)$$

$$q_R = \frac{r_1 \left(M_{\text{vir}}^{(\text{Hubble})} \right)^{r_2} + r_3}{r_{\text{vir}}^{(\text{template})}} \quad (5.9)$$

$$q_T = \frac{t_1 \left(M_{\text{vir}}^{(\text{Hubble})} \right)^{t_2} + t_3}{t_1 \left(M_{\text{vir}}^{(\text{template})} \right)^{t_2} + t_3}. \quad (5.10)$$

The parameters r_i and t_i , $i \in \{1, 2, 3\}$, describing the scaling in size q_R and in temperature q_T were derived from template data: Fits to the virial radius as a function of mass and of the mean temperature inside the virial sphere as a function of mass were applied to the data of simulation outputs binned in five data sets. This approach leaves the map construction independent of idealised assumptions, like the prediction of cluster temperatures from the spherical collapse model, or from electron temperature measurements deduced from X-ray observations and keeps the weak trend of cluster temperature with redshift z as contained in the simulations.

Although the scaling has been constructed in order to yield the best possible match between the template cluster and the target cluster from the Hubble-volume simulation, there are artifacts in irregular systems due to inconsistencies in cluster masses $M_{\text{fof}}^{(\text{template})}$ determined with a friends-of-friends algorithm for identifying cluster member particles and the virial mass estimates $M_{\text{vir}}^{(\text{template})}$ following from applying the spherical overdensity code. After the scaling, these mismatches may be expressed as:

$$a_Y = q_M q_T M_{\text{fof}}^{(\text{template})} / M_{\text{vir}}^{(\text{Hubble})} \quad \text{and} \quad (5.11)$$

$$a_W = q_M M_{\text{fof}}^{(\text{template})} / M_{\text{vir}}^{(\text{Hubble})}. \quad (5.12)$$

Fig. 5.2 shows the distribution of ratios a_Y and a_W for the entire Hubble-volume catalogue. Clearly, one recognises large tails towards high values, because clusters have on average to be scaled to higher masses. This is due to the fact that the hydro-simulation outlined in Sect. 5.3.2 does not sample the high-mass end of the Press-Schechter function satisfactorily, simply because of its small volume. Nevertheless, the mean of the distributions is close to one, which implies that the mismatches average out for the bulk of clusters.

5.4.3. Projection onto the celestial sphere

For storing all-sky maps the HEALPix³ tessellation of the sphere proposed by Górski et al. (2002) has been chosen. In order to support structures as small as clusters, the N_{side} parameter has been set to 2048, resulting in a total number of $12 N_{\text{side}}^2 = 50331648$ pixels. The side length of one pixel is then approximately 1'71, which is well below the anticipated PLANCK beam size of 5'0 in the highest frequency channels.

The scaled cluster maps are projected onto the spherical map by means of stereographic projection at the south ecliptic pole of the celestial sphere. By dividing the (comoving) position vector (x, y) of a given pixel on the template map by the comoving angular diameter distance $\chi(z)$ at redshift z , one obtains the coordinates (α, β) on the tangential plane. Then, the stereographic projection formulae yield the (Cartesian) position vector (ξ, η, ζ) of this point projected onto the unit sphere:

$$\mathbf{r} = (\xi, \eta, \zeta + 1) = \left(\frac{4\alpha}{4 + \alpha^2 + \beta^2}, \frac{4\beta}{4 + \alpha^2 + \beta^2}, \frac{\alpha^2 + \beta^2}{4 + \alpha^2 + \beta^2} \right). \quad (5.13)$$

In order to assign a Comptonisation amplitude to a given HEALPix pixel in the projection process, a solid angle weighted average is performed. For close-by clusters, the mesh size of the templates converted to angular units is larger than the HEALPix pixel scale. For those clusters, the map is refined iteratively by subdivision of a pixel into 4 smaller pixels subtending a quarter of the original solid angle until the pixel size is well below the HEALPix pixel scale. Before projection, the template maps are smoothed with a Gaussian kernel with $\Delta\theta = 2'0$, which is comparable to the HEALPix pixel scale. In this way, it is avoided that structures are destroyed by the combination of multiple template map pixels into a single HEALPix pixel. This convolution does not affect the later usage for simulations concerning PLANCK: A second successive convolution with the narrowest beam results in an effective smoothing of 5.38', which corresponds to a decrease in angular resolution of roughly 7.5%.

Additionally, a rotation of the template map around the \mathbf{e}_z -axis about a random angle is performed in order to avoid spurious alignments of clusters. The projected pixels are then transported by Euler-rotations of the vector (ξ, η, ζ) to the position requested by the Hubble catalogue.

5.4.4. Completeness of the all-sky SZ-maps

The angular resolution of PLANCK will not allow to spatially resolve low-mass and high-redshift clusters. There will be a Compton- y background $\langle y_{\text{bg}} \rangle_\theta$ due to the higher number density of low-mass clusters compared to high-mass clusters which overcompensates their lower individual SZ-signature. Since ideally any isotropic background could be removed, I only have to take into account the average background fluctuation level $\langle y_{\text{bg}}^2 \rangle_\theta$ which is described by power spectrum statistics.

This section studies the influence of the background of unresolved SZ-clusters in my all-sky map of SZ-clusters on power spectrum statistics. My simulation neglects the SZ-signal of clusters both with masses smaller than $5 \times 10^{13} M_\odot/h$ and redshifts $z > 1.5$. In principle, these missing clusters could be accounted for by drawing them from a particular realisation of a *Poissonian random field* such that they obey the correct relative phase correlations, i.e. that they exhibit the observed local clustering properties.

However, there are large uncertainties about the baryon fraction $f_B = \Omega_B/\Omega_M$ of low-mass halos ($M_{\text{halo}} < 5 \times 10^{13} M_\odot/h$) especially at higher redshifts. Analyses of X-ray observations of 45 local clusters ($z < 0.18$, only 4

³<http://www.eso.org/science/healpix/>

of them lie at $z > 0.1$) carried out by [Mohr et al. \(1999\)](#) and [Arnaud & Evrard \(1999\)](#) suggest a weak trend of the cluster baryon fraction f_B with cluster mass M and a deviation from the universal value, which may be due to feedback processes like galactic winds that more effectively deplete the ICM of baryons in low-mass compared to high-mass clusters. The behaviour of f_B at high redshifts is very uncertain, among other reasons because the relative importance of the different feedback processes at high redshift is yet unknown. This uncertainty is also reflected in different cooling rates and mechanisms, governing the ionisation fraction of the electrons and the resulting SZ flux of a particular cluster. In the following, I study the contribution to the SZ flux of clusters both with masses smaller than $5 \times 10^{13} M_\odot/h$ and redshifts $z > 1.5$. Although the impact of this cluster population to the $\langle y_{\text{bg}} \rangle$ -statistics amounts to a significant fraction, this population has a negligible contribution to the more relevant $\langle y_{\text{bg}}^2 \rangle$ -statistics which will be shown in the following. The unresolved cluster population is assumed to follow scaling relations derived from the spherical collapse model. Temperature T and halo mass M are assumed to be related by

$$\frac{k_B T}{6.03 \text{ keV}} = \left(\frac{M}{10^{15} M_\odot/h} \right)^{2/3} (1+z) \left(\frac{\Omega_0}{\Omega(z)} \right)^{1/3} \left(\frac{\Delta_c(z)}{178} \right)^{1/3} \quad (5.14)$$

(e.g. [Eke et al. 1996](#), [Navarro et al. 1995](#)). The temperature $k_B T = 6.03 \text{ keV}$ for a cluster with $M = 10^{15} M_\odot/h$ has been adopted from [Mathiesen & Evrard \(2001\)](#). The density parameter at redshift z is denoted by $\Omega(z)$, and Δ_c is the mean overdensity of a virialised sphere,

$$\Delta_c = 9\pi^2 \left\{ 1 + \alpha [\Omega(z) - 1] + \Omega(z)^\beta \right\} \quad (5.15)$$

with $(\alpha, \beta) = (0.7076, 0.4403)$ for a flat cosmology ([Stöhr 1999](#)). Assuming that the total number N_e of thermal electrons within the cluster virial radius is proportional to the virial mass yields

$$N_e = \frac{1 + f_H}{2} f_B \frac{M}{m_p}, \quad (5.16)$$

where f_H is the hydrogen fraction of the baryonic mass ($f_H \approx 0.76$) and m_p is the proton mass. From X-ray data of an ensemble of 45 clusters, [Mohr et al. \(1999\)](#) derived $f_B = 0.075 h^{-3/2}$. Traditionally, the number density of dark matter haloes is described by the Press-Schechter formalism ([Press & Schechter 1974](#)). The comoving Press-Schechter mass function can be written as

$$n_{\text{PS}}(M, z) = \frac{\bar{\rho}}{\sqrt{2\pi} D_+(z) M^2} \left(1 + \frac{n}{3} \right) \left(\frac{M}{M_*} \right)^{(n+3)/6} \exp \left[-\frac{1}{2 D_+^2(z)} \left(\frac{M}{M_*} \right)^{(n+3)/3} \right], \quad (5.17)$$

where M_* and $\bar{\rho}$ are the nonlinear mass today and the mean background density at the present epoch, and $D_+(z)$ is the linear growth factor of density perturbations, normalised to unity today, $D_+(0) = 1$. $n \approx -1$ denotes the effective exponent of the dark matter power spectrum at the cluster scale. [Sheth & Tormen \(1999\)](#) recently proposed a significantly improved analytic derivation of the mass function while [Jenkins et al. \(2001\)](#) measured the mass function of dark matter haloes in numerical simulations and found a fitting formula very close to Sheth & Tormen's, however, being of slightly lower amplitude at high masses. Thus, the fitting formula found by Jenkins et al. was used in my study.

The total Compton- y parameter per unit solid angle is given by

$$\mathcal{Y}_\Omega = d_A^2 \int d^2\theta y(\theta) = \frac{k_B T_e}{m_e c^2} \sigma_T N_e, \quad (5.18)$$

where d_A is the angular-diameter distance to the cluster. The mean background level of SZ fluctuations is given by

$$\begin{aligned} \langle y_{\text{bg}} \rangle_\theta(z, M_0) &= \int dz \left| \frac{dV}{dz} \right| (1+z)^3 \int_{M_0} dM n_{\text{PS}}(M, z) \mathcal{Y}_\Omega(M, z) \\ &= \int dM \int dV \mathcal{Y}_\Omega(M, z) \frac{d^2 N(M, z)}{dM dV}, \end{aligned} \quad (5.19)$$

where dV is the cosmic volume per unit redshift and unit solid angle, $n_{\text{PS}}(M, z)$ is the mass function of collapsed halos (5.17), and $\mathcal{Y}_\Omega(M, z)$ is the integrated Compton- y parameter per unit solid angle from (5.18) expressed in terms of halo mass M and redshift z . Background fluctuations are due to Poisson fluctuations in the number of

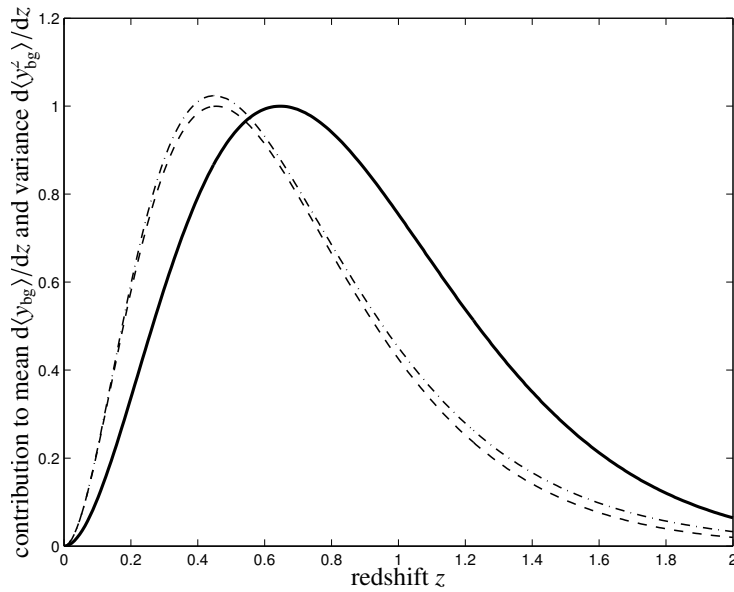


Figure 5.3: Comparison of the mean background level $\langle y_{\text{bg}} \rangle_{\theta}(z, 5 \times 10^{13} M_{\odot}/h)$ (solid) and the variances $\langle y_{\text{bg}}^2 \rangle_{\theta}(z, 5 \times 10^{13} M_{\odot}/h)$ (dashed) and $\langle y_{\text{bg}}^2 \rangle_{\theta}(z, 10^{13} M_{\odot}/h)$ (dash-dotted). The differential curves show qualitatively the smaller impact of low-mass and high-redshift clusters on the variance compared to the mean background of SZ fluctuations.

clusters per unit mass and volume if cluster correlations are neglected. The variance of the background fluctuations reads

$$\langle y_{\text{bg}}^2 \rangle_{\theta}(z, M_0) = \int_{M_0} dM \int dV [\mathcal{Y}_{\Omega}(M, z)]^2 \frac{d^2 N(M, z)}{dM dV}. \quad (5.20)$$

Fig. 5.3 shows a qualitative comparison of the influence of the background of unresolved SZ-clusters on the mean background level $\langle y_{\text{bg}} \rangle_{\theta}(z, M_0)$ and the variance $\langle y_{\text{bg}}^2 \rangle_{\theta}(z, M_0)$. For studying this influence quantitatively, the ratio of mean background levels and variances is defined via:

$$r_{\text{mean}} = \frac{\langle y_{\text{bg}} \rangle_{\theta}(z_{\text{sim}}, M_{\text{sim}})}{\langle y_{\text{bg}} \rangle_{\theta}(z_{\text{max}}, M_{\text{min}})}, \quad (5.21)$$

$$r_{\text{var}} = \frac{\langle y_{\text{bg}}^2 \rangle_{\theta}(z_{\text{sim}}, M_{\text{sim}})}{\langle y_{\text{bg}}^2 \rangle_{\theta}(z_{\text{max}}, M_{\text{min}})}, \quad (5.22)$$

where the numerator accounts for the resolved clusters in my simulation with $z < z_{\text{sim}} = 1.5$ and $M > M_{\text{sim}} = 5 \times 10^{13} M_{\odot}/h$ while the denominator accounts for all collapsed halos contributing to the SZ-flux in my analytic estimate ($z < z_{\text{max}} = 20$ and $M > M_{\text{min}} = 1 \times 10^{13} M_{\odot}/h$). Performing these integrals yields ratios of $r_{\text{mean}} = 40.6\%$ and $r_{\text{var}} = 93.3\%$ and thus confirms the qualitative picture of Fig. 5.3. Therefore, I conclude that one can safely neglect the effect of the background of unresolved SZ clusters on power spectrum statistics of my SZ all-sky map, especially when considering the mentioned uncertainties in f_{B} and the ionisation fraction of electrons in low-mass halos.

5.5. Results

This section provides various characterisations of the SZ-cluster sample and properties of the resulting map. First, a visual impression of the SZ-maps is given in Sect. 5.5.1. Distribution of the angular sizes and of the integrated thermal and kinetic Comptonisations are presented in Sect. 5.5.2 and in Sect. 5.5.3, respectively. The distribution of pixel amplitudes and a discussion of the sky-averaged thermal Comptonisation is given in Sect. 5.5.4. The angular

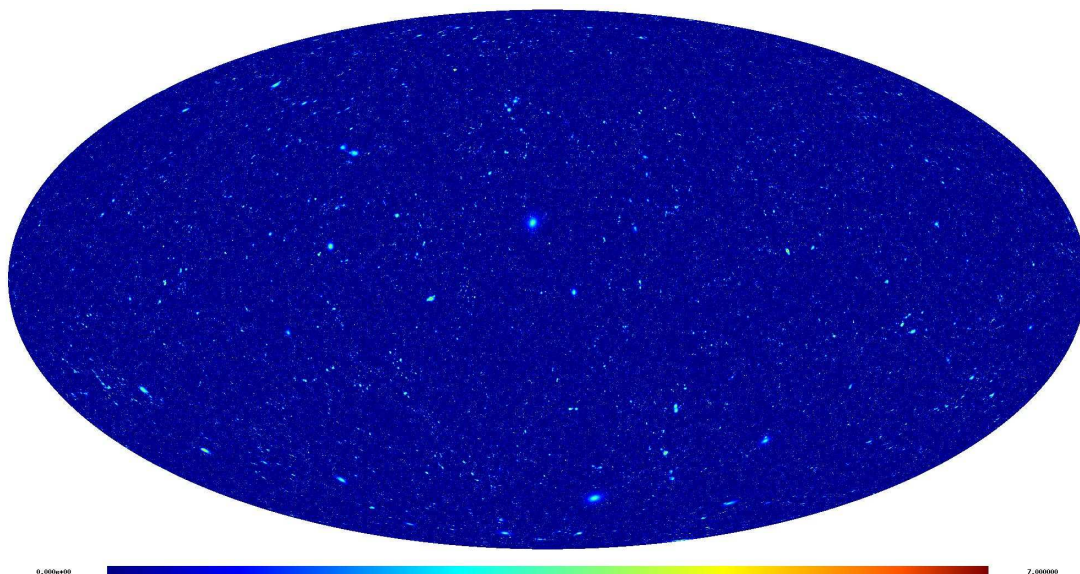


Figure 5.4.: All-sky map of the thermal Comptonisation parameter y in Mollweide projection. The shading is proportional to $\text{arsinh}(10^6 \times y)$.

power-spectra in comparison to those obtained in high-resolution simulations performed by [White et al. \(2002\)](#) is shown in Sect. 5.5.5. Finally, source counts in three relevant PLANCK-channels are given in Sect. 5.5.6.

In order to quantify the deviations resulting in using template SZ-maps instead of relying solely on analytical profiles and idealised scaling relations, the distributions following from the respective approach are contrasted in Sect. 5.5.2 (angular sizes), Sect. 5.5.3 (integrated Comptonisations) and Sect. 5.5.6 (source count at three selected PLANCK-frequencies).

5.5.1. Sky views

In order to give a visual impression of the sky maps, all-sky views in Mollweide projection of the Compton- y parameter (Fig. 5.4) as well as of the Compton- w parameter (Fig. 5.5) are presented. Apart from those images, detailed maps of small regions of the SZ-sky are presented in Fig. 5.6 for the thermal and in Fig. 5.7 for the kinetic SZ-effects, respectively. These detailed maps display interesting features: Clearly, cluster substructure is visible in the maps, e.g. at position $(\lambda, \beta) \approx (134^\circ 60, 45^\circ 25)$.

Secondly, massive clusters that generate a strong thermal signal, are rare, such that in drawing a peculiar velocity from a Gaussian distribution large values are less likely to be obtained. Consequently, these clusters commonly show only a weak kinetic signal, a nice example can be found at the position $(\lambda, \beta) \approx (135^\circ 25, 44^\circ 75)$. Closeby, the inverse example can be found at $(\lambda, \beta) \approx (135^\circ 40, 44^\circ 50)$, where a low-mass cluster shows only a weak thermal signal, but has sufficient optical depth and a high enough peculiar velocity to give rise to a strong kinetic signal. Finally, at $(\lambda, \beta) \approx (135^\circ 90, 45^\circ 75)$, there is an example of a merging cluster, with a dipolar variation of the subcluster velocities.

The occurrence of high kinetic SZ-amplitudes is a subtle point: Cluster velocities follow a Gaussian distribution with mean consistent with zero, because the large scale structure is at rest in the comoving CMB-frame and with a standard deviation of $\sigma_v = 312.8 \pm 0.2$ km/s. This value has been measured for clusters in the Hubble-volume catalogue and is noticeably smaller compared to $\sigma_v = 400$ km/s proposed by [Aghanim et al. \(1997\)](#). As Fig. 5.8 illustrates, the velocity-distribution does *not* depend on the cluster mass, because on the scales of typical cluster separation, linear structure formation is responsible for accelerating the clusters to their peculiar velocity. Massive clusters are rare and thus a high peculiar velocity is seldomly drawn from the underlying Gaussian distribution. Despite the seemingly large separation, it would be incorrect to draw the velocities independently from a Gaussian distribution. Instead, the kinetic SZ-map ensures the consistency that the density and velocity fields have grown

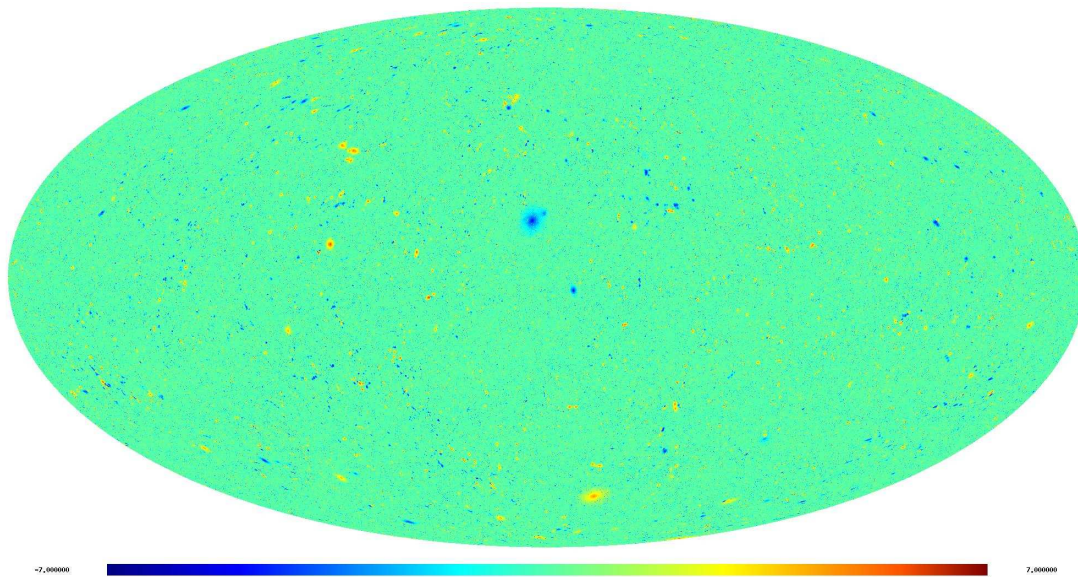


Figure 5.5.: All-sky map of the kinetic Comptonisation parameter w in Mollweide projection. The shading is proportional to $\text{arsinh}(10^7 \times w)$.

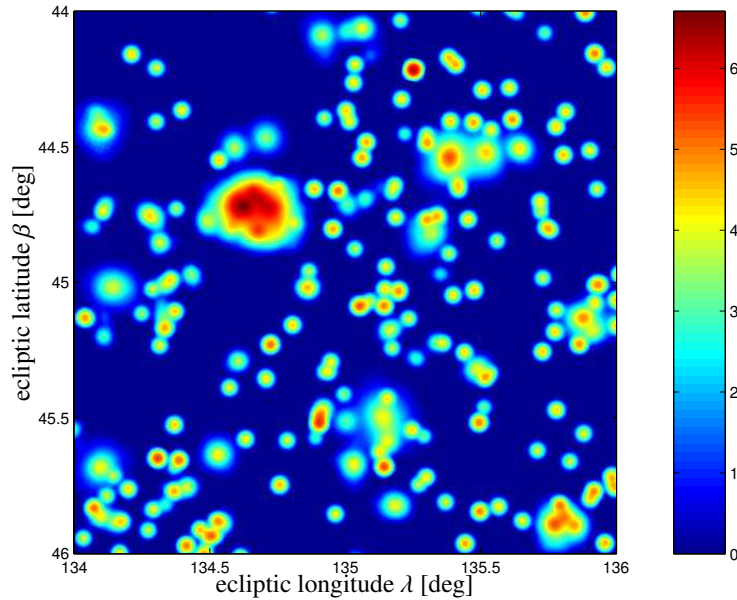


Figure 5.6.: Detail of the thermal Comptonisation map: A $2^\circ \times 2^\circ$ wide cut-out centered on the ecliptic coordinates $(\lambda, \beta) = (135^\circ, 45^\circ)$ is shown. The smoothing imposed was a Gaussian kernel with $\Delta\theta = 2'.0$ (FWHM). The shading indicates the value of the thermal Comptonisation y and is proportional to $\text{arsinh}(10^6 \times y)$. This map resulted from a projection on a Cartesian grid with mesh size $\sim 14''$, i.e. no HEALPix pixelisation can be seen.

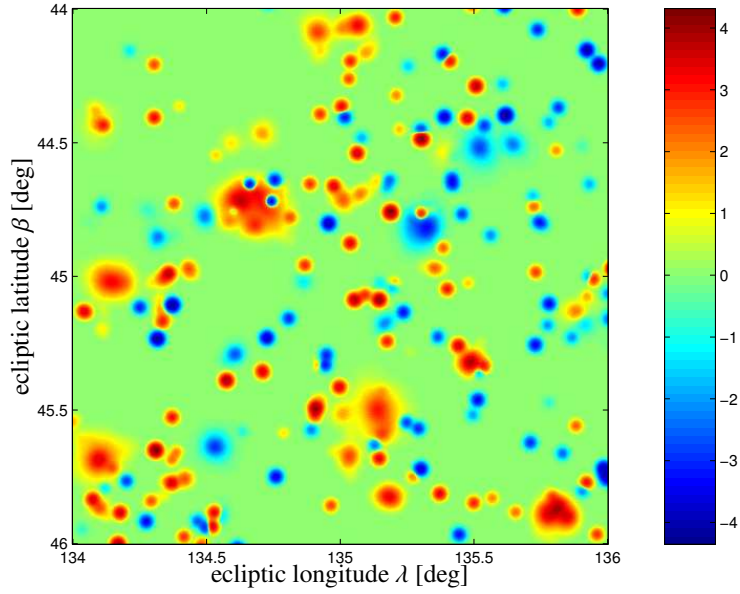


Figure 5.7.: Detail of the kinetic Comptonisation map: A $2^\circ \times 2^\circ$ wide cut-out centered on the same position as Fig. 5.6, i.e. at the ecliptic coordinates $(\lambda, \beta) = (135^\circ, 45^\circ)$ is shown. The smoothing imposed was a Gaussian kernel with $\Delta\theta = 2.0$ (FWHM). The kinetic Comptonisation w is indicated by the shading which is proportional to $\text{arsinh}(10^6 \times w)$.

from the initial Gaussian random field by linear structure formation and have the correct relative phases.

Similar to the clustering on large angular scales that the thermal SZ-map shows due to the formation of superclusters, the kinetic SZ-map is expected to exhibit clustering on the same angular scales. This is because in the formation of superclusters, the velocity vectors of infalling clusters point at the dynamical centre and are thus correlated despite the large separation.

5.5.2. Distribution of angular sizes

The distribution of cluster sizes is an important characteristic of the sky maps. For the derivation of core sizes, two different paths have been pursued in order to contrast the ideal case, in which cluster sizes follow from the well-known virial relations to the simulated and realistic case, in which the sizes are measured on the template maps themselves. First, the cluster sizes are measured on the data by fitting a King-profile (Cavaliere & Fusco-Femiano 1978) to the thermal and kinetic template maps:

$$y(\mathbf{r}) = y_0 \cdot \left[1 + \left(\frac{|\mathbf{r}|}{r_c^{(y)}} \right)^2 \right]^{-1} \quad (5.23)$$

$$w(\mathbf{r}) = w_0 \cdot \left[1 + \left(\frac{|\mathbf{r}|}{r_c^{(w)}} \right)^2 \right]^{-1}, \quad (5.24)$$

yielding the core radii $r_c^{(y)}$ for the thermal and $r_c^{(w)}$ for the kinetic map, respectively. The β -fits have been centered on the pixel with the highest amplitude, and as free parameters only the central amplitudes y_0 and w_0 were used apart from the core radii. The resulting radii have been averaged over all three projections of the cluster. Together with the comoving distance of the cluster as given by the Hubble-volume catalogue and the scaling factor required to match the size (compare Sect. 5.4.2), the core radii have been converted into angular diameters.

Secondly, an angular extent has been derived from the virial radius. Template data suggests the relation

$$r_c \simeq 0.12 r_{\text{vir}} \quad (5.25)$$

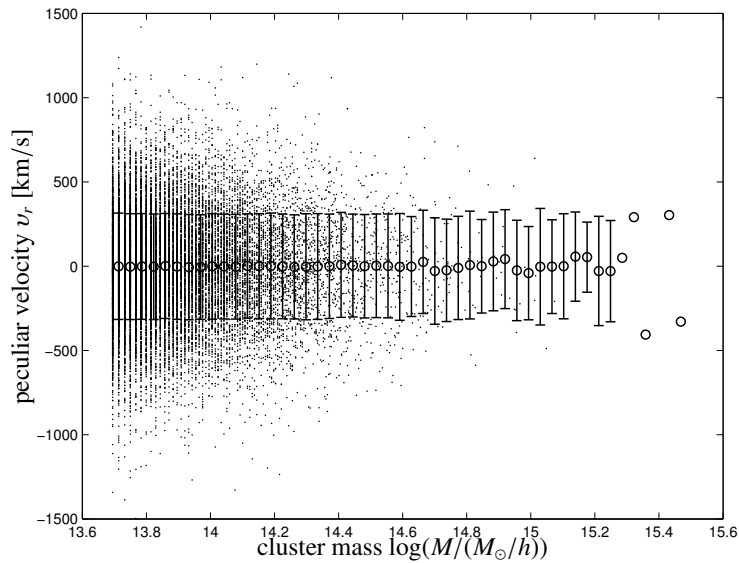


Figure 5.8.: Mean value and variance of the (Gaussian) distribution of peculiar velocities v_r as a function of cluster mass M . The parameters of the distribution do not depend on mass, i.e. the mean is consistent with zero and the standard deviation has values ≈ 320 km/s irrespective of mass. Standard deviations for the five bins corresponding to the largest cluster masses have been omitted due to poor statistics. The underlying data points represent 1% randomly selected entries of the Hubble-volume catalogue.

rather than the value of $r_c \approx 0.07 r_{\text{vir}}$ advocated by [Lloyd-Davies et al. \(2000\)](#) and [Kay et al. \(2001\)](#). In analogy, the angular diameter was then determined with the cluster distance given by the Hubble-volume catalogue.

In Fig. 5.9, the size distributions for the thermal as well as for the kinetic clusters are given. Clearly, most clusters have angular diameters small compared to PLANCK's beam, and would appear as point sources. Here, it should be emphasised, that the HEALPix tessellation with the chosen N_{side} -parameter does not resolve structures smaller than $1'.71$. In the process of smoothing the clusters imposed prior to projection (compare Sect. 5.4.3), clusters with diameters smaller than $2'.0$ have been replaced by 2-dimensional Gaussians with $\sigma = 2'.0$. Their normalisation corresponds to the integrated Comptonisations \mathcal{Y} and \mathcal{W} measured on the template maps. The smoothing is an absolute necessity because otherwise the HEALPix map would need $\sim 10^4$ times as many pixels for supporting the most distant and hence smallest clusters in the Hubble sample and hence $\sim 10^4$ times the storage space. A further point to notice is the remarkably good agreement between diameters derived from the various prescriptions.

5.5.3. Distribution of the integrated thermal and kinetic Comptonisation

The signal strength of a cluster in an SZ observation is not given by the line-of-sight Comptonisation, but rather the Comptonisation integrated over the solid angle subtended by the cluster. These quantities are referred to as the integrated thermal Comptonisation \mathcal{Y} and kinetic Comptonisation \mathcal{W} and are defined as:

$$\mathcal{Y} = \int d\Omega y(\theta) \quad \text{and} \quad \mathcal{W} = \int d\Omega w(\theta). \quad (5.26)$$

For a simple model of the integrated Comptonisations as functions of cluster mass M , distance z and peculiar velocity v_r , it is assumed that the SZ-flux originates from inside a sphere of radius r_{vir} , that the baryon fraction is equal to its universal value $f_B = \Omega_B/\Omega_M$, that the ICM is completely ionised and has a uniform temperature predicted by the spherical collapse model laid down in eqn. (5.14). In this model, the actual distribution of electrons

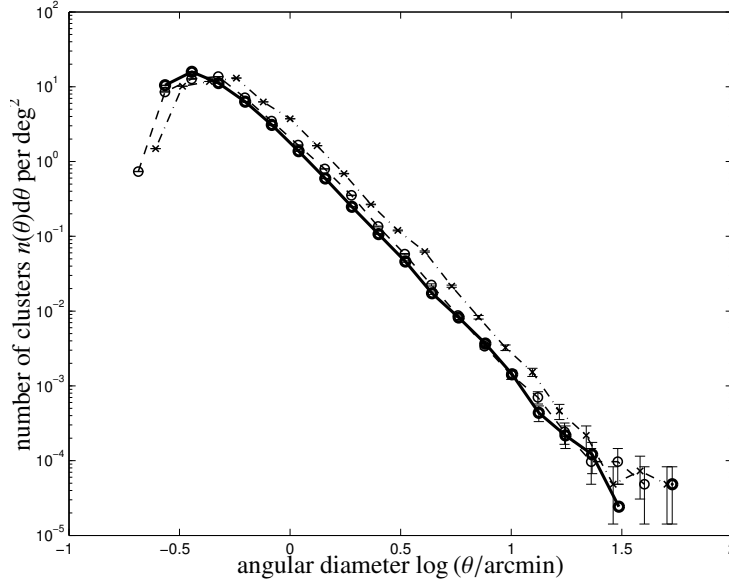


Figure 5.9.: The number of clusters $n(\theta)d\theta$ per square degree for given angular diameter θ is shown without taking beam convolution into account, for thermal clusters (circles, dashed line) and kinetic clusters (crosses, dash-dotted line) as following from β -model fits to template data. For comparison, the distribution of angular diameters obtained via the virial theorem (solid line) is also plotted.

inside the virial sphere is of no importance. Then, the integrated Comptonisations are approximated by:

$$\frac{\mathcal{Y}_{\text{vir}}}{\text{arcmin}^2} = 1.98 \frac{f_B}{h} \left(\frac{M_{\text{vir}}}{M_\star} \right)^{\frac{5}{3}} \left(\frac{d_A}{d_\star} \right)^{-2} (1+z) \left(\frac{\Omega_0}{\Omega} \right)^{\frac{1}{3}} \left(\frac{\Delta_c}{178} \right)^{\frac{1}{3}}, \quad (5.27)$$

$$\frac{\mathcal{W}_{\text{vir}}}{\text{arcmin}^2} = 0.29 \frac{f_B}{h} \left(\frac{M_{\text{vir}}}{M_\star} \right) \left(\frac{d_A}{d_\star} \right)^{-2} \left(\frac{v_r}{v_\star} \right), \quad (5.28)$$

respectively. The reference values have been chosen to be $M_\star = 10^{15} M_\odot/h$, $d_\star = 100 \text{ Mpc}/h$ and $v_\star = 1000 \text{ km/s}$. d_A is the angular diameter distance to the cluster. $\Omega = \Omega(z)$ denotes the mass density at redshift z and $\Delta_c = \Delta_c(z)$ the overdensity of a virialised sphere, an approximate description is given by eqn. (5.15). For typical values for mass, distance and velocity, the thermal and kinetic SZ-effects differ by approximately one order of magnitude. The baryon fraction is set to the universal value $f_B = \Omega_B/\Omega_M = 0.133$ for the remainder of this chapter.

Distributions of the integrated thermal and kinetic Comptonisations are shown in Figs. 5.10 and 5.11, respectively. The distributions have been derived from actual scaled template data in comparison to the values obtained from (5.27) and (5.28).

Fig. 5.10 shows the number of clusters per deg^2 with integrated thermal Comptonisation \mathcal{Y} . It can be seen that the approach relying on the virial theorem underestimates the number of cluster by a factor 2-3 for large integrated Comptonisations. Alternatively, one could state that the distributions are separated at high Comptonisations by slightly less than 0.5 dex. The reason for the significantly larger integrated Comptonisations determined from template data is due to the fact that the template clusters were matched to the catalogue entries given by the Hubble-volume simulation by their virial masses. In irregular clusters, there is a significant fraction of the gas located outside the virial sphere and thus the integrated Comptonisation is systematically underestimated when applying a spherical overdensity code to simulation data, as previously examined in Fig. 5.2. In scaling the template clusters up to the masses required by the Hubble-volume catalogue, this difference is amplified because in the sparsely sampled region of the M - z -diagram (compare Figs. 5.1 and 5.2) clusters have on average to be scaled to higher masses, which explains the offset in the distributions. A second effect is the evolution of ICM temperature. Compared to the temperature model eqn. (5.14) based on spherical collapse theory, the plasma temperatures are smaller by approximately 25%, i.e. the mean SPH-temperature of the particles inside the virial sphere is smaller than expected

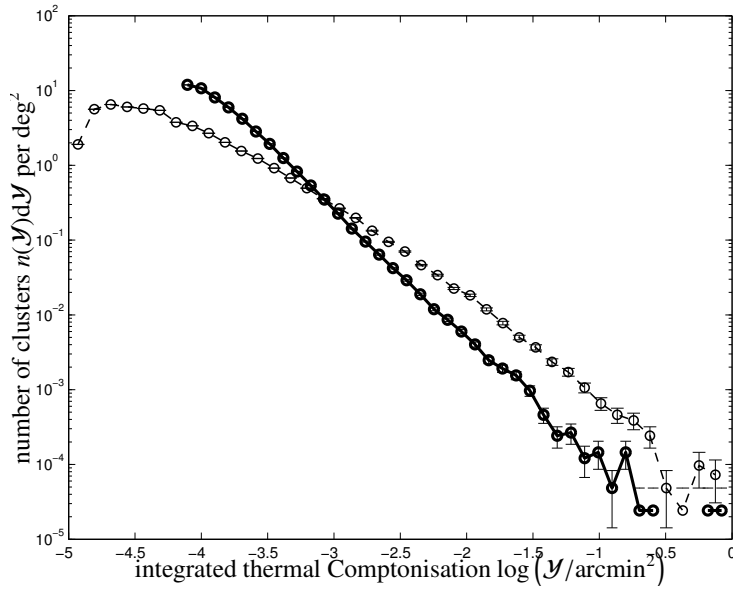


Figure 5.10.: The number of clusters $n(\mathcal{Y})d\mathcal{Y}$ per square degree for given integrated thermal Comptonisation \mathcal{Y} derived from template data (dashed line) in comparison to the analogous quantity based on virial estimates (solid line).

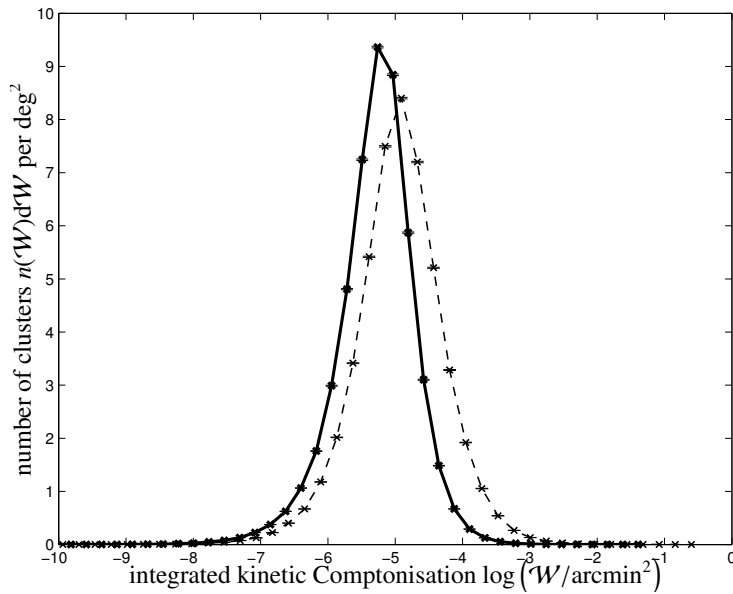


Figure 5.11.: The number of clusters $n(\mathcal{W})d\mathcal{W}$ per square degree for given integrated kinetic Comptonisation \mathcal{W} derived from template data (dashed line) in comparison to the analogous quantity based on virial estimates (solid line). Here, the scaling of the vertical axis is linear, in contrast to Fig. 5.10, such that the underlying Gaussian distribution of peculiar velocities becomes apparent.

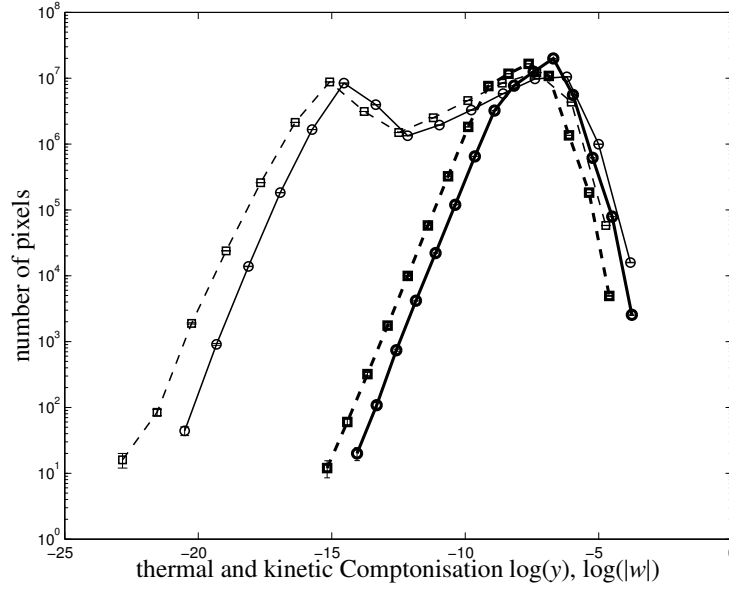


Figure 5.12.: Distribution of pixel amplitudes of the thermal Comptonisation parameter y (circles, solid) and of the absolute value of the kinetic Comptonisation $|w|$ (squares, dashed). Zero values have been deliberately excluded. The figure illustrates the occurrence of clusters comparable to the HEALPix pixel scale: The thin set of lines shows an additional peak at small Comptonisations, that vanish after convolution with a beam of $\Delta\theta = 5'0$ (FWHM), i.e. comparable to PLANCK, as shown by the thick lines.

from spherical collapse theory and reflects the departure from isothermality: The template clusters do show a temperature profile that declines towards the outskirts of the clusters, which decreases the integrated Comptonisation relative to the values derived by means of the virial theorem.

Furthermore, the dependence of electron temperature on cluster mass is noticeably weaker than the $M^{2/3}$ -scaling: The cluster number weighted average for the exponent α in the scaling $T \propto M^\alpha$ relating temperature to mass was found to be $\langle\alpha\rangle = 0.624$, and at the redshifts around unity, where most of the clusters reside, values as small as $\alpha = 0.605$ were derived. Using this scaling, the Compton- y parameter and hence the integrated thermal Comptonisation \mathcal{Y} shows a significantly shallower distribution compared to the distribution relying on simple scaling arguments.

The same argument applies to the kinetic Comptonisation \mathcal{W} , as depicted in Fig. 5.11: Here a shifting of the values to smaller kinetic Comptonisations is observed when comparing estimates following from the virial theorem to actual simulation data. The shift of the peak of the distribution amounts to about one third dex, as explained above for the thermal Comptonisations. Keeping the $M^{2/3}$ -scaling of the thermal SZ-effect in mind, the shift in the \mathcal{W} -distribution is then consistent with the shift of the \mathcal{Y} -distribution. A very illustrative demonstration how asphericity affects the SZ-observables of a cluster is given by Puy et al. (2000).

5.5.4. Distribution of Comptonisation per pixel

Fig. 5.12 shows the distribution of the pixel amplitudes of the thermal SZ-map as well as of their absolute values in the kinetic SZ-map. Clearly, the kinetic and thermal SZ-effects are separated by approximately one order of magnitude.

The distribution of pixel amplitudes is very broad, encompassing the largest line-of-sight Comptonisations of $y \simeq 1.5 \times 10^{-4}$ and $|w| \simeq 1.6 \times 10^{-5}$ down to very low signals below $\log(y) \simeq -20$. The distribution is bimodal, which is a pixelisation artefact and which is caused by the replacement of faint and small clusters with a very narrow Gaussian, the extent of which is slightly above the pixel scale, once the cluster is smaller than $\simeq 2'0$ in diameter. These clusters are more concentrated than the King-profiles of resolved clusters. There is a caveat when applying an expansion into spherical harmonics $Y_m^\ell(\theta)$ to the SZ-maps: The smallest clusters are only a few pixels in diameter. Working with the HEALPix tessellation, reliable expansion coefficients can only be obtained up to

multipole moments of order $\ell \simeq 2 \times N_{\text{side}}$, i.e. up to $\ell \simeq 4096$ in my case, which corresponds to angular scales of $2'.64$. The pixel scale is $1'.71$ for this choice of the N_{side} -parameter. Consequently, the small clusters will not be contained in an expansion into spherical harmonics, as shown by the set of thick lines in Fig. 5.12: Here, the map has been decomposed in $a_{\ell m}$ -coefficients (compare eqn. (5.31)), multiplied with the $a_{\ell 0}$ -coefficients of a Gaussian beam of $\Delta\theta = 5'.0$ (FWHM) and synthesised again. Then, the resulting smoothed map does not contain small clusters, because the decomposition into spherical harmonics has not been able to resolve structures that extend over only a few pixels.

The mean value of the thermal Comptonisation y has been determined to be $\langle y \rangle = 3.01 \times 10^{-7}$ and the pixel-to-pixel variance is $\sigma_y = \sqrt{\langle y^2 \rangle - \langle y \rangle^2} = 1.85 \times 10^{-6}$. In analogy, the value $\langle w \rangle = 6.28 \times 10^{-9}$ has been derived for the kinetic map, with variance $\sigma_w = \sqrt{\langle w^2 \rangle - \langle w \rangle^2} = 3.78 \times 10^{-7}$, i.e. the mean kinetic Comptonisation is consistent with zero, due to the peculiar velocities following a Gaussian distribution with zero mean. The mean value of the moduli of the pixel amplitudes of the kinetic map is $\langle |w| \rangle = 7.65 \times 10^{-8}$.

The value for the mean Comptonisation $\langle y \rangle$ measured on the map should account for roughly 40% of the mean thermal Comptonisation as derived in Sect. 5.4.4, due to the lower mass threshold inherent to the simulation. Keeping in mind the absence of any diffuse component of the thermal Comptonisation, the value derived here is compatible with the value of $\simeq 10^{-6}$ given by Refregier et al. (2000) and Scaramella et al. (1993), but falls short of the value derived by White et al. (2002) by a factor of less than two. Myers et al. (2004) performed a cross-correlation of WMAP-data with clusters from the APM survey and found the mean Comptonisation to be significantly larger and to be in accordance with Persi et al. (1995), but in contradiction with expectations from CDM models.

5.5.5. Angular power spectra of the thermal and kinetic SZ-effects

In this section, the angular power spectra are given for the all-sky maps. They follow from a decomposition of the spherical data set into spherical harmonics $Y_\ell^m(\theta)$:

$$y_{\ell m} = \int_{4\pi} d\Omega y(\theta) Y_\ell^m(\theta)^*, \quad (5.29)$$

$$w_{\ell m} = \int_{4\pi} d\Omega w(\theta) Y_\ell^m(\theta)^*, \text{ and} \quad (5.30)$$

$$w'_{\ell m} = \int_{4\pi} d\Omega |w(\theta)| Y_\ell^m(\theta)^*, \quad (5.31)$$

respectively. The spherical harmonical transform $w'_{\ell m}$ has been determined from the absolute values of the kinetic map amplitudes. The reason for doing so is the vanishing expectation value of the peculiar velocities in the comoving frame such that for a given cluster in the thermal SZ-map, both signs of the kinetic SZ-effect are equally likely to occur and the cross-power averages out to zero. The angular power spectra and the cross power spectrum are defined via:

$$C_{yy}(\ell) = \frac{1}{2\ell + 1} \sum_{m=-\ell}^{+\ell} y_{\ell m} y_{\ell m}^*, \quad (5.32)$$

$$C_{ww}(\ell) = \frac{1}{2\ell + 1} \sum_{m=-\ell}^{+\ell} w_{\ell m} w_{\ell m}^*, \quad (5.33)$$

$$C_{yw'}(\ell) = \frac{1}{2\ell + 1} \sum_{m=-\ell}^{+\ell} w'_{\ell m} y_{\ell m}^*, \quad (5.34)$$

with the asterisk denoting complex conjugation. The resulting power spectra are given in Fig. 5.13 in comparison to the power-spectra derived by White et al. (2002) in simulations covering smaller angular scales. The curves match well, and the remaining discrepancies may be explained by the fact that in the maps presented here, power is missing on small scales due to the low-mass cutoff, whereas the simulation by White is missing power on large scales due to the smallness of their simulation box. The bending-over of the spectra derived from my SZ-maps is also due to the fact that the expansion in spherical harmonics cannot be computed for angular scales approaching the pixel scale and thus does not include very small clusters of sizes comparable to the pixel size, as already discussed in Sect. 5.5.4.

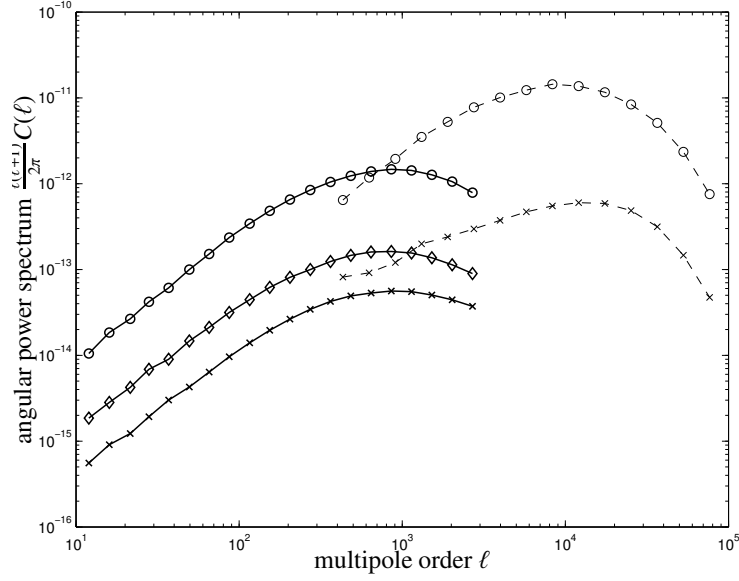


Figure 5.13.: Angular power spectra of the thermal and kinetic SZ-effect: $C_{yy}(\ell)$ (circles, solid line), $C_{ww}(\ell)$ (crosses, solid line) and the cross power spectrum $C_{yw}(\ell)$ (diamonds, solid line) are shown in comparison to the power spectra of the thermal SZ-effect (circles, dashed line) and the kinetic SZ-effect (crosses, dashed line) obtained by White et al. (2002) at smaller scales, i.e. at higher multipole order ℓ .

If clusters were randomly positioned point-sources on the sky, the number of clusters per solid angle element would be a Poisson-process and the resulting power spectrum should be flat, i.e. $C(\ell) \propto N$ (N is the number of sources), as shown by Seljak et al. (2001). Contrarily, the brightness distribution of clusters assigns additional weight to the large angular scales and giving rise to a significant deviation in the slope of the power spectra $C(\ell) \propto \ell^{-\gamma}$ as a function of ℓ : The measured slope is $2 + \gamma = 1.53 \pm 0.07$ for the thermal and $2 + \gamma = 1.45 \pm 0.07$ for the kinetic SZ-effect, which reflects the deviation from pure Poissonianity. In the fitting, the values for ℓ have been restricted to $1 \leq \ell \leq 100$ and the errors derived correspond to the 95% confidence intervals.

Furthermore, Fig. 5.13 shows the cross-correlation between the thermal SZ-map and the absolute value of the kinetic SZ-map. As expected, the amplitude of the cross-power spectrum is at an intermediate level compared to autocorrelations of the thermal and kinetic SZ-maps.

5.5.6. Source counts at PLANCK frequencies

As the last point in this analysis, I address the SZ source counts, i.e. the number N of SZ-clusters giving rise to flux changes exceeding a certain flux threshold S_{\min} . The SZ flux modulation as a function of frequency is given by:

$$S(x) = S_0 \int d\Omega [y g(x) - \beta\tau h(x)] \quad (5.35)$$

$$= S_0 [\mathcal{Y}g(x) - \mathcal{W}h(x)] = S_{\mathcal{Y}}(x) - S_{\mathcal{W}}(x), \quad (5.36)$$

where $S_0 = 22.9 \text{ Jy/arcmin}^2$ is the flux density of the CMB and \mathcal{Y} and \mathcal{W} denote the integrated thermal and kinetic Comptonisations. The functions $g(x)$ and $h(x)$ are the flux modulations caused by the thermal and kinetic SZ-effects for non-relativistic electron velocities:

$$g(x) = \frac{x^4 \exp(x)}{(\exp(x) - 1)^2} \left[x \frac{\exp(x) + 1}{\exp(x) - 1} - 4 \right], \quad (5.37)$$

$$h(x) = \frac{x^4 \exp(x)}{(\exp(x) - 1)^2}. \quad (5.38)$$

	1	2	3	4	5	6	7	8	9
ν_0	30 GHz	44 GHz	70 GHz	100 GHz	143 GHz	217 GHz	353 GHz	545 GHz	857 GHz
$\Delta\nu$	3.0 GHz	4.4 GHz	7.0 GHz	16.7 GHz	23.8 GHz	36.2 GHz	58.8 GHz	90.7 GHz	142.8 GHz
$\langle S_{\mathcal{Y}} \rangle$	-12.2 Jy	-24.8 Jy	-53.6 Jy	-82.1 Jy	-88.8 Jy	-0.7 Jy	146.0 Jy	76.8 Jy	5.4 Jy
$\langle S_{\mathcal{W}} \rangle$	6.2 Jy	13.1 Jy	30.6 Jy	55.0 Jy	86.9 Jy	110.0 Jy	69.1 Jy	15.0 Jy	0.5 Jy
$\Delta T_{\mathcal{Y}}$	-440 nK	-417 nK	-356 nK	-267 nK	-141 nK	-0.5 nK	38 nK	8.4 nK	0.2 nK
$\Delta T_{\mathcal{W}}$	226 nK	220 nK	204 nK	179 nK	138 nK	76 nK	18 nK	1.6 nK	0.02 nK

Table 5.2.: Characteristics of PLANCK’s LFI- and HFI-receivers: centre frequency ν , frequency window $\Delta\nu$ (as defined in eqn. (5.40)), fluxes $\langle S_{\mathcal{Y}} \rangle$ and $\langle S_{\mathcal{W}} \rangle$ (see eqn. (5.36)) generated by the respective Comptonisation of $\mathcal{Y} = \mathcal{W} = 1 \text{ arcmin}^2$ and the corresponding changes in antenna temperature $\Delta T_{\mathcal{Y}}$ and $\Delta T_{\mathcal{W}}$. Due to PLANCK’s symmetric frequency response window, the thermal SZ-effect does not vanish entirely at $\nu = 217 \text{ GHz}$.

Here, x again denotes the dimensionless frequency $x = h\nu/(k_B T_{\text{CMB}})$. The averaged flux $\langle S \rangle_{\nu_0}$ at the fiducial frequency ν_0 is obtained by weighted summation with the frequency response window function $R_{\nu_0}(\nu)$ and can readily be converted to antenna temperature T_A by means of eqn. (5.39):

$$\langle S \rangle_{\nu_0} = \frac{\int d\nu S(\nu) R_{\nu_0}(\nu)}{\int d\nu R_{\nu_0}(\nu)} = 2 \frac{\nu_0^2}{c^2} k_B T_A. \quad (5.39)$$

The main characteristics of PLANCK’s receivers and the conversion factors from 1 arcmin^2 of thermal or kinetic Comptonisation to fluxes in Jansky and changes in antenna temperature measured in nK is given by Table 5.2. For the derivation of the values a top-hat shaped frequency response function $R_{\nu_0}(\nu)$ has been assumed:

$$R_{\nu_0}(\nu) = \begin{cases} 1, & \nu \in [\nu_0 - \Delta\nu, \nu_0 + \Delta\nu] \\ 0, & \nu \notin [\nu_0 - \Delta\nu, \nu_0 + \Delta\nu] \end{cases}. \quad (5.40)$$

Figures 5.14, 5.15 and 5.16 show the source counts stated in number of clusters perdeg² as a function of averaged flux $\langle S \rangle_{\nu_0}$ for PLANCK’s $\nu_0 = 143 \text{ GHz}$ -, $\nu_0 = 217 \text{ GHz}$ -, and $\nu_0 = 353 \text{ GHz}$ -channels, respectively.

The source counts $N(S)$ are well approximated by power laws of the form:

$$N(\langle S \rangle > S_{\text{min}}) = N_0 S^\alpha. \quad (5.41)$$

Values for the normalisations N_0 and the slopes α have been obtained by fits to the source counts for the three relevant PLANCK-frequencies and are stated in Table 5.3. In the fits, the four rightmost bins have been excluded because of poor statistics. The parameters of the power law has been derived for the fluxes following from the idealised case based on the virial theorem and compared to fluxes determined from template cluster data.

The slopes derived from fits to the cluster number counts are slightly steeper for the virial estimates compared to template data ($\alpha \simeq -5/3$ versus $\alpha \simeq -1.4$), which again reflects the weaker dependence on cluster mass observed in template data. Comparing data sets for different frequencies, the slopes α are of course almost identical, because only amplitudes are changed by the choice of a different frequency band. The number of clusters N_0 stays roughly constant in the case of the kinetic SZ-effect, but reflects the distinct frequency modulation in the case of the thermal SZ-effect. Here, it should be emphasised, that the thermal SZ-effect does not vanish entirely at $\nu = 217 \text{ GHz}$ due to PLANCK’s symmetric frequency response window. The difference in numbers between the estimates based on virial quantities to those measured on template data amounts to roughly half an order of magnitude in the kinetic SZ-effect, but rises almost an order of magnitude at small fluxes for the thermal SZ-effect. There is however good agreement in the number counts of thermal SZ clusters at high fluxes.

The difference in slope of the thermal versus kinetic SZ-cluster number counts is caused by the $M^{5/3}$ -scaling of the thermal SZ-effect relative to the proportionality to M of the kinetic effect. Due to the difference in slope, the effects are separated by two orders of magnitude for the largest fluxes, while this difference increases to eight orders of magnitude for the smallest fluxes, which hints at the difficulties to be faced in detecting kinetic clusters compared to even faint thermal detections. The slopes derived here are in good agreement with the those obtained by Kay et al. (2001)

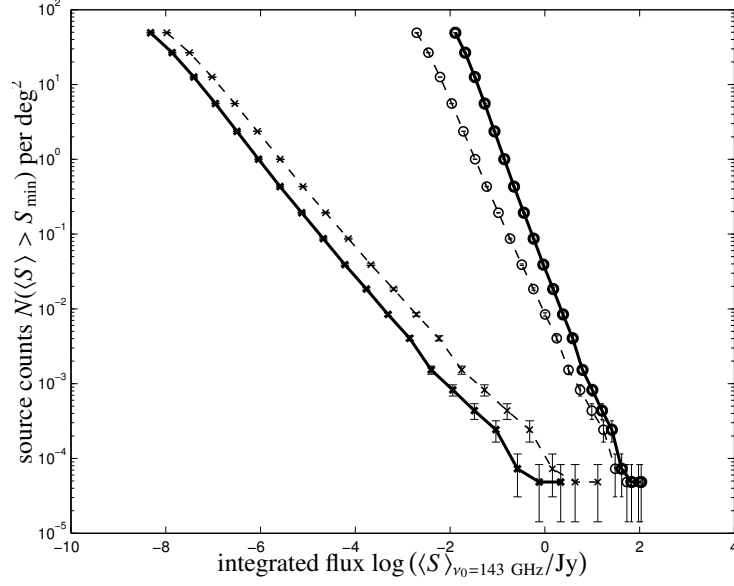


Figure 5.14.: Source counts $N(\langle S \rangle > S_{\min})$ for thermal (circles) and kinetic clusters (crosses) for PLANCK's $\nu_0 = 143$ GHz channel and for fluxes measured on the scaled template clusters (dashed line) in comparison to virial fluxes (solid line).

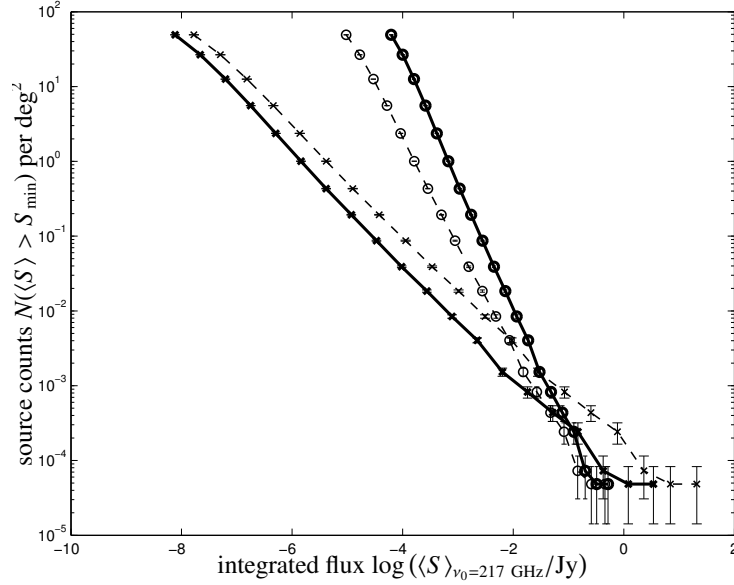


Figure 5.15.: Source counts $N(\langle S \rangle > S_{\min})$ for thermal (circles) and kinetic clusters (crosses) for PLANCK's $\nu_0 = 217$ GHz channel, the dashed and solid lines contrast the fluxes measured on the template data and those following from virial scaling relations, respectively. For the given frequency response function $R_{\nu_0}(\nu)$, the thermal SZ-effect does not vanish entirely at $\nu_0 = 217$ GHz.

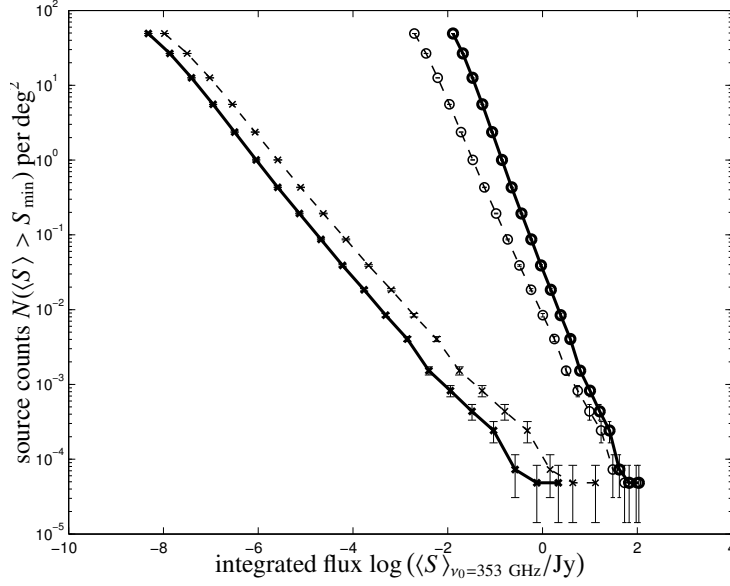


Figure 5.16.: Source counts $N(\langle S \rangle > S_{\min})$ for thermal (circles) and kinetic clusters (crosses) for PLANCK's $\nu_0 = 353$ GHz channel, again for fluxes derived from template data (dashed line) in comparison to fluxes following from virial scaling relations (solid line).

channel	$\nu_0 = 143$ GHz	$\nu_0 = 217$ GHz	$\nu_0 = 353$ GHz
thermal SZ-effect, virial estimate	$\log N_0 = -1.78 \pm 0.02$ $\alpha = -1.67 \pm 0.03$	$\log N_0 = -5.31 \pm 0.02$ $\alpha = -1.67 \pm 0.07$	$\log N_0 = -1.42 \pm 0.22$ $\alpha = -1.66 \pm 0.02$
kinetic SZ-effect, virial estimate	$\log N_0 = -4.49 \pm 0.01$ $\alpha = -0.76 \pm 0.06$	$\log N_0 = -4.42 \pm 0.01$ $\alpha = -0.76 \pm 0.05$	$\log N_0 = -4.57 \pm 0.01$ $\alpha = -0.76 \pm 0.06$
thermal SZ-effect, simulation	$\log N_0 = -2.36 \pm 0.02$ $\alpha = -1.40 \pm 0.03$	$\log N_0 = -5.31 \pm 0.02$ $\alpha = -1.40 \pm 0.06$	$\log N_0 = -2.06 \pm 0.02$ $\alpha = -1.40 \pm 0.03$
kinetic SZ-effect, simulation	$\log N_0 = -3.95 \pm 0.01$ $\alpha = -0.72 \pm 0.04$	$\log N_0 = -3.88 \pm 0.01$ $\alpha = -0.72 \pm 0.05$	$\log N_0 = -4.02 \pm 0.01$ $\alpha = -0.72 \pm 0.05$

Table 5.3.: Values obtained from fits of a power law of the type $N(S) = N_0 S^\alpha$ to the cumulative source counts as a function of flux exceeding the threshold S for both SZ-effects. In the table, values obtained from virial estimates are contrasted to values following from measurements on template data. The errors quoted denote the 95% confidence intervals.

5.6. Summary

All-sky maps for the thermal and kinetic Sunyaev-Zel'dovich effects are presented and their characteristics are described in detail. The maps because of their angular resolution and the data storage format chosen (HEALPix) especially suited for simulations for PLANCK.

- The all-sky maps of the thermal and kinetic SZ-effects presented here incorporate the correct 2-point correlation function, the evolving mass function and the correct size distribution of clusters, to within the accuracy of the underlying Hubble-volume simulation and the small-scale adiabatic gas simulations.
- The maps presented here exhibit significant cluster substructure (compare Sect. 5.5.1). In spite of this, fits to the Comptonisation maps yield angular core radii, the distribution of which are close to the expectation based on the virial theorem (Sect. 5.5.2).
- The difference in the distribution of the integrated Comptonisations \mathcal{Y} and \mathcal{W} (Sect. 5.5.3) and source counts $N(\langle S \rangle > S_{\min})$ (Sect. 5.5.6) between values derived from scaling relations compared to those following from template data have been found to be substantial, which hints at possible misestimations of the number of clusters detectable for PLANCK.
- An analytic investigation in Sect. 5.4.4 quantified the contribution of the cluster sample to the sky averaged mean thermal Comptonisation $\langle y \rangle$ and its variance σ_y . It was found that the clusters within the boundaries in mass ($M > 5 \times 10^{13} M_{\odot}/h$) and redshift ($z < 1.48$) make up $\simeq 40\%$ of the mean Comptonisation, but account for $\sim 98\%$ of the variance. The value for the mean Comptonisation corresponds well to that obtained by other authors (Sect. 5.5.4).
- The power spectra (Sect. 5.5.5) are compatible in amplitude and slope to the ones found by [White et al. \(2002\)](#). On large angular scales, i.e. at small multipole ℓ , deviations from the Poissonianity in the slope of the power spectrum have been found.
- The velocities of the kinetic SZ-map correspond to the actual cosmological density environment, i.e. correlated infall velocities are observed due to the formation of superclusters, which highlights a significant improvement in comparison to methods that draw a cluster peculiar velocity from a (Gaussian) distribution and enables searches for the kinetic SZ-effect by considering spatial correlations with the thermal SZ-effect. The cross correlation of the thermal with the kinetic SZ-map yields a spectrum similar in shape at intermediate amplitudes (see Sect. 5.5.5).

Despite the high level of authenticity that the all-sky SZ-maps exhibit, there are quite a few issues not being taken account of: The baryon distribution and temperature inside the ICM is governed by processes beyond adiabatic gas physics, for example in the form of supernova feedback and radiative cooling. Especially the latter process gives rise to cool cores which may enhance the thermal SZ-signal. The ionisation inside the clusters was assumed to be complete. Furthermore, the maps contain only collapsed objects and hence filamentary structures or diffuse gas are not included. Concerning the thermal history of the ICM, reionisation had to be neglected. The kinetic map has been constructed without taking account of velocity fluctuations inside the cluster. This does not pose a problem for PLANCK, but needs to be remedied in high-resolution SZ-surveys to be undertaken with the *Atacama Cosmology Telescope* and the *South Pole Telescope*. Yet another imperfection is the lack of non-thermal particle populations that cause the relativistic SZ-effect ([Enßlin & Kaiser 2000](#)), whose detectability with PLANCK is still a matter of debate.

The results of this chapter were worked out in collaboration with M. Bartelmann (ITA, Heidelberg) and C. Pfrommer (MPA, Garching). V. Springel (MPA, Garching) and L. Herquist (CfA, Harvard) provided the adiabatic hydrodynamical simulations. A paper entitled Detecting Sunyaev-Zel'dovich clusters with PLANCK: I. Construction of all-sky thermal and kinetic SZ-maps which summarises the results of this chapter has been submitted to the journal Monthly Notices of the Royal Astronomical Society and is available online ([astro-ph/0407089](#)).

6. Microwave emission components of the Milky Way and the Solar system

Abstract

In order to assess PLANCK's SZ-capabilities in the presence of spurious signals, a simulation is presented that combines maps of the thermal and kinetic SZ-effects with a realisation of the cosmic microwave background (CMB), in addition to Galactic foregrounds (synchrotron emission, free-free emission, thermal emission from dust, CO-line radiation) as well as the sub-millimetric emission from celestial bodies of our Solar system. Additionally, observational issues such as the finite angular resolution and spatially non-uniform instrumental noise of PLANCK's sky maps are taken into account, yielding a set of all-sky flux maps, the auto-correlation and cross-correlation properties of which are examined in detail.

6.1. Introduction

The Sunyaev-Zel'dovich (SZ) effect (Sunyaev & Zel'dovich 1972, 1980, Rephaeli 1995, Birkinshaw 1999) is the most important extragalactic source of secondary anisotropies in the CMB sky. The thermal SZ-effect is explained by the fact that CMB photons are put in thermal contact with electrons of the hot intra-cluster medium (ICM) by Compton-interactions which causes a transfer of energy from the ICM to the CMB. Because of the smallness of the Thompson cross-section and of the diluteness of the ICM this transfer of thermal energy is small. In the direction of a cluster, low-energetic photons with frequencies below $\nu = 217$ GHz are removed from the line-of-sight. At frequencies above $\nu = 217$ GHz CMB photons are scattered into the line-of-sight, causing a distinct modulation of the CMB surface brightness as a function of observing frequency, which enables the detection of clusters of galaxies in microwave data.

In contrast, in the kinetic effect it is the peculiar motion of a cluster along the line of sight relative to the CMB frame that induces CMB surface brightness fluctuations. The peculiar motion of the cluster causes the CMB to be anisotropic in the cluster frame. Due to this symmetry breaking of the scattering geometry, photons scattered into the line-of-sight are shifted in frequency, namely to higher frequencies, if the cluster is moving towards the observer.

The PLANCK-mission will be especially suited to detect SZ-clusters due to its sensitivity, its spectroscopic capabilities, sky coverage and spatial resolution. It is expected to yield a cluster catalogue containing $\approx 10^4$ entries. Extensive literature exists on the topic, but so far the influence of foregrounds and details of PLANCK's instrumentation and data acquisition have not been thoroughly addressed. In this work we aim at modelling the astrophysical and instrumental issues connected to the observation of SZ-clusters as exhaustively as possible: A simulation is presented that combines realistic maps of both SZ-effects with a realisation of the CMB, with four different Galactic foreground components (thermal dust, free-free emission, synchrotron emission and emission from rotational transitions of CO molecules), with maps containing the sub-millimetric emission from planets and asteroids of the Solar system and with instrumental noise. PLANCK's frequency response and beam shapes are modelled conforming to the present knowledge of PLANCK's receivers and its optical system. In order to extract the SZ-cluster signal, filtering schemes based on matched and scale-adaptive filtering are extended to spherical data sets.

The chapter is structured as follows: After a brief recapitulation of the SZ-effect in Sect. 6.2, the PLANCK-satellite and instrumental issues connected to the observation of CMB anisotropies are described in Sect. 6.3. The foreground emission components are introduced in Sect. 6.4. The steps in the simulation of flux maps for the various PLANCK-channels are described and their correlation properties are examined in Sect. 6.5. A summary in Sect. 6.6 concludes the chapter.

Throughout the chapter, the cosmological model assumed is the standard Λ CDM cosmology, which has recently been supported by observations of the WMAP satellite (Spergel et al. 2003). Parameter values have been chosen as

$\Omega_M = 0.3$, $\Omega_\Lambda = 0.7$, $H_0 = 100 h \text{ km s}^{-1} \text{ Mpc}^{-1}$ with $h = 0.7$, $\Omega_B = 0.04$, $n_s = 1$ and $\sigma_8 = 0.9$.

6.2. Sunyaev-Zel'dovich definitions

The Sunyaev-Zel'dovich effects are the most important extragalactic sources of secondary anisotropies in the CMB. Inverse Compton scattering of CMB photons with electrons of the ionised ICM gives rise to these effects and induce surface brightness fluctuations of the CMB sky, either because of the thermal motion of the ICM electrons (thermal SZ-effect) or because of the bulk motion of the cluster itself relative to the comoving CMB-frame along the line-of-sight (kinetic SZ-effect).

The relative change $\Delta T/T$ in thermodynamic CMB temperature at position θ as a function of dimensionless frequency $x = h\nu/(k_B T_{\text{CMB}})$ due to the thermal SZ-effect is given by:

$$\frac{\Delta T}{T}(\theta) = y(\theta) \left(x \frac{e^x + 1}{e^x - 1} - 4 \right) \text{ with} \quad (6.1)$$

$$y(\theta) = \frac{\sigma_T k_B}{m_e c^2} \int dl n_e(\theta, l) T_e(\theta, l), \quad (6.2)$$

where the amplitude y of the thermal SZ-effect is commonly known as the thermal Comptonisation parameter, that itself is defined as the line-of-sight integral of the temperature weighted thermal electron density. m_e , c , k_B and σ_T denote electron mass, speed of light, Boltzmann's constant and the Thompson cross section, respectively. The kinetic SZ-effect arises due to the motion of the cluster parallel to the line of sight relative to the CMB-frame:

$$\frac{\Delta T}{T}(\theta) = -w(\theta) \text{ with } w(\theta) = \frac{\sigma_T}{c} \int dl n_e(\theta, l) v_r(\theta, l). \quad (6.3)$$

Here, v_r is the radial component of the cluster's velocity. The convention is such that $v_r < 0$, if the cluster is moving towards the observer. In this case, the CMB temperature is increased. In analogy, the quantity w is referred to as the kinetic Comptonisation. The SZ-observables are the line-of-sight Comptonisations integrated over the solid angle subtended by the cluster. The quantities \mathcal{Y} and \mathcal{W} are referred to as the integrated thermal and kinetic Comptonisations, respectively:

$$\mathcal{Y} = \int d\Omega y(\theta) = d_A^{-2}(z) \frac{\sigma_T k_B}{m_e c^2} \int dV n_e T_e \quad (6.4)$$

$$\mathcal{W} = \int d\Omega w(\theta) = d_A^{-2}(z) \frac{\sigma_T}{c} \int dV n_e v_r \quad (6.5)$$

Here, $d_A(z)$ denotes the angular diameter distance of a cluster situated at redshift z .

6.3. Submillimetric observations with PLANCK

The PLANCK-mission^{1,2} will perform a polarisation sensitive survey of the complete microwave sky in nine observing frequencies from the Lagrange point L_2 in the Sun-Earth system. It will observe at angular resolutions of up to $5'0$ in the best channels and will achieve micro-Kelvin sensitivity relying on bolometric receivers (high frequency instrument HFI, described in Lamarre et al. 2003) and on high electron mobility transistors (low frequency instrument LFI, see Villa et al. 2003, Bersanelli & Mandolesi 2000). The main characteristics are summarised in Table 6.1. PLANCK's beam characteristics are given Sect. 6.3.1 and the scanning strategy and the simulation of spatially non-uniform detector noise is outlined in Sect. 6.3.2.

6.3.1. Beam shapes

The beam shapes of PLANCK are well described by azimuthally symmetric Gaussians $b(\theta) = \frac{1}{2\pi\sigma_\theta^2} \exp\left(-\frac{\theta^2}{2\sigma_\theta^2}\right)$ with $\sigma_\theta = \frac{\Delta\theta}{\sqrt{8 \ln(2)}}$. Examples of PLANCK's beams are given in Fig. 6.1. The residuals from the ideal Gaussian

¹<http://planck.mpa-garching.mpg.de/>

²<http://astro.estec.esa.nl/Planck/>

	1	2	3	4	5	6	7	8	9
ν_0	30 GHz	44 GHz	70 GHz	100 GHz	143 GHz	217 GHz	353 GHz	545 GHz	857 GHz
$\Delta\nu$	3.0 GHz	4.4 GHz	7.0 GHz	16.7 GHz	23.8 GHz	36.2 GHz	58.8 GHz	90.7 GHz	142.8 GHz
$\Delta\theta$	33'4	26'8	13'1	9'2	7'1	5'0	5'0	5'0	5'0
σ_N	1.01 mK	0.49 mK	0.29 mK	5.67 mK	4.89 mK	6.05 mK	6.80 mK	3.08 mK	4.49 mK
$\langle S_{\mathcal{Y}} \rangle$	-12.2 Jy	-24.8 Jy	-53.6 Jy	-82.1 Jy	-88.8 Jy	-0.7 Jy	146.0 Jy	76.8 Jy	5.4 Jy
$\langle S_{\mathcal{W}} \rangle$	6.2 Jy	13.1 Jy	30.6 Jy	55.0 Jy	86.9 Jy	110.0 Jy	69.1 Jy	15.0 Jy	0.5 Jy
$\Delta T_{\mathcal{Y}}$	-440 nK	-417 nK	-356 nK	-267 nK	-141 nK	-0.5 nK	38 nK	8.4 nK	0.2 nK
$\Delta T_{\mathcal{W}}$	226 nK	220 nK	204 nK	179 nK	138 nK	76 nK	18 nK	1.6 nK	0.02 nK

Table 6.1.: Characteristics of PLANCK's LFI-receivers (column 1-3) and HFI-bolometers (column 4-9): centre frequency ν_0 , frequency window $\Delta\nu$ as defined in eqns. (6.27) and (6.28), angular resolution $\Delta\theta$ stated in FWHM, effective noise level σ_N , fluxes $\langle S_{\mathcal{Y}} \rangle$ and $\langle S_{\mathcal{W}} \rangle$ generated by the respective Comptonisation of $\mathcal{Y} = \mathcal{W} = 1 \text{ arcmin}^2$ and the corresponding changes in antenna temperature $\Delta T_{\mathcal{Y}}$ and $\Delta T_{\mathcal{W}}$. Due to PLANCK's symmetric frequency response window, the thermal SZ-effect does not vanish entirely at $\nu = 217 \text{ GHz}$.

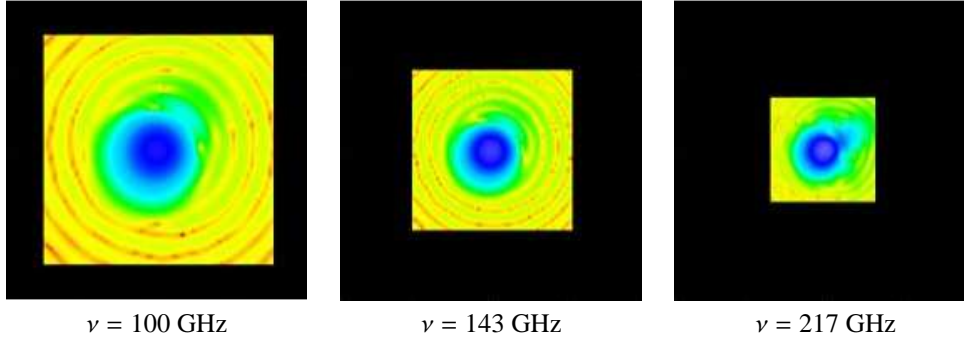


Figure 6.1.: Beam shapes of various PLANCK channels in logarithmic colour coding. The beam patterns show interesting features such as asymmetries and diffraction rings. The images followed from a ray-tracing simulation of PLANCK's optical system including diffraction on the mirrors and detector entry windows.

shape (ellipticity, higher order distortions, diffraction rings, far-side lobes, pick-up of stray-light) are expected not to exceed the percent level and are neglected for the purpose of this work. Table 6.1 gives the angular resolution $\Delta\theta$ in terms of FWHM of each PLANCK-channel for reference.

6.3.2. Scanning strategy and noise-equivalent maps

CMB observations by PLANCK will proceed in great circles fixed on the ecliptic poles. A single scan will start at the North ecliptic pole, will follow a meridian to the South ecliptic pole and back to the North ecliptic pole by following the antipodal meridian. Such a scan will last one minute and will be repeated sixty times. After that, the rotation axis will be shifted in a precessional motion for 2'5 (approximately half a beam diameter) and the scan repeated. In this way, the entire sky is mapped once in 180 days.

Fourier transform of the noise time series of PLANCK's receivers yields a noise power spectrum $P(f)$ of the shape

$$P(f) = \sigma_N^2 \left[1 + \left(\frac{f}{f_{\text{knee}}} \right)^{-\alpha} \right], \quad (6.6)$$

i.e. the noise consists of two components: a power law component in frequency f , described by the spectral index α that assuming values $0 \leq \alpha \leq 2$ and a white noise component, smoothly joined at the frequency f_{knee} .

The $f^{-\alpha}$ -part of the noise spectrum originates from zero point drifts of the detector gain on large time scales.

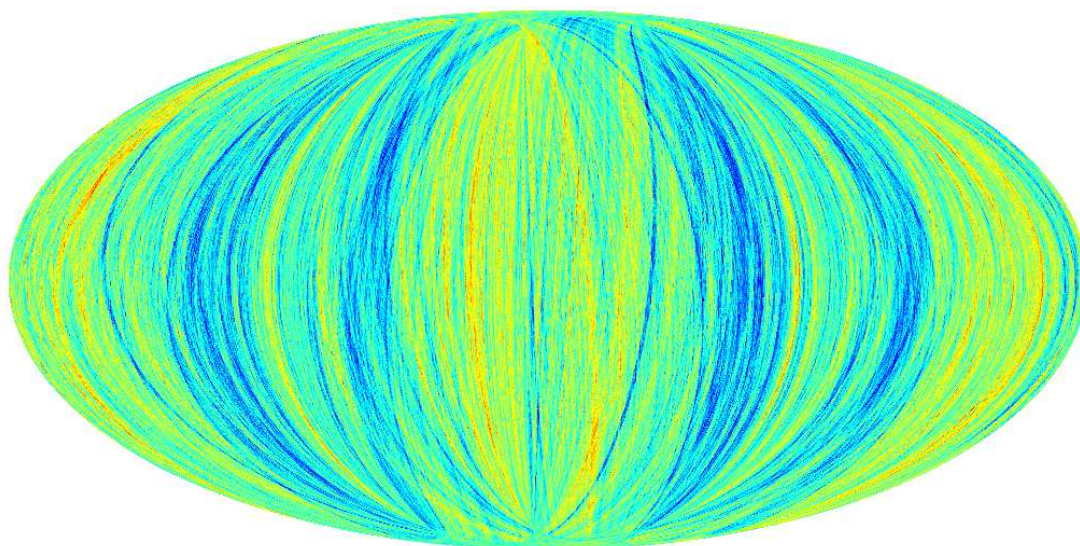


Figure 6.2.: A sky map with the stripe pattern caused by the long-wavelength $f^{-\alpha}$ -noise with $\alpha = 1$. The relative skewness of single scan paths is caused by the non-ideal detector pointing of PLANCK.

This power law component exhibits low-frequency variations that lead to the typical stripe pattern in simulated PLANCK-maps due to the scanning strategy (Maino et al. 1999). Algorithms for destriping the maps are a current research topic (for example, the Mirage-algorithm proposed by Yvon & Mayet (2004), MAPCUMBA by Doré et al. (2001) the max-likelihood algorithm by Natoli et al. (2001), and the Madam-algorithm proposed by Keihanen et al. (2004)), but it can be expected that the destriping can be done very efficiently such that the remaining noise largely consists of uncorrelated pixel noise. An example of such a sky map is given in Fig. 6.2.

In order to incorporate uncorrelated pixel noise into the simulation, a set of maps has been constructed, where at each pixel a number from a Gaussian distribution with width σ_N has been drawn. For PLANCK's HFI-receivers, the rms-fluctuations σ_N in antenna temperature can be calculated from the noise equivalent power NEP and the sampling frequency $\nu_{\text{sampling}} = 200$ Hz via:

$$\sigma_N = \frac{2 \text{NEP} \sqrt{\nu_{\text{sampling}}}}{k_B \Delta\nu} \quad (\text{HFI}) \quad (6.7)$$

Alternatively, for PLANCK's LFI-receivers, the rms-fluctuations σ_N in antenna temperature are given by:

$$\sigma_N = \sqrt{2} \frac{T_{\text{noise}} + T_{\text{CMB}}}{\sqrt{\Delta\nu/\nu_{\text{sampling}}}} \quad (\text{LFI}) \quad (6.8)$$

Values for T_{noise} and NEP can be obtained from PLANCK's simulation pipeline manual. The resulting effective noise level for all PLANCK channels for a single observation of a pixel is given in Table 6.1. Formulae and respective parameters are taken from the PLANCK simulation manual, available via PLANCK's website.

The rms-fluctuations σ_N in antenna temperature have to be scaled by $\sqrt{n_{\text{det}}}$ (assuming Poissonian statistics), where n_{det} denotes the number of redundant receivers per channel, because they provide independent surveys of the microwave sky.

From simulated scanning paths it is possible to derive an exposure map using the `simmission-` and `multimod-` utilities. An example of such an exposure map in the vicinity of the North ecliptic pole is given in Fig. 6.3. Using the number of observations n_{obs} per pixel, it is possible to scale down the noise amplitudes by $\sqrt{n_{\text{obs}}}$ and to obtain a realistic noise map for each channel. Here, I apply the simplification that all detectors of a given channel are arranged collinearly. In this case, the exposure maps will have sharp transitions from well-observed regions around the ecliptic poles to the region around the ecliptic equator. In real observations these transitions will be smoothed out due slight displacements of the optical axes among each other which causes the effective exposure pattern to be a superposition of rotated and distorted single-receiver exposure patterns.

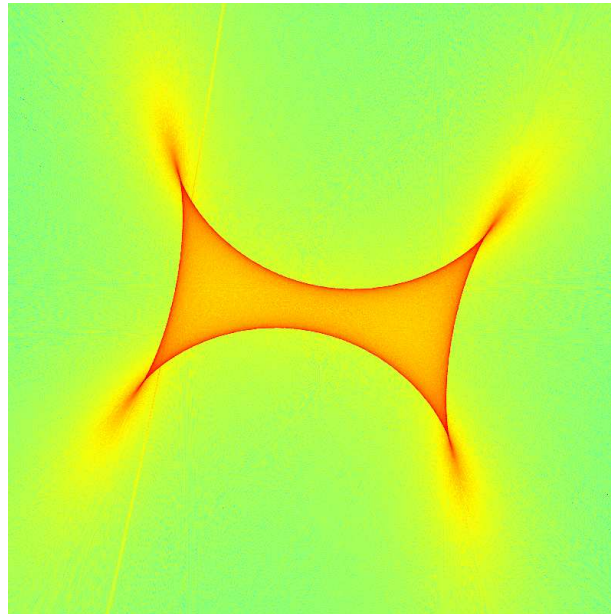


Figure 6.3.: Exposure map (side length $\approx 70^\circ$) of a single $\nu = 353$ GHz-receiver at the North ecliptic pole in logarithmic shading: The displacement of the receiver with respect to the optical axis causes the observational rings not to overlap exactly at the pole, but gives rise to the lozenge-shaped pattern in the sky-coverage map. On average, the pixels inside the lozenge are observed roughly 100 times, compared to ~ 20 times outside. Pixels on the edges of the lozenge are observed a few thousand times. The best observed pixels are situated on the tips of the lozenge, where values as high as 2×10^4 are attained. The numbers correspond to the planned mission lifetime of 1 year. The faint diagonal tangential line on the left side is caused by 2008's being a leap year: The mapping of the entire sky would be completed in 365 days, but there is an additional day available.

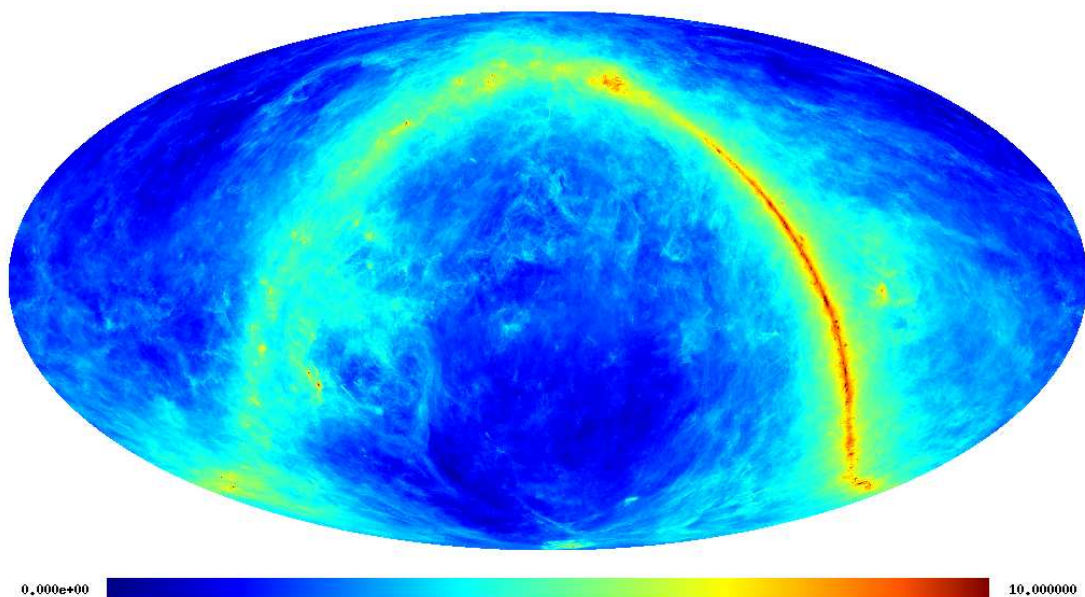


Figure 6.4.: Sky map of the antenna temperature increase caused by dust emission in the $\nu = 100$ GHz-channel: The shading is proportional to $\text{arsinh}(T_A(\nu = 100 \text{ GHz})/\mu\text{K})$. Ecliptic coordinates have been chosen. This map has been derived from the dust-template map provided by [Schlegel et al. \(1998\)](#).

6.4. Foreground emission components

The observation of the CMB and of SZ-clusters is seriously impeded by various Galactic foregrounds and by the thermal emission of celestial bodies of our Solar system. In order to describe these emission components, template maps from microwave surveys are used. [Bouchet & Gispert \(1999\)](#) give a comprehensive review for the foreground components relevant for the PLANCK mission. As foreground components, I include thermal emission from dust in the Galactic plane (Sect. 6.4.1), Galactic synchrotron (Sect. 6.4.2) and free-free emission (Sect. 6.4.3), line emission from rotational transitions of carbon monoxide molecules in giant molecular clouds (Sect. 6.4.4), sub-millimetric emission from planets (Sect. 6.4.5) and from minor bodies of the Solar system (Sect. 6.4.6). Foreground components omitted at this stage are discussed in Sect. 6.4.7.

In this work, no attempt is made at modelling the interactions between various foreground components because of poorly known parameters such as the spatial arrangement along the line-of-sight of the emitting and absorbing components. Exemplarily, the reader is referred to [Finkbeiner \(2003\)](#), where the absorption of Galactic free-free emission by dust is discussed.

6.4.1. Galactic dust emission

At frequencies above ~ 100 GHz, the thermal emission from dust in the disk of the Milky Way is the most prominent feature in the microwave sky. Considerable effort has been undertaken to model the thermal emission from Galactic dust ([Schlegel et al. 1997, 1998](#), [Finkbeiner et al. 1999, 2000](#)). The thermal dust emission is restricted to low Galactic latitudes and the thin disk is easily discernible.

The input template map (see Fig. 6.4) is derived from an observation at a wavelength of $\lambda = 100 \mu\text{m}$, i.e. $\nu_0 = 3$ THz. Its amplitudes A_{dust} are given in MJy/sr, which are extrapolated to the actual frequency channels of PLANCK using a two-component model suggested by C. Baccigalupi (personal communication). Despite the fact that the dust is expected to spread over a large range of temperatures, the model reproduces the thermal emission

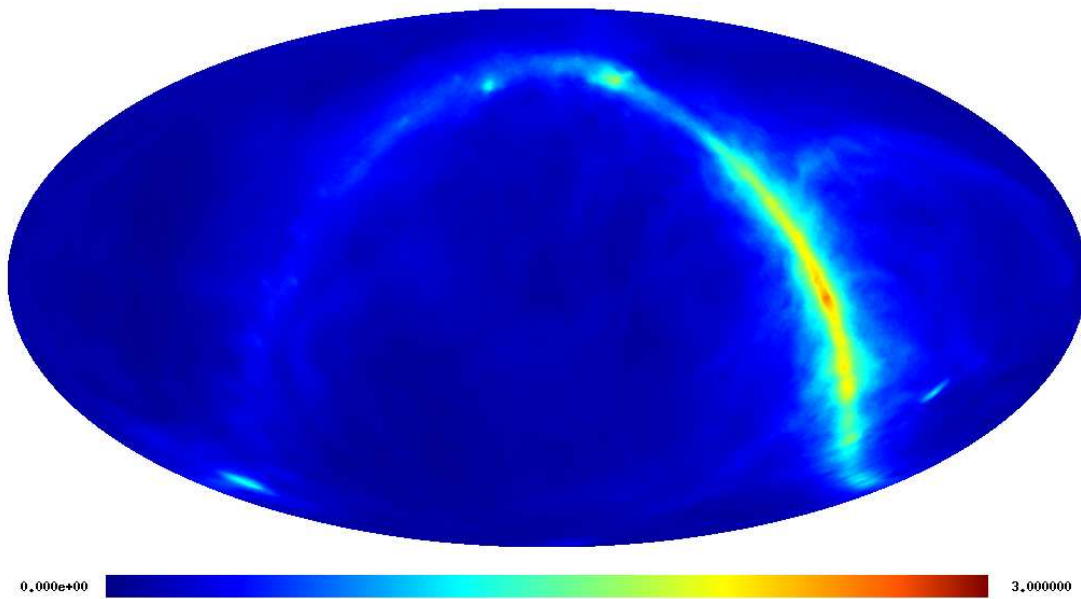


Figure 6.5.: Sky map of the antenna temperature increase caused by synchrotron emission in the $\nu = 100$ GHz-channel in ecliptic coordinates: The shading is proportional to $\text{arsinh}(T_A(\nu = 100 \text{ GHz})/\mu\text{K})$. The survey undertaken by [Haslam et al. \(1982\)](#) was used to construct this template.

remarkably well. This model yields for the flux $S_{\text{dust}}(\nu)$:

$$S_{\text{dust}}(\nu) = \frac{f_1 q \left(\frac{\nu}{\nu_0}\right)^{\alpha_1} B(\nu, T_1) + f_2 \left(\frac{\nu}{\nu_0}\right)^{\alpha_2} B(\nu, T_2)}{f_1 q B(\nu_0, T_1) + f_2 B(\nu_0, T_2)} A_{\text{dust}}. \quad (6.9)$$

The choice of parameters used is: $f_1 = 0.0363$, $f_2 = 1 - f_1$, $\alpha_1 = 1.67$, $\alpha_2 = 2.70$, $q = 13.0$. The two dust temperatures are $T_1 = 9.4$ K and $T_2 = 16.2$ K. The function $B(\nu, T)$ denotes the Planckian emission-law:

$$B(\nu, T) = \frac{2h}{c^2} \frac{\nu^3}{\exp(h\nu/k_B T) - 1}. \quad (6.10)$$

An improvement over this dust model would be the IRIS-map³ constructed by [Miville-Deschenes & Lagache \(2004\)](#), who used IRAS data for constructing sky maps showing the infrared dust emission of the Galactic disk, infrared cirrus at high Galactic latitudes, infrared point sources and zodiacal light. Like the current dust model, the map follows from an observation at 100 GHz, but has much better angular resolution.

6.4.2. Galactic synchrotron emission

Relativistic electrons of the interstellar medium produce synchrotron radiation by spiralling around magnetic field lines, which impedes CMB observations most strongly at frequencies below 100 GHz. The synchrotron emission reaches out to high Galactic latitude and is an important ingredient for modelling foreground emission in microwave observations. An all-sky survey at an observing frequency of 408 MHz has been compiled by [Haslam et al. \(1981, 1982\)](#) and adopted for usage with PLANCK by [Giardino et al. \(2002\)](#) (see Fig. 6.5). The average angular resolution of this survey is $0^\circ.85$ (FWHM).

Recent observations with WMAP ([Bennett et al. 2003](#)) indicate that the spectral slope of the synchrotron emission changes dramatically from $\gamma = -0.75$ at frequencies below 22 GHz to $\gamma = -1.25$ above 22 GHz. Theoretically, this may be explained by a momentum-dependent diffusion coefficient for cosmic ray electrons. In order to take account

³<http://www.cita.utoronto.ca/mamd/IRIS/IrisTechnical.html>

of this spectral steepening, the amplitudes A_{synchro} are multiplied with a prefactor in order to obtain the synchrotron fluxes at $\nu = 22$ GHz. This value is then extrapolated to PLANCK's observing frequencies with a spectral index of $\gamma = -1.25$: The amplitudes A_{synchro} of the input map are given in units of MJy/sr, and for the flux $S_{\text{synchro}}(\nu)$ one thus obtains:

$$S_{\text{synchro}}(\nu) = \sqrt{\frac{22 \text{ GHz}}{408 \text{ MHz}}} A_{\text{synchro}} \left(\frac{\nu}{408 \text{ MHz}}\right)^{-1.25}. \quad (6.11)$$

Here, the fact that the synchrotron spectral index shows significant variations across the Milky Way due to varying magnetic field strength is ignored. Instead, a spatially constant spectral behaviour is assumed.

6.4.3. Galactic free-free emission

The Galactic ionised plasma produces free-free emission, which is an important source of contamination in CMB observations, as recently confirmed by [Bennett et al. \(2003\)](#) in WMAP observations. Aiming at modelling the free-free emission at microwave frequencies, I rely on an H_α -template provided by [Finkbeiner \(2003\)](#). Modelling of the free-free emission component on the basis of an H_α -template is feasible because both emission processes depend on the emission measure $\int n_e^2 dl$, where n_e is the number density of electrons. This template is a composite of three H_α -surveys and is because of its high resolution (on average 6.0 FWHM) particularly well suited for CMB foreground modelling. The morphology of the free-free map is very complex and the emission reaches out to intermediate Galactic latitude.

For relating H_α -fluxes A_{H_α} given in units of Rayleighs to the free-free signal's antenna temperature $T_{\text{free-free}}$ measured in Kelvin, [Valls-Gabaud \(1998\)](#) gives the formula:

$$\frac{T_{\text{free-free}}(\mu\text{K})}{A_{H_\alpha}(R)} \simeq 14.0 \left(\frac{T_p}{10^4 \text{ K}}\right)^{0.317} 10^{290 \text{ K} T_p^{-1}} g_{\text{ff}} \left(\frac{\nu}{10 \text{ GHz}}\right)^{-2}. \quad (6.12)$$

T_p denotes the plasma temperature and is set to 10^4 K in this work. An approximation for the Gaunt factor g_{ff} valid for microwave frequencies in the range $\nu_p \ll \nu \ll k_B T/h$ (ν_p is the plasma frequency) is given by [Finkbeiner \(2003\)](#):

$$g_{\text{ff}} = \frac{\sqrt{3}}{\pi} \left[\ln \left(\frac{(2k_B T_p)^{3/2}}{\pi e^2 \nu \sqrt{m_e}} \right) - \frac{5}{2} \gamma_E \right], \quad (6.13)$$

where e and m_e denote electron charge and mass (in Gaussian units) and $\gamma_E \simeq 0.57721$ is Euler's constant. The contribution of fractionally ionised helium to the free-free emissivity as well as the absorption by interstellar dust has been ignored because of its being only a small contribution in the first case and because of poorly known parameters in the latter case. The antenna temperature can be converted to the free-free flux $S_{\text{free-free}}(\nu)$ by means of:

$$S_{\text{free-free}}(\nu) = 2 \frac{\nu^2}{c^2} k_B T_{\text{free-free}}(\text{K}). \quad (6.14)$$

Concerning the free-free emission, there might be the possibility of an additional free-free component uncorrelated with the H_α -emission. This hot gas, however, should emit X-ray line radiation, which has not been observed.

6.4.4. CO-lines from giant molecular clouds

In a spiral galaxy such as the Milky Way, a large fraction of the interstellar medium is composed of molecular hydrogen, that resides in giant molecular clouds (GMC), objects with masses of $10^4 - 10^6 M_\odot$ and sizes of 50–200 pc. Apart from molecular hydrogen, the GMCs contain carbon monoxide (CO) molecules in significant abundance. The rotational transitions of the CO molecule at 115 GHz and higher harmonics thereof constitute a source of contamination for all PLANCK HFI-channels. An extensive search for atomic and molecular transition lines was undertaken by [Bennett et al. \(1994\)](#) with the FIRAS instrument onboard COBE.

The CO-contamination is modelled by employing a mosaic of CO-surveys assembled by [Dame et al. \(1996, 2001\)](#). It shows the velocity-integrated intensity of the transition from the first excited state ($J = 1$) to the ground state ($J = 0$) close to the Galactic plane ($b < 5^\circ$), and additionally comprises a few CO clouds at higher Galactic latitude, as well as the Large Magellanic Cloud and the Andromeda galaxy M 31. Due to the composition of the map, the angular resolution is not uniform, but the best resolution of $\simeq 7.5$ is reached for a large area around the Galactic plane.

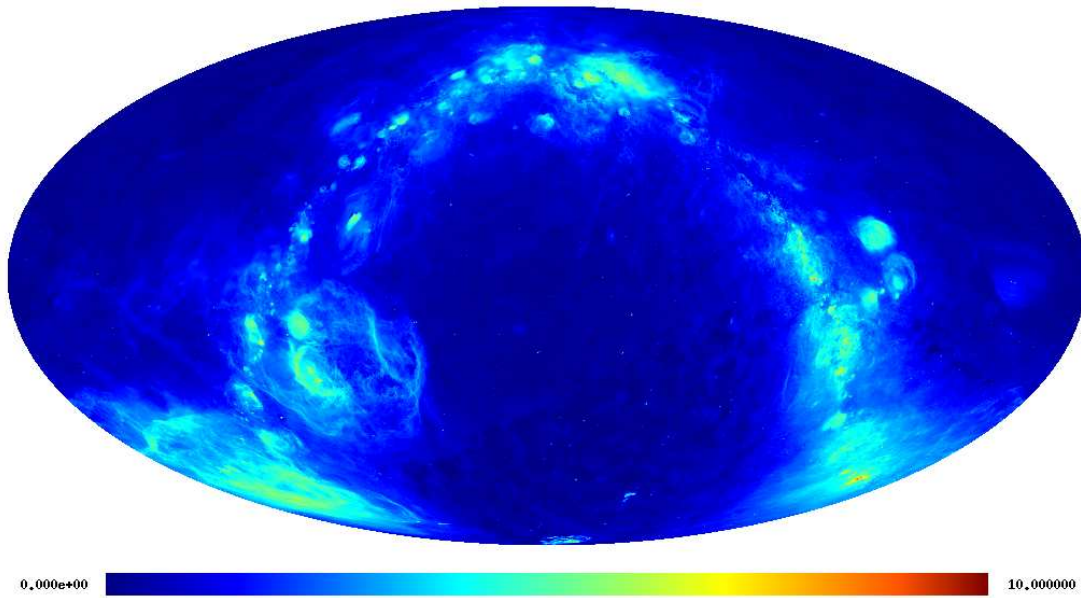


Figure 6.6.: Sky map of the antenna temperature increase caused by free-free emission in the $\nu = 100$ GHz-channel: The shading is proportional to $\text{arsinh}(T_A(\nu = 100 \text{ GHz})/\mu\text{K})$. Ecliptic coordinates have been chosen. This map has been derived from the H_α -template map provided by [Finkbeiner \(2003\)](#).

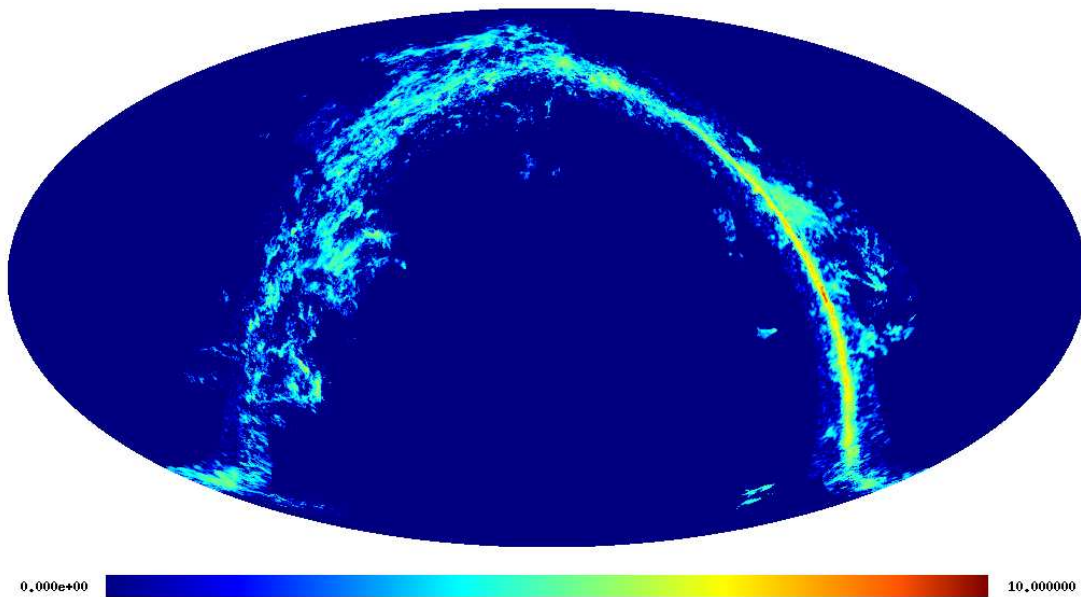


Figure 6.7.: Sky map of the increment in antenna temperature due to CO-line emission in the $\nu = 100$ GHz-channel in ecliptic coordinates: The shading is proportional to $\text{arsinh}(T_A(\nu = 100 \text{ GHz})/\mu\text{K})$. The maps shows the rotational transition of the CO molecule from the first excited state into the ground state at $\nu_{0\leftrightarrow 1} = 115$ GHz as derived by [Dame et al. \(2001\)](#) for a temperature of $T_{\text{CO}} = 20$ K.

From this map, it is possible to derive the line intensities of the higher harmonics, assuming thermal equilibrium: The frequency ν for a transition from a state of rotational quantum number J to a state with quantum number $J + 1$ follows from elementary quantum mechanics: The rotational energy of a CO-molecule with moment of inertia θ and angular momentum \mathbf{J} is $E_{\text{rot}} = \mathbf{J}^2/2\theta = \hbar^2 J(J + 1)/2\theta$. In the last step the quantum number J was introduced. For the transition energy between two subsequent rotation levels, one obtains:

$$\nu_{J \leftrightarrow J+1} = 2Qc(J + 1) = 115 \text{ GHz}(J + 1), \quad (6.15)$$

where $Q = h/8\pi^2c\theta$ is a measure of the inverse moment of inertia of the molecule and c denotes the speed of light. Thus, the spectrum consists of equidistant lines. The relative intensities of those lines is given by the ratio of their occupation numbers χ_J :

$$\chi_J = (2J + 1) \exp\left(-\frac{Qhc}{k_B T_{\text{CO}}} J(J + 1)\right), \quad (6.16)$$

i.e. the relative line intensities $q_{J \leftrightarrow J+1}$ of two consecutive lines is given by:

$$q_{J \leftrightarrow J+1} = \frac{\chi_{J+1}}{\chi_J} = \frac{2J + 3}{2J + 1} \exp\left(-\frac{2Qhc}{k_B T_{\text{CO}}} (J + 1)\right) \quad (6.17)$$

χ_J is determined by a statistical weight $(2J + 1)$ reflecting the degeneracy of angular momentum and a Boltzmann factor. For the determination of line intensities thermal equilibrium is assumed, common estimates for the temperature inside GMCs are $T_{\text{CO}} = 10 - 30$ K. For the purpose of this work, I choose $T_{\text{CO}} = 20$ K. From the brightness temperature T_A one obtains the CO-flux $S_{\text{CO-line}}(\nu)$ by means of the following equation:

$$S_{\text{CO-line}}(\nu) = 2\frac{\nu^2}{c^2} k_B T_A(\text{K}) p(\nu - \nu_{J \leftrightarrow J+1}), \quad (6.18)$$

where the line shape $p(\nu - \nu_{J \leftrightarrow J+1})$ is assumed to be small in comparison to PLANCK's frequency response windows such that its actual shape (for instance, a Voigt-profile) is irrelevant. Sadly, the inclusion of other molecular and atomic lines, e.g. O_2 (424.75 GHz), C (492.23 and 809.44 GHz), H_2O (556.89, 1113.3, and 1716.6 GHz), N^+ (1461.1 and 2459.4 GHz), C^+ (1900.5GHz), O (2060.1 GHz), Si (2311.7 GHz), and CH (2589.6 GHz), was not feasible, although a measurement from the FIRAS experiment onboard COBE exists (Bennett et al. 1994). These sky maps have comparatively low resolution and there are numerous gaps in the data. Furthermore, there are large variations in the abundance of the molecular species relative to carbon monoxide from pixel to pixel, so that the modelling based on the CO-map would not be reliable.

6.4.5. Planetary submillimetric emission

Planets produce infra-red and sub-millimetric radiation by absorbing sunlight and by re-emitting this thermal load imposed by the Sun. The investigation of the thermal properties of Mars, Jupiter and Saturn has been the target of several space missions (Goldin et al. 1997, Griffin et al. 1986, to name but a few). For the description of the submillimetric thermal emission properties of planets, an extension to the Wright & Odenwald model (Wright 1976, Neugebauer et al. 1971) was used. The orbital motion of the planets is sufficiently fast such that their movements including their epicyclic motion relative to the Lagrangian point L_2 , PLANCK's observing position, has to be taken into account. All planets are imaged twice in approximate half-year intervals due to PLANCK's scanning strategy, while showing tiny displacements from the ecliptic plane because of the Lissajous-orbit of PLANCK around L_2 and their orbital inclinations.

The heat balance equation for a planet or asteroid reads as:

$$E + F + W \equiv P_{\text{emission}} = P_{\text{absorption}} \equiv I + R, \quad (6.19)$$

where E denotes the heat loss by thermal emission (i.e. the signal for PLANCK), F the heat flux outward from the interior of the planet, W is the heat lost by conduction to the planet's atmosphere, I is the Solar radiation absorbed and R is the heating of the planet caused by the back-scattering of radiation emanating from the surface of the planet by the atmosphere. The definition of these quantities is given by eqns. (6.20) through (6.24):

$$E = \epsilon \sigma T_{\text{planet}}^4, \quad (6.20)$$

$$F = k \frac{\partial T_{\text{planet}}}{\partial x}, \quad (6.21)$$

$$I = \frac{(1-A)G}{r^2} \cos(\theta^*) \cos\left(\frac{2\pi t}{\tau}\right), \quad (6.22)$$

$$R = \gamma \frac{(1-A)G}{r^2} \cos(\theta^*) \cos\left(\frac{2\pi t}{\tau}\right) = \gamma I_{\text{max}}, \text{ and} \quad (6.23)$$

$$W = \kappa F. \quad (6.24)$$

Here, ϵ is the surface emissivity of the planet, σ is the Stefan-Boltzmann constant, T_{planet} is the planet's temperature, k the coefficient of heat conduction, A the planet's bolometric albedo, G the Solar constant (i.e. the energy flux density of Solar irradiation at the Earth's mean distance), r the distance of the planet to the Sun in astronomical units, τ the planet's rotation period and θ^* the geographical latitude of the radiation absorbing surface element. The temperature distribution in the interior of the planet at radial position x is controlled by the heat conduction equation:

$$c \frac{\partial T_{\text{planet}}}{\partial t} = k \frac{\partial^2 T_{\text{planet}}}{\partial x^2}, \quad (6.25)$$

with the specific heat per unit volume c .

In the model, the heat loss R of the planet's surface due to conduction to the planet's atmosphere is taken to be a constant fraction of the heat flux F outward from the interior of the planet, the constant of proportionality being κ , for which I assumed $\kappa = 0.1$. Similarly, the heat gain by back-scattering radiation by the atmosphere R was assumed to be a constant fraction γ of the local noon Solar flux I_{max} , where γ was taken to be $\gamma = 0.01$. The system of differential eqns. (6.20) - (6.24) dependent on time t and on Solar distance r constitutes a heat conduction problem with periodic excitation (by the planet's rotation). Thus, the heat balance of the planets is modelled by periodic solutions of the Laplacian heat conduction differential equations. It was solved iteratively by applying Laplace transforms with periodic boundary conditions. The integration over the planet's surface then yields the radiation flux. In the calculation, I addressed rocky and gaseous planets differently with respect to their thermal properties. Furthermore, the giant gaseous planets are known to have internal sources of heat generation, which also has been taken account of.

The brightest point source in the microwave sky due to the planetary thermal emission is Jupiter, causing an increase in antenna temperature of $T_{\text{Jupiter}} = 93.6$ mK in the $\nu = 100$ GHz-channel, followed by Saturn with $T_{\text{Saturn}} = 15.0$ mK. All outer planets apart from Pluto will be visible for PLANCK. Estimates show that even Galilean satellites Ganymede, Callisto, Io and Europa and Saturn's moon Titan are above the detection threshold of PLANCK, but they are outshone by the stray-light from Jupiter and Saturn, respectively and for that reason not included in my analysis.

Due to the planet's being point sources, their fast movement and their diverse surface temperatures it is not feasible to produce a template and extrapolate the fluxes with a common emission law to PLANCK-frequencies. Instead, flux maps have been produced directly for each of the nine PLANCK-channels separately taking account of the planetary motion, the solution of the heat balance equation laid down above and the finite beam-width. The analogous holds for asteroids, that are covered by the next chapter.

6.4.6. Submillimetric emission from asteroids

Asteroids and minor bodies of the Solar system are easily observed by infrared satellites such as ISO and possibly by sub-millimetric observatories (Müller 2001, Müller & Lagerros 1999). An estimation by Cremonese et al. (2002) shows that a large number of asteroids (~ 400) should yield signals detectable by PLANCK. The orbital motion of all asteroids is fast enough to cause double detections at different positions in the sky separated by half a year due to PLANCK's scanning strategy. In contrast to planets, asteroids are not well restricted to the ecliptic plane and appear up to ecliptic latitudes of $\beta \lesssim 30^\circ$.

The thermal emission properties of asteroids are well understood (for a comprehensive and detailed review, see Lagerros 1996a,b, 1997, 1998) such that asteroids have been used for calibrating detectors (e.g. the ISO mission,

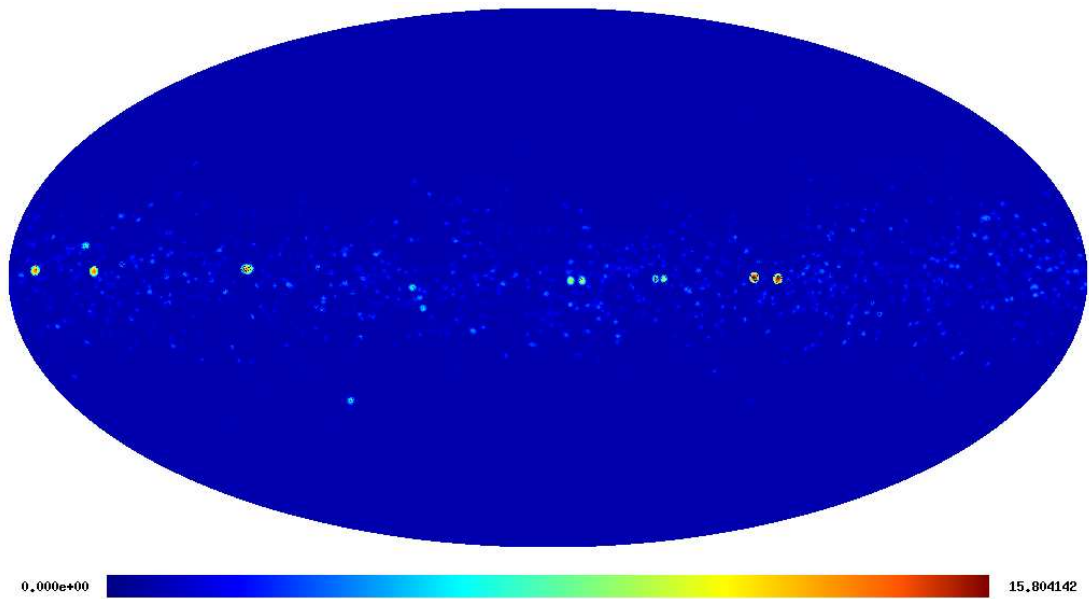


Figure 6.8.: Sky map of increment in antenna temperature T_A produced by planets and asteroids in the $\nu = 30$ GHz channel at 33.4 resolution (FWHM). The colour coding is proportional to $\text{arsinh}(T_A(\nu = 100 \text{ GHz})/nK)$. The asteroids reach ecliptic latitudes of $|\beta| \lesssim 30^\circ$. The pronounced signals are produced by planets, which (due to PLANCK's scanning strategy) appear twice. The observable planets comprise (from left to right) Saturn, Mars, Uranus, Neptune and Jupiter. The epicyclic motion of Mars is sufficiently fast to counteract the parallactic displacement such that it appears only once.

c.f. Müller & Lagerros 1998, 2002) and for determining beam shapes. The thermal model used for describing the submillimetric emission by asteroids is the same extension of the Wright & Odenwald model as for rocky planets. However, additional features that had to be incorporated was the beamed emission due to surface roughness. Furthermore, in the system of differential eqns. (6.20) - (6.24) terms W and R were neglected due to the absence of atmospheres in asteroids.

Information about the diameter and albedo was derived using the HG-magnitude system in case of asteroids for which those quantities are unknown, otherwise literature values were taken (from Moore 2000, and IAU's *Minor Planet Centre*⁴). For the description of the rotation period, an empirical relation that expresses the rotation period as a function of mass was used in the cases where the rotation period is unknown. The brightest sources include Ceres ($T_{\text{Ceres}} = 19.7 \mu\text{K}$), Pallas ($T_{\text{Pallas}} = 7.2 \mu\text{K}$), Vesta ($T_{\text{Vesta}} = 6.7 \mu\text{K}$) and Davida ($T_{\text{Davida}} = 2.1 \mu\text{K}$). The temperatures stated are antenna temperatures measured in the $\nu = 100$ GHz-channel at the brightness maximum.

The simulation shows that the number of detectable asteroids is overestimated by Cremonese et al. (2002), who did not take the expected observation geometry and detector response into account. Typical surface temperatures of asteroids are of the order of 150 K, and therefore, PLANCK is observing their thermal emission in the Rayleigh-Jeans regime. For that reason, the number of detectable asteroids increases with observing frequency. For the sample of 5×10^4 asteroids of the *Minor Planet Centre*'s catalogue, I find a couple of asteroids at $\nu = 30$ GHz, a few tens of asteroids at $\nu = 100$ GHz and up to 100 asteroids in the highest frequency band at $\nu = 857$ GHz. Approximately 1200 asteroids will have fluxes above half of PLANCK's single-band detection limit estimated for ideal observation conditions and thus they constitute an abundant population of point sources that possibly hampers the detection of SZ-clusters.

The prediction of comets is very uncertain for the years 2007 through 2009: Many comets are not detected yet, non-active comets are too faint with few exceptions and the coma thermal emission features of active comets is very complex. For these reasons, they have been excluded from the analysis.

⁴<http://cfa-www.harvard.edu/cfa/ps/mpc.html>

6.4.7. Future work concerning PLANCK's foregrounds

Foreground components not considered so far include microwave point sources, such as infra-red galaxies and microwave emitting AGNs. The emission of infra-red galaxies is associated with absorption of star light by dust and re-emission at longer wavelengths. Galaxies with ongoing star formation can have large fractions ($\sim 90\%$) of their total emission at infra-red wavelengths, compared to about one third in the case of local galaxies. The integrated emission from unresolved infra-red galaxies accounts for the cosmic infra-red background (CIB) (Puget et al. 1996, Lagache & Puget 2000), the fluctuations of which are impeding SZ-observations at frequencies above $\nu \simeq 100$ GHz (Aghanim et al. 2004).

Lagache (2003) and White & Majumdar (2003) have estimated the number counts of unresolved infra-red galaxies at PLANCK-frequencies, which was used by Aghanim et al. (2004) in order to estimate the level of fluctuation in the PLANCK-beam. In the easiest case, the sources are uncorrelated and the fluctuations obey Poissonian statistics, but the inclusion of correlations is expected to boost the fluctuations by a factor of ~ 1.7 (Song et al. 2003). According to Aghanim et al. (2004), the resulting fluctuations vary between a few 10^2 Jy/sr and 10^5 Jy/sr, depending on observing channel. A proper modelling would involve a biasing scheme for populating halos, the knowledge of the star formation history and template spectra in order to determine the K-corrections.

AGNs are another extragalactic source of submillimetric emission. Here, synchrotron emission is the radiation generating mechanism. The spectra show a variety of functional behaviours, with spectral indices α generally ranging from -1 to -0.5 , but sources with inverted spectra $\alpha > 0$ are commonplace. This variety makes it difficult to extrapolate fluxes to observing frequencies of CMB experiments. Two studies (Toffolatti et al. 1998, Sokasian et al. 2001) have estimated the fluctuations generated by radio emitting AGNs at SZ-frequencies and found them to amount to $10^3 - 10^4$ Jy/sr. However, AGNs are known to reside in high-density environments and the proper modelling would involve a (poorly known) biasing scheme in order to assign AGN to the dark matter halos. Apart from that, one would have to assume spectral properties from a wide range of spectral indices and AGN activity duty cycles. Therefore, the study of extragalactic sources has been omitted from this analysis.

Yet another source of microwave emission in the Solar system is the zodiacal light (Leinert et al. 2002, Reach et al. 2003b). Modelling of this emission component is very difficult due to the Lissajous-orbit of PLANCK around the Lagrangian point L_2 . The disk of interplanetary dust is viewed under varying angles depending on the orbital period and the integration over the spatially non-uniform emission features is very complicated. Reach et al. (2003a) have investigated the thermal emission by interplanetary dust from measurements by ISO and have found dust temperatures of $T_{\text{zodiacal}} = 250 - 300$ K and fluxes on the level of $\simeq 10^3$ Jy/sr, i.e. the equilibrium temperature is separated by two orders of magnitude from the CMB temperature, which means that the intensities are suppressed by a factor of $\sim 10^4$ due to the Rayleigh-Jeans regime of the zodiacal emission in which PLANCK is observing and by a factor of 10^5 due to PLANCK's narrow beams. From this it is concluded that the emission from zodiacal light is unlikely to exceed values of a few $\sim \mu\text{Jy}$ in observations by PLANCK which compares to the fluxes generated by faint asteroids. Thus, the zodiacal light constitutes only a weak foreground emission component at submillimetric wavelengths and can safely be neglected.

6.5. Simulating SZ-observations by PLANCK

The simulation for assessing PLANCK's SZ-capabilities proceeds in four steps. Firstly, all-sky maps of the thermal and kinetic SZ-effects are prepared, the details of map-construction are given in Sect. 6.5.1. Secondly, a realisation of the CMB was prepared for the assumed cosmological model (Sect. 6.5.2). The amplitudes were co-added with the Galactic and ecliptic foregrounds introduced in the previous section, subsequently degraded in resolution with PLANCK's beams (Sect. 6.5.3). Finally, uncorrelated pixel noise as well as the emission maps comprising planets and asteroids were added. In the last section, cross-correlation properties of the various astrophysical and instrumental noise components are discussed (Sect. 6.5.4).

At this stage it should be emphasised that I work exclusively with spherical harmonics expansion coefficients $a_{\ell m}$ of the flux maps. The expansion of a function $a(\theta)$ into spherical harmonics $Y_{\ell}^m(\theta)$ and the corresponding inversion is given by:

$$a_{\ell m} = \int d\Omega a(\theta) Y_{\ell}^m(\theta)^* \quad \text{and} \quad a(\theta) = \sum_{\ell=0}^{\infty} \sum_{m=-\ell}^{+\ell} a_{\ell m} Y_{\ell}^m(\theta). \quad (6.26)$$

Here, $d\Omega$ denotes the differential solid angle element. For reasons of computational feasibility, I assume isotropic

spectral properties of each emission component, i.e. the template map is only providing the amplitude of the respective emission component, but the spectral dependences are assumed to remain the same throughout the sky. While this is an excellent approximation for the CMB and the SZ-effects (in the non-relativistic limit), it is a serious limitation for Galactic foregrounds, where e.g. the synchrotron spectral index or the dust temperatures show significant spatial variations.

Adopting this approximation, the steps in constructing spherical harmonics expansion coefficients $\langle S_{\ell m} \rangle_{\nu_0}$ of the flux maps $S(\boldsymbol{\theta}, \nu)$ for all PLANCK channels consist of deriving the expansion coefficients of the template, converting the template amplitudes to flux units, extrapolate the fluxes with a known or assumed spectral emission law to PLANCK's observing frequencies, to finally convolve the emission law with PLANCK's frequency response window for computing the spherical harmonics expansion coefficients of the average measured flux $\langle S_{\ell m} \rangle_{\nu_0}$ at nominal frequency ν_0 by using eqn. (6.27).

$$\langle S_{\ell m} \rangle_{\nu_0} = \frac{\int d\nu S_{\ell m}(\nu) R_{\nu_0}(\nu)}{\int d\nu R_{\nu_0}(\nu)} = 2 \frac{\nu_0^2}{c^2} k_B T_{\ell m}. \quad (6.27)$$

Here, $S_{\ell m}(\nu)$ describes the spectral dependence of the emission component considered, and $R_{\nu_0}(\nu)$ the frequency response of PLANCK's receivers centered on the fiducial frequency ν_0 . Assuming spatial homogeneity of the spectral behaviour of each emission component it is possible to decompose $S_{\ell m}(\nu)$ into $S_{\ell m}(\nu) = q(\nu) a_{\ell m}$, i.e. a frequency dependent function $q(\nu)$ and the spherical harmonics expansion coefficients $a_{\ell m}$ of the template describing the morphology. This is possible due to the fact that the decomposition eqn. (6.26) is linear. Additionally, eqn. (6.27) gives the conversion from the averaged flux $\langle S_{\ell m} \rangle_{\nu}$ in a PLANCK-channel to antenna temperature $T_{\ell m}$.

PLANCK's frequency response function $R_{\nu_0}(\nu)$ is well approximated by a top-hat function:

$$R_{\nu_0}(\nu) = \begin{cases} 1, & \nu \in [\nu_0 - \Delta\nu, \nu_0 + \Delta\nu] \\ 0, & \nu \notin [\nu_0 - \Delta\nu, \nu_0 + \Delta\nu] \end{cases} \quad (6.28)$$

The centre frequencies ν_0 and frequency windows $\Delta\nu$ for PLANCK's receivers are summarised in Table 6.1. In this way it is possible to derive a channel-dependent prefactor relating the flux expansion coefficients $\langle S_{\ell m} \rangle_{\nu_0}$ to the template expansion coefficients $A_{\ell m}$. The superposition of the various emission components in spherical harmonics and the determination of response-folded fluxes is most conveniently done using the `almixer`-utility of PLANCK's simulation package.

6.5.1. SZ-map preparation

For constructing an all-sky Sunyaev-Zel'dovich map, a hybrid approach has been pursued. Due to the SZ-clusters being detectable out to very large redshifts, due to their clustering properties on very large angular scales, and due to the requirement of reducing cosmic variance when simulating all-sky observations as will be performed by PLANCK, there is the need for very large simulation boxes, encompassing redshifts of $z \simeq 1$ which corresponds to comoving scales exceeding 2 Gpc. Unfortunately, a simulation incorporating dark matter and gas dynamics that covers cosmological scales of that size down to cluster scales and possibly resolving cluster substructure is beyond computational feasibility. For that reason, two simulations have been combined: The Hubble-volume simulation (Jenkins et al. 2001, Colberg et al. 2000), and a smaller scale simulation including (adiabatic) gas physics by White et al. (2002) performed with GADGET (Springel et al. 2001, Springel & Hernquist 2002). Details of the map construction and its properties are given in Sect. 5.

The fluxes generated by the thermal SZ-effect $S_{\mathcal{Y}}(x)$ and of the kinetic SZ-effect $S_{\mathcal{W}}(x)$ are given by eqns. (6.29) and (6.30), respectively. The dimensionless frequency is defined as $x = h\nu/(k_B T_{\text{CMB}})$ and the flux density of the CMB is given by $S_0 = (k_B T_{\text{CMB}})^3 \pi^3 / c^2 / h^2 / 5400 = 22.9 \text{ Jy/arcmin}^2$:

$$S_{\mathcal{Y}}(x) = S_0 \mathcal{Y} \frac{x^4 \exp(x)}{(\exp(x) - 1)^2} \left[x \frac{\exp(x) + 1}{\exp(x) - 1} - 4 \right]. \quad (6.29)$$

$$S_{\mathcal{W}}(x) = S_0 \mathcal{W} \frac{x^4 \exp(x)}{(\exp(x) - 1)^2}. \quad (6.30)$$

Table 6.1 summarises the fluxes $S_{\mathcal{Y}}$ and $S_{\mathcal{W}}$ and the corresponding changes in antenna temperature $T_{\mathcal{Y}}$ and $T_{\mathcal{W}}$ for the respective Comptonisation of $\mathcal{Y} = \mathcal{W} = 1 \text{ arcmin}^2$ for all PLANCK-channels.

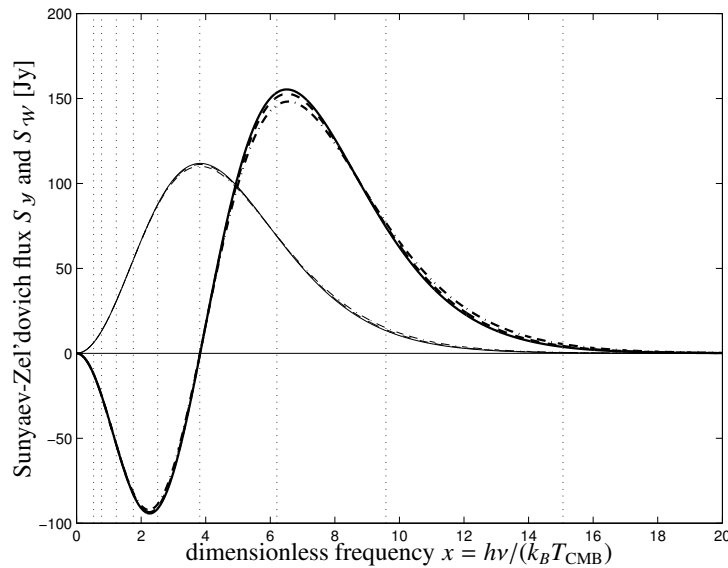


Figure 6.9.: Frequency dependence of the thermal (thick lines) and of the kinetic SZ-flux (thin lines), for ideal δ -like frequency responses (solid lines), for a top-hat window function with a relative width of 10% corresponding to PLANCK's LFI-instrument and for a top-hat window function with a relative width of 16.7%, as planned for PLANCK's HFI-instrument. The fluxes stated correspond to the integrated Comptonisation of $\mathcal{Y} = \mathcal{W} = 1 \text{ arcmin}^2$. The vertical lines indicate the centre frequencies of PLANCK's receivers.

Fig. 6.9 shows how the frequency dependence of the SZ-signal is altered by PLANCK's relatively broad frequency response functions. The relative deviations of curves in which the frequency window has been taken into account to the unaltered curve amounts to 5...15%, depending on observation frequency.

6.5.2. CMB-map generation

The angular power spectrum C_ℓ is computed for a flat Λ CDM-cosmology using the CMBfast code by Seljak & Zaldarriaga (1996). In addition to the cosmological parameters being already given in Sect. 6.1, I use adiabatic initial conditions, set the CMB monopole to $T_{\text{CMB}} = 2.725 \text{ K}$ (Mather et al. 1999) and the primordial He-mass fraction to $X_{\text{He}} = 0.24$. The reionisation optical depth τ was set to $\tau = 0.17$ and the reionisation redshift was taken to be $z_{\text{reion}} = 20$ (Bennett et al. 2003). The angular power spectrum of the CMB is normalised to COBE data. With the spectrum of C_ℓ -coefficients, a set of $a_{\ell m}$ -coefficients was synthesised by using the synalm code based on synfast by Hivon et al. (1998). The factors for converting the $a_{\ell m}$ -coefficients of the CMB map showing the thermodynamic temperature and to the corresponding fluxes for each channel were then derived by convolution of the Planckian emission law eqn. (6.31),

$$S_{\text{CMB}}(\nu) = S_0 \frac{x^3}{\exp(x) - 1}, \quad (6.31)$$

with PLANCK's frequency response function eqns. (6.27) and (6.28). Again, $S_0 = 22.9 \text{ Jy/arcmin}^2$ is the energy flux density of the CMB. The realisation of the CMB used in this work is given in Fig. 6.10. I did not use a constrained realisation of the CMB, where the low multipoles are the specific $a_{\ell m}$ -coefficients determined by e.g. WMAP. At the scales where SZ-detections are expected, the fluctuations of the CMB are yet unknown and extrapolated with the knowledge of the cosmological model. The filtering scheme to be used for extracting and amplifying the SZ-signal will suppress low- ℓ fluctuations and a specific choice of $a_{\ell m}$ -coefficients at low ℓ should not have any influence on the cluster detection.

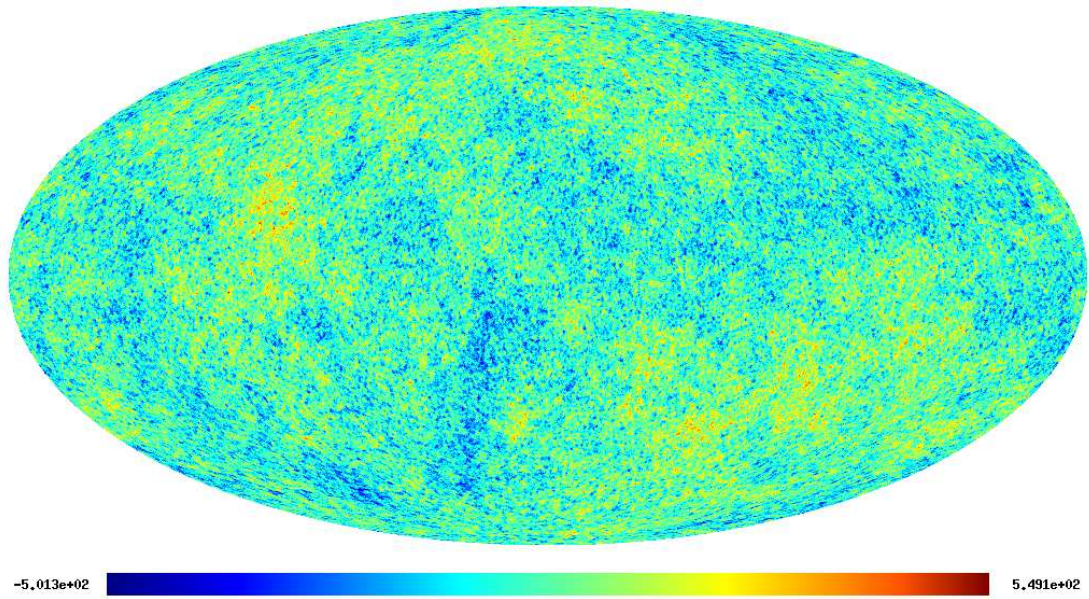


Figure 6.10.: All-sky map of the CMB realisation used in this work. The amplitudes are antenna temperatures measured in the $\nu = 100$ GHz channel in units of μK .

6.5.3. Preparation of simulation data sets

The expansion coefficients of the flux maps are multiplied with the respective beam's $b_{\ell 0}$ -coefficients in order to describe the finite angular resolution. After that, expansion coefficients of the pixel noise maps and those of the planetary maps have been added. In total, three atlases consisting of nine flux $\langle S_{\ell m} \rangle_{\nu_0}$ -sets belonging to each of PLANCK's channels with fiducial frequency ν_0 have been compiled:

- The reference data set is a combination of the CMB, the SZ-maps and the instrumental noise maps. They should provide the cleanest detection of clusters and the measurement of their properties. Apart from the inevitable instrumental noise, this data set only contains cosmological components. In the remainder of the chapter, this data set will be referred to as COS.
- The second data set adds Galactic foregrounds to the CMB, the SZ-maps and the instrumental noise map. Here, I try to assess the extend to which Galactic foregrounds impede the SZ-observations. Thus, this data set will be denoted GAL.
- In the third data set the emission from bodies inside the Solar system was included to the CMB, the SZ-maps, the Galactic foregrounds and the instrumental noise. Because of the planets and asteroids being loosely constrained to the ecliptic plane, this data set will be called ECL.

An example of a synthesised map showing the combined emission of the SZ-clusters and all Galactic and ecliptic components including neither CMB fluctuations nor instrumental noise at a location close to the Galactic plane is given by Fig. 6.11. The observing frequency has been chosen to be $\nu = 143$ GHz, correspondingly, the map has been smoothed with a (Gaussian) beam of $\Delta\theta = 7'.1$ (FWHM).

6.5.4. PLANCK-channel correlation properties

In this section the auto- as well as the cross-correlation properties of the various foregrounds in different PLANCK-channels are studied. The cross power spectra, defined formally by eqn. (6.32) are determined by using:

$$C_{\ell, \nu_1 \nu_2} = \frac{1}{2\ell + 1} \sum_{m=-\ell}^{+\ell} \langle S_{\ell m} \rangle_{\nu_1} \langle S_{\ell m} \rangle_{\nu_2}^*. \quad (6.32)$$

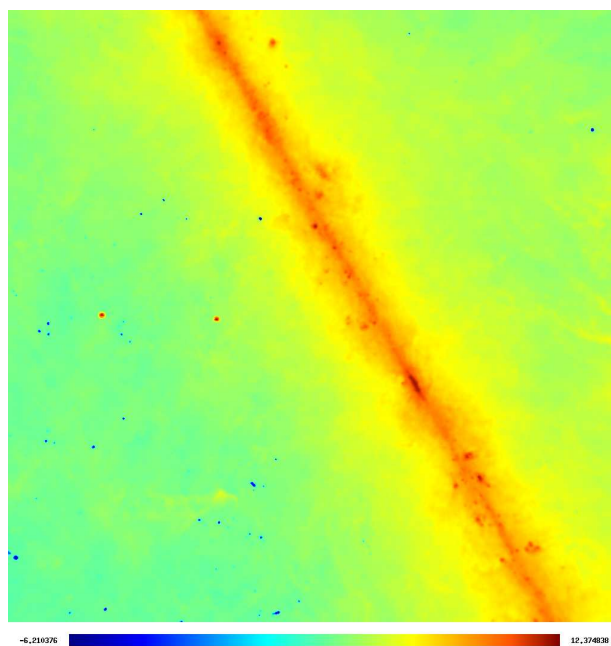


Figure 6.11.: A $50^\circ \times 50^\circ$ wide composite centered on the ecliptic coordinates $(\lambda, \beta) = (-85^\circ, 0^\circ)$, i.e. close to the Galactic centre for PLANCK's $\nu = 143$ GHz-channel. The shading is proportional to $\text{arsinh}(T_A(\nu = 143 \text{ GHz})/\mu\text{K})$. The map is smoothed with the corresponding beam of diameter $\Delta\theta = 7'.1$ (FWHM). SZ-clusters are observed in absorption in this channel and are discernible by eye even at close proximity ($b \lesssim 20^\circ$) to the Galactic plane. For clarity, the CMB fluctuations as well as the instrumental noise have been excluded. The two point sources on the ecliptic equator are twin detections of Jupiter.

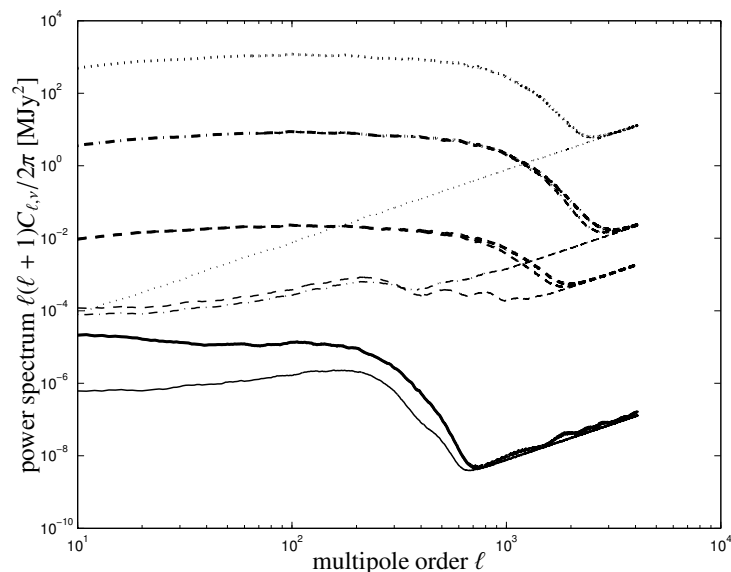


Figure 6.12.: Power spectra in various PLANCK-channels: $\nu = 30$ GHz (solid), $\nu = 143$ GHz (dashed), $\nu = 353$ GHz (dash-dotted) and $\nu = 857$ GHz (dotted) for COS data set (thin line), the GAL data set (medium line) and the ECL data set (thick line).

From this definition, the auto-correlation spectra are obtained by setting $\nu_1 = \nu_2$, i.e. $C_{\ell,\nu} = C_{\ell,\nu\nu}$. The band-pass averaged fluxes $\langle S_{\ell m} \rangle_\nu$ are defined in eqn. (6.27). In Fig. 6.12, the power spectra are shown for the $\nu = 30$ GHz-, $\nu = 143$ GHz-, $\nu = 353$ GHz- and the $\nu = 847$ GHz-channels. The spectra have been derived including various Galactic and ecliptic noise components in order to study their relative influences. For visualisation purposes, the spectra are smoothed with a moving average filter with a filter window comprising 11 bins.

Distinct acoustic peaks of the CMB are clearly visible in the clean COS data sets, but are overwhelmed by the Galactic noise components. At small scales, i.e. high multipole order ℓ , differences between the GAL and ECL data sets become apparent, the latter showing a higher amplitude. The (single) acoustic peak measurable in the $\nu = 33$ GHz channel is shifted to larger angular scales due to the coarse angular resolution of that particular channel. The $\nu = 857$ GHz-curve of the COS data set behaves like a power law due to the fact that the CMB is observed in the Wien-regime and is consequently strongly suppressed, such that the angular power spectrum is dominated by uncorrelated pixel noise.

Fig. 6.13 shows exemplarily a couple of cross power spectra. The cross-correlation spectra derived for the COS data set nicely shows the CMB power spectrum if two neighboring channels close to the CMB maximum are chosen, but the correlation is lost in two widely separated channels. This is especially the case if one considers the two lowest *LFI*-channels at angular scales which the receivers are not able to resolve. In this regime the pixel noise is still very small and the cross-correlation spectrum drops to very small values.

In order to illustrate the complexity of spectral and morphological behaviour of the power spectra, they are given as contour plots depending on both the observing frequency ν and the multipole order ℓ . Fig. 6.14 and 6.15 contrast the auto-correlation properties of the different data sets. The COS data set, shown in Fig. 6.14, containing nothing but the CMB and instrumental noise apart from the SZ-contribution, shows clearly the acoustic oscillations with the first peak at $\ell \approx 200$ and the consecutive higher harmonics. They are most pronounced in the $\nu = 100$ GHz- and $\nu = 143$ GHz-channels. At higher multipole moments, the power spectra are dominated by instrumental noise which leads to a rapid (power law) incline.

Adding Galactic foregrounds yields the spectra depicted in Fig. 6.15. Inclusion of Galactic foregrounds significantly complicates the picture and masks off the primary anisotropies. The spectra are dominated by large-scale emission structures of the Milky Way, most notably the emission from thermal dust that causes the spectra to increase with increasing frequency ν .

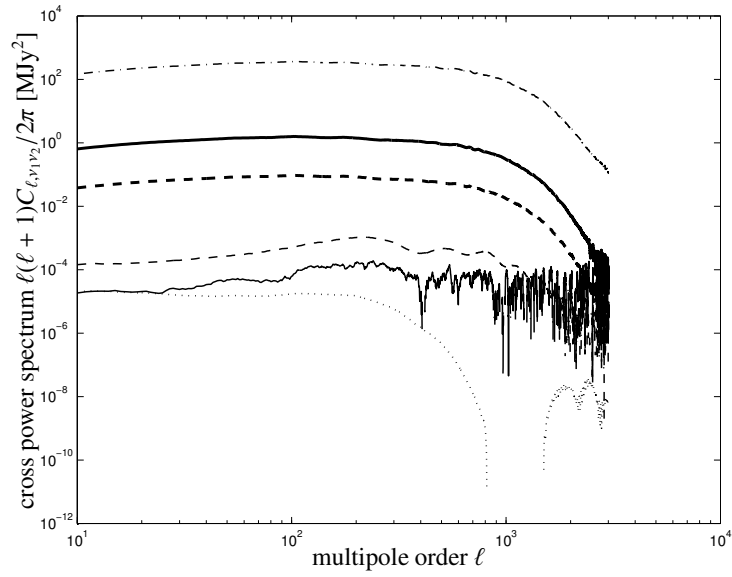


Figure 6.13.: Cross-correlations: The spectra $C_{\ell, \nu_1=143 \text{ GHz}, \nu_2=545 \text{ GHz}}$ (solid line) and $C_{\ell, \nu_1=143 \text{ GHz}, \nu_2=217 \text{ GHz}}$ (dashed line) are contrasted for the COS data set (thin lines) versus the GAL data set (thick line). Furthermore, the spectrum $C_{\ell, \nu_1=545 \text{ GHz}, \nu_2=857 \text{ GHz}}$ (dash-dotted line) as well as $C_{\ell, \nu_1=30 \text{ GHz}, \nu_2=44 \text{ GHz}}$ (dotted line) is shown as derived from the ECL data set.

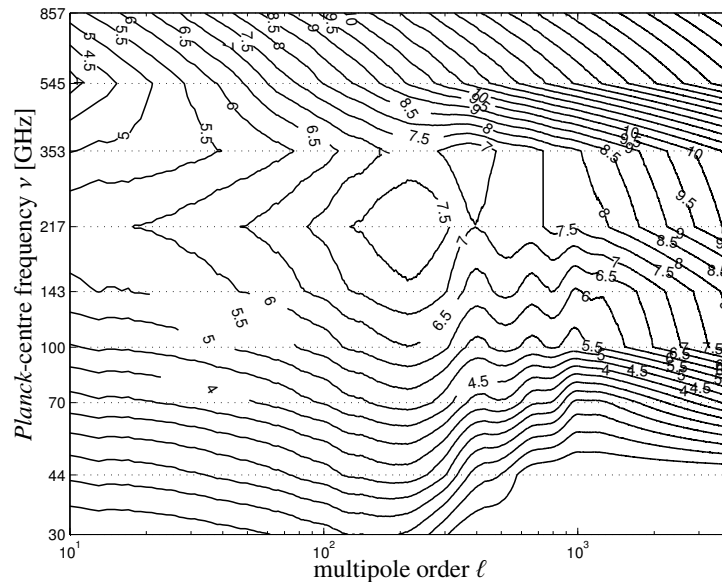


Figure 6.14.: Auto-correlations: The power spectral $C_{\ell, \nu}$ -coefficients are shown as a function of observing frequency ν and multipole order ℓ in the usual representation $\ell(\ell+1)C_{\ell, \nu}/2\pi$. The amplitudes are given in μK^2 and the contours are linearly spaced. Note the logarithmic scaling of the frequency axis. In the data set displayed, the CMB, both SZ-effects and instrumental noise are included. The first three acoustic oscillation peaks are clearly visible.

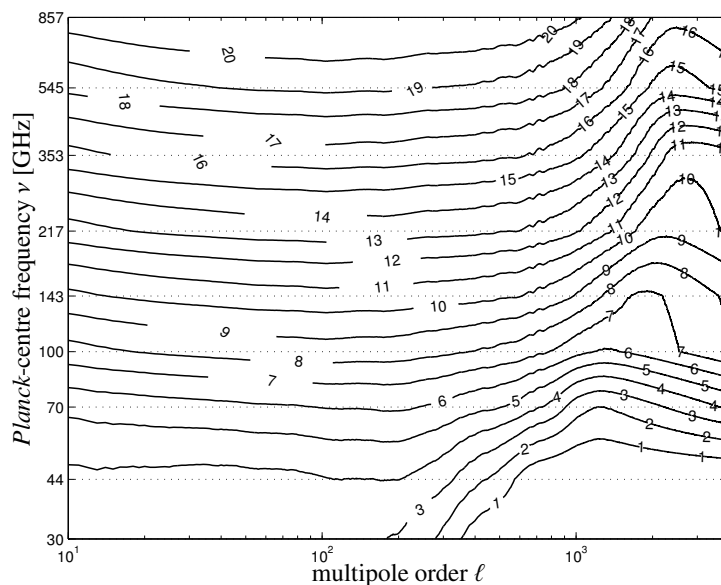


Figure 6.15.: Auto-correlations: The power spectral $C_{\ell,\nu}$ -coefficients are shown as a function of observing frequency ν and multipole order ℓ in the usual representation $\ell(\ell + 1)C_{\ell,\nu}/2\pi$. The amplitudes are given in $\log(\mu\text{K}^2)$ with logarithmically equidistant contours. In the data set displayed, the CMB, both SZ-effects, all Galactic foregrounds and instrumental noise are included.

6.6. Summary and conclusion

A simulation for assessing PLANCK's SZ-capabilities in the presence of spurious signals is presented that combines maps of the thermal and kinetic SZ-effects with a realisation of the cosmic microwave background (CMB), in addition to Galactic foregrounds (synchrotron emission, free-free emission, thermal emission from dust, CO-line radiation) as well as the sub-millimetric emission from celestial bodies of our Solar system. Additionally, observational issues such as the finite angular resolution and spatially non-uniform instrumental noise of PLANCK are taken into account.

- Templates for modelling the free-free emission and the carbon monoxide-line emission have been added to the PLANCK-simulation pipeline. The free-free template relies on an H_α -survey of the Milky Way. The spectral properties of both foregrounds are modelled with reasonable parameter choices, i.e. $T_p = 10^4$ K for the free-free plasma temperature and $T_{\text{CO}} = 20$ K for the mean temperature of giant molecular clouds.
- An extensive package for modelling the sub-millimetric emission from planet and asteroids has been implemented for PLANCK, that solves the heat balance equation of each celestial body. It takes the movement of the planets and asteroids into account, which causes, due to PLANCK's scanning strategy, double detections separated by approximate half-year intervals. The total number of asteroids implemented is ≈ 1200 .
- The foregrounds have been combined under proper inclusion of PLANCK's frequency response windows in order to yield a set of flux maps. The auto- and cross-correlation properties of those maps are investigated in detail. Furthermore, their decomposition into spherical harmonics $\langle S_{\ell m} \rangle_\nu$ serve as the basis for the filter construction. It should be emphasised that the spectral properties of a foreground component were assumed to be isotropic.

7. Matched and scale-adaptive multifiltering

Abstract

In this chapter, filtering schemes based on scale-adaptive and matched filtering are extended to spherical data sets, that enable the amplification of the weak SZ-signal in the presence of all contaminations stated above. The theory of scale-adaptive and matched filtering in the framework of spherical maps is developed, the resulting filter kernel shapes are discussed and their functionality is verified.

7.1. Introduction: multi-frequency optimised filtering

One challenge in the analysis of two-dimensional all-sky surveys is the extraction of sources of interest which are superposed on a background of noise of varying morphology and spectral behaviour. In the presence of small-scale noise the conventional method to extract sources is low-pass filtering (e.g. with a Gaussian kernel) while wavelet analysis is most suitably applied if large scale noise fluctuations dominate. These methods, however, fail if the characteristic scale of the background fluctuations is comparable with the scale of the signal structures. Other methods have been proposed in order to separate different components in multifrequency CMB observations: They include Wiener filtering (Tegmark & Efstathiou 1996, Bouchet & Gispert 1999, Bouchet et al. 1999), maximum-entropy methods (Hobson et al. 1998, 1999), Mexican-hat wavelet analysis (Vielva et al. 2001, Cayón et al. 2000), fast independent component analysis (Maino et al. 2002), matched filter analysis (Tegmark & de Oliveira-Costa 1998), adaptive filtering techniques (Sanz et al. 2001, Herranz et al. 2002), and non-parametric Bayesian approaches (Diego et al. 2002).

However, a comparison between these methods is difficult because they all assume different priors about the spatial properties and frequency dependence. Using prior knowledge about the frequency dependence and statistical properties of several images at different channels, the maximum-entropy method and Wiener filtering are able to separate the components of interest. Contrarily, wavelet analysis is well suited in order to detect compact sources. A combination of these different techniques improves the quality of component separation (Vielva et al. 2001). Although component separation methods which assume a prior knowledge about the data are quite powerful, they yield biased or even wrong results in the case of incorrect or idealised assumptions about the data. Any error in the separation of one component propagates to the separation of the other components owing to normalisation constraints. In particular, this is the case in non-centrally symmetric source profiles, oversimplified spectral extrapolations of Galactic emission surveys into other wavebands, variations of the assumed frequency dependence, or non-Gaussian noise properties the statistics of which can not fully be characterised by power spectra. Thus, the application of a specific component separation method is a trade-off between robustness and effectiveness with regard to the particular problem.

Filtering techniques relying on Mexican-hat wavelets and on matched and scale-adaptive filters are single component separation methods. They all project either spatial structure or frequency properties (within a given functional family) of the component of interest in the presence of other components acting as background in this context. While Mexican-hat wavelet analysis assumes Gaussian profiles superimposed on large scale variations of the background noise, the matched and scale-adaptive filter generalises to arbitrary source profiles and noise properties which are assumed to be locally homogeneous and isotropic (Sanz et al. 2001, Herranz et al. 2002).

This section generalises the matched and scale-adaptive filter techniques to global spherical topologies which find application in all-sky surveys such as the case of PLANCK's microwave/submillimetric survey. In addition, optimised filters for the detection of compact sources in single frequency all-sky observations are derived in the appendix in a more detailed fashion. The proposed method aims at simultaneously localising SZ-clusters and measuring both their amplitudes and angular extent. It can also be applied for localising microwave point sources

and estimating their spectral properties.

I choose the spherical filtering approach rather than tiling the sky with a set of two-dimensional flat maps for the following reasons: On the sphere, one does not have to worry about double detections due to overlaps in the tessellation. Secondly, my approach provides a physical interpretation of my filter shapes in harmonic space even for the smallest multipole moments in contrast to the case of a flat map where the smallest wavenumbers are determined by the map size. Finally, my approach circumvents projection failures of the noise properties such as stretching effects in the case of conformal mapping which would introduce artificial non-Gaussianity in my maps and distort profile shapes close to the map boundaries.

I pursue the concept of the *multi-frequency approach* rather than the *combination method* (c.f. [Herranz et al. 2002](#)). In other words, I filter each channel separately while taking into account the different cross-correlations between the different channels and the frequency dependence of the signal when constructing the optimised filters. This method seems to be superior to the *combination method* which tries to find a optimised combination of the different channels with regard to the signal-to-noise ratio of the sources and successively applies filters to the combined map.

The concept is introduced and central definitions are laid down in Sect. 7.1.1. The concept of constructing filter kernels is outlined in Sect. 7.1.2. Subsequently, the matched and scale-adaptive filters are derived for expansions of spherical data sets into spherical harmonics in Sect. 7.1.3 and Sect. 7.1.4. Then, the numbers of merit are defined in Sect. 7.1.5. Caveats in the numerical derivation are listed in Sect. 7.2.1. A discussion of filter kernel shapes in Sect. 7.2.2 for actual simulation data. The application of the filter kernels to my simulated sky maps and the extraction of the SZ-cluster signal is described in Sect. 7.2.3.

7.1.1. Assumptions and definitions

When constructing the particular filters, I assume centrally symmetric profiles of the sources to be detected. This approximation is justified for most of the clusters of PLANCK's sample whose angular extent will be comparable in size to PLANCK's beams, i.e. the instrumental beam renders them azimuthally symmetric irrespective of their intrinsic shape. Azimuthal symmetry is no general requirement for the filters which can be generalised to detect e.g. elliptic clusters using expansions into vector rather than scalar spherical harmonics.

I furthermore assume the background to be statistically homogeneous and isotropic, i.e. a complete characterisation can be given in terms of the power spectrum. This assumption obviously fails for non-Gaussian emission features of the Galaxy or of the exposure-weighted instrumental noise on large angular scales. However, the spherical harmonics expansion of any expected compact source profile, which I aim to separate, peaks at high values of the multipole moment due to the smallness of the clusters where the non-Gaussian influence is negligible. Thus, I only have to require homogeneity and isotropy of the background on small scales.

In order to construct filters, I consider a set of all-sky maps of the detected scalar field $s_\nu(\boldsymbol{\theta})$ for the different frequency channels

$$s_\nu(\boldsymbol{\theta}) = f_\nu y_\nu(|\boldsymbol{\theta} - \boldsymbol{\theta}_0|) + n_\nu(\boldsymbol{\theta}), \quad \nu = 1, \dots, N, \quad (7.1)$$

where $\boldsymbol{\theta} = (\vartheta, \varphi)$ denotes a two-dimensional vector on the sphere, $\boldsymbol{\theta}_0$ is the source location, and N is the number of frequencies (respectively, the number of maps). The first term on the right-hand side represents the amplitude of the signal caused by the thermal and kinetic SZ-effect, $y(|\boldsymbol{\theta} - \boldsymbol{\theta}_0|)$ and $w(|\boldsymbol{\theta} - \boldsymbol{\theta}_0|)$, respectively, while the second term corresponds to the generalised noise which is composed of CMB radiation, all Galactic and ecliptic emission components, and additional instrumental noise. The frequency dependence of the SZ-effect is described by f_ν in terms of average flux,

$$f_\nu \equiv \langle S_y \rangle_\nu \text{ and } f_\nu \equiv \langle S_W \rangle_\nu \quad (7.2)$$

where $\langle S \rangle_\nu$ denotes the flux weighted by the frequency response at the fiducial frequency ν (c.f. eqn. (6.27)) and S_y and S_W denote the SZ-fluxes given by eqns. (6.29) and (6.30).

I expect a multitude of clusters to be present in my all-sky maps. In order to sketch the construction of the optimised filter, I assume an individual cluster situated at the North pole ($\boldsymbol{\theta}_0 = \boldsymbol{\theta}$) with a characteristic angular SZ-signal $y_\nu(\theta = |\boldsymbol{\theta}|) = A\tau_\nu(\theta)$, where I separate the true amplitude A and the spatial profile normalised to unity, $\tau_\nu(\theta)$. The underlying cluster profile $p(\theta)$ is assumed to follow a generalised King-profile with an exponent λ which is a parameter in my analysis. At each observation frequency this profile is convolved with the (Gaussian) beam of

the respective PLANCK-channel (c.f. Sect. 6.3.1) yielding:

$$\tau_\nu(\theta) = \int d\Omega' p(\theta') b_\nu(|\theta - \theta'|) = \sum_{\ell=0}^{\infty} \tau_{\ell 0, \nu} Y_\ell^0(\cos \theta), \quad (7.3)$$

$$p(\theta) = \left[1 + \left(\frac{\theta}{\theta_c} \right)^2 \right]^{-\lambda}, \quad \text{and} \quad \tau_{\ell 0, \nu} = \sqrt{\frac{4\pi}{2\ell + 1}} b_{\ell 0, \nu} p_{\ell 0}. \quad (7.4)$$

For the second step in eqn. (7.4) I used the convolution theorem on the sphere to be derived in Appendix B.2. The background $n_\nu(\theta)$ is assumed to be a compensated homogeneous and isotropic random field with a cross power spectrum $C_{\ell, \nu_1 \nu_2}$ defined by

$$\langle n_{\ell m, \nu_1} n_{\ell' m', \nu_2}^* \rangle = C_{\ell, \nu_1 \nu_2} \delta_{\ell \ell'} \delta_{mm'}, \quad \text{where} \quad \langle n_\nu(\theta) \rangle = 0, \quad (7.5)$$

$n_{\ell m, \nu}$ denotes the spherical harmonics expansion coefficient of $n_\nu(\theta)$, $\delta_{\ell \ell'}$ denotes the Kronecker symbol, and $\langle \cdot \rangle$ corresponds to an ensemble average. Assuming ergodicity of the field under consideration allows taking spatial averages over sufficiently large areas $\Omega = O(4\pi)$ instead of performing the ensemble average.

7.1.2. Concepts in filter construction

The idea of an optimised matched filter for multifrequency observations was recently proposed by Herranz et al. (2002) for the case of a flat geometry. For each observing frequency, I aim at constructing a centrally symmetric optimised filter function $\psi_\nu(\theta)$ operating on a sphere. Its functional behaviour induces a family of filters $\psi_\nu(\theta, R_\nu)$ which differ only by a scaling parameter R_ν . For a particular choice of this parameter, I define the filtered field $u_\nu(R_\nu, \beta)$ to be the convolution of the filter function with the observed all-sky map at frequency ν ,

$$u_\nu(R_\nu, \beta) = \int d\Omega s_\nu(\theta) \psi_\nu(|\theta - \beta|, R_\nu) = \sum_{\ell=0}^{\infty} \sum_{m=-\ell}^{+\ell} u_{\ell m, \nu} Y_\ell^m(\beta) \quad \text{with} \quad (7.6)$$

$$u_{\ell m, \nu} = \sqrt{\frac{4\pi}{2\ell + 1}} s_{\ell m, \nu} \psi_{\ell 0, \nu}(R_\nu). \quad (7.7)$$

For the second step, the convolution theorem to be derived in Appendix B was used. The combined filtered field is defined by

$$u(R_1, \dots, R_N; \beta) = \sum_\nu u_\nu(R_\nu, \beta). \quad (7.8)$$

Taking into account the vanishing expectation value of the noise $\langle n_\nu(\theta) \rangle = 0$, the expectation value of the filtered field at the North pole $\beta = \mathbf{0}$ is given by

$$\langle u_\nu(R_\nu, \mathbf{0}) \rangle = A f_\nu \sum_{\ell=0}^{\infty} \tau_{\ell 0, \nu} \psi_{\ell 0, \nu}(R_\nu). \quad (7.9)$$

The assumption that the cross power spectrum of the signal is negligible compared to the noise power spectrum is justified because the thermal and kinetic amplitudes are small compared to unity, $A_{y,w} \ll 1$. Thus, the variance of the combined filtered field (7.8) is determined by

$$\begin{aligned} \sigma_u^2(R_1, \dots, R_N) &= \langle [u(R_1, \dots, R_N; \beta) - \langle u(R_1, \dots, R_N; \beta) \rangle]^2 \rangle \\ &= \sum_{\nu_1, \nu_2} \sum_{\ell=0}^{\infty} C_{\ell, \nu_1 \nu_2} \psi_{\ell 0, \nu_1}(R_{\nu_1}) \psi_{\ell 0, \nu_2}(R_{\nu_2}). \end{aligned} \quad (7.10)$$

The optimised filter functions $\psi_\nu(\theta)$ are chosen to detect the clusters at the North pole of the sphere (to which they have been translated). They are described by a singly peaked profile which is characterised by the scale $R_\nu^{(0)}$ as given by eqn. (7.3). While the optimised *matched filter* is defined to obey the first two of the following conditions, the optimised *scale-adaptive filter* is required to obey all three conditions:

1. The combined filtered field $u(R_1^{(0)}, \dots, R_N^{(0)}; \boldsymbol{\theta})$ is an unbiased estimator of the source amplitude A :

$$\langle u(R_1^{(0)}, \dots, R_N^{(0)}; \boldsymbol{\theta}) \rangle = A. \quad (7.11)$$

2. The variance of $u(R_1, \dots, R_N; \boldsymbol{\beta})$ has a minimum at the scales $R_1^{(0)}, \dots, R_N^{(0)}$ ensuring that the combined filtered field is an efficient estimator.
3. The expectation value of the filtered field at the source position has an extremum with respect to the the scale $R_v^{(0)}$, implying

$$\frac{\partial}{\partial R_v^{(0)}} \langle u_v(R_v, \boldsymbol{\theta}) \rangle = 0. \quad (7.12)$$

7.1.3. Matched filter

For convenience, I introduce the column vectors $\boldsymbol{\psi}_\ell \equiv [\psi_{\ell 0, v}]$, $\mathbf{F}_\ell \equiv [f_v \tau_{\ell 0, v}]$, and the inverse $\hat{\mathbf{C}}_\ell^{-1}$ of the matrix $\hat{\mathbf{C}}_\ell \equiv [C_{\ell, v_1 v_2}]$. In terms of spherical harmonic expansion coefficients, constraint (i) reads

$$\sum_v \sum_{\ell=0}^{\infty} f_v \tau_{\ell 0, v} \psi_{\ell 0, v} = \sum_{\ell=0}^{\infty} \mathbf{F}_\ell^T \boldsymbol{\psi}_\ell = 1. \quad (7.13)$$

Performing functional variation (with respect to the filter function $\boldsymbol{\psi}_\ell$) of $\sigma_u^2(R_1, \dots, R_N)$ while incorporating the (isoperimetric) boundary condition (7.13) through a Lagrangian multiplier yields the spherical matched filter $\boldsymbol{\psi}_\ell$

$$\boldsymbol{\psi}_\ell = \alpha \hat{\mathbf{C}}_\ell^{-1} \mathbf{F}_\ell, \quad \text{where} \quad \alpha^{-1} = \sum_{\ell=0}^{\infty} \mathbf{F}_\ell^T \hat{\mathbf{C}}_\ell^{-1} \mathbf{F}_\ell. \quad (7.14)$$

In any realistic application, the cross power spectrum $C_{\ell, v_1 v_2}$ can be computed from observed data provided the cross power spectrum of the signal is negligible. The quantities α , $\mathbf{F}_{\ell 0}$, and thus $\boldsymbol{\psi}_{\ell 0}$ can be computed in a straightforward manner for a specific frequency dependence f_v and for a model source profile $\tau_v(\theta)$.

7.1.4. Scale-adaptive filter on the sphere

The scale-adaptive filter $\boldsymbol{\psi}_\ell$ satisfying all three conditions is given by

$$\boldsymbol{\psi}_\ell = \hat{\mathbf{C}}_\ell^{-1} (\alpha \mathbf{F}_\ell + \mathbf{G}_\ell), \quad \text{with} \quad \mathbf{G}_\ell \equiv [\mu_{\ell, v} \beta_v], \quad \text{and} \quad (7.15)$$

$$\mu_{\ell, v} \equiv f_v \tau_{\ell 0, v} \left(2 + \frac{d \ln \tau_{\ell 0, v}}{d \ln \ell} \right) = f_v [2\tau_{\ell 0, v} + \ell (\tau_{\ell 0, v} - \tau_{\ell-1 0, v})]. \quad (7.16)$$

As motivated in Appendix B, the logarithmic derivative of $\tau_{\ell 0}$ with respect to the multipole order ℓ is a shorthand notation of the differential quotient which is only valid for $\ell \gg 1$. The quantities α and β_v are given by the components

$$\alpha = (\hat{\mathbf{A}}^{-1})_{00}, \quad \beta_v = (\hat{\mathbf{A}}^{-1})_{v0}, \quad (7.17)$$

where $\hat{\mathbf{A}}$ is the $(1 + N) \times (1 + N)$ matrix with elements

$$A_{00} \equiv \sum_{\ell=0}^{\infty} \mathbf{F}_\ell^T \hat{\mathbf{C}}_\ell^{-1} \mathbf{F}_\ell, \quad A_{0v} \equiv \sum_{\ell=0}^{\infty} \mu_{\ell, v} \left(\mathbf{F}_\ell^T \hat{\mathbf{C}}_\ell^{-1} \right)_v \quad (7.18)$$

$$A_{v0} \equiv \sum_{\ell=0}^{\infty} \mu_{\ell, v} \left(\hat{\mathbf{C}}_\ell^{-1} \mathbf{F}_\ell \right)_v, \quad A_{vv'} \equiv \sum_{\ell=0}^{\infty} \mu_{\ell, v} \mu_{\ell, v'} \left(\hat{\mathbf{C}}_\ell^{-1} \right)_{vv'}. \quad (7.19)$$

In these equations, no summation over the indices is implied.

7.1.5. Detection level and gain

As described by Sanz et al. (2001), the concept of constructing an optimised filter function for source detection aims at maximising the signal-to-noise ratio D_u ,

$$D_u \equiv \frac{\langle u(R_1, \dots, R_N; \boldsymbol{\theta}) \rangle}{\sigma_u(R_1, \dots, R_N)} = A \frac{\sum_{\ell=0}^{\infty} \mathbf{F}_{\ell} \boldsymbol{\psi}_{\ell}}{\sqrt{\sum_{\ell=0}^{\infty} \boldsymbol{\psi}_{\ell}^T \hat{\mathbf{C}}_{\ell} \boldsymbol{\psi}_{\ell}}}. \quad (7.20)$$

Computing the dispersion of the unfiltered field on the sphere yields the signal-to-noise ratio D_s of a signal on the fluctuating background:

$$\sigma_s^2 = \sum_{\nu_1, \nu_2} \sum_{\ell=0}^{\infty} C_{\ell, \nu_1 \nu_2} \Rightarrow D_s = \frac{A}{\sigma_s}. \quad (7.21)$$

These considerations allow introducing the *gain* for comparing the signal-to-noise ratios of a peak before and after convolution with a filter function:

$$g \equiv \frac{D_u}{D_s} = \frac{\sigma_s}{\sigma_u(R_1, \dots, R_N)}. \quad (7.22)$$

If the noise suppression is successful, the gain g will assume values larger than one. If the filters are constructed efficiently, they are able to reduce the dispersion ($\sigma_u(R_1, \dots, R_N) < \sigma_s$) while simultaneously retaining the expectation value of the field (7.9). Due to the additional third constraint, the scale-adaptive filter is expected to achieve smaller gains compared to the matched filter.

7.2. Optimised SZ-filters for PLANCK

7.2.1. Numerical derivation of filter kernels

For the derivation of suitable filter kernels the source profiles are assumed to be generalised King-profiles as described by eqn. (7.4) convolved with the respective PLANCK-beam superimposed on fluctuating background given by template $\langle S_{\ell m} \rangle_{\nu}$ -coefficients. The inversion of the matrix $\hat{\mathbf{C}}_{\ell}$ (c.f. eqns. (6.32) and (6.32)) can be performed using either Gauss-Jordan elimination or LU decomposition, which both were found to yield reliable results. In the derivation of the scale-adaptive filters, however, it is numerically advantageous to artificially exclude the lower multipoles $\ell \leq 1$ from the calculation. Due to the sub-millimetric emission of the Milky Way, the lower multipoles are very large. Consequently, the corresponding $\psi_{\ell m}$ -coefficients, $\ell \leq 1$, have been set to zero, which is not a serious intervention since the filters are designed to amplify structures at angular scales well below a degree. For consistency, the multipoles below the quadrupole have been artificially removed in the derivation of the matched filters as well.

In contrast to the PLANCK-simulation pipeline all numerical calculations presented here are carried out in terms of fluxes measured in Jy and not in antenna temperatures for the following reason: Cross-power spectra $C_{\ell, \nu_1 \nu_2}$ given in terms of antenna temperatures are proportional to $(\nu_1 \nu_2)^{-2}$ which results in a suppression of the highest frequency channels by a factor of almost 10^5 compared to the lowest frequency channels.

Furthermore, by working with fluxes instead of antenna temperatures, the filters for extracting the SZ-signal show frequency dependences which can be understood intuitively. The frequency dependence is described by eqns. (6.29) and (6.30). The normalisation \mathcal{Y} has been chosen to be 1 arcmin^2 , which corresponds to typical signal levels detectable with PLANCK. Because of the smallness of the source profiles to be detected, the calculations were carried out to multipole orders of $\ell_{\max} = 4096$, which ensures that the beams as well as the source profiles are well described. In the plots in Sect. 7.2.2, the filters depicted are smoothed with a moving average window comprising eleven bins for better visualisation. Details of the numerics of the filter construction are given in Appendices C and B.

7.2.2. Discussion of filter kernels

7.2.2.1. Matched filter

The spherical harmonics expansion coefficients $\psi_{\ell 0, \nu}$ following from the matched filter algorithm are depicted in Fig. 7.1 for four frequencies most relevant to SZ-observations, namely for $\nu = 100 \text{ GHz}$, $\nu = 143 \text{ GHz}$, $\nu = 217 \text{ GHz}$

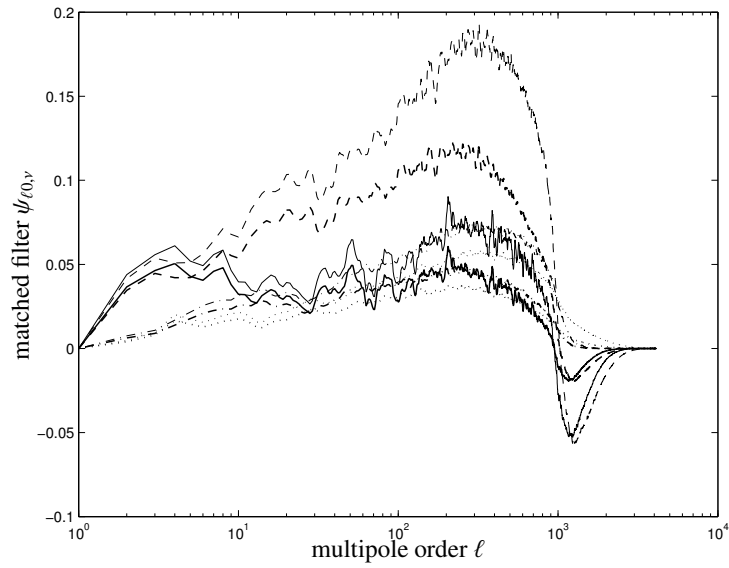


Figure 7.1.: Spherical harmonics coefficients $\psi_{\ell 0, \nu}$ as derived with the matched filter algorithm, for $\nu = 100$ GHz (solid line), $\nu = 143$ GHz (dashed line), $\nu = 217$ GHz (dash-dotted line) and $\nu = 353$ GHz (dotted line) for a dataset containing the CMB, both SZ-effect and instrumental noise.

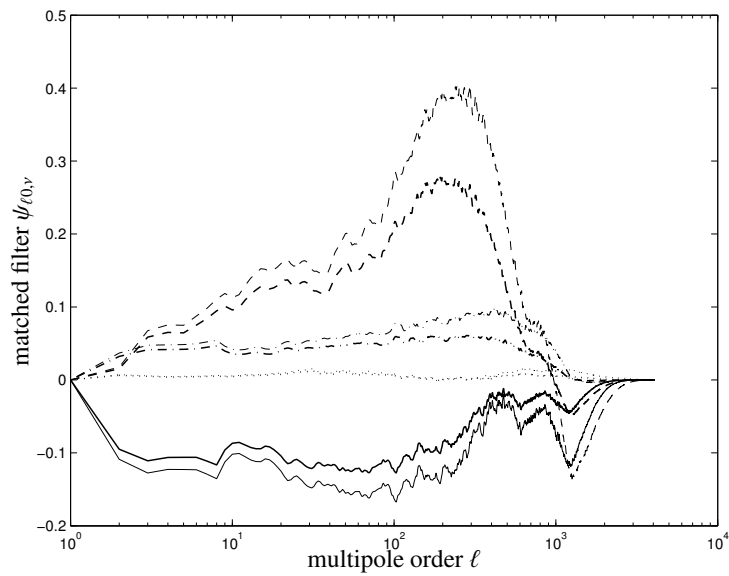


Figure 7.2.: Spherical harmonics coefficients $\psi_{\ell 0, \nu}$ as derived with the matched filter algorithm, for $\nu = 100$ GHz (solid line), $\nu = 143$ GHz (dashed line), $\nu = 217$ GHz (dash-dotted line) and $\nu = 353$ GHz (dotted line) for a dataset containing all Galactic foregrounds in addition to the CMB, both SZ-effect and instrumental noise.

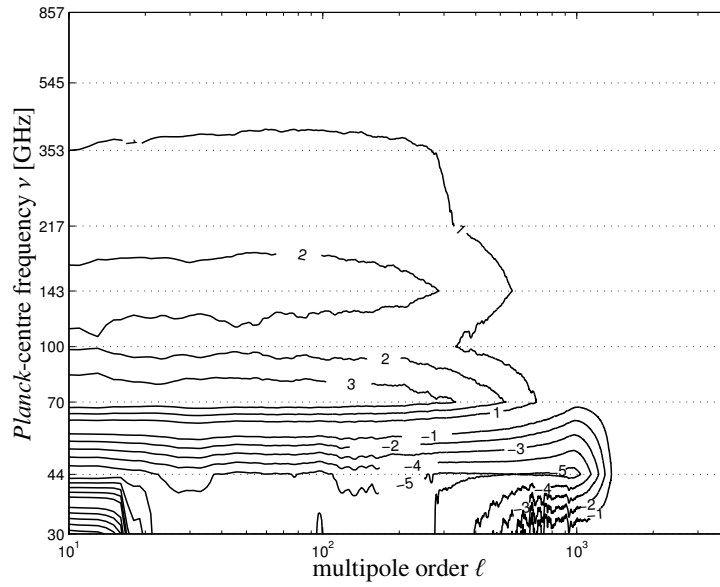


Figure 7.3.: Contour plot of the spherical harmonics expansion coefficients $\psi_{\ell 0, \nu}$ derived with the matched filter algorithm as a function of both the multipole moment order ℓ and PLANCK's observing frequency ν . The filter kernels have been derived for an optimised detection of a generalised King-profile with $(\theta_c, \lambda) = (15'0, 1.0)$ superimposed on the fluctuating CMB and instrumental noise. The contours are linearly spaced in $\text{arsinh}(10^2 \psi_{\ell 0, \nu})$.

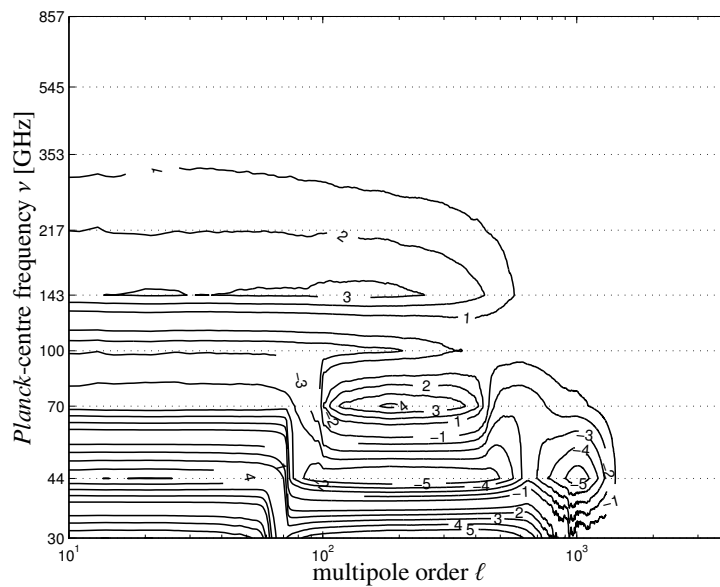


Figure 7.4.: Contour plot of the spherical harmonics expansion coefficients $\psi_{\ell 0, \nu}$ derived with the matched filter algorithm as a function of both the multipole moment order ℓ and PLANCK's observing frequency ν . The filter kernels have been derived for an optimised detection of a generalised King-profile with $(\theta_c, \lambda) = (15'0, 1.0)$ superimposed on the fluctuating CMB, Galactic foregrounds and instrumental noise. The contours are linearly spaced in $\text{arsinh}(10^2 \psi_{\ell 0, \nu})$.

and $\nu = 353$ GHz. As background noise components the clean COS data set (left column) and the exhaustive GAL data set (right column) are contrasted. The filter kernels have been derived for optimised detection of sources described by a generalised King-profile with angular core radii $\theta_c = 3'0$ and $\theta_c = 5'0$ and asymptotic slope $\lambda = 1.0$.

The principle how the matched filter extracts the SZ-signal from the maps is explained by Fig. 7.1: The SZ-profiles the filter has been optimised are small structures at angular scales corresponding to multipole moments of $\ell \simeq 10^3$. In channels below $\nu = 217$ GHz, the clusters are observed in absorption and the fluxes are decreased. For that reason, the filters have negative amplitudes at small angular scales for these specific frequencies. At larger scales, the fluctuations are suppressed by linear combination of the various channels, while the filtering functions show very similar shapes. Optimising the filters for detection of core radii of $5'0$ instead of $3'0$ result in a shift of the negative peak at $\ell \simeq 10^3$ to smaller multipole orders. Instrumental noise which is important at even higher multipoles is suppressed by the filter's exponential decline at high ℓ above $\ell \gtrsim 2000$. The unwanted CMB fluctuations and all Galactic contributions at scales larger than the cluster scale are suppressed by weightings with varying sign so that the foregrounds are subtracted at the stage of forming linear combinations of the $\langle S_{\ell m} \rangle_\nu$ -coefficients.

Furthermore, the contours of the matched filter kernels are given in Fig. 7.1 as functions of both inverse angular scale ℓ and observing frequency ν for differing noise contributions. The figures compare filters derived for differing background noise compositions. The filters shown serve for the optimised detection of generalised King-profiles with core radius $\theta_c = 15'0$ and asymptotic slope $\lambda = 1.0$. These (rather large) values have been chosen for visualisation purposes. For clarity, the contour denoting zero values has been omitted due to noisy data. In these figures it is apparent how the filters combine the frequency information in order to achieve a suppression of the unwanted foregrounds: At multipole moments of a few hundred, the filters exhibit changes in sign, such that the measurements at low frequencies are subtracted from the measurements at high frequencies in the linear combination of the filtered maps.

Fig. 7.5 illustrates the filter kernels $\psi_\nu(\theta)$ in real space for the same selection of frequencies and background noise components as given above. The filter kernels $\psi_\nu(\theta)$ have been synthesised from the $\psi_{\ell 0, \nu}$ -coefficients using the `alm2grid`-utility of the PLANCK-simulation package. Here, the parameters of the King-profile to be detected are $(\theta_c, \lambda) = (5'0, 1.0)$. The filter kernels are similar in shape to Mexican-hat wavelets, but show more than one oscillation. Their action on the sky maps is to apply high-pass filtering, such that all long-wavelength modes are eliminated. At the cluster scale, they implement a linear combination of the sky maps that aims at amplifying the SZ-signal: The kernels derived for both the $\nu = 100$ GHz- and $\nu = 143$ GHz-channel exhibit a central depression which is used to convert the SZ-signal to positive amplitudes. The other two channels resemble simple Gaussian kernels which smooth the maps to a common effective angular resolution. At frequencies of $\nu = 217$ GHz and $\nu = 353$ GHz the most important emission feature is Galactic Dust, which is suppressed by the filter's small amplitudes. In this way, the weak SZ-signal is dissected.

In Fig. 7.6, filter kernels derived with both algorithms for point sources (i.e. with beam profiles of the respective PLANCK-channels) are compared, that have been optimised for the detection of varying spectral behaviour of the signal, in this case the thermal SZ-effect, the kinetic SZ-effect and a Planckian thermal emitter with a surface temperature T_{surface} of 150 K, such as an asteroid or planet. The filter kernels depicted correspond to observing frequencies of $\nu = 143$ GHz and $\nu = 217$ GHz. The filters clearly reflect the spectral behaviour of the emission laws of the sources one aims at detecting: While the filter kernels designed for detecting thermal SZ-clusters reflect the peculiar change in sign in the SZ-effect's frequency dependence, the other two curves show the behaviour to be expected for a Planckian emitter and the kinetic SZ-effect, respectively. Again, the better angular resolution of the $\nu = 217$ GHz-channel is apparent by the shifting of the curves to higher multipole order ℓ .

7.2.2.2. Scale-adaptive filter

The spherical harmonics expansion coefficients $\psi_{\ell 0, \nu}$ following from the scale-adaptive filter algorithm for the frequencies $\nu = 100$ GHz, $\nu = 143$ GHz, $\nu = 217$ GHz and $\nu = 353$ GHz are given in the upper panel of Fig. 7.7. The left and right columns compare the filter kernels for differing noise components. Their functional shape has a number of important features in common with the matched filters: They suppress the uncorrelated pixel noise, which is dominant at high ℓ by their exponential decline at $\ell \gtrsim 2000$. Furthermore, the filters amplify the SZ-signal, which is negative at frequencies below $\nu = 217$ GHz, by assuming large negative values and hence converting the SZ-signal to yield positive amplitudes. Additionally, the filters show a distinct secondary peak at $\ell \simeq 2000$ which causes the kernels to be more compact after transformation to real space and enables the size measurement. A more general observation is that the scale-adaptive filter kernel shapes are more complex and noisier in comparison to the

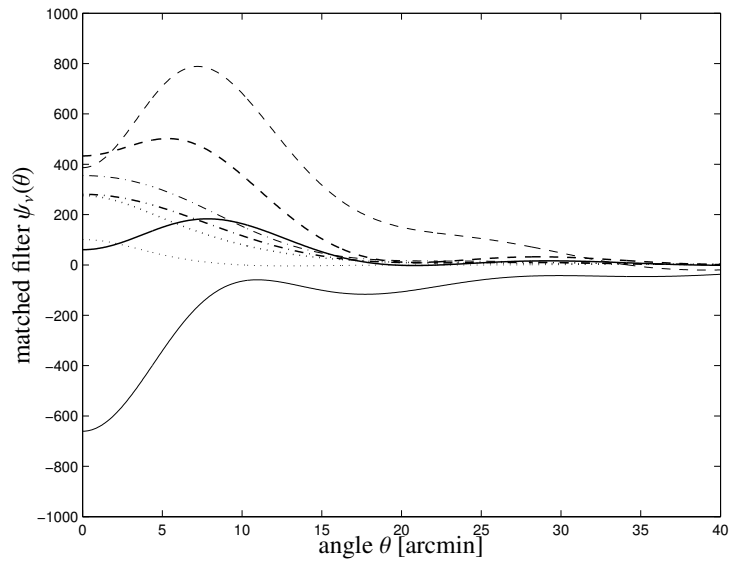


Figure 7.5.: Matched filter kernels $\psi_\nu(\theta)$ in real space at SZ-frequencies, i.e. for $\nu = 100$ GHz (solid line), $\nu = 143$ GHz (dashed line), $\nu = 217$ GHz (dotted line) and $\nu = 353$ GHz (dash-dotted line), for a data set including the CMB, Galactic foregrounds and instrumental noise (thin lines) and for a data set containing all Galactic components in addition to the CMB and instrumental noise (thick lines). The filter kernel is optimised for the detection of a generalised King-profile with core radius $\theta_c = 5.0$ and asymptotic slope $\lambda = 1.0$.

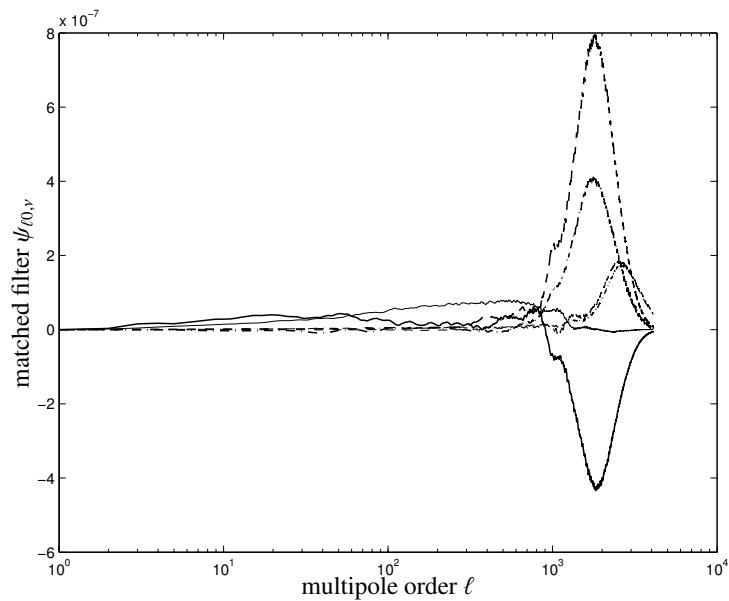


Figure 7.6.: Comparison of filter kernel $\psi_{\ell 0, \nu}$ -coefficients derived for differing spectral dependences of the signal: thermal SZ-effect (solid line), kinetic SZ-effect (dashed line) and a Planckian emitter with surface temperature of $T_{\text{surface}} = 150$ K (dash-dotted line). All sources are assumed to be point-like, i.e. they appear to have the shape of the PLANCK-beam. The curves are given for observing frequencies of $\nu = 143$ GHz (thin line) and $\nu = 217$ GHz (thick line) and have been derived with the matched filter algorithm. The noise is a composite of CMB fluctuations, Galactic and ecliptic foregrounds and instrumental noise.

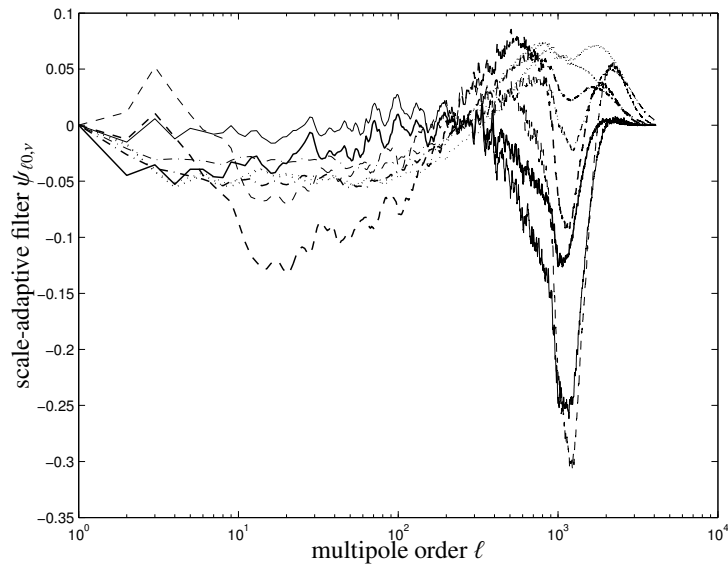


Figure 7.7.: Spherical harmonics coefficients $\psi_{\ell 0, \nu}$ as derived with the scale-adaptive filter algorithm, for $\nu = 100$ GHz (solid line), $\nu = 143$ GHz (dashed line), $\nu = 217$ GHz (dash-dotted line) and $\nu = 353$ GHz (dotted line). The filter kernel is optimised for the detection of generalised King-profiles with core radii $\theta_c = 3.0$ (thin lines) and $\theta_c = 5.0$ (thick lines) and asymptotic slope $\lambda = 1.0$. Noise components include CMB fluctuations and instrumental noise.

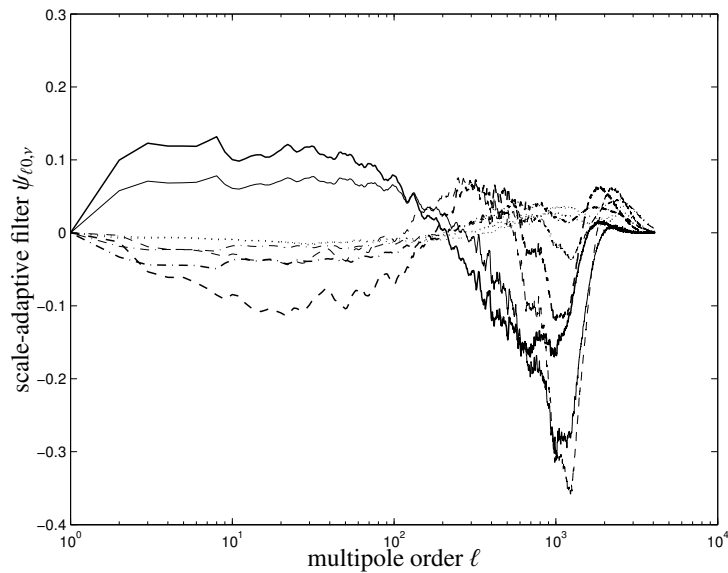


Figure 7.8.: Spherical harmonics coefficients $\psi_{\ell 0, \nu}$ as derived with the scale-adaptive filter algorithm, for $\nu = 100$ GHz (solid line), $\nu = 143$ GHz (dashed line), $\nu = 217$ GHz (dash-dotted line) and $\nu = 353$ GHz (dotted line). The filter kernel is optimised for the detection of generalised King-profiles with core radii $\theta_c = 3.0$ (thin lines) and $\theta_c = 5.0$ (thick lines) and asymptotic slope $\lambda = 1.0$. Noise components include CMB fluctuations, Galactic foregrounds, and instrumental noise.

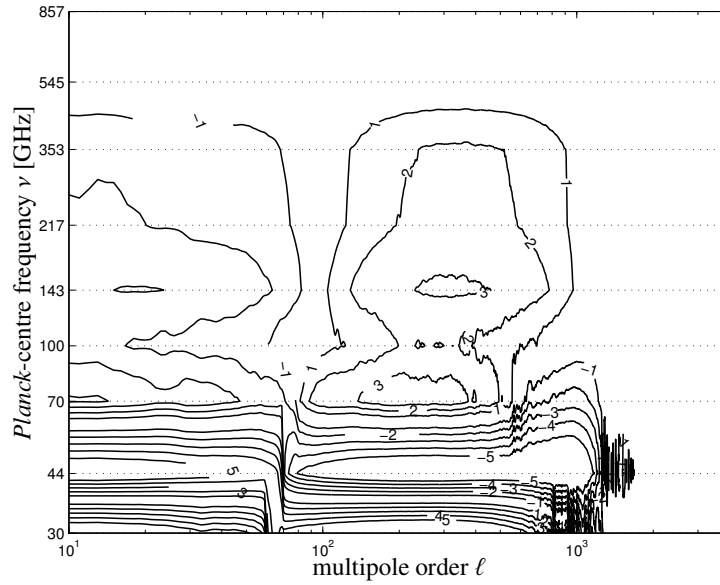


Figure 7.9.: Contour plots of the spherical harmonics expansion coefficients $\psi_{\ell, \nu}$ derived with the scale-adaptive filter algorithm as a function of both the multipole moment order ℓ and PLANCK's observing frequency ν are shown. The filter kernels have been derived for an optimised detection of a generalised King-profile with $(\theta_c, \lambda) = (15^\circ, 1.0)$. The contours are linearly spaced in $\text{arsinh}(10^2 \psi_{\ell, \nu})$. In this plot, CMB fluctuations and instrumental noise were considered in the filter construction.

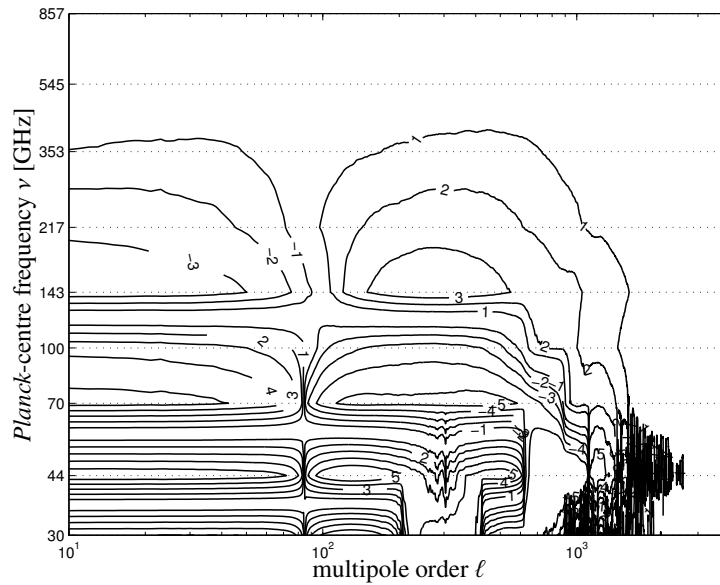


Figure 7.10.: Contour plots of the spherical harmonics expansion coefficients $\psi_{\ell, \nu}$ derived with the scale-adaptive filter algorithm as a function of both the multipole moment order ℓ and PLANCK's observing frequency ν are shown. The filter kernels have been derived for an optimised detection of a generalised King-profile with $(\theta_c, \lambda) = (15^\circ, 1.0)$. The contours are linearly spaced in $\text{arsinh}(10^2 \psi_{\ell, \nu})$. In this plot, Galactic foregrounds entered the filter construction, apart from CMB fluctuations and instrumental noise.

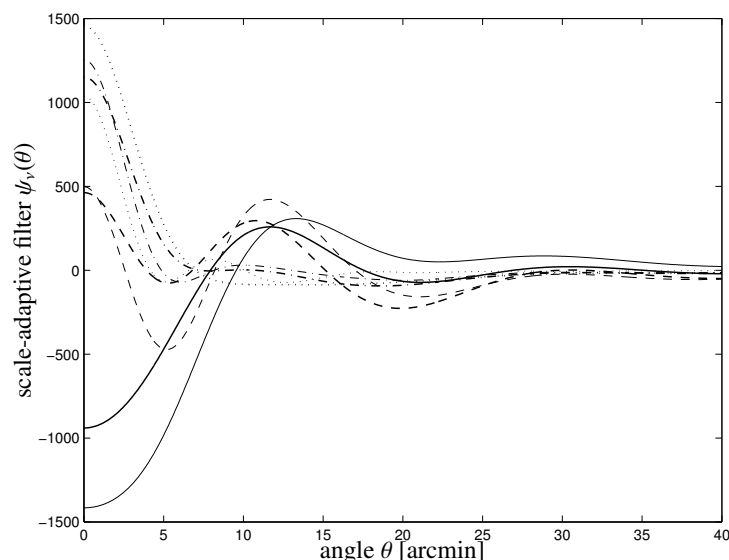


Figure 7.11.: Scale-adaptive filter kernels $\psi_\nu(\theta)$ in real space, for $\nu = 100$ GHz (solid line), $\nu = 143$ GHz (dashed line), $\nu = 217$ GHz (dotted line) and $\nu = 353$ GHz (dash-dotted line), for a data set incorporating the CMB, Galactic foregrounds and instrumental noise. The filter kernel is optimised for the detection of a generalised King-profile with parameters $(\theta_c, \lambda) = (5'.0, 1.0)$.

matched filter, especially at high ℓ .

The scale-adaptive filter makes even stronger use of the spectral information than the matched filter. Especially the contour plots in Fig. 7.7 show that the scale-adaptive filter exhibits alternating signs when varying the observing frequency ν while keeping the angular scale ℓ fixed. In this way, the noise contributions are isolated in angular scale and subsequently suppressed by linear combination of the maps. Furthermore, one notices a change in sign at multipole order $\ell \simeq 200$ which is common to the frequencies $\nu = 100 \dots 353$ GHz, at which the CMB signal is strongest. Aiming at reducing the variance of the filtered maps, the scale-adaptive filter is suppressing the $\langle S_{\ell m} \rangle_\nu$ -coefficients by assuming small values. Fig. 7.11 gives the filter kernels $\psi_\nu(\theta)$ in real space for selected frequencies and background noise components. The scale-adaptive filters work similarly as the matched filters like Mexican-hat wavelets and subject the sky maps to high pass filtering.

In Fig. 7.12, filter kernels derived with both algorithms for point sources (i.e. with beam profiles of the respective PLANCK-channels) are compared, that have been optimised for the detection of varying spectral behaviour of the signal, in this case the thermal SZ-effect, the kinetic SZ-effect and a Planckian thermal emitter with a surface temperature T_{surface} of 150 K, such as an asteroid or planet. The filter kernels depicted correspond to observing frequencies of $\nu = 143$ GHz and $\nu = 217$ GHz. As in the case of the matched filter, the frequency dependence of the signal is reflected by the sign of the filter kernel at the anticipated angular scale of the profile to be detected.

7.2.3. Filter renormalisation and synthesis of likelihood maps

Once the filter kernels are derived, the filtered fields $u_\nu(R_\nu, \beta)$ can be synthesised from the $u_{\ell m, \nu}$ -coefficients (defined in eqn. (7.7)) and the resulting maps can be added in order to yield the co-added, filtered field $u(R_1, \dots, R_N, \beta)$ (see eqn. (7.8)), which can be normalised by the level of fluctuation σ_u (given by eqn. (7.10)) to yield the likelihood map $D(\theta)$. It is favourable to divide the filter kernels by the variance σ_u and to apply a renormalisation:

$$\psi_{\ell 0, \nu} \longrightarrow \psi'_{\ell 0, \nu} = \frac{\psi_{\ell 0, \nu}}{\sqrt{\sum_{\ell} \psi_{\ell}^T \hat{C}_{\ell} \psi_{\ell}}}. \quad (7.23)$$

In this case, the filter kernels are invariant under changes in profile normalisation. With these kernels, the filtered flux maps can be synthesised from the set of $\langle S_{\ell m} \rangle_\nu$ -coefficients and the resulting maps can be co-added to yield

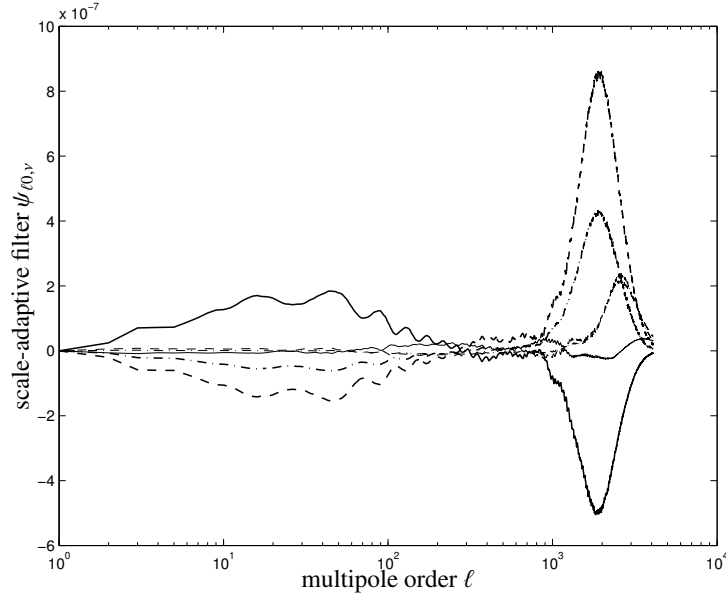


Figure 7.12.: Comparison of filter kernel $\psi_{\ell 0, \nu}$ -coefficients derived for differing spectral dependences of the signal: thermal SZ-effect (solid line), kinetic SZ-effect (dashed line) and a Planckian emitter with surface temperature of $T_{\text{surface}} = 150$ K (dash-dotted line). All sources are assumed to be point-like, i.e. they appear to have the shape as the PLANCK-beam. The curves are given for observing frequencies of $\nu = 143$ GHz (thin line) and $\nu = 217$ GHz (thick line) and have been derived with the scale-adaptive filter algorithm. The noise is a composite of CMB fluctuations, Galactic and ecliptic foregrounds and instrumental noise.

the final normalised likelihood map $D(\beta)$. It is computationally advantageous, however, to interchange the last two steps,

$$D_u(\beta) = \frac{u(\beta)}{\sigma_u} = \frac{1}{\sigma_u} \sum_{\nu} u_{\nu}(\beta) \quad (7.24)$$

$$= \sum_{\nu} \sum_{\ell=0}^{\infty} \sum_{m=-\ell}^{+\ell} \sqrt{\frac{4\pi}{2\ell+1}} \langle S_{\ell m} \rangle_{\nu} \frac{\psi_{\ell 0, \nu}}{\sqrt{\sum_{\ell} \psi_{\ell}^T \hat{C}_{\ell} \psi_{\ell}}} Y_{\ell}^m(\beta) \quad (7.25)$$

$$= \sum_{\ell=0}^{\infty} \sum_{m=-\ell}^{+\ell} \underbrace{\sqrt{\frac{4\pi}{2\ell+1}} \left[\sum_{\nu} \langle S_{\ell m} \rangle_{\nu} \psi'_{\ell 0, \nu} \right]}_{\equiv D_{\ell m}} Y_{\ell}^m(\beta), \quad (7.26)$$

and to derive the $D_{\ell m}$ -coefficients first, such that the synthesis has to be performed only once. Due to the restriction to axially symmetric kernels, the convolution can be carried out using the `alm2map`-utility rather than `totalconvolve`.

Fig. 7.13 gives a visual impression of the capability of the above described filtering schemes: The figure shows a $30^{\circ} \times 30^{\circ}$ wide field at the ecliptic North pole at a frequency of $\nu = 353$ GHz (at the SZ-maximum) as observed by PLANCK, i.e. the image is smoothed to an angular resolution of $\Delta\theta = 5'0$ (FWHM) and contains the fluctuating CMB, all Galactic and ecliptic foregrounds as well as pixel noise. Matched and scale-adaptive filter kernels were derived for isolating point sources, i.e. for sources that appear to have profiles equal to PLANCK's beams of the corresponding channel. For clarity, only amplitudes exceeding a threshold value of 1.0 are shown.

For comparison, Fig. 7.13 shows the same detail of the input thermal SZ-map as well. It is immediately apparent that the observation of SZ-clusters without foreground- and noise suppression is not possible and that one has to rely on filtering schemes. As a comparison with Fig. 7.13 shows, the filters are clearly able to isolate the SZ-clusters and to strongly suppress all spurious noise contributions. The matched filter, however, shows a slightly better

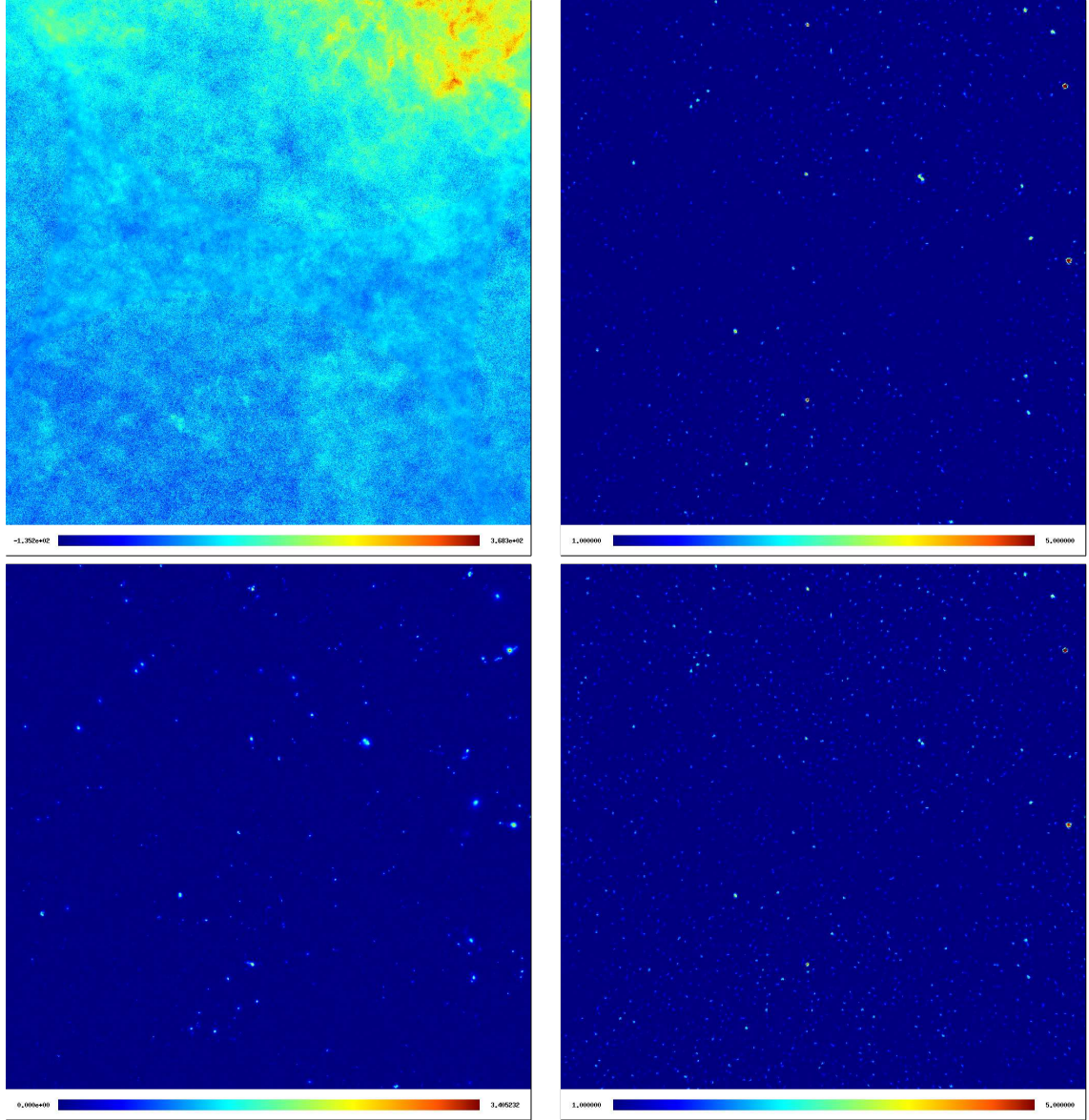


Figure 7.13.: *Upper left panel:* A $30^\circ \times 30^\circ$ wide field centered on the ecliptic North pole as synthesised from a data set containing the CMB, all Galactic and ecliptic foregrounds and instrumental noise for an observing frequency of $\nu = 353$ GHz is shown. The amplitudes are proportional to $\text{arsinh}(T_A(\nu = 353 \text{ GHz})/\mu\text{K})$ and the field is smoothed with the corresponding PLANCK-beam of $\Delta\theta = 5'.0$ (FWHM). *Upper right panel:* The same field is shown after reconstruction from the $D_{\ell m}$ -coefficients. Here, filters derived with the matched filter algorithm optimised for detecting point sources were employed. The amplitudes are given in detection significances and the shading scales linearly. *Lower right panel:* Again, the same field is shown after synthesis from the $D_{\ell m}$ -coefficients but in this case, filters derived with the scale-adaptive filter algorithm optimised for detecting point sources were used. The amplitudes are stated as detection significances and the shading is linear. In the *lower left panel*, the corresponding field taken from the original thermal SZ-map is given for comparison. The amplitudes are $\propto \text{arsinh}(10^4 y)$.

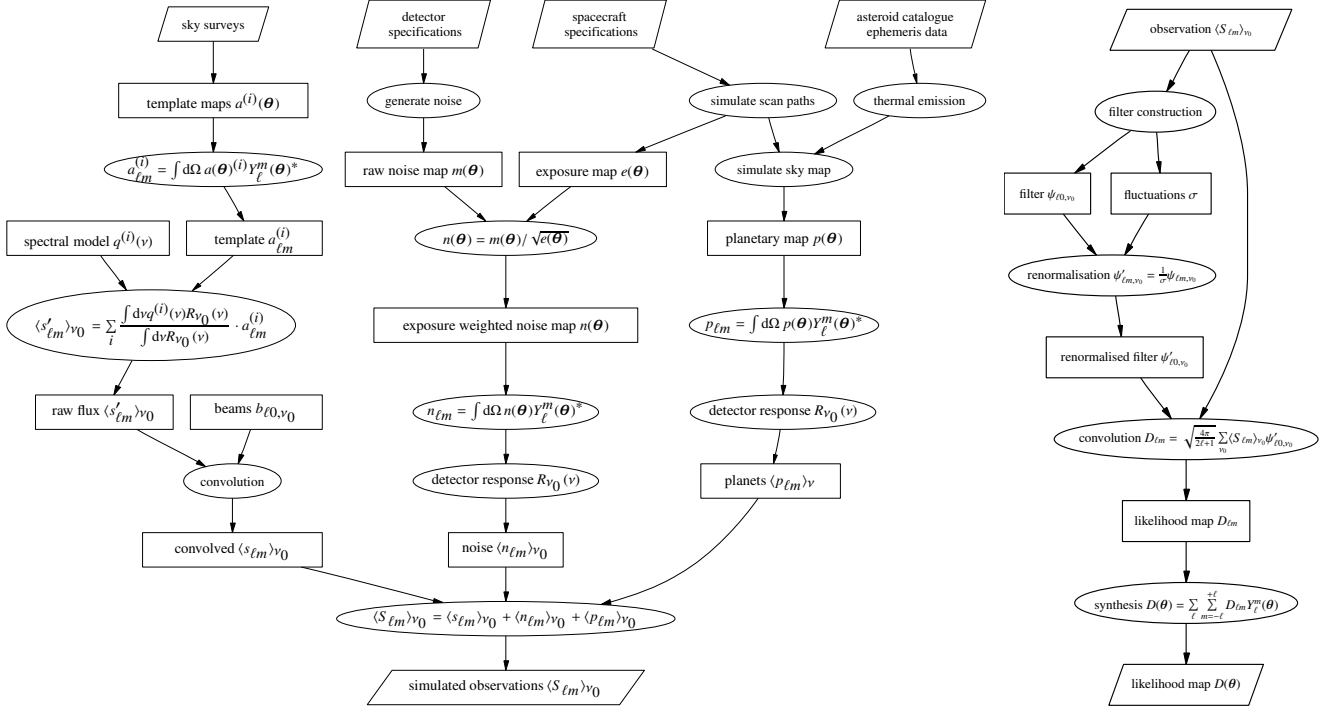


Figure 7.14: Flow chart summarising all steps involved in the simulation of PLANCK-observations and the derivation of $\langle S_{\ell m} \rangle_{\nu}$ -coefficients (left panel) and in the filter construction and signal extraction (right panel).

performance and yields more significant peaks due to better background suppression. There are weak residuals present in both maps due to incomplete foreground reduction. These residuals however, have small amplitudes compared to the SZ-detections. The highest peaks exhibit detection significances amounting to 10.6σ in the case of the matched filter and 9.1σ in the case of the scale-adaptive filter.

It should be emphasised that the filters work exceptionally well despite the fact that the Milky Way clearly is a non-Gaussian feature, whereas Gaussianity of the fluctuating background was an important assumption in the derivation of the filter kernels. Furthermore, the filters successfully separate and amplify the weak SZ-signal in the presence of seven different noise contributions (CMB, four Galactic foregrounds, thermal emission from bodies of the Solar system and instrumental noise) that exhibit different spectral behaviours by relying on just nine broad-band measurements. Fig. 7.14 summarises all steps involved in the simulation of PLANCK-observations, filter derivation and signal extraction.

7.3. Summary and conclusion

- In order to separate the SZ-Signal and to suppress the foreground components, the theory of matched and scale-adaptive filtering has been extended to spherical data sets. The formulae in the context of spherical coordinates and Y_{ℓ}^m -decomposition are analogous to those derived for Cartesian coordinate systems and Fourier-transforms.
- The global properties of filter kernel shapes are examined as functions of observing channel, composition of noise, parameters of the profile to be detected and spectral dependence of the signal. Transformation of the filter kernels to real space yields functions that resemble the Mexican-hat wavelets, but show more than one oscillation. The shape of the filter kernels can be understood intuitively: They subject the maps to high-pass filtering while retaining structures similar in angular extent to the predefined profile size. The signal is then

amplified by linear combination of the maps, which again is apparent in the sign of the filter kernels.

- The functionality of the filtering scheme is verified by applying them to simulated observations. It is found that the Galactic foregrounds can be suppressed very effectively so that the SZ-cluster signals can be retrieved. Comparing the two filters, the scale-adaptive filter performs not as good as the matched filter, which is in accordance to the findings of [Herranz et al. \(2002\)](#). It should be emphasised that for the derivation of the filter kernels nothing but a model profile and all cross-power spectra (in PLANCK's case a total number of 45 independent $C_{\ell, \nu_1 \nu_2}$ -sets) are used.

The results of this and the preceding chapter were worked out in collaboration with M. Bartelmann (ITA, Heidelberg), C. Pfrommer and R. M. Hell (both MPA, Garching). A paper entitled Detecting Sunyaev-Zel'dovich clusters with PLANCK: II. Foreground components and optimised filtering schemes which summarises the results of this and the previous chapter has been submitted to the journal Monthly Notices of the Royal Astronomical Society and is available online ([astro-ph/0407090](#)).

8. Properties of PLANCK's SZ-cluster sample

Abstract

In this chapter, the properties of the filter algorithms and of the recovered cluster sample are analysed in detail. After the description of the simulation setup and the peak extraction (Sect. 8.1), the noise properties are analysed and the distribution of the significances of correctly identified clusters is given (Sect. 8.2). Then, the number of detected cluster as a function of model profile parameters is investigated (Sect. 8.3). The population of SZ-clusters in mass and redshift and the influence of various noise contributions, the distribution of integrated Comptonisations and the position accuracy (Sect. 8.4) are the main results of this chapter. The chapter concludes with the spatial distribution of the detected clusters (Sect. 8.5) and with the distribution of peculiar velocities (Sect. 8.6). Finally, the key results are summarised and compared to other studies (Sect. 8.7).

8.1. Simulation setup and peak extraction

Filter kernels following from the matched and scale-adaptive multifrequency filtering algorithm are subjected to a thorough analysis. They are tested on two different data sets, one containing just CMB fluctuations and (non-isotropic) instrumental noise, and a second data set, which comprises all Galactic foregrounds in addition. From the comparison of the two data sets one will be able to quantify by how much the number of detections drop due to Galactic foregrounds and how uniform the cluster distribution will be provided the removal of Galactic foregrounds can be done efficiently.

8.1.1. Filter construction and synthesis of likelihood maps

Filter kernels optimised for detecting King-profiles $y(\theta) \propto [1 + (\theta/\theta_c)^2]^{-\lambda}$ were derived for a range of core radii θ_c and asymptotic slopes λ . Specifically, seven values of θ_c ,

$$\theta_c = 0'0, \quad 1'0, \quad 2'0, \quad 4'0, \quad 8'0, \quad 16'0, \quad 32'0, \quad (8.1)$$

and five values of λ ,

$$\lambda = 0.6, \quad 0.8, \quad 1.0, \quad 1.2, \quad 1.4 \quad (8.2)$$

were considered, keeping the large range in core radii in mind. Using different values for λ is motivated by asymmetric clusters and in order to allow for the influence of the convolution with the instrumental beam. The sky maps were convolved with the filter kernels, co-added, normalised to unit variance, as described in the previous chapter and synthesised to yield likelihood maps. In the synthesis, all multipole coefficients up to $\ell = 4096$ have been considered and the angular resolution of the resulting maps ($N_{\text{side}} = 1024$, pixel side length $\approx 3'4$) is high enough to resolve single likelihood peaks.

An important numerical issue of spherical harmonic transforms is the fact that the variance (measured in real space) of a map synthesised from the $a_{\ell m}$ -coefficients is systematically smaller with increasing ℓ than the variance $C(\ell)$ required by the $a_{\ell m}$ -coefficients on the scale $\Delta\theta \approx \pi/\ell$. This is compensated by an empirical function, the so-called *pixel window*, which lifts the amplitudes $a_{\ell m}$ towards increasing values of ℓ prior to the reconstruction. This effectively results in higher signal-to-noise ratios of the detected clusters.

8.1.2. Morphology of SZ-clusters in filtered sky-maps

Figs. 8.3 and 8.4 give an impression how the morphology of a peak in the likelihood map changes if filter kernels optimised for the detection of profiles with varying diameter and asymptotic behaviour are used. I picked an

association of two clusters at a redshift of $z \simeq 0.1$, which generates a signal strong enough to yield a significant detection irrespective of the choice of θ_c and λ . The matched filter yields larger values for the detection significance, which is defined to be the signal-to-noise ratio of the central object, in comparison to the scale-adaptive filter for that particular pair of clusters. Secondly, if filters optimised for large objects, i.e. large θ_c and small λ are used, the two peaks merge in the case of the matched filter, but stay separated in case of the scale-adaptive filter. Hence the scale-adaptive filter is more appropriate in the investigation of closeby objects. Additionally, the matched filter seems to be more sensitive to the choice of θ_c and λ . Within the range of these two parameters considered here, the significance of the cluster detection under consideration varies by a factor of four in the case of the matched filter, but changes only by 25% in the case of the scale-adaptive filter.

8.1.3. Peak extraction and cluster identification

It is an important point to notice that cluster positions derived from PLANCK are not very accurate. In this analysis, the SZ-clusters are extended themselves and possibly asymmetric, they are convolved with PLANCK's instrumental beams in the observation and reconstructed from filtered data, where an additional convolution with a kernel is carried out. Furthermore, the pixelisation is relatively coarse (typically a few arcmin). All these effects add up to a position uncertainty of a few tens of arc minutes, depending on the filter kernel.

All peaks above 3σ were extracted from the synthesised likelihood maps and cross checked with a cluster catalogue. A peak was taken to be a detection of a cluster if its position did not deviate more than $30''.0$ from the nominal cluster position. Peaks that did not have a counterpart with integrated Comptonisation \mathcal{Y} larger than a predefined threshold value were registered as false detections, likewise peaks were not considered that did not exceed the threshold value of 3σ in more than two contiguous pixels. In this way, a catalogue is obtained which is essentially free of false detections and, where the fraction of unidentified peaks amounts to 5 – 7% for a realistic threshold of $\mathcal{Y}_{\min} = 3 \times 10^{-4}$ arcmin² (Haehnelt 1997, Bartelmann 2001). The cluster catalogues following from observations with specific (θ_c, λ) -pairs of parameters were merged to yield summary catalogues for both filter algorithms and both noise compositions. If more than one cluster is found in the aperture, the cluster with the largest value for the integrated Comptonisation is assumed to generate the signal. In the merging process, I determine which choice of (θ_c, λ) yielded the most significant detection for a given object.

8.2. Noise properties and peak statistics

8.2.1. Noise in the filtered and co-added maps

In this section, the statistical properties of the noise in the filtered maps is examined. The filter construction algorithm gives the variance σ of the filtered and co-added fields as a function of filter shapes $\psi_{v_i}(\ell)$ and cross-channel power spectra $C_{v_i v_j}(\ell)$ by virtue of $\sigma^2 = \sum_{\ell} \sum_i \sum_j \psi_{v_i}(\ell) C_{v_i v_j}(\ell) \psi_{v_j}(\ell)$. Due to deviations from Gaussianity of many noise components considered (especially Galactic foregrounds), it is important to verify if the variance is still a sensible number. Fig. 8.1 gives the distribution of pixel amplitudes for a combination of noise components and filtering schemes.

Although the distribution of pixel amplitudes seems to follow a Gaussian distribution with zero mean and unit variance in all cases, there are notable deviations from this first impression. As summarised in Table 8.1, the mean of the distributions is compatible with zero in all cases, but the standard deviation is less than unity. Furthermore, the kurtosis of all distributions is nonzero, hence they are more outlier-prone as the normal distribution (barykurtic), which leads to a misestimation of statistical significances of peaks based on the assumption of unit variance of the filtered map, which the filtered map should have due to the renormalisation. This effect is strongest in the case of the matched filter. For the derivation of these numbers, only pixels with amplitudes smaller than $|d| \leq 4\sigma$ have been considered, such that the statistical quantities are dominated by the noise to be examined and not by the actual signal. The distributions are slightly skewed towards positive values, which is caused by weak signals below 4σ . The near-Gaussianity suggests that the residual noise in the filtered map is mostly caused by uncorrelated pixel noise and filters seem to be well capable of suppressing unwanted foregrounds.

Is it important to notice that the comparatively low threshold of 3σ imposed for extracting the peaks alone would yield a considerable number of false detections. Supposing that the variance of the filtered maps is mainly caused by uncorrelated pixel noise which is smoothed to an angular scale of $\simeq 20'$ by the instrumental beam and by the

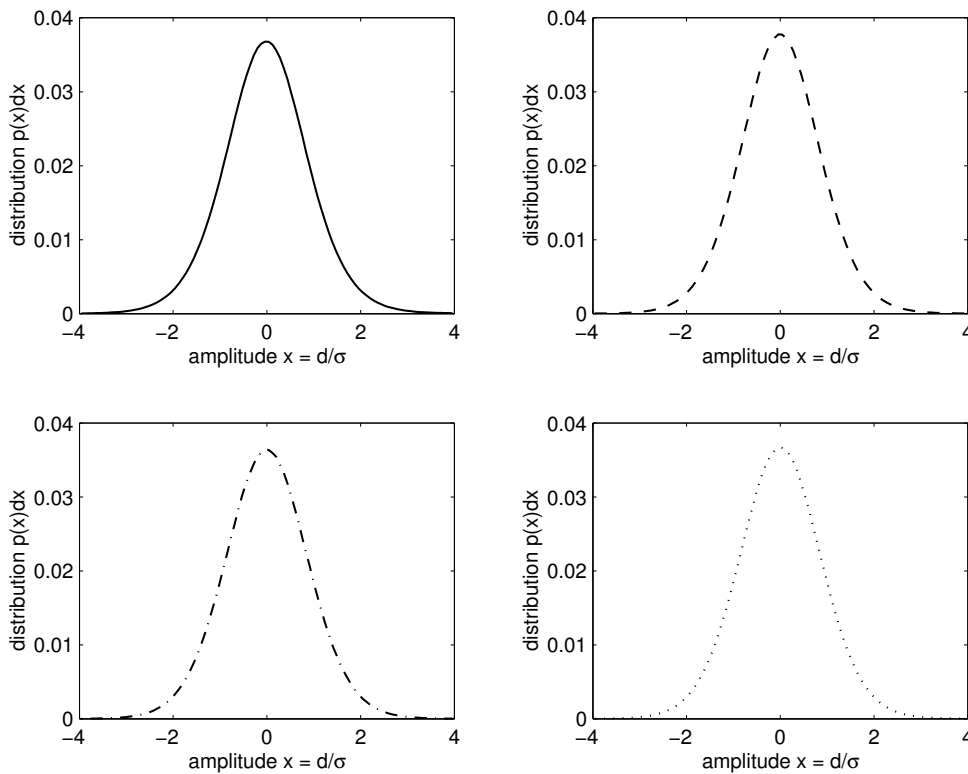


Figure 8.1.: Distribution of pixel amplitudes d of the filtered and co-added maps, normalised to the variance σ predicted in the filter kernel derivation, for a data set including CMB fluctuations and instrumental noise, filtered with the matched filter (upper left, solid line), for a data set including Galactic foregrounds in addition (upper right, dashed line), for a data set containing the CMB and instrumental noise, filtered with the scale-adaptive filter (lower left, dash-dotted line) and finally a data set with CMB, instrumental noise and Galactic foregrounds, filtered with the scale-adaptive filter (lower right, dotted line). The filters have been optimised for the detection of beam-shaped profiles.

filters causes the filtered maps to be composed of $4\pi(180/\pi)^2 \cdot 3^2 \simeq 4 \times 10^5$ unconnected patches. Of these patches, a fraction of $\text{erfc}(3/\sqrt{2}) \simeq 10^{-4}$ naturally fluctuates above the threshold of 3σ . In this way a total number of $\simeq 400$ patches have significances above 3σ . The requirement that the counterpart of the peak in the cluster catalogue generates a Comptonisation above a (conservative) value of \mathcal{Y}_{\min} , i.e. that a cluster candidate is confirmed by spectroscopy, removes these false peaks from the data sample.

8.2.2. Detection significances

The distribution of detection significances is given in Fig. 8.2. One obtains about 10^3 detections at the significance threshold which drops to a few highly significant detections exceeding 20σ . At small σ , the scale-adaptive filter yields more detections than the matched filter, which catches up at roughly 5σ .

The total number of detections for each filter algorithm, for each data set and for two values of the minimally required Comptonisation \mathcal{Y}_{\min} for spectroscopic confirmation are compiled in Table 8.2. Due to its better yield of detections marginally above the threshold the scale-adaptive filter outperforms the matched filter by almost 30%. The reason for the increased number of low-significance detections is the systematically higher value of the variance of the residual noise field in the case of the scale-adaptive filter. The number of detections decreases by $\simeq 25\%$ if Galactic foregrounds are included, relative to the data set containing only CMB fluctuations and instrumental noise. In a realistic observation, one can expect a total number of $\sim 6 \times 10^3$ clusters of galaxies, compared to $\simeq 8 \times 10^3$ clusters if only the CMB and instrumental noise were present. When comparing the total number of detections to analytic estimates (e.g. [Aghanim et al. 1997](#), [Kay et al. 2001](#)), it is found that the number of clusters detected here

data set	filter algorithm	mean μ	variance σ	skewness s	kurtosis $k - 3$
matched	COS	-0.0038 ± 0.0005	0.9272 ± 0.0003	0.0334	0.5297
matched	GAL	-0.0009 ± 0.0005	0.8902 ± 0.0003	0.0154	0.4232
scale-adaptive	COS	-0.0012 ± 0.0005	0.9090 ± 0.0004	0.0142	0.2923
scale-adaptive	GAL	-0.0005 ± 0.0005	0.9023 ± 0.0004	0.0076	0.3125

Table 8.1.: Statistical properties of the filtered and co-added maps, derived from the first four moments of the amplitude distributions in Fig. 8.2, for all data sets and filter algorithms. The filters have been optimised for the detection of beam-shaped profiles. The errors given for the mean μ and standard deviation σ of the distribution of pixel amplitudes correspond to 95% confidence intervals.

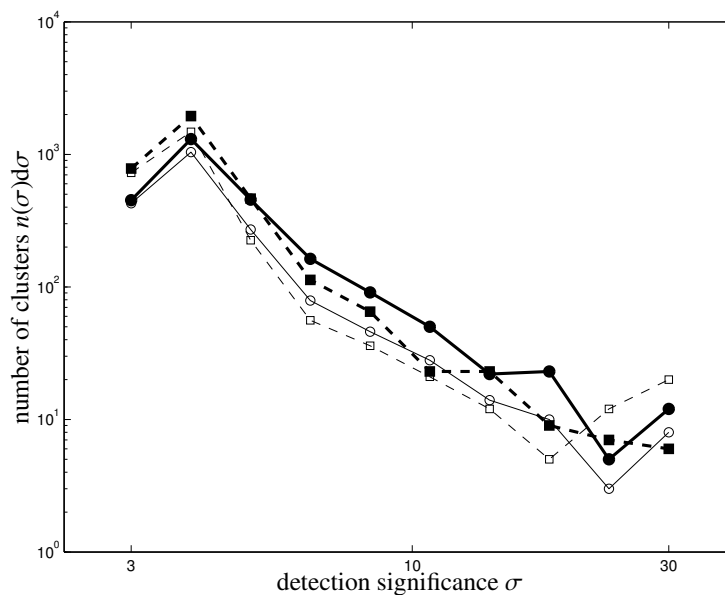


Figure 8.2.: Distribution $n(\sigma)d\sigma$ of the detection significances σ , for the matched filter (solid line, circles) in comparison to the scale-adaptive filter (dashed line, squares). The distributions are given for the clean data set including only the CMB, both SZ-effects and instrumental noise (thick lines, closed symbols) and in comparison, the data set where all Galactic foreground components are included in addition (thin lines, open symbols).

filter	data set	$\mathcal{Y}_{\min} = 10^{-3} \text{ arcmin}^2$	$\mathcal{Y}_{\min} = 3 \times 10^{-4} \text{ arcmin}^2$
matched filter	COS	2402	5376
matched filter	GAL	1801	4199
scale-adaptive filter	COS	3234	8020
scale-adaptive filter	GAL	2428	6270

Table 8.2.: Total number of detections in both data sets and with both filters, for a minimally required Comptonisation of $\mathcal{Y}_{\min} = 10^{-3} \text{ arcmin}^2$ and $\mathcal{Y}_{\min} = 3 \times 10^{-4} \text{ arcmin}^2$.

is smaller, by a factor of less than two.

One should keep in mind that the noise due to PLANCK’s scanning paths is highly structured on the cluster scale and below, such that the assumption of isotropy of the noise is not valid. This has two important consequences: Firstly, assuming a simple flux threshold in analytic estimates is not valid because the noise is not uniform on the cluster scale and secondly the assumption of isotropy which is essential to the filter construction is violated which affects the sensitivity of the filters.

8.3. Cluster detectability as a function of filter parameters

The way the significance of a detection of a cluster changes when the core size θ_c and the asymptotic slope λ are varied is illustrated in Fig. 8.3 for the matched filter and in Fig. 8.4 for the scale-adaptive filter. In general, the matched filter yields significances that are almost twice as large for the specific example considered and consequently finds more clusters above a certain detection threshold. Furthermore, the matched filter shows a stronger dependence of the significance on the filter parameters θ_c and λ : The significance for the detection of the same object varies by a factor of four in case of the matched filter but only by 25% in the case of the scale-adaptive filter. This means that the derivation of cluster properties based on the filter parameter that yielded the most significant detection is likely to work for the matched filter, but not for the scale-adaptive filter. It should be emphasised, however, that the scale-adaptive filter keeps the likelihood distributions of the two objects from merging, in contrast to the matched filter, as can be seen in the lower left part of Figs. 8.3 and 8.4. For that reason, the scale-adaptive filter may be better suited for the investigation of associations and pairs of SZ-clusters.

Fig. 8.5 shows the number density of detectable clusters as a function of the King-profile’s core size θ_c that entered the filter construction. Whereas the matched filter yields most detections at small values of θ_c , the scale-adaptive filter is better suited to detect extended objects. Most of the detections are registered at core sizes $\theta_c = 8'$. Additionally, the scale-adaptive filter’s capability of detecting extended objects suffers from the inclusion of Galactic foregrounds, which cause the total number of detections to drop by 20%. In contrast, the matched filter is able to deliver a comparable performance for all values of θ_c if Galactic foregrounds are included.

The number density of clusters as a function of the King-profile’s asymptotic slope λ which the filters are optimised for is given in Fig. 8.6. The number of detections following from scale-adaptive filtering is relatively insensitive to particular choices of λ , whereas the matched filter yields a higher number of detections in the case of compact objects, irrespective of the noise components included in the analysis. Fig. 8.7 illustrates how the number of detections changes as a function of both θ_c and λ . It should be emphasised that none of the graphs depicted in Figs. 8.5, 8.6 and 8.7 is corrected for double detections of objects at more than (θ_c, λ) -pair.

8.4. Cluster properties of the recovered SZ-sample

8.4.1. Cluster population in the mass-redshift plane

Scatter plots describing the population of detectable clusters in the mass-redshift-plane are shown in Fig 8.8 for the matched filter and in Fig. 8.9 for the scale-adaptive filter. The clusters populate the $\log(M)$ - z -plane in a fairly well defined region. There are only few detections beyond redshifts of $z = 0.8$, but the shape of the detection criterion suggests the existence of a region of low-mass low-redshift clusters which should be detectable but which

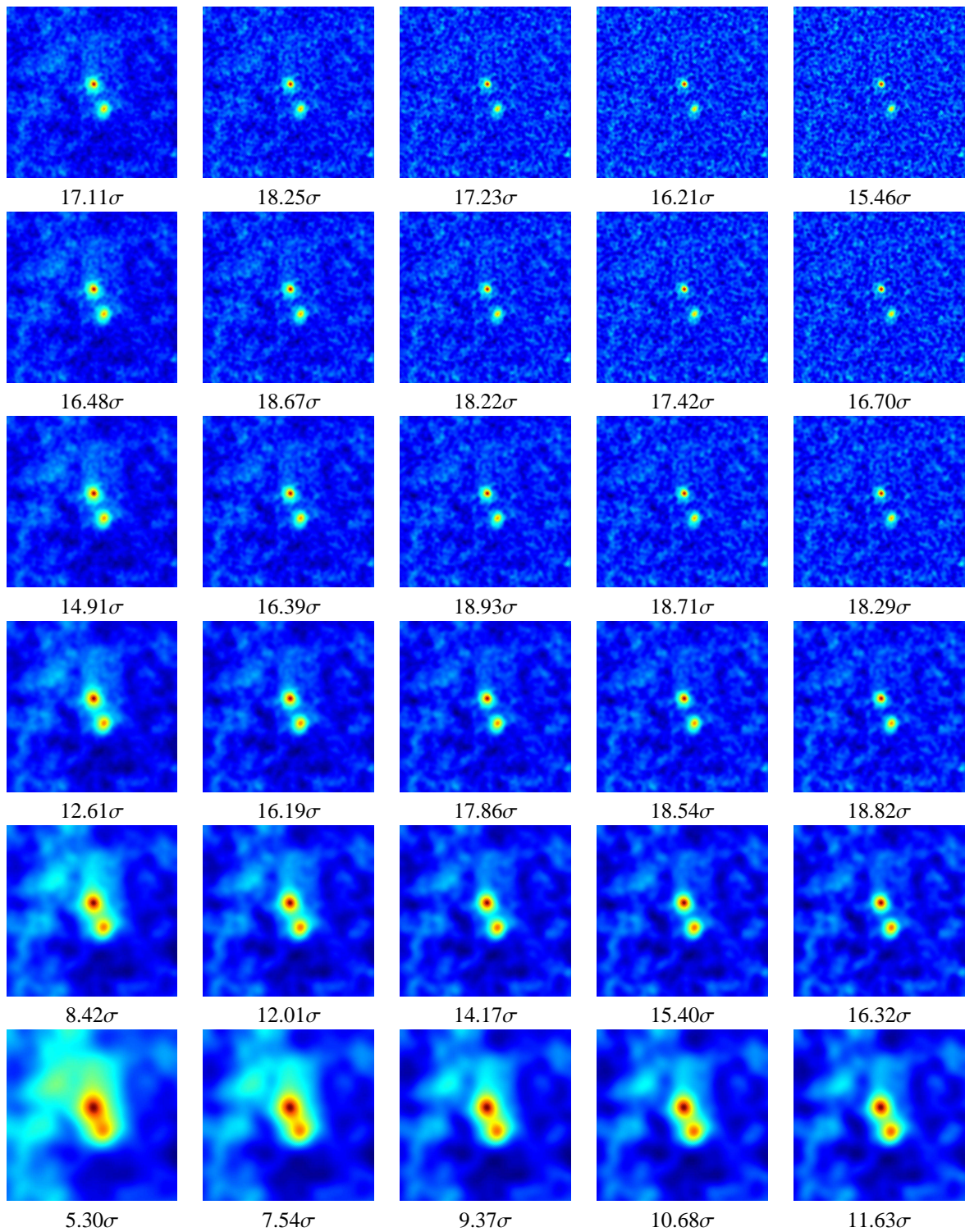


Figure 8.3.: An association of two clusters at $z \approx 0.1$, extracted from a map containing all Galactic components, CMB fluctuations and instrumental noise with the matched multifilter. The table gives the likelihood maps and the statistical significances of the detection of the cluster at the image centre in units of σ , for $\lambda = 0.6, 0.8, 1.0, 1.2, 1.4$ (columns) and $\theta_c = 1'0, 2'0, 4'0, 8'0, 16'0, 32'0$ (rows). The side length of the panels is 4° .

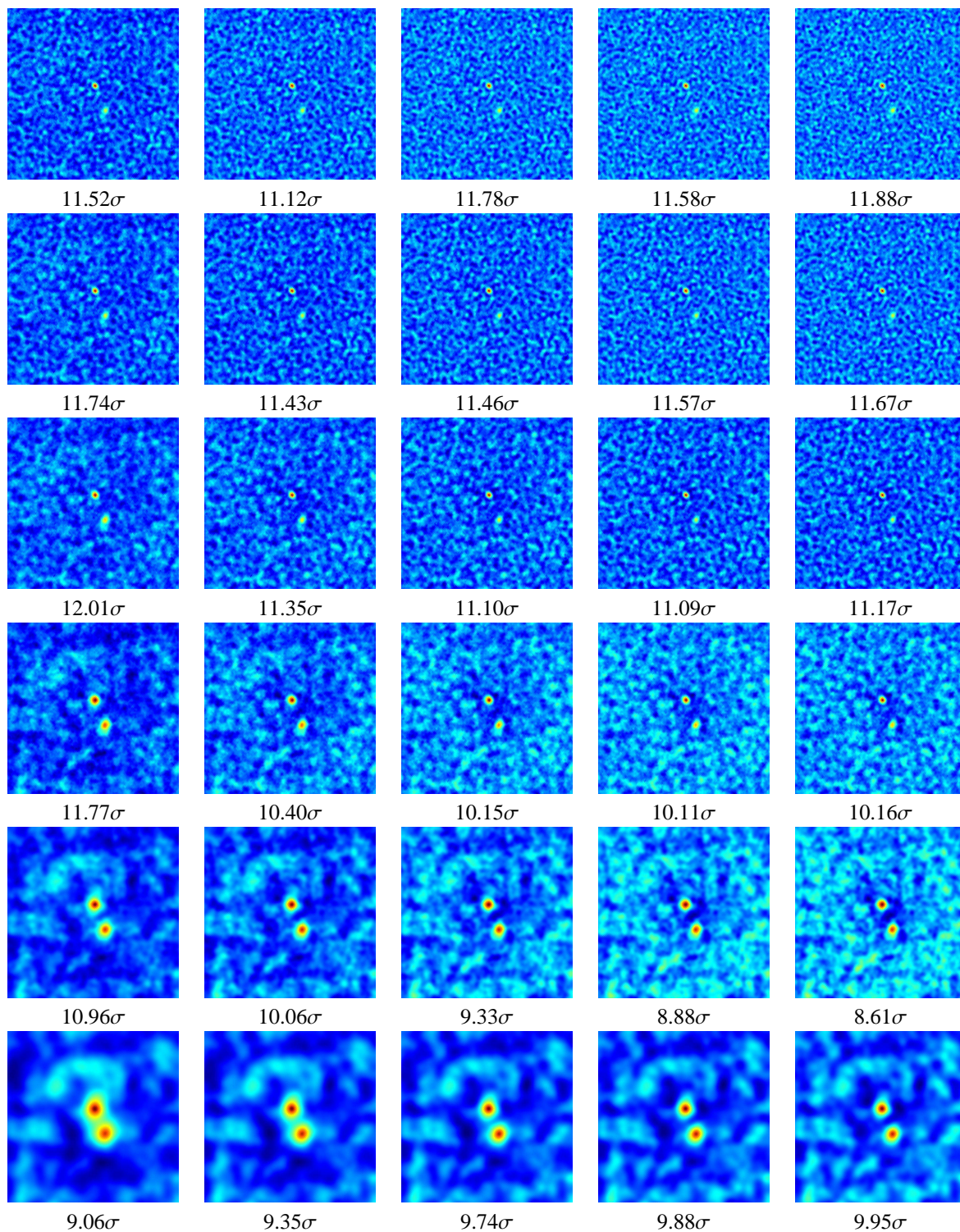


Figure 8.4.: The same association of two clusters at $z \approx 0.1$, extracted from a map containing all Galactic components, CMB fluctuations and instrumental noise with the scale-adaptive multifilter. The table gives the likelihood maps and the statistical significances of the detection of the cluster at the image centre in units of σ , for $\lambda = 0.6, 0.8, 1.0, 1.2, 1.4$ (columns) and $\theta_c = 1'0, 2'0, 4'0, 8'0, 16'0, 32'0$ (rows). The side length of the panels is 4° .

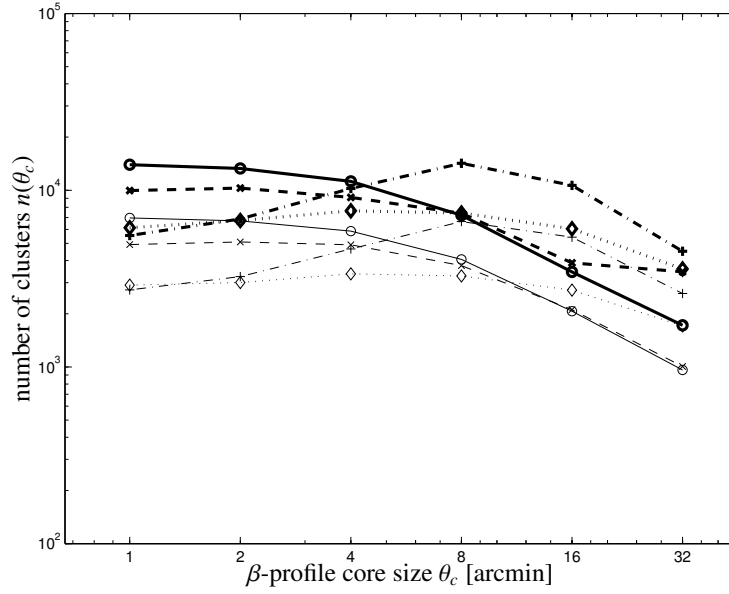


Figure 8.5.: Number density $n(\theta_c)$ of clusters as a function of the filter parameter core size θ_c , for a data set including CMB fluctuations and instrumental noise, filtered with the matched filter (circles, solid line), for a data set including Galactic foregrounds in addition (crosses, dashed line), for a data set containing the CMB and instrumental noise, filtered with the scale-adaptive filter (plus signs, dash-dotted line) and finally a data set with CMB, instrumental noise and Galactic foregrounds, filtered with the scale-adaptive filter (diamonds, dotted line). The thick and thin lines denote detections and peaks above 10^{-3} arcmin² and 3×10^{-4} arcmin², respectively.

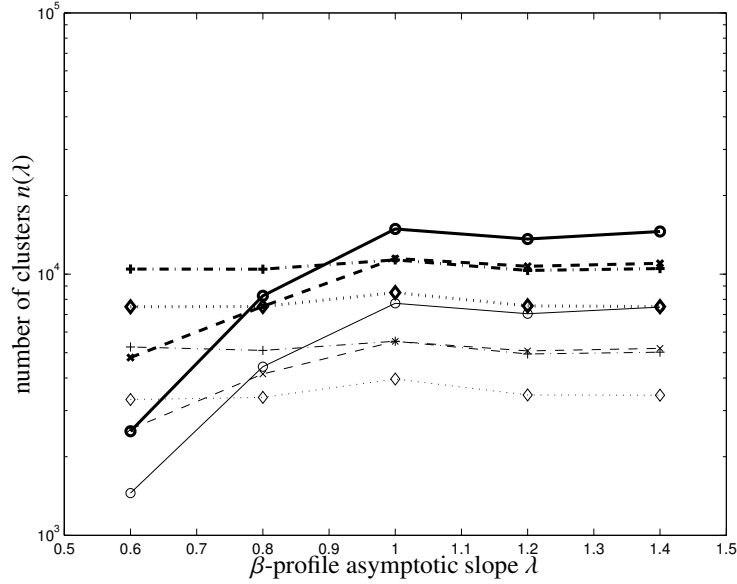


Figure 8.6.: Number density $n(\lambda)$ of clusters as a function of the filter parameter asymptotic slope λ , for a data set including CMB fluctuations and instrumental noise, filtered with the matched filter (circles, solid line), for a data set including Galactic foregrounds in addition (crosses, dashed line), for a data set containing the CMB and instrumental noise, filtered with the scale-adaptive filter (plus signs, dash-dotted line) and finally a data set with CMB, instrumental noise and Galactic foregrounds, filtered with the scale-adaptive filter (diamonds, dotted line). The thick and thin lines denote detections and peaks above 10^{-3} arcmin² and 3×10^{-4} arcmin², respectively.

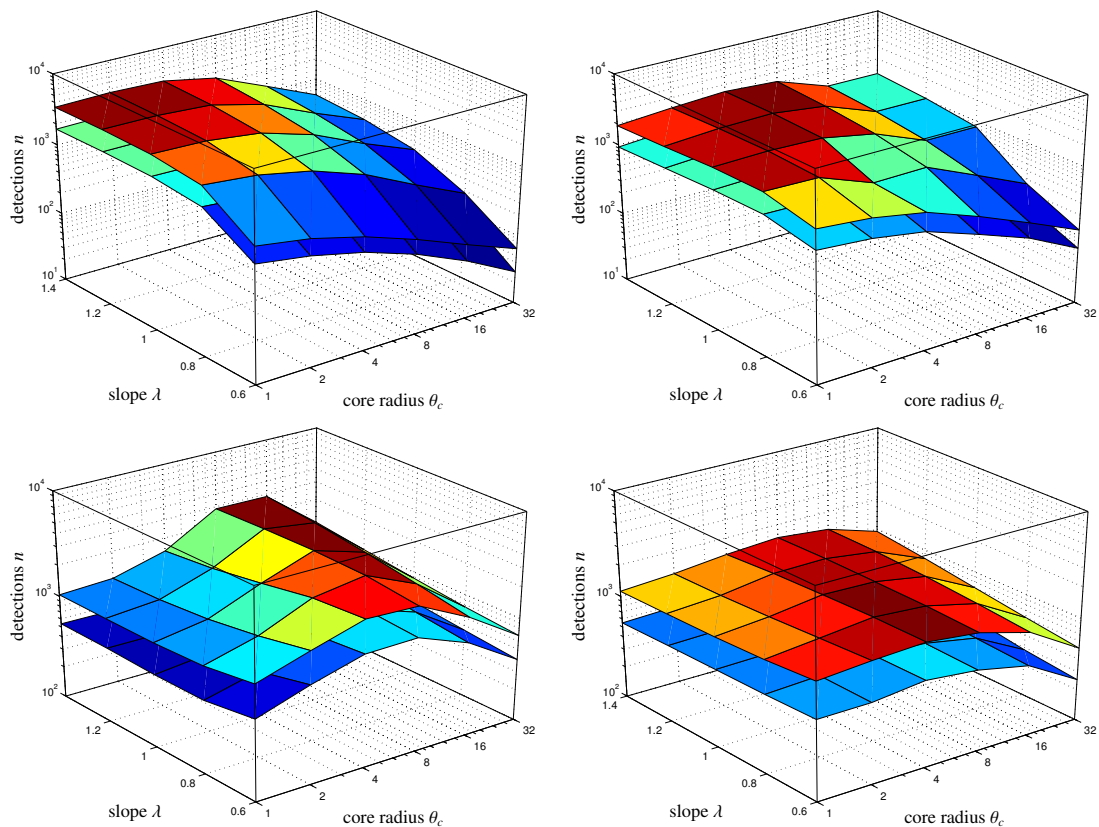


Figure 8.7.: Number of detections $n(\theta_c, \lambda)$ as a function of both filter parameters core size θ_c and asymptotic slope λ , for the matched filter (top row) in comparison to the scale-adaptive filter (bottom row). The figure compares the number density following from a clean data set containing the CMB, the SZ-effects and instrumental noise (left column) with a data set containing all Galactic components in addition (right column). $n(\theta_c, \lambda)$ is given for the minimal signal strength $\mathcal{Y}_{\min} = 3 \times 10^{-4} \text{ arcmin}^2$ (upper plane) compared to $\mathcal{Y}_{\min} = 10^{-3} \text{ arcmin}^2$ (lower plane).

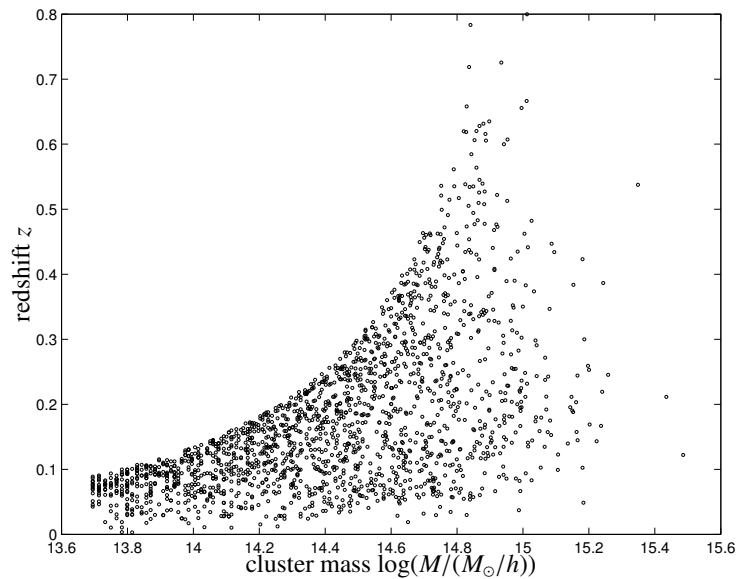


Figure 8.8.: Population of clusters in the $\log(M)$ - z -plane detected with the matched multifilter for the data set containing the CMB, instrumental noise and all Galactic foregrounds. The minimal signal strength was required to be $\mathcal{Y}_{\min} = 10^{-3} \text{ arcmin}^2$.

are not included in the map construction. It is difficult to predict the SZ properties of low-mass clusters because many complications in the sector of baryonic physics come into play such as preheating, deviation from scaling laws and incomplete ionisation, which makes it difficult to predict the number of clusters missing in my analysis. Together with K. Dolag I am preparing an auxiliary SZ-map from a gas-dynamical constrained simulation of the local universe that would fill in the gap and provide clusters with masses $M < 5 \times 10^{13} M_{\odot}/h$ below redshifts of $z < 0.1$.

Fig. 8.10 gives the marginalised distribution in redshift z of the cluster sample. The shape of the redshift distribution is determined by the competition of two effects: With increasing redshift z the observed volume increases, but contrariwise, the number of massive clusters decreases as described by the Press-Schechter function and the SZ-signal becomes smaller proportional to $d_A^{-2}(z)$. Most of the clusters are observed at redshifts of $z \approx 0.2$ and the detection limit is reached at redshifts of $z \approx 0.8$. This applies to both filter algorithms and data sets alike.

Fig. 8.11 gives the marginalised distribution of the cluster's logarithmic mass $m = \log(M/(M_{\odot}/h))$. At high masses, both filtering schemes detect cluster reliably, but with decreasing mass, the filter algorithms start to show differences in their efficiency. The mass functions peak at a value of $2.5 \times 10^{14} M_{\odot}/h$, and decrease towards smaller values for the mass due to the decrease in number density of objects and smaller SZ-signal strength \mathcal{Y} . Fig. 8.12 gives the distribution of the cluster's Compton- \mathcal{Y} parameter. The distribution is close to a power law as expected from virial estimates (c.f. Chapter. 5), but at low Comptonisations, all distributions evolve shallower, which is due to the fact that clusters fail to generate a peak in the likelihood map exceeding the threshold value.

8.4.2. Position accuracy of PLANCK's SZ-clusters

A histogram of the deviations between actual and reconstructed cluster position is given by Fig. 8.13. The position accuracy is given in terms of the squared angular distance $\Delta = \theta_{\text{arc}}^2$ because a uniform distribution would yield a flat histogram. The distribution is sharply peaked towards $\Delta = 0 \text{ arcmin}^2$. A fraction of 50% of all clusters are detected within $10'$ from the nominal source position, but there is a tail in the distribution towards larger angular separations. For most of the clusters, this position accuracy is good enough for direct follow-up studies at X-ray wavelengths, but not good enough for optical observations.

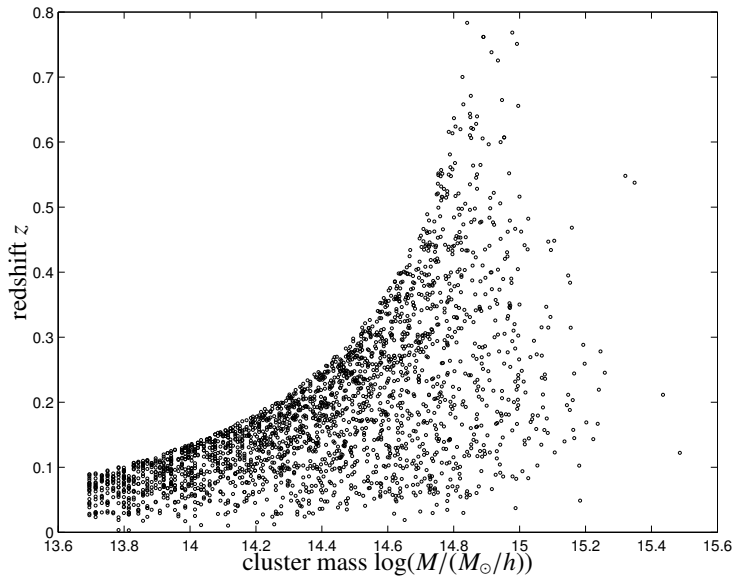


Figure 8.9.: Population of clusters in the $\log(M)$ - z -plane detected with the scale-adaptive multifilter. Here, the detections are given for a data set containing the CMB, instrumental noise and all Galactic foregrounds. All peaks exceed a minimal Comptonisation of $\mathcal{Y}_{\min} = 10^{-3} \text{ arcmin}^2$.

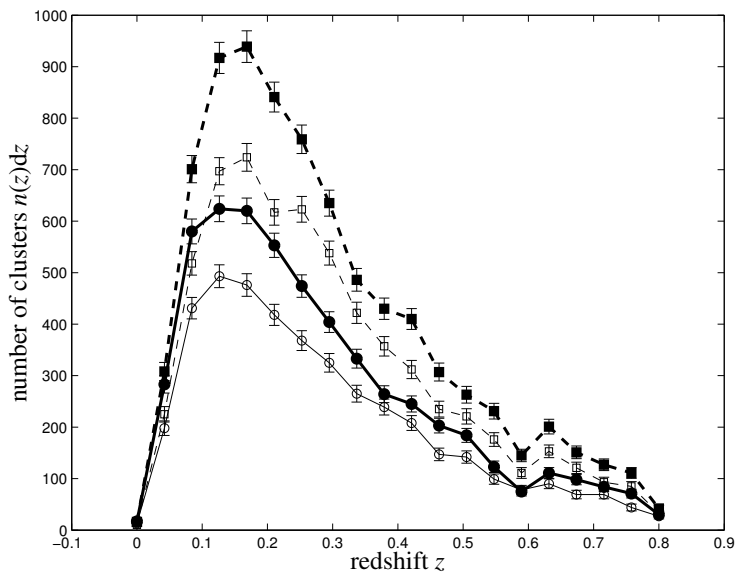


Figure 8.10.: Distribution $n(z)dz$ of the detected clusters in redshift z , for the matched filter (solid line, circles) in comparison to the scale-adaptive filter (dashed line, squares). The figure compares detections in a clean data set containing the CMB, both SZ-effects and instrumental noise (thick lines, closed symbols) to a data set with all Galactic components in addition (thin lines, open symbols). Again \mathcal{Y}_{\min} was set to $3 \times 10^{-4} \text{ arcmin}^2$.

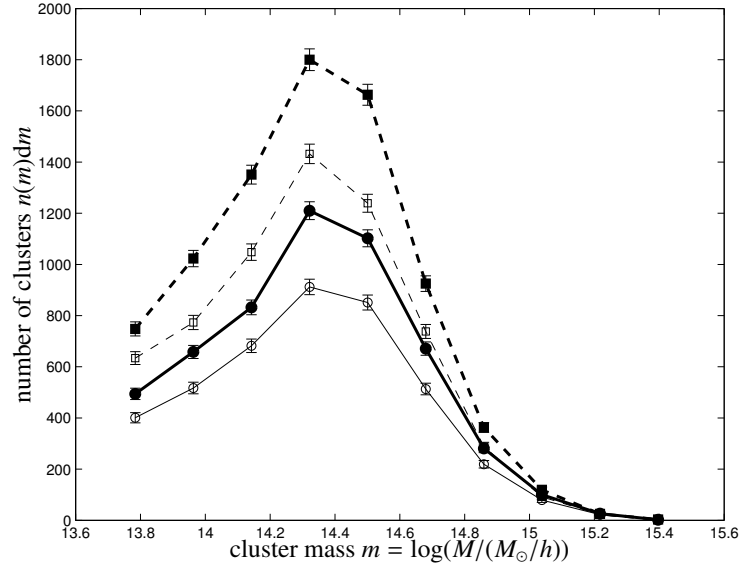


Figure 8.11.: Distribution $n(m)dm$ of the detected clusters in logarithmic mass $m = \log(M/(M_{\odot}/h))$, for the matched filter (solid line, circles) in comparison to the scale-adaptive filter (dashed line, squares). Here, the distributions are given for a data set including only the CMB, both SZ-effects and instrumental noise (thick lines, closed symbols) in comparison to a data set containing moreover all Galactic foreground emission components (thin lines, open symbols). The minimal Comptonisation for spectroscopic confirmation was $\mathcal{Y}_{\min} = 3 \times 10^{-4} \text{ arcmin}^2$.

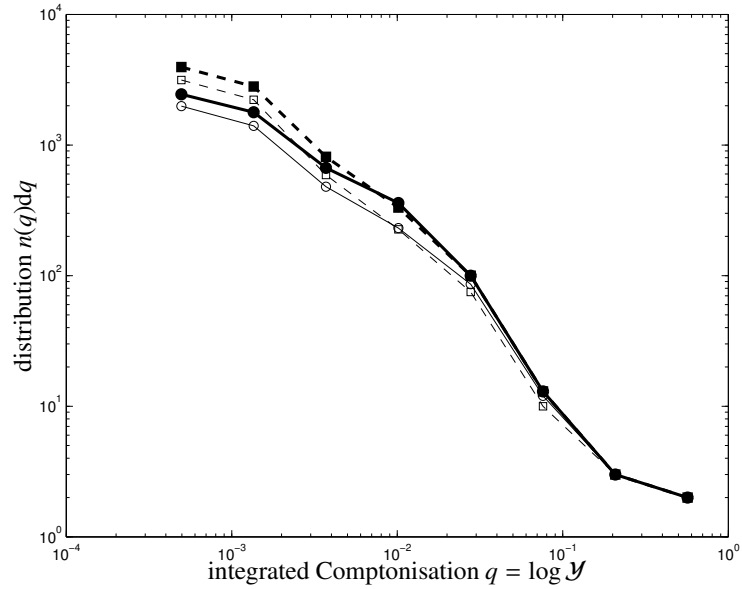


Figure 8.12.: Distribution $n(q)dq$ of the logarithmic integrated Comptonisation, $q = \log(\mathcal{Y})$, for the matched filter (solid line, circles) in comparison to the scale-adaptive filter (dashed line, squares). Here, the distributions are given for a data set including only the CMB, both SZ-effects and instrumental noise (thick lines, closed symbols) in comparison to a data set containing moreover all Galactic foreground emission components (thin lines, open symbols).

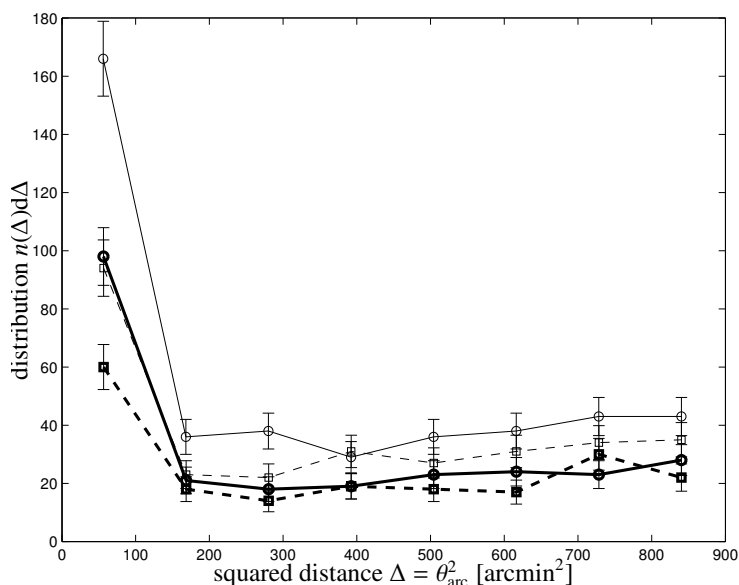


Figure 8.13: Distribution of the squared angular distance $\Delta = \theta_{\text{arc}}^2$ between actual and reconstructed source position on a great circle, for the matched filter (solid line, circles) in comparison to the scale-adaptive filter (dashed line, squares). The figure compares detections above 4σ (thin lines) with detections above 5σ for clusters detected with the parameter $\theta_c = 8'0$. The clusters were required to generate a Comptonisation \mathcal{Y}_{min} exceeding 3×10^{-4} arcmin².

8.5. Spatial homogeneity of PLANCK's SZ-cluster sample

Fig. 8.14 shows the number density of clusters as a function of ecliptic latitude $y \equiv \cos\beta$. The figure states that the PLANCK cluster sample extracted with the specific filters is highly non-uniform for low significance thresholds, where most of the clusters are detected on a belt around the celestial sphere, but gets increasingly more uniform with higher threshold values for the significance. This is due to the incomplete removal of low- ℓ modes in the filtered maps, which bears interesting analogies to the *peak-background split* (White et al. 1987, Cole & Kaiser 1989) in biasing schemes for linking galaxy number densities to dark matter densities: Essentially, the likelihood maps are composed of a large number of small-scale fluctuations superimposed on a background exhibiting a large-scale modulation. In regions of increased amplitudes due to the long-wavelength mode one observes an enhanced abundance of peaks above a certain threshold and hence an enhanced abundance of detected objects.

As Fig. 8.15 indicates, the filtered and co-added maps do have large amplitudes for the octupole or the hexadecupole which are certainly not in agreement with the near-Poissonian slope of $C(\ell) \propto \ell^2$ typical for a random distribution of small sources. The incomplete removal of low- ℓ modes shows that the assumptions about isotropy is violated on large scales and $C(\ell)$ ceases to be a fair description of the variance contained in the $a_{\ell m}$ -coefficients. Clearly, this is a serious limitation to the spherical harmonic approach. In general, the low- ℓ fluctuations are more pronounced for extended objects, i.e. large θ_c and small λ , and they are stronger in the case of the matched filter compared to the scale-adaptive filter.

Similarly, detection significances near the detection threshold are inaccurate due to the long-wavelength modes. A way to remedy this would be to introduce local estimates of the mean and variance, for example by considering the average and the standard deviation of the amplitudes in an aperture with a few degrees in radius. One must keep in mind that in the filtered map, the signal is strong and likely to affect these two values.

Fig. 8.16 for example shows all-sky maps of the filtered and co-added data, where the filter kernels are optimised for the detection of extremely extended signals. The particular (pathological) choice of the King-profile parameters was $\theta_c = 32'0$ and $\lambda = 0.6$. The likelihood map reconstructed with the matched filter shows strong long-wavelength variations of mainly octupolar structure, where the amplitude of this artefact amounts to roughly 1σ . The extraction of peaks from this map would yield a spatially highly non-uniform data sample. Compared to that, the scale-adaptive filter is doing much better: The likelihood map does not show large-scale variations as strong as in the case of the

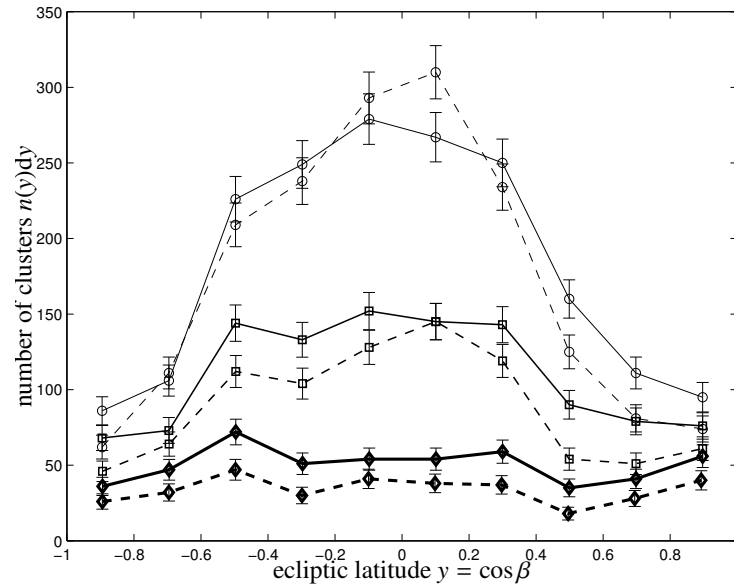


Figure 8.14.: Number $n(y)dy$ of clusters as a function of ecliptic latitude $y = \cos \beta$, for the matched filter (solid line) in comparison to the scale-adaptive filter (dashed line). The figure compares the number of detected clusters as a function of ecliptic latitude for detection significances $> 4.2\sigma$ (circles, thin lines), $> 4.8\sigma$ (squares, medium lines) and $> 6.0\sigma$ (diamonds, thick lines).

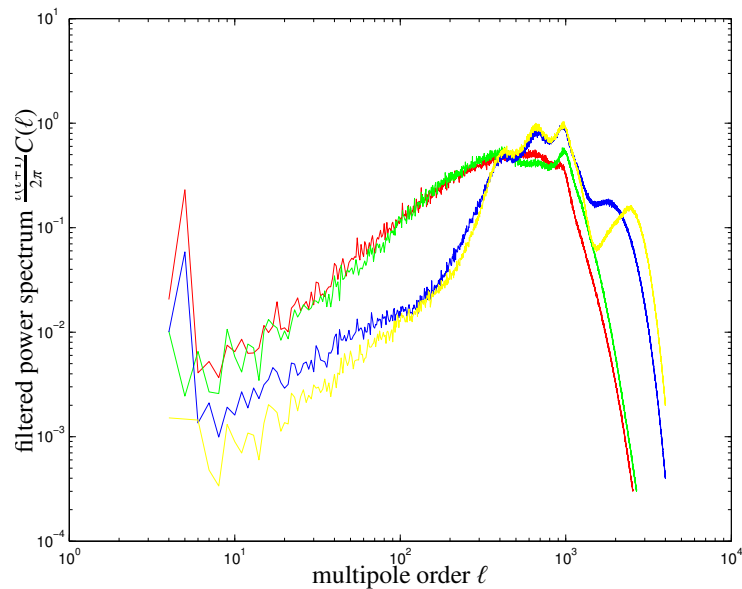


Figure 8.15.: Power spectra $C(\ell)$ of the filtered and co-added maps, where the filter kernels are derived for the parameters $(\theta_c, \lambda) = (4'0, 1.0)$, for the matched filter and the COS data set (red line), for the matched filter and the GAL data set (green line), for the scale-adaptive filter and the COS data set (blue line) and for the scale-adaptive filter and the GAL data set (yellow line).

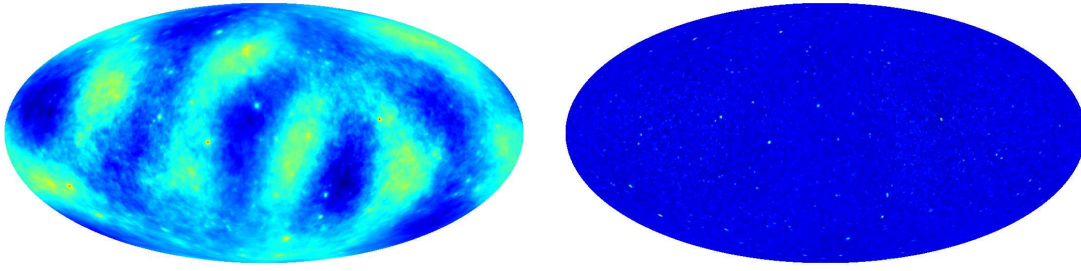


Figure 8.16.: Low- ℓ fluctuations in an all-sky map filtered with the matched filter (left panel) and for the scale-adaptive filter (right panel). The filter kernels have been derived for detecting King-profiles with (pathological) values $(\theta_c, \lambda) = (32', 0, 0.6)$.

matched filter and the peaks are situated on much flatter background. In order to avoid numerical difficulties it is advisable to discard multipoles below $\ell \lesssim 10$ altogether.

8.6. Distribution of peculiar velocities

In this section, I give the distribution of peculiar velocities in PLANCK's SZ-cluster sample, which is an important guide for kinetic SZ-follow ups. As Fig. 8.17 indicates, the distribution of peculiar velocities are well approximated by a Gaussian with zero mean and standard deviation $\sigma_{\text{vel}} \approx 300$ km/s. For a dedicated search for the kinetic SZ-effect in PLANCK's SZ-cluster sample, velocities are drawn from this distribution, hence cluster bulk motions up to 300 km/s can be expected in 68% of all cases and velocities in excess of 1000 km/s only for 11 to 16 objects, depending on the filtering scheme.

8.7. Summary and conclusion

The properties of the likelihood maps and of the cluster catalogues following from applying matched and scale-adaptive filtering to the simulated flux maps are characterised in detail. According to my simulation, PLANCK can detect a number of ≈ 6000 clusters of galaxies in a realistic observation with Galactic foregrounds (compared to over 8000 clusters if only the CMB and instrumental noise were present), which does not confirm the high numbers claimed by analytic estimates.

- The noise properties of the filtered and co-added maps was examined in detail. It was found that the noise is very close to Gaussian after filtering, despite the fact that the initial flux maps had considerable anisotropic non-Gaussian features and despite the fact that the noise is highly structured and anisotropic on the cluster scale. Quantitatively, the variance of the filtered maps is smaller compared to the prediction based on the cross- and autocorrelation functions of the maps convolved with the filter. This discrepancy, which amounts to $\approx 10\%$ is due to numerics, but has the effect that significances of peaks are slightly underestimated. The cluster detectability as a function of filter parameters showed that the matched filter performs better on compact objects, where its delivered significance depends strongly on the choice of λ . The scale-adaptive filter works well on extended objects and is relatively insensitive to λ .
- The physical properties of the detected SZ-cluster sample made in terms of mass M , redshift z and integrated Comptonisation \mathcal{Y} : The cluster population in the mass-redshift plane is fairly well defined, and the marginalisation over the mass resulted most of the clusters being detected at redshifts of $z \approx 0.2$, where the distribution starts decreasing to values of $z \approx 0.8$, where no clusters are detected. The distribution of detected SZ-clusters in mass M confirmed that the high-mass end of the Press-Schechter function is well sampled, that most of the clusters detected have masses $\approx 2.5 \times 10^{14} M_{\odot}/h$ and that clusters of lower mass are increasingly difficult to detect.

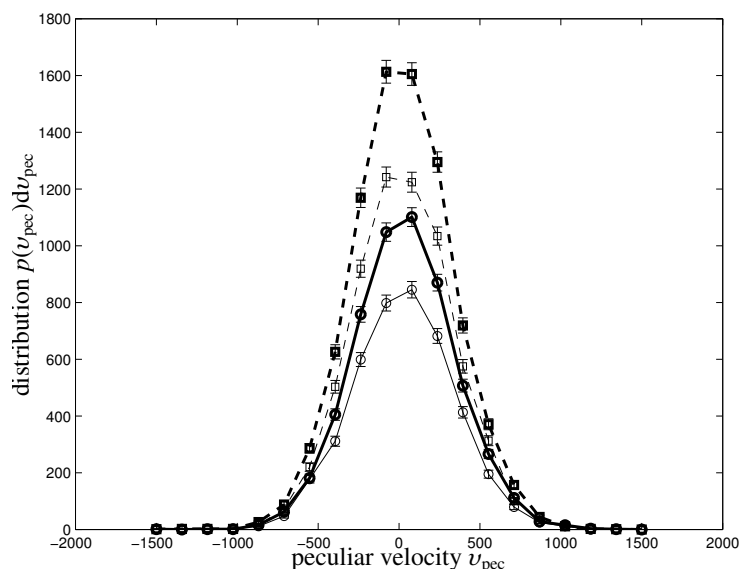


Figure 8.17.: Number $n(u_{\text{pec}})du_{\text{pec}}$ of clusters, for the matched filter (solid line, circles) in comparison to the scale-adaptive filter (dashed line, squares). Again, the detections in a data set containing the CMB, both SZ-effects and instrumental noise (thick lines, closed symbols) are compared to a data set containing all Galactic foregrounds in addition (thin lines, open symbols).

- The position accuracy is better than $10'$ in half of the cases, which is sufficient for X-ray follow-up studies, but the distribution exhibits a tail towards high discrepancies between the cluster position and the position of the peak in the likelihood map.
- The investigation of the spatial distribution, especially in ecliptic latitude showed that the distribution of clusters gets increasingly uniform with increasing detection threshold. This is due to the fact that the filtered and co-added maps exhibit long-wavelength variations due to insufficient filtering at low multipoles.

The simulation as presented in the last chapters has a number of shortcomings that may affect the SZ-sensitivity:

- It was assumed for reasons of computational feasibility that all Galactic foregrounds had isotropic spectral properties. While this is an excellent approximation for the CMB, Galactic components can be expected to exhibit spatially varying spectral properties. For example, the spectral index of the Galactic synchrotron emission is likely to change with the properties of the population of relativistic electrons and the magnetic field and the spectrum of thermal dust changes with the dust temperature. The filter construction as it would be applicable to those cases as well despite the fact that at fixed angular scale π/ℓ , the cross power spectrum $C_{\nu_i\nu_j}(\ell)$ between frequencies ν_i and ν_j ceases to be a good description of the variance contained in the $a_{\nu_i\nu_j}(\ell m)$ -coefficients.
- I did not include ICM physics beyond adiabaticity. Cooling processes in the centres of clusters give rise to cool cores, which can be shown to boost the line-of-sight Comptonisation y by a factor of $\sim 2 - 3$. The volume fraction occupied by such a cool core is very small compared to the entire cluster and hence the total integrated Comptonisation \mathcal{Y} does not change significantly. For a low-resolution observatory like PLANCK, the primary observable is \mathcal{Y} , and for that reason, SZ-observations carried out with PLANCK should not be affected by cool cores. A further complication is the existence of non-thermal particle populations in the ICM, but their contribution to the SZ-flux modulation is very small.
- There is a serious issue concerning completeness. The population of detections in the M - z suggests that low-mass clusters at redshifts $z < 0.1$ should be detectable by PLANCK. This particular region of the M - z -plane is not covered by the SZ-map construction, but PLANCK would certainly add detections in this particular region of the M - z -plane.

- Extragalactic point sources were excluded from the analysis due to poorly known spectra and clustering properties. In the simplest case of homogeneously distributed sources, there is a Poisson fluctuation in the number of point sources inside the beam area, which causes an additional noise component with power spectrum $C(\ell) \propto \ell^2$ similar to uncorrelated pixel noise. If these sources have similar spectral properties, they could be efficiently suppressed by the linear combination of observations at different frequencies.
- I did to attempt to simulate effects arising in the map making process and complications due to the $1/f$ -noise. So far it has not been investigated how well small structures can be reconstructed from time-ordered data streams. The map-making algorithms are chiefly optimised to yield good reconstructions of the CMB fluctuations by recursively minimising the noise, but to my knowledge the reconstruction of compact objects like SZ-clusters or minor planets has not been simulated for these algorithms. At the cluster scale, the dominating noise component is uncorrelated pixel noise, so that the contamination by $1/f$ -noise does not play a role on these scales.
- Gaps in the data are a serious issue for the filtering schemes: Blank patches in the observed sky cause the power spectra $C_{\nu_1\nu_2}(\ell)$ at different multipole order ℓ to be coupled due to convolution with the sky window function. This is due to the fact that the $Y_{\ell m}(\theta, \phi)$ -basis ceases to be an orthonormal system if the integration can not be carried out over the entire surface of the celestial sphere. Because the linear combination coefficients are determined separately for each multipole moment ℓ from the inverse of the covariance matrix $C_{\nu_1\nu_2}(\ell)$, correlations between the covariance matrices at differing ℓ are likely to yield an insufficient reduction of foregrounds.
- Galactic templates, especially the carbon monoxide map and the free-free map, are restricted to relatively low values in ℓ and do not extend to high multipoles covered by PLANCK. For that reason, foreground subtraction at high values of ℓ is likely to be more complicated in real data. Furthermore, one should keep in mind that the frequencies above 100 GHz are a yet uncharted territory and although the existence of an unknown Galactic emission component seems unlikely, the extrapolation of fluxes by two to three orders of magnitude in frequency may fail.

Comparing my simulation to other works is difficult because competing papers concentrate mostly on single aspects of SZ-observations with PLANCK, partly employ different cosmological models or use outdated information about PLANCK sensitivities and mission characteristics. The earliest works addressing SZ-observations with PLANCK use cluster number densities from a Press-Schechter-type mass function, determine the integrated Comptonisation \mathcal{Y} from the cluster mass M with a fixed baryon fraction Ω_B/Ω_M and temperatures following from spherical collapse theory. Analytic estimates of PLANCK's SZ-capabilities have been the subject of many papers, e.g. [Aghanim et al. \(1997\)](#) and [Kay et al. \(2001\)](#), who impose (different) flux thresholds and, in the case of [Bartelmann \(2001\)](#), require the Comptonisation to exceed the fluctuations of the Comptonisation background by a certain value. These analyses estimate the number of detectable clusters to range between 10^4 and 4×10^4 and draw important conclusions for X-ray and lensing follow-up studies.

The very interesting papers written by [Sanz et al. \(2001\)](#) and [Herranz et al. \(2002\)](#), who developed the concept of matched and scale-adaptive multifiltering based on an extremal principle for flat topologies and Fourier-decomposition as the harmonic system, concentrate mainly on filter construction. They employ analytic SZ-profiles and use simplified models for the instrumental noise. Their work constitutes the basis of my analysis, which incorporates quite a number of improvements ranging from baryonic physics, foreground components and instrumental imperfections. ([Herranz et al. 2002](#)) advocate a number of $\approx 10^4$ clusters to be detectable by PLANCK. Compared to this number, my analysis falls short by a factor of two.

A serious competitor is the paper by [Geisbüsich et al. \(2004\)](#). The filter scheme employed in the paper by Geisbüsich et al. is the powerful harmonic-space maximum entropy method introduced by [Stolyarov et al. \(2002\)](#). Its computational demand is much higher than matched and scale-adaptive filtering: In fact, the computations presented in this work can be run on a notebook-class computer. The-SZ signal they put into the simulation is determined from idealised scaling relations and uses spherically symmetric analytic profiles. Furthermore, this method is optimised for component separation rather than the detection of individual objects. In addition, instrumentation issues such as non-isotropic detector noise are not properly incorporated into the simulation and their modelling of Galactic foregrounds is not in concordance with WMAP observations (see [Bennett et al. 2003](#)). They find a total number of up to 1.5×10^4 clusters depending on the power spectrum normalisation σ_8 and the M - T -relation, and their distribution

in redshift z is quite similar in shape compared to mine - neither of us finds high-redshift clusters beyond $z = 1$. A grand result is their extraction of the SZ power spectrum, which my analysis due to its focus on the detection of individual peaks is not able to deliver. It should be kept in mind, however, that the component separation method, despite its prowess, assumes prior approximate knowledge of the emission component's power spectra, which are only partially available at HFI frequencies above $\nu = 100$ GHz.

In conclusion, the simulation presented in the last four chapters demonstrates the abilities of PLANCK with respect to detecting Sunyaev-Zel'dovich clusters of galaxies even in the presence of anisotropic non-Gaussian noise components with complicated spectral dependences. Despite the fact that the high number of detections claimed by analytical estimates need to be adjusted, it was shown that the numerical tools for analysing the cross- and autocorrelation properties of all PLANCK channels and for filtering the data work reliably up to the high multipoles of $\ell = 4096$ considered here. The PLANCK catalogue of SZ-clusters of galaxies will surpass X-ray catalogues (e.g. the REFLEX catalogue compiled by [Böhringer et al. 2004](#), on the basis of ROSAT data) in numbers as it reaches deeper in redshift and is able to detect low-mass systems. It will contribute to the determination of cosmological parameters related to structure formation and shed light on baryonic physics inside clusters of galaxies.

9. A Peano-Hilbert partition for HEALPix tessellated spheres

Abstract

A Peano-Hilbert partition for HEALPix tessellated spheres is proposed that makes quantities such as the pairwise pixel covariance matrix algorithmically accessible. For pixel numbering schemes based on Peano-Hilbert partitions geometrically nearby pixels are likewise related in the pixel numbering. When focusing on relatively short-range correlations on scales of a few beam diameters up to scales where the $1/f$ -noise becomes dominant, the covariance matrix can be brought to band diagonal shape by using pixel numbering schemes based on Peano-Hilbert partitions.

9.1. Motivation

The central quantity in many all-sky CMB data analysis tasks such as map-making (related to PLANCK, see see Natoli et al. 2001, Doré et al. 2001, Keihanen et al. 2004), foreground subtraction and estimation of power spectra (Efstathiou 2004) is the covariance matrix, which is defined as the expectation value of the product of the amplitudes a_i and a_j in pixels i and j : $A_{ij} \equiv \langle a_i a_j \rangle$. This matrix contains information about the signal, unwanted Galactic foregrounds and, most importantly, about non-isotropic, correlated and non-Gaussian noise components such as $1/f$ -noise. Sadly, despite its usefulness, A_{ij} has many unwanted properties that defy its algorithmic access:

- The matrix A_{ij} can be very large. In the case of the PLANCK-surveyor with its superior angular resolution, all-sky maps comprise as many as 5×10^7 pixels, thus, the covariance matrix (being symmetric, $A_{ij} = A_{ji}$) has approximately 1.25×10^{15} entries, which require a storage space of about 9000 terabytes, or 9 petabytes.
- In many applications one is interested in the correlation properties described by A_{ij} on relatively small angular scales, ranging from few beam diameters to scales where the $1/f$ -noise becomes dominant. By discarding correlations linking pixels on larger angular scales, A_{ij} becomes infested with zeros, but retains despite of its sparseness a complicated shape and is by no means easy to handle.

In this chapter, I propose a partition of a spherical surface based on a space filling Peano-Hilbert curve specifically tailored for the HEALPix tessellation that reduces the difficulties outlined above. The paper is structured as follows: In Sect. 9.2, properties of the HEALPix tessellation are summarised. In Sect. 9.3, I introduce Peano-Hilbert partitions and investigate their properties in Sect. 9.4. The key results are summarised in Sect. 9.5.

9.2. HEALPix tessellation

HEALPix¹ is a pixelisation of the sphere introduced by Gorski et al. (2004). HEALPix has three important properties, which are illustrated in Fig. 9.1 and which form the acronym **h**ierarchical **e**qual **a**rea **i**so-**l**atitude **p**ixelisation of the sphere.

- All pixels are of the same size, hence integrations can be carried out very efficiently.
- In HEALPix, the sphere is tessellated with twelve base pixels, that are iteratively subdivided into four smaller pixels. Due to this hierarchical ordering, maps can be easily up- and downsampled in resolution.

¹<http://www.eso.org/science/healpix>

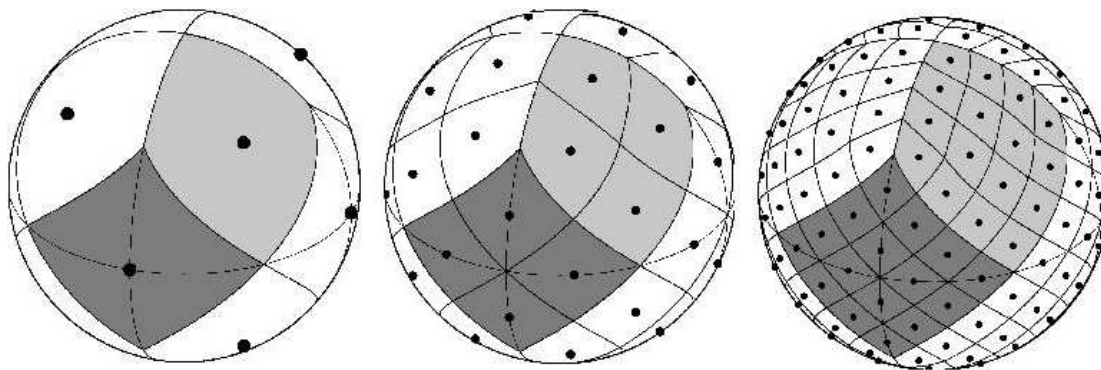


Figure 9.1. The twelve basis pixels (left panel) and the first order (48 pixels) and second order (192 pixels) refinements (centre and right panel, respectively) of the dodecaedric tessellation of the sphere used in HEALPix. The illustration above was taken from the HEALPix manual.

- The pixels are arranged in rings of constant latitude. This enables spherical harmonic transforms,

$$\tau_{\ell m} = \int d\Omega \tau(\boldsymbol{\theta}) Y_{\ell m}^*(\boldsymbol{\theta}) \leftrightarrow \tau(\boldsymbol{\theta}) = \sum_{\ell} \sum_{m=-\ell}^{\ell} \tau_{\ell m} Y_{\ell m}(\boldsymbol{\theta}), \text{ with} \quad (9.1)$$

$$Y_{\ell m}(\boldsymbol{\theta}) = \sqrt{\frac{2\ell+1}{4\pi}} \sqrt{\frac{(\ell-|m|)!}{(\ell+|m|)!}} P_{\ell m}(\cos \theta) \exp(im\phi) \quad (9.2)$$

to be computed easily: At fixed latitude θ , the $Y_{\ell m}$ -decomposition reduces to a Fourier transform, for which very fast numerical algorithms are available.

The pixels may be numbered according to two distinct schemes, the first of which numbers pixels in rings at constant latitude, such that the $d\phi$ -integration in the spherical harmonics transform can be carried out easily. The second numbering scheme takes account of the nested, hierarchical ordering, and allows for cross-referencing pixels on maps with different resolution. HEALPix was successfully employed in the analysis of CMB maps, most notably of COBE and WMAP, and has been chosen as the default pixelisation to be used for PLANCK data analysis as well.

9.3. Peano-Hilbert curves for HEALPix

Despite the usefulness of the HEALPix tessellation for spherical harmonical transform, the covariance matrix A_{ij} has a complicated shape in both HEALPix numberings. In order to make matrix manipulations of A_{ij} possible, a new pixel numbering scheme based on fractal, self-similar Peano-Hilbert partitions is proposed. A similar approach has been taken by [Dennis \(2003\)](#), who constructed a Peano-Hilbert curve running through all faces of a cube for the purpose of load balancing a parallelised global atmospheric modelling code. For HEALPix, however, one needs to construct a Peano-Hilbert curve for the dodecaedric base symmetry of HEALPix, where almost all pixels have eight neighbours, but certain pixels (eight in total) at the position where polar base pixels meet equatorial base pixels have just seven neighbours. The curve should be continuous and should link neighboring pixels such that the off-diagonals of the covariance matrix have non-zero entries.

A possible Peano-Hilbert curve for HEALPix is shown in [Fig. 9.2](#), where the zeroth order curve always links pixels on the North pole with pixels on the South pole via a pixel on the equator. The curve can be iteratively refined into four subpixels with the *Lindenmayer*-rules graphically depicted in [Fig. 9.2](#). This particular Lindenmayer-system uses three distinct base pixels, which are an effective left turn, a right turn and a straight passage through a pixel. The resulting Peano-Hilbert numbering is shown in [Fig. 9.3](#). Clearly, the fractal nature of the Peano-Hilbert partition can be seen.

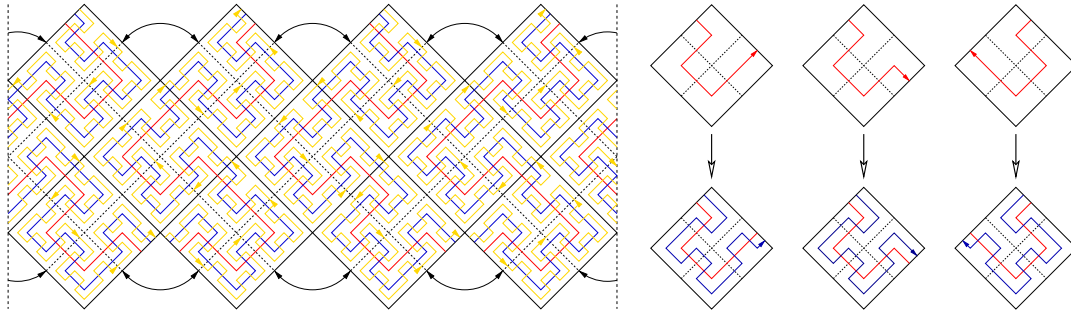


Figure 9.2.: Peano-Hilbert zeroth order curve (red), second order curve (blue) and third order curve (yellow) for the dodecaedric tessellation used in HEALPix (left panel), and the Lindenmayer rules for recursive refinement of the three basis pixels (right panel).

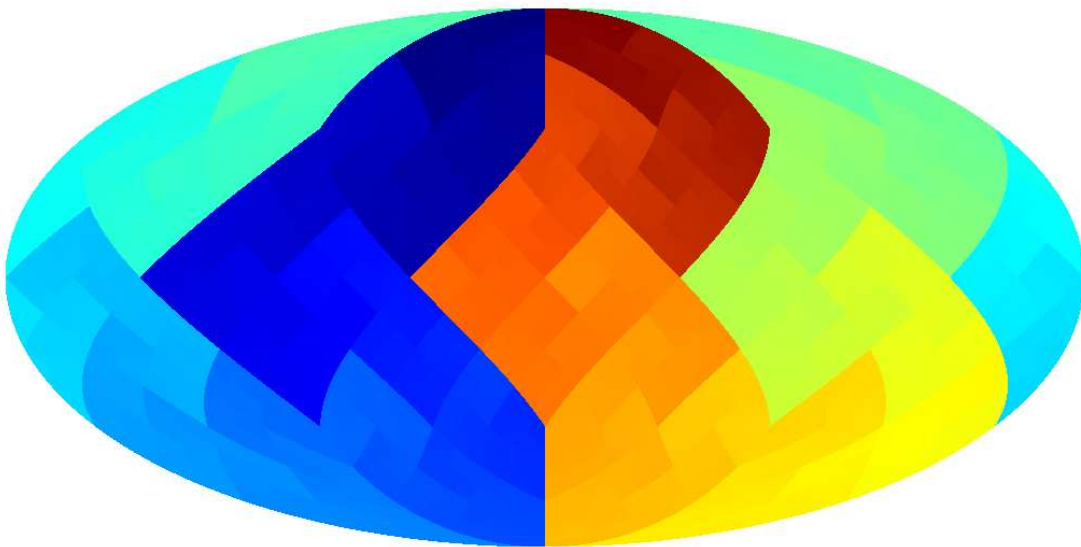


Figure 9.3.: A large HEALPix map ($N_{\text{side}} = 128$) with the Peano-Hilbert partition. The shading reflects the pixel number.

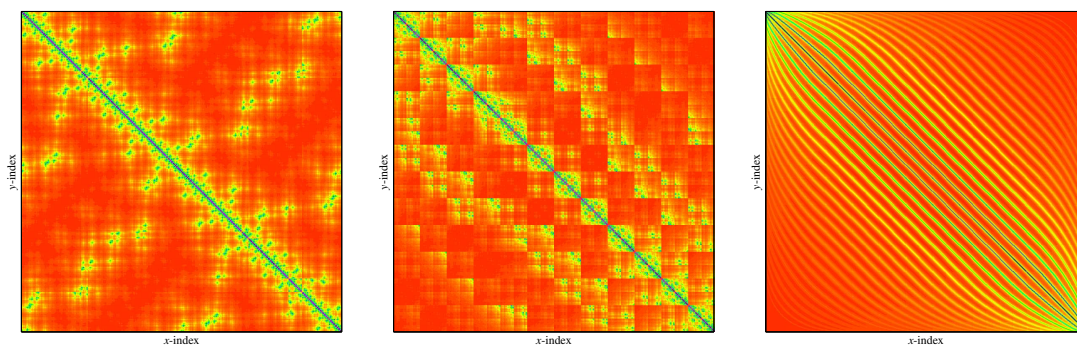


Figure 9.4.: Shape of covariance matrices for correlations $C(\theta_{\text{arc}})$ proportional to θ_{arc}^{-1} where θ_{arc} denotes the separation between two pixels measured along a great circle, for the Peano-Hilbert partition (left panel), the nested numbering scheme (centre panel) and the ring numbering scheme (right panel). These images followed from sky maps with $N_{\text{side}} = 8 \rightarrow N_{\text{pix}} = 768$.

9.4. Properties of the Peano-Hilbert ordering

The most important question is the performance of the Peano-Hilbert partition in comparison to the two existing HEALPix numbering schemes with respect to locality. In Fig. 9.4, the covariance matrix is plotted for each of the respective pixel numbering schemes for correlations that decrease with the inverse of the angular separation θ_{arc} between two pixels, measured along a great circle. An example for such a correlation is the troublesome $1/f$ -noise. The Peano-Hilbert partition shows a good performance in comparison to the nested scheme: high correlation amplitudes are predominantly found in the vicinity of the diagonal, with few islands at large distances away from the diagonal. The nested scheme, being intrinsically fractal as well, exhibits broad stripes of large correlation amplitudes parallel to the diagonal. Finally, the ring scheme shows a large number of fine stripes parallel to the diagonal, at even larger distances. From this it can be concluded that the Peano-Hilbert partition is the pixel numbering of choice when manipulating the pairwise pixel covariance matrix.

Fig. 9.5 analyses the qualitative findings of Fig. 9.4 in a more quantitative manner. In order to compare the locality of the Peano-Hilbert partition with the (fractal) nested numbering scheme, a numerical experiment has been performed, where $N = 10^4$ pairs of points on the sphere with fixed angular separation θ_{arc} were randomly generated: Two vectors \mathbf{e}_1 and \mathbf{e}_2 situated on the unit sphere with $\mathbf{e}_1 = (0, 0, 1)$ pointing to the North pole and $\mathbf{e}_2 = (\sin \theta_{\text{arc}}, 0, \cos \theta_{\text{arc}})$ with angular separation θ_{arc} from \mathbf{e}_1 on the $\phi = 0$ meridian were rotated in three successive Euler rotations around the z -axis, the x -axis and again around the z -axis for randomly drawn angles $\alpha, \beta, \gamma \in [0 \dots 2\pi]$. In this way, randomly positioned pairs \mathbf{e}_i of points on the unit sphere with fixed angular separation can be produced:

$$\mathbf{e}'_i = \begin{pmatrix} \cos \gamma & \sin \gamma & 0 \\ -\sin \gamma & \cos \gamma & 0 \\ 0 & 0 & 1 \end{pmatrix} \begin{pmatrix} 1 & 0 & 0 \\ 0 & \cos \beta & \sin \beta \\ 0 & -\sin \beta & \cos \beta \end{pmatrix} \begin{pmatrix} \cos \alpha & \sin \alpha & 0 \\ -\sin \alpha & \cos \alpha & 0 \\ 0 & 0 & 1 \end{pmatrix} \mathbf{e}_i \text{ with } i \in \{1, 2\}. \quad (9.3)$$

For resulting pairs of points, the logarithmic separation Δ in pixel number in the nested numbering scheme and along the Peano-Hilbert curve was computed and the distribution of separations $p(\Delta)d\Delta$ was examined. As Fig. 9.5 suggests, the distribution of Δ peaks at slightly smaller values of Δ , although the difference between the two curves is not large. Similarly, Fig. 9.6 shows the distribution $p(\Delta, \theta_{\text{arc}})d\Delta$ as a function of both Δ and θ_{arc} . Especially at large angular separations θ_{arc} , the distribution of Δ shows a peculiar increase at large Δ in case of the nested numbering, which is reduced in the Peano-Hilbert numbering. This hints at the fact that on large scales the Peano-Hilbert curve has better properties with respect to locality than the nested numbering scheme.

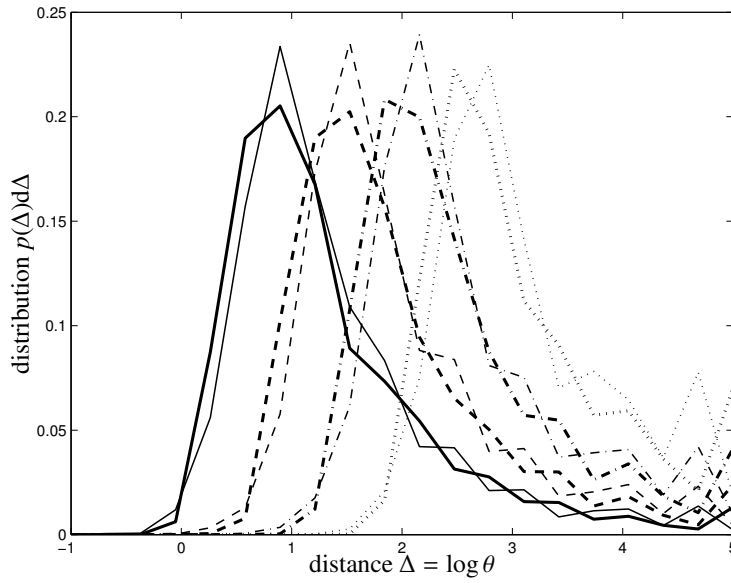


Figure 9.5.: Distribution $p(\Delta)d\Delta$ of logarithmic difference in pixel number Δ for a given separation along a great circle θ_{arc} , of the Peano numbering scheme (thick lines) in comparison to the nested numbering scheme (thin lines). Distributions are given for $\theta_{arc} = 1$ pixel (solid line), $\theta_{arc} = 2$ pixels (dashed line), $\theta_{arc} = 4$ pixels (dash-dotted line) and $\theta_{arc} = 8$ pixels (dotted line).

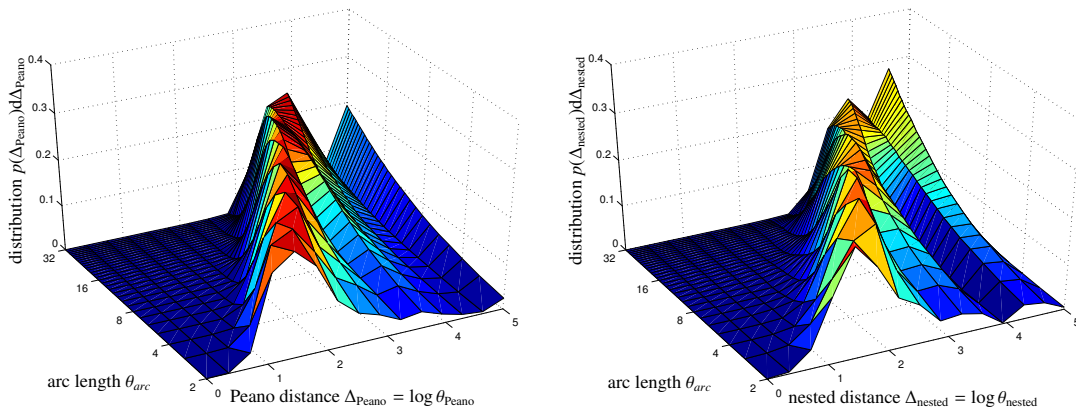


Figure 9.6.: Distribution $p(\Delta, \theta_{arc})d\Delta$ of logarithmic difference in pixel number Δ as a function of geometric pixel separation θ_{arc} , for the Peano numbering scheme (left panel) and for the nested numbering scheme (right panel).

9.5. Summary

A new pixel numbering scheme for the HEALPix tessellation of the sphere is proposed, which is based on a fractal Peano-Hilbert curve. It could be shown that the pairwise pixel covariance matrix acquires an approximate band-diagonal shape in this numbering, if long-range correlations are discarded. In this respect, the Peano-Hilbert numbering is superior to the two existing numbering schemes, because efficient algorithms for manipulating band-diagonal matrices exist such that computing the determinant or deriving the inverse of the covariance matrix becomes feasible, even for the large number of pixels of contemporary CMB observatories.

10. Redshift estimation of clusters by wavelet decomposition of their SZ-morphology

Abstract

A method for estimating redshifts of galaxy clusters based solely on resolved Sunyaev-Zel'dovich (SZ) images is proposed. Given a high resolution SZ-cluster image (with FWHM of $\sim 1'$), the method indirectly measures its structure related parameters (amplitude, size, etc.) by fitting a model function to the higher order wavelet moments of the cluster's SZ-morphology. The applicability and accuracy of the wavelet method is assessed by applying it to maps of a set of clusters extracted from hydrodynamical simulations of cosmic structure formation. The parameters, derived by a fit to the spectrum of wavelet moments as a function of scale, are found to show a dependence on redshift z that is of the type $x(z) = x_1 \exp(-z/x_2) + x_3$, where the monotony of this functional behaviour and the non-degeneracy of those parameters allow inversion and estimation of the redshift z . The average attainable accuracy in the z -estimation relative to $1 + z$ is $\sim 4 - 5\%$ out to $z \approx 1.2$, which is comparable to photometric redshifts. For single-frequency SZ-interferometers, where the ambient fluctuating CMB is the main noise source, the accuracy of the method drops slightly to $\langle \Delta z / (1 + z) \rangle \sim 6 - 7\%$. Other complications addressed include instrumental noise, cold cores and systematic trends in baryon fraction with cluster mass.

10.1. Introduction

Inverse Compton scattering of cosmic microwave background (CMB) photons off thermal electrons within the hot intra-cluster medium (ICM) of galaxy clusters produce fluctuations in the surface brightness of the CMB, an effect known as the thermal Sunyaev-Zel'dovich (SZ) effect (e.g. [Sunyaev & Zel'dovich 1972, 1980](#), [Rephaeli 1995](#)). Imaging clusters of galaxies through their SZ-signature has, until recently, been a very challenging undertaking. To date, the development of detectors and new techniques have allowed high quality interferometric imaging of more than fifty clusters of galaxies ([Carlstrom et al. 2002](#)), despite incomplete coverage of the Fourier plane. In the foreseeable future, the availability of detectors in the microwave regime with angular resolutions surpassing $1'$ and sensitivities below μK (e.g., the *South Pole Telescope*, described in detail in [Carlstrom et al. 2002](#)), will probe the hot plasma in galaxy clusters out to large redshifts providing SZ-based wide field galaxy cluster catalogues and yielding a multitude of information about cluster formation and the cosmological model ([Birkinshaw 1999](#)).

In particular, the abundance of clusters as a function of redshift has been shown to be a very sensitive probe of the cosmological model ([Eke et al. 1998](#), [Henry 2000](#)). The near independence of the line-of-sight SZ-amplitude on cluster redshift makes the SZ-effect the main tool for detecting galaxy clusters at high redshifts, $0.5 \lesssim z \lesssim 2$ (the upper limit depends on cosmology quite sensitively). This range of redshifts is especially important for probing the nature of the dark energy of the universe, since during this era it is expected to evolve rapidly until it eventually dominates over the other cosmological fluids. In order to obtain precise constraints on cosmological models it is essential to have accurate measurements of the redshift distribution of galaxy clusters (see [Haiman et al. 2001](#)).

Normally, one determines the distance to the cluster by photometric or spectroscopic observations of the cluster member galaxies. Unfortunately, this is a very challenging and time consuming task, in particular, when one considers the very large number of mostly high redshift clusters expected to be observed with sensitive future SZ-instruments – The PLANCK satellite alone is expected to detect about 10^4 clusters ([Bartelmann 2001](#)). In order to replace photometric follow-ups I aim at inferring the distance to a cluster from SZ-data alone for a future generation of experiments with increased angular resolution of about $1'$.

Theoretically, the cold dark matter (CDM) hierarchical clustering paradigm predicts a universal profile for dark matter halos that depends only on two parameters: core radius and density ([Navarro et al. 1995](#)). In addition, the same theory provides a very simple recipe for the mass accretion history of a certain halo as a function of its

formation and observation redshift (Wechsler et al. 2002, van den Bosch 2002, Zhao et al. 2003). Using these relations together with simple assumptions like hydrostatic equilibrium and isothermality, one can expect that in the framework of the spherical collapse model the observable SZ-flux and apparent size should provide measures of the cluster's mass and distance.

Indeed, using scaling relations, Diego et al. (2003) have demonstrated the viability of determining reliable *morphological redshifts* and examined different SZ-observables with respect to their distance sensitivity. Among those observables, they showed that the cluster apparent size and central amplitude are promising distance indicators, once their degeneracy is broken.

The main goal of this work is to derive redshifts of clusters based solely on their resolved SZ-images by modeling the evolution of their structural parameters with redshift from the data set itself. This phenomenological approach does not depend on a priori assumptions about scaling relations that are valid only for spherically symmetric and relaxed systems.

Specifically, the structural morphology of the cluster's pressure profile in an SZ-observation is characterised by wavelet analysis.¹ I am able to show that there is a simple relation between the distribution of moments over various scales in wavelet space and the cluster properties which can be described with simple phenomenological functions. Furthermore, the parameters of these functions are shown to follow a well defined and simple redshift dependence. Wavelet analysis has been chosen because it maintains the scale and positional information of cluster morphology, hence, it makes isolation and suppression of various unwanted contributions to the observed signal possible while it reliably upholds the underlying behaviour. We note however, that Fourier space analysis could in principle yield very similar results.

Hydrodynamically simulated clusters are used to demonstrate the method and to set limits on the redshift uncertainty expected in this approach. The simulated clusters used in the analysis are close to virialisation, e.g. merging systems are excluded. Under this restriction, both the relation between the observed quantity and the cluster physical parameters as well as the structural parameters are well defined. In addition, simulated clusters ignore radiative and feedback processes, the effect of which is discussed later in the paper.

In the observational application, the evolution of the structural parameters following from wavelet decomposition could be calibrated from a (relatively small) training set of high quality SZ-clusters with known (photometric/spectroscopic) redshifts.

Our method relies crucially on the availability of resolved SZ-cluster images. Therefore, throughout the paper I assume an instrumental resolution of $1'$, where massive clusters should be resolved even at the largest redshifts considered here. Indeed, future instruments such as the South Pole Telescope² (Carlstrom et al. 2002) or the Atacama Cosmology Telescope³ are designed to yield observations of up to 10^4 galaxy clusters with masses $\gtrsim 10^{14} M_{\odot}$ ($1 \mu\text{K}$ sensitivity) and $\approx 1'$ resolution.

This article is organised as follows: After basic definitions concerning the SZ-effect in Sect. 10.2 and wavelets in Sect. 10.3, the simulations are outlined in Sect. 10.4. The capability of wavelets with respect to distance estimation is examined in Sect. 10.5. Possible systematics are addressed in Sect. 10.6. A summary of the techniques in Sect. 10.7 and of the results in Sect. 10.8 concludes the article.

10.2. Sunyaev-Zel'dovich definitions

The SZ-effect has been described in detail by many authors (for a comprehensive review, see Birkinshaw 1999); here I briefly review its main aspects. The SZ-effect arises because CMB photons experience Compton-scattering off electrons of the diffuse intra-cluster plasma. The CMB spectrum is modulated as photons are redistributed from the low-frequency part of the spectrum below 217 GHz to higher frequencies. The change in thermodynamic CMB temperature due to the thermal SZ-effect is

$$\frac{\Delta T}{T}(\phi) = y(\phi) \left(x \frac{e^x + 1}{e^x - 1} - 4 \right) \approx -2y(\phi) \quad \text{for } x \ll 1, \quad (10.1)$$

¹There are also various ways of characterising the cluster's density profile in an SZ-observation that are more or less susceptible to noise, for instance the fitting of a β -profile (Cavaliere & Fusco-Femiano 1978) to the electron density.

²<http://astro.uchicago.edu/spt/>

³<http://www.hep.upenn.edu/~angelica/act/act.html>

where $x = hv/k_B T_{\text{CMB}}$ is the dimensionless frequency. In the Rayleigh-Jeans limit ($x \ll 1$), the change in temperature is asymptotically equal to $-2y(\phi)$. The SZ-amplitude at location ϕ , which is known as the Comptonisation parameter $y(\phi)$, is defined as the line-of-sight integral of the temperature-weighted thermal electron density:

$$y(\phi) = \frac{\sigma_T k_B}{m_e c^2} \int dl n_e(\phi, l) T_e(\phi, l). \quad (10.2)$$

where m_e , c and k_B denote electron mass, speed of light and Boltzmann's constant, respectively. $T_e(\phi, l)$ and $n_e(\phi, l)$ are electron temperature and electron number density at position ϕ and distance l .

10.3. Wavelets

10.3.1. Wavelet definitions

During the last decade, wavelet analysis has become a popular tool in various data analysis and image processing applications. The main appeal of wavelet functional bases stems from their simultaneous localisation of a signal in both the wavenumber and position domain, where they make orthogonal and complete projections on modes belonging to both spaces possible. In particular, the discrete wavelet families, by virtue of their constituting a complete basis, provide a unique and fast decomposition of the images into wavelet expansion coefficients. Statistics in terms of the q^{th} moments of the distribution of wavelet coefficients as a function of scale compresses the signal contained in an image into a small number of parameters and yields information surpassing that derived in traditional Fourier analysis. A particularly nice example of wavelets applied in an astrophysical context is given in the paper by [Pierpaoli et al. \(2004\)](#), who proposed wavelet-based method to construct SZ-images from multifrequency CMB data.

Following [Daubechies & Bates \(1993\)](#) and [Muzy et al. \(1993\)](#), the wavelet transform of a 2-dimensional image is defined as a convolution of the function $y(\mathbf{x})$ to be analysed with the wavelet $\psi_\sigma(|\mathbf{x} - \boldsymbol{\mu}|)$:

$$\chi(\boldsymbol{\mu}, \sigma) = \int d^2x y(\mathbf{x}) \cdot \psi_\sigma(|\mathbf{x} - \boldsymbol{\mu}|). \quad (10.3)$$

High values for $\chi(\boldsymbol{\mu}, \sigma)$ are obtained in case of a match between the features of $y(\mathbf{x})$ and the wavelet $\psi_\sigma(\mathbf{x})$ at position $\boldsymbol{\mu}$ and scale σ . From the wavelet expansion coefficients $\chi(\boldsymbol{\mu}, \sigma)$ on scale σ at location $\boldsymbol{\mu}$ one obtains the wavelet moments $X_q(\sigma)$ by integration over all displacements $\boldsymbol{\mu}$:

$$X_q(\sigma) = \int d^2\boldsymbol{\mu} |\chi(\boldsymbol{\mu}, \sigma)|^q. \quad (10.4)$$

The exponent $q \in \mathbb{N}$ defines the order of the wavelet moment $X_q(\sigma)$. Values for q equal or larger than 2 allow noise suppression. The logarithm $\ln X(\sigma, q)$ of the wavelet moment as a function of logarithmic scale $\ln \sigma$ constitutes the wavelet spectrum. The $X_q(\sigma)$ -statistic is the main tool used in this study for characterising the morphology of SZ-clusters.

10.3.2. Application of wavelets to a cluster profile

10.3.2.1. Analytic wavelet transform of a cluster y -profile

In order to illustrate my idea of determining cluster sizes via wavelet decomposition, the wavelet transform of a King profile, which is known to describe the SZ-morphology of clusters to first order, is performed. As an analysing wavelet, the Mexican-hat wavelet was chosen for simplicity.

It is favourable to compute the convolution in the definition of $\chi(\boldsymbol{\mu}, \sigma)$ in the Fourier domain. By virtue of eqn. (10.5),

$$\chi(\boldsymbol{\mu}, \sigma) = \int d^2x y(\mathbf{x}) \psi_\sigma(\mathbf{x} - \boldsymbol{\mu}) = (2\pi)^2 \int d^2k Y(\mathbf{k}) \Psi_\sigma(-\mathbf{k}) \exp(i\mathbf{k}\boldsymbol{\mu}), \quad (10.5)$$

the convolution reduces to a mere multiplication of the Fourier transforms $Y(\mathbf{k})$ and $\Psi_\sigma(\mathbf{k})$ of the image $y(\mathbf{x})$ and the wavelet $\psi_\sigma(\mathbf{x})$, respectively. Restricting the order of the wavelet moment to $q = 2$ and inserting the convolution

theorem (10.5) into the definition (10.4) yields:

$$X_2(\sigma) = (2\pi)^4 \int d^2\mu \left| \int d^2k Y(\mathbf{k}) \Psi_\sigma(-\mathbf{k}) \exp(i\mathbf{k}\mu) \right|^2 = (2\pi)^6 \int d^2k |Y(\mathbf{k})|^2 |\Psi_\sigma(\mathbf{k})|^2, \quad (10.6)$$

where the replacement $|\Psi_\sigma(-\mathbf{k})|^2 = |\Psi_\sigma(\mathbf{k})|^2$ holds for real wavelets.

The Mexican-hat wavelet is defined as the negative Laplacian of a Gaussian:

$$\psi_{\text{MH}}(\mathbf{x}) = \psi_{\text{MH}}(x) = -\nabla_x^2 \left[\frac{1}{2\pi\sigma^2} \exp\left(-\frac{\mathbf{x}^2}{2\sigma^2}\right) \right], \quad (10.7)$$

whereof the Fourier transform $\Psi_{\text{MH}}(\mathbf{k})$ is derived by twofold partial integration:

$$\Psi_{\text{MH}}(k) = \int \frac{d^2x}{(2\pi)^2} \psi_{\text{MH}}(x) \exp(-i\mathbf{k}\mathbf{x}) \quad (10.8)$$

$$= \frac{1}{(2\pi)^2 \sigma^6} \int r dr (2\sigma^2 - r^2) \exp\left(-\frac{r^2}{2\sigma^2}\right) J_0(kr) \quad (10.9)$$

$$= \frac{k^2}{(2\pi)^2} \cdot \exp\left(-\frac{k^2\sigma^2}{2}\right), \quad (10.10)$$

where the azimuthal symmetry and the definition of the zeroth order Bessel function of the first kind, $2\pi J_0(kr) = \int_0^{2\pi} d\phi \exp(ikr \cos \phi)$ was used in the first step. Thus, the Fourier transform of the wavelet, $\Psi_\sigma(k)$, is given by the Hankel transform of the Laplacian of a Gaussian.

For the determination of $Y(\mathbf{k})$, I assume that the projected thermal electron density can be described by a spherically symmetric King profile, i.e. a β -model (Cavaliere & Fusco-Femiano 1978) with $\beta = 1$, core radius r_c and central value of the Comptonisation parameter y_0 :

$$y(\mathbf{x}) = y(r) = y_0 \left[1 + \left(\frac{r}{r_c} \right)^2 \right]^{-1}. \quad (10.11)$$

Then, the Fourier transform is easily computed:

$$Y(k) = \int \frac{d^2x}{(2\pi)^2} y(x) \exp(-i\mathbf{k}\mathbf{x}) = \frac{y_0 r_c^2}{2\pi} \int dr \frac{r}{r_c^2 + r^2} J_0(kr) = \frac{y_0 r_c^2}{2\pi} \cdot K_0(kr_c), \quad (10.12)$$

where in eqn. (10.12) the definition of the zeroth order modified Bessel function of the second kind $K_0(kr_c)$ was inserted.

Substituting eqns. (10.10) and (10.12) into eqn. (10.6) and exploiting the azimuthal symmetry of the functions $y(x)$ and $\psi(x)$ yields an analytic integral for $X_2(\sigma)$:

$$X_2(\sigma) = 2\pi y_0^2 r_c^4 \int_0^\infty dk k^5 \exp(-\sigma^2 k^2) K_0^2(kr_c). \quad (10.13)$$

After evaluation of the integral in eqn. (10.13), the wavelet transform of the β -profile reads as follows:

$$X_2(\sigma) = \frac{\pi^{3/2} y_0^2}{2r_c^2} \alpha^6 \cdot \mathcal{G}_{2,3}^{3,1} \left(\alpha^2 \middle| \begin{matrix} -2 \\ 000 \end{matrix} \right), \quad (10.14)$$

where $\alpha = r_c/\sigma$ has been substituted. The function \mathcal{G} is Meijer's G-function, the exact definition of which is given by Gradshteyn & Ryzhik (1994). It is an interesting consistency to note that apart from the normalisation, the functional shape of eqn. (10.14) only depends on α , i.e. on the core radius r_c expressed in units of the wavelet scale σ .

10.3.2.2. Analogous result for the analytic wavelet transform in 1-d

The analogous computation of the wavelet transform of a β -profile with the Mexican-hat wavelet in one dimension yields for $X_2(\sigma)$:

$$X_2(\sigma) = \pi y_0^2 r^2 \int_0^\infty dk k^4 \exp(-\sigma^2 k^2 - 2rk). \quad (10.15)$$

This integral can be evaluated by completing the square in the exponent to yield:

$$X_2(\alpha) = \frac{\pi y_0^2}{8r^3} \alpha^5 \left[\sqrt{\pi} \operatorname{erfcx}(\alpha) P(\alpha) - Q(\alpha) \right], \quad \text{with} \quad (10.16)$$

$$P(\alpha) = 4\alpha^4 + 12\alpha^2 + 3 \quad \text{and} \quad (10.17)$$

$$Q(\alpha) = 4\alpha^3 + 10\alpha \quad (10.18)$$

where again $\alpha = r/\sigma$ has been substituted. $\operatorname{erfcx}(\alpha)$ is the scaled complementary error function:

$$\operatorname{erfcx}(\alpha) = \exp(\alpha^2) \cdot \left(1 - \frac{2}{\sqrt{\pi}} \int_0^\alpha dt \exp(-t^2) \right). \quad (10.19)$$

The functional shape and the asymptotic behaviour of these formulae correspond well to the 2-d case discussed above.

10.3.2.3. Asymptotics of the analytical wavelet transform

The asymptotic behavior of $X_2(\sigma)$ at the limit of $\sigma \ll r_c$ can be explored by substituting the expressions given in eqns. (10.11) and (10.7) into eqn. (10.5), and exchanging, by partial integration, the function on which the Laplacian operates. In the limit of interest the Gaussian can be replaced by a Dirac- δ distribution. Substituting all of this into eqn. (10.4) yields that $\lim_{\sigma \rightarrow 0} X_2(\sigma)$ is proportional to y_0^2 and independent of σ , i.e. the normalisation of the wavelet spectrum measures the square of the central Comptonisation parameter y_0 :

$$X_2(\sigma) = \frac{32\pi}{15} \cdot \frac{y_0^2}{r_c^2} \quad \text{for} \quad \sigma \ll r_c. \quad (10.20)$$

In the opposite limit, i.e. $r_c \ll \sigma$, one can use the fact that the King-profile is highly peaked at the center and that it is convolved with a Mexican-hat wavelet guaranteeing the convergence of the integral in eqn. (10.13) at ∞ . In the limit of $r_c \rightarrow 0$ this integral is dominated by the value at $k = 0$. Therefore, one can approximate the King-profile with a Dirac- δ distribution and show that asymptotically the $\lim_{r_c \rightarrow 0} X_2(\sigma)$ is proportional to σ^{-6} :

$$X_2(\sigma) \propto \frac{y_0^2 r_c^4}{\sigma^6} \quad \text{for} \quad \sigma \gg r_c. \quad (10.21)$$

The sensitivity of the wavelet spectrum $X_2(\sigma)$ on cluster size r_c is illustrated by Fig. 10.5. The wavelet spectrum is constant for $\sigma \ll r_c$, has an r_c -dependent break and drops off asymptotically $\propto \sigma^{-6}$ for $\sigma \gg r_c$. Naturally, the scale σ at which the transition from one asymptotic regime to the other occurs, is determined by the value of r_c , i.e. the cluster size.

Motivated by this example, the wavelet moments $X_q(\sigma)$ obtained from real data (Sect. 10.5.3) will be fitted with a power law with an exponential cutoff, where the cutoff indicates the cluster size and the amplitude is proportional to some power of the central Comptonisation parameter y_0 .

10.3.2.4. Finite instrumental resolution

The influence of finite instrumental resolution can easily be incorporated by an additional factor $|B(k)|^2$ in eqn. (10.6):

$$X_2(\sigma) = (2\pi)^6 \int d^2k |Y(k)|^2 |\Psi_\sigma(k)|^2 |B(k)|^2, \quad (10.22)$$

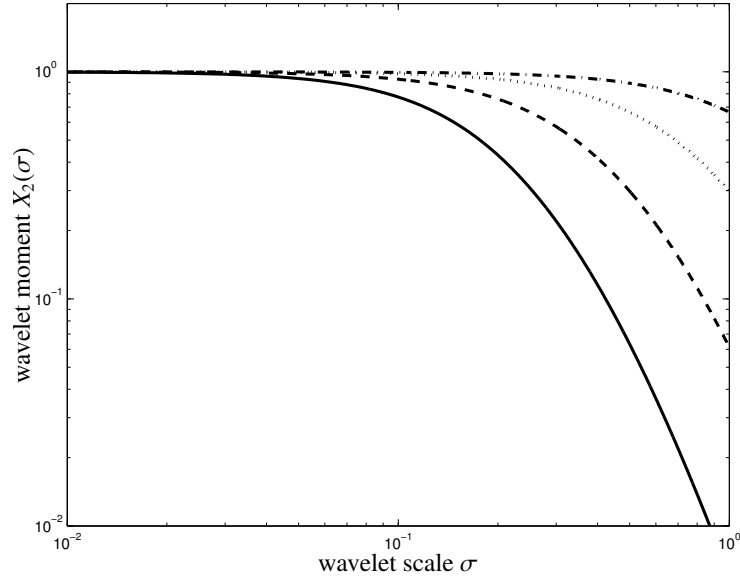


Figure 10.1.: Sensitivity of the wavelet spectrum on the cluster size: The second order wavelet moments $X_2(\sigma)$ are shown as a function of σ for various core sizes $r_c = 0.5$ (solid), $r_c = 1$ (dashed), $r_c = 2$ (dotted) and $r_c = 4$ (dash-dotted). The curves have been normalised to their asymptotic values for $\sigma \rightarrow 0$.

where $B(k)$ is the Fourier transform of the (azimuthally symmetric) beam profile $b(x)$, which is for simplicity assumed to be of Gaussian shape with FWHM = $\sqrt{8 \ln(2)} \cdot \sigma_b$:

$$B(k) = \int \frac{d^2x}{(2\pi)^2} b(x) \exp(-ikx) \text{ with} \quad (10.23)$$

$$b(x) = \frac{1}{2\pi\sigma_b^2} \exp\left(-\frac{x^2}{2\sigma_b^2}\right). \quad (10.24)$$

This effectively replaces σ in eqn. (10.14) by the harmonic mean $\sqrt{\sigma^2 + \sigma_b^2}$, which limits the range of accessible wavelet scales to $\sigma > \sigma_b$.

10.3.3. Analogy to power spectra in Fourier analysis

By interpreting the wavelet spectrum in eqn. (10.6) as the variance of the fluctuations on the scale σ , one may draw an analogy to Fourier decomposition:

$$\text{var}[y(x)] = X_2(\sigma) = (2\pi)^4 \int d^2k P(k) |\Psi_\sigma(k)|^2, \quad (10.25)$$

where $P(k) = (2\pi)^2 \langle |Y(k)|^2 \rangle$ is the Fourier power spectrum. The wavelet $\psi(x)$ now adopts the role of a filter function on scale σ . This filter function reads in real space in the case of the Mexican hat wavelet:

$$\psi_{\text{MH}}(x) = \frac{2\sigma^2 - x^2}{2\pi\sigma^6} \cdot \exp\left(-\frac{x^2}{2\sigma^2}\right). \quad (10.26)$$

Therefore, my method is equivalent to considering power spectral analysis of filtered fields and higher order Fourier space moments.

10.4. Simulations

The accuracy in the determination of redshift z was assessed by examining the performance on numerical simulations: First, simulations of cosmological structure formation including gas physics have been carried out in order to model the evolution of clusters (Sect. 10.4.1). Subsequently, maps of the Compton- y parameter have been produced by using an interpolation kernel with an adaptive smoothing length for projecting the Compton- y parameter along the line-of-sight (Sect. 10.4.2). By applying selection criteria favouring virialised systems a cluster sample was compiled (Sect. 10.4.3). Finally, aiming at realistic single frequency SZ-observations, we simulated the ambient CMB fluctuations that act as the primary source of noise (Sect. 10.4.4) and combined the resulting realisations of the CMB with the cluster maps (Sect. 10.4.5).

The assumed cosmological model is the standard Λ CDM cosmology, which has recently been supported by the WMAP satellite (Bennett et al. 2003, Spergel et al. 2003). Parameter values have been chosen as $\Omega_M = 0.3$, $\Omega_\Lambda = 0.7$, $H_0 = 100 h \text{ kms}^{-1} \text{ Mpc}^{-1}$ with $h = 0.7$, $\Omega_B = 0.04$, $n_s = 1$ and $\sigma_8 = 0.9$.

10.4.1. SPH cluster simulations

A simulation of cosmological structure formation kindly provided by V. Springel and L. Hernquist (Springel & Hernquist 2002, White et al. 2002) constitutes the basis of my analysis. In a cubical box of comoving side length $100 \text{ Mpc}/h$ with periodic boundary conditions a smoothed particle hydrodynamic (SPH) simulation comprising 216^3 dark matter particles as well as 216^3 gas particles was run and snapshots were saved at 23 redshifts ranging from $z = 0.102$ out to $z = 1.114$. The comoving spacing along the line-of-sight of two subsequent boxes is $100 \text{ Mpc}/h$. Purely adiabatic gas physics and shock heating were included, but radiative cooling and star formation were ignored, which however does not result in significant differences in SZ-morphology, as shown by White et al. (2002) but impacts on the scaling relations as demonstrated by da Silva et al. (2001).

Overdensities are identified using a friends-of-friends algorithm with the linking length $b = 0.164$, which yields all member particles of a cluster in conjunction with a spherical overdensity code, from which virial quantities are estimated. I computed the mass M_{vir} inside a sphere of radius r_{vir} , interior to which the average density was 200 times the critical density $\rho_{\text{crit}} = 3H_0^2/(8\pi G)$. The angle subtended by twice the virial radius is denoted as θ_{vir} . I imposed a lower mass threshold of $M_{\text{vir}} \geq 5 \cdot 10^{13} M_\odot/h$.

The simulation used here seems to be appropriate for assessing the redshift estimation accuracy for a number of reasons: It provides a large number of suitable systems, so that the influence of morphological variety can be studied, and the clusters are very well resolved with respect to their baryonic profiles. Furthermore, the cluster's evolution has been modelled taking account of their cosmological environment.

A justified objection might be that the simulation is biased toward low-mass systems, because high-mass systems form less frequently and especially in small simulation boxes, the high-mass end of the Press-Schechter function is sampled insufficiently. This shortcoming could be remedied by using simulations of single objects, but in this case it would have been difficult to accumulate sufficient statistics, or by using even larger simulation boxes while upholding the mass resolution, which rapidly becomes computationally unfeasible.

10.4.2. SZ-map preparation

Square maps of the Compton- y parameter of the selected clusters were generated by SPH projection of all member gas particles onto a cubical grid with 128^2 mesh points. The (comoving) side length s of the map was adapted to the cluster size, such that the comoving resolution $g = s/128$ of the grid is specific to a given map. Examples of Sunyaev-Zel'dovich maps are given in Fig. 10.2.

If the particle p at position $\mathbf{r}_p = (x_p, y_p, z_p)$ has a smoothing length h_p , an SPH electron number density estimate n_p , and an SPH electron temperature T_p , the Compton- y parameter at the pixel at position \mathbf{x} is given by:

$$y(\mathbf{x}) = \frac{\sigma_T k_B}{m_e c^2} \frac{h_p^3}{g^2} \sum_p \left[\int_{x-g/2}^{x+g/2} dx_p \int_{y-g/2}^{y+g/2} dy_p \int_{-h_p}^{h_p} dz_p \mathcal{K}\left(\frac{r}{h_p}\right) \cdot n_p T_p \right] \quad (10.27)$$

$$\text{with } r = \sqrt{(x_p - x)^2 + (y_p - y)^2 + z_p^2}. \quad (10.28)$$

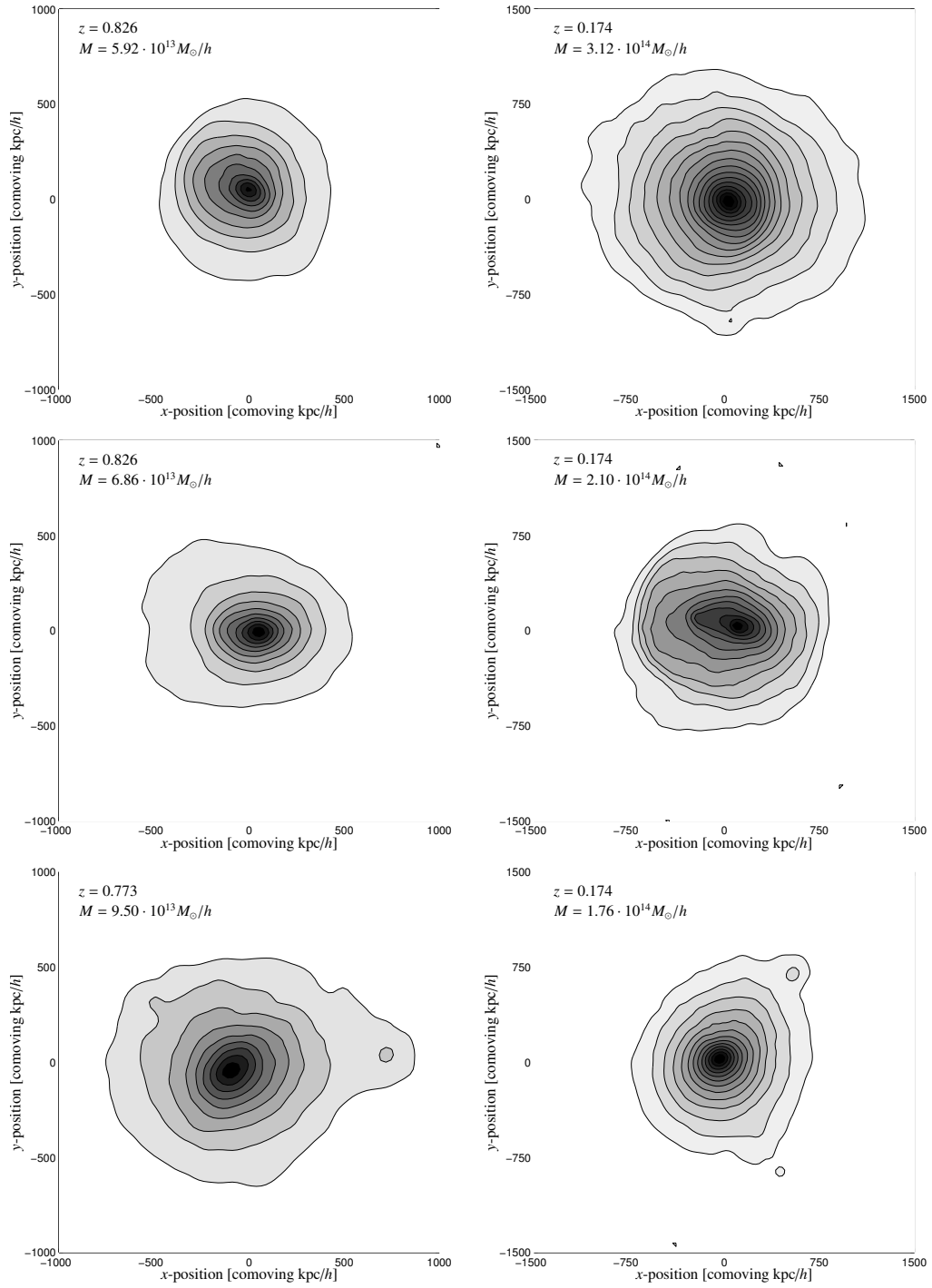


Figure 10.2.: Picture book of Sunyaev-Zel'dovich clusters: The left column shows clusters at high redshifts of $z \approx 0.8$, in comparison to clusters at low redshifts of $z = 0.174$ in the right column. The columns contrast different morphologies in an exemplary fashion: relaxed systems (upper row), elongated clusters (centre row) and clusters in the phase of minor merging or mass accretion (bottom row). The grey scale denotes the amplitude of $y(\mathbf{x})' = \log [1 + 10^5 \cdot y(\mathbf{x})]$ and the contours have a logarithmically equidistant spacing of 0.1 dex, i.e. the lowest contour denotes a common value of $y = 2.5 \cdot 10^{-6}$. All of the clusters depicted above meet the selection criteria discussed in Sect. 10.4.3.

Here, I assumed complete ionisation and primordial element composition of the ICM for the determination of electron number density and temperature. In this way I produced projections along each of the three coordinate axes. The function w is the spherically symmetric cubic spline kernel suggested by Monaghan & Lattanzio (1985), which was also used in the SPH simulation. Details of the SPH projection can be found in Appendix A:

$$\mathcal{K}(u) = \frac{8}{\pi} \cdot \begin{cases} 1 - 6u^2 + 6u^3, & 0 \leq u \leq 1/2 \\ 2(1 - u)^3, & 1/2 < u \leq 1 \\ 0, & u > 1 \end{cases} \quad \text{with } u = r/h_p. \quad (10.29)$$

10.4.3. Cluster selection

Clearly, the wavelet redshift estimation relies on the clusters not being in the state of violent merging, such that the cluster observables, namely the apparent size and integrated SZ-flux are linked via scaling relations. Secondly, the wavelet analysis derives a single parameter describing the extension of the cluster from the break in the spectrum $X_q(\sigma)$ of wavelet parameters and hence elongated clusters should be excluded from the analysis, because in those systems, the extension can not be measured unambiguously. Consequently, apart from the minimal mass of $M_{\min} = 5 \cdot 10^{13} M_{\odot}/h$, that translates into a minimally required line-of-sight Comptonisation amplitude y_{\min} , clusters have been selected in order to show neither double cores nor pronounced substructure. From the resulting sample, 10 clusters were selected randomly from each redshift bin. In this sample, the ellipticity and the residual deviation from a β -profile was measured, in order to provide a solid quantification:

- The SZ-morphology is required not to be too elongated. By fitting a 2-dimensional β -model $y_{\beta}(\mathbf{x})$ to the SZ-profile $y_{\text{data}}(\mathbf{x})$, values for the semi-axes r_x and r_y are derived. 90% of the clusters within the selected sample have axis ratios $q = r_y/r_x$ smaller than 0.8 and ellipticities $e = \sqrt{r_x^2 - r_y^2}/r_x$ below 0.6.
- Residual deviations from the canonical β -profile ought to be small. The *rms*-deviation v of the cluster from the best-fitting β -profile,

$$v = \sqrt{\left\langle \left(\frac{y_{\text{data}}(\mathbf{x}) - y_{\beta}(\mathbf{x})}{y_{\beta}(\mathbf{x})} \right)^2 \right\rangle_{\mathbf{x}}}, \quad (10.30)$$

was smaller than 25% for 90% of my cluster data sample.

The 10 selected clusters from each of the 23 redshift bins, yielding with the three orthogonal projections of each cluster a total number of 690 maps with which the accuracy of the wavelet method in estimating redshifts was assessed. The distributions of the ellipticities e and the integrated residuals v are shown in Fig. 10.3. The same distributions were derived for the smoothed cluster maps, were the effects of finite instrumental resolution have been incorporated. As Fig. 10.3 suggests, the beam does not have a major impact on the morphological properties of most of the cluster sample, which is due to its narrowness of only $1'$ (FWHM).

10.4.4. CMB map generation

CMB anisotropies are assumed to be a particular realisation of a *Gaussian random field*. Aiming at simulating a realisation of the CMB on a square, flat map, I take temperature fluctuations $\theta(\phi)$ relative to the average CMB temperature of $\langle T \rangle = 2.726\text{K}$ to be the independent random field,

$$\theta(\phi) \equiv \frac{T(\phi) - \langle T \rangle}{\langle T \rangle}. \quad (10.31)$$

The flat, two-dimensional power spectrum $P_{\theta}(\ell)$ is defined via:

$$\langle \Theta(\ell) \Theta^*(\ell') \rangle \equiv (2\pi)^{-2} \delta_D(\ell - \ell') P_{\theta}(|\ell|), \quad (10.32)$$

where $\Theta(\ell)$ denotes the Fourier transform of $\theta(\phi)$. The simulation of the CMB temperature fluctuations on a flat square map now consists of the following two steps:

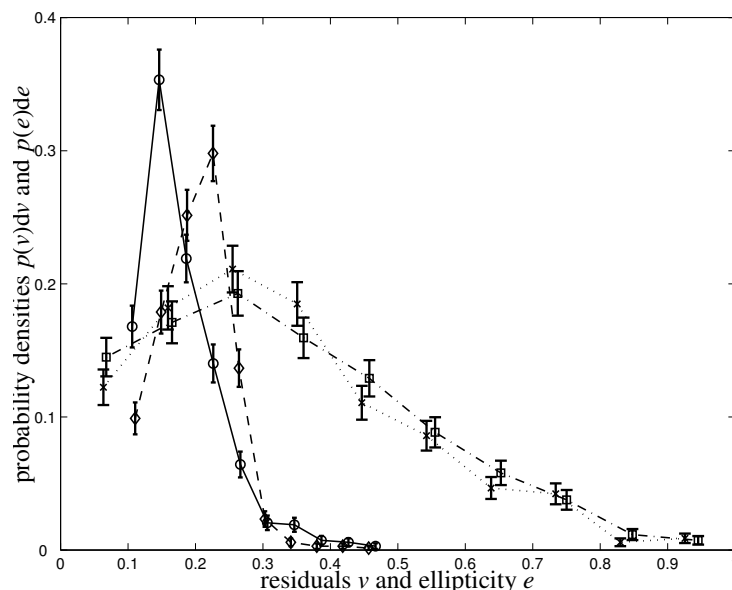


Figure 10.3.: Selection criteria: distribution of residual deviations v from the best-fitting β -profile for unsmoothed (solid, circles) and smoothed (dashed, diamonds) maps. The second set of lines shows the distribution of the ellipticities e with (dash-dotted, squares) and without smoothing (dotted, crosses).

- The angular power spectrum C_ℓ is computed for the flat Λ CDM-Universe using the CMBfast code by [Seljak & Zaldarriaga \(1996\)](#). In addition to the cosmological parameters being already described in Sect. 10.4, I use adiabatic initial conditions and set the primordial He-mass fraction to $X_{\text{He}} = 0.24$ and the Thomson optical depth to $\tau = 0.17$ ([Spergel et al. 2003](#)). The angular power spectrum of the CMB is normalised to COBE data. Since the SZ-effect distorts the CMB only on small angular scales, the flat sky approximation $\ell \gg 1$ is fulfilled and it is appropriate to replace the spherical harmonics with plane waves. [Hu \(2000b\)](#) has shown that the 2-dimensional flat power spectrum $P_\theta(\ell)$ is approximately equal to its angular analogue: $C_\ell \simeq P_\theta(\ell)$.
- Then, Gaussian random variables are generated on a complex two-dimensional grid in Fourier space with variance $\sigma^2(\ell) = P_\theta(\ell)$ according to the absolute value of their wave vectors ℓ . Inverse Fourier transform brings the elementary waves to interference and yields a realisation of the temperature anisotropies $\theta(\phi)$.

10.4.5. Simulated single-frequency SZ-observations

For SZ-clusters observed with a single-frequency interferometer (e.g., the CBI experiment, [Halverson et al. 2002](#))¹, it is important to examine the applicability of the $X_q(\sigma)$ -statistic. For the purpose of this chapter, it suffices to consider observations at small frequencies ν . Thus, the Compton- y maps are combined with realisations of the CMBfluctuations by using eqn. (10.1) in the Rayleigh-Jeans limit,

$$T(\phi) = [1 - 2y(\phi)][1 + \theta(\phi)] \langle T \rangle. \quad (10.33)$$

Fig. 10.4 shows the Compton- y map of a nearby cluster of $2.2 \cdot 10^{14} M_\odot/h$ at redshift $z = 0.102$ combined with a patch of the CMB constructed by the algorithm described above. In this map, the average CMB temperature $\langle T \rangle$ was subtracted. In order to mimic observations, the resulting combined maps are smoothed with a Gaussian beam with FWHM of $\sqrt{8 \ln(2)} \cdot \sigma_b = 1'$.

In the case of multi-frequency SZ-observations the SZ-signature can be easily distinguished from the CMB signal. Therefore, for these cases the CMB background is ignored and not included in the simulated cluster SZ-images. Nevertheless, finite instrumental resolution was taken care of and the SZ-maps were convolved with a Gaussian

¹<http://www.astro.caltech.edu/~tjp/CBI/>

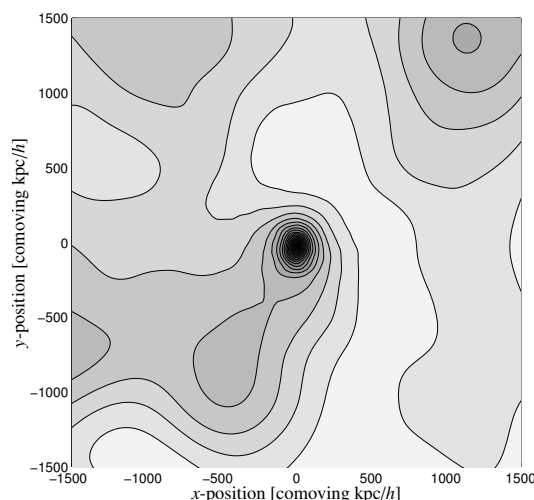


Figure 10.4.: Simulated temperature map of the CMB combined with a foreground SZ-cluster at $z = 0.102$ with virial quantities $M_{\text{vir}} = 2.2 \cdot 10^{14} M_{\odot}/h$, $r_{\text{vir}} = 1.47 \text{ Mpc}/h$ and $k_B T_{\text{vir}} = 1.52 \text{ keV}$. At the cluster centre, the SZ-temperature decrement amounts to -1.8 mK and the CMB temperature fluctuation with the highest amplitude is equal to 0.23 mK . A total of 30 linearly spaced isothermals are drawn. In this case, the comoving scale $1 \text{ Mpc}/h$ corresponds to $11.5'$.

kernel of $\sqrt{8 \ln(2)} \cdot \sigma_b = 1'$ (FWHM). This approach is optimistic considering instrumental noise and point sources, that distort the SZ-frequency dependence and provide additional flux at the SZ-decrement frequencies. While the second effect primarily diminishes the SZ-detectability, it too generates noise similar to instrumental noise due to the Poisson fluctuation of the number of sources within an aperture. A detailed discussion can be found in Sect. 10.5.8.

The beam width was assumed to be 1 arcmin (FWHM), which is a reasonable choice considering the design values of currently planned dedicated SZ-telescopes. These experiments are able to marginally resolve clusters out to redshifts of $z = 0.7$: At these distances, the beam size (in terms of standard deviation) becomes comparable to the core sizes of the least massive clusters considered here. At the largest redshifts of $z \approx 1.1$ examined in this chapter, the beam is approximately twice as large as the cluster core.

10.5. Analysis

In this section, the analysis is explained step by step: After introducing the wavelet families (Sect. 10.5.1), the wavelet spectrum and the parameters deduced from it are described (Sect. 10.5.2 and Sect. 10.5.3). The correlations of the wavelet spectral parameters with physical quantities are discussed (Sect. 10.5.4). The measurement principle and the breaking of degeneracy is illustrated in Sect. 10.5.5. Successively, the intercorrelation of the wavelet parameters and the shape of the parameter space is explored by principal component analysis (Sect. 10.5.6). Then, gauge functions for modelling the redshift dependence of the parameters are proposed (Sect. 10.5.7). Several issues for observers are discussed in Sect. 10.5.8, for instance the influence of instrumental noise (Sect. 10.5.8.1), the influence of primary CMB fluctuations on the wavelet spectrum and their suppression (Sect. 10.5.8.2), and the impact of sub-millimetric point sources on the wavelet estimation technique (Sect. 10.5.8.3). Finally, the redshift of the clusters are estimated by maximum likelihood techniques (Sect. 10.5.9).

10.5.1. Wavelet basis functions

In the analysis a wide range of wavelets with different functional shapes was employed, although the *symlet* wavelet basis introduced by Daubechies & Bates (1993) yielded particularly good results. Due to their symmetry and peakiness, *symlets* are seemingly especially suited for analysing SZ-morphologies, because they do not impose a strong smoothing on the image in determining the wavelet moments $X_q(\sigma)$. Other wavelet families that found application in my analysis were Daubechies' wavelets, *coiflets* and *biorthogonal* wavelets. Fig. 10.5 compares the

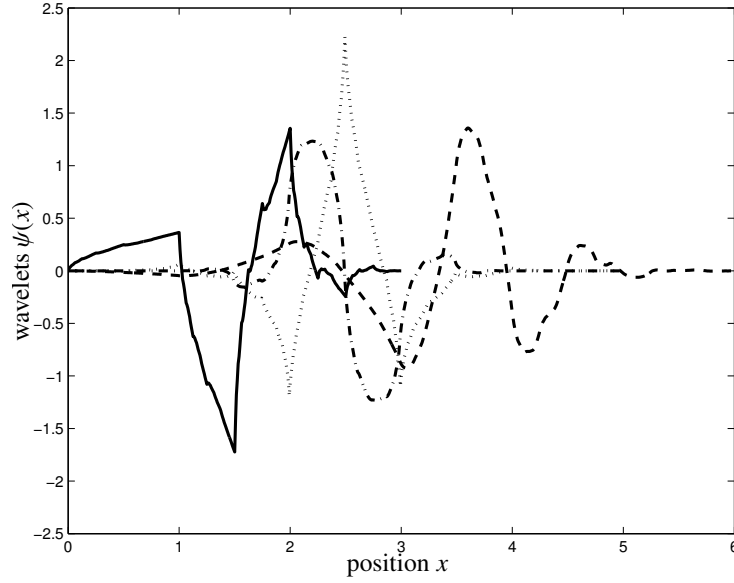


Figure 10.5.: The wavelet basis functions $\psi(x)$ chosen for the analysis: symlet *sym2* (solid), Daubechies' wavelet *db4* (dashed), coiflet *coif1* (dotted) and the biorthogonal wavelet *bior1.3* (dash-dotted).

functional shape of the different wavelet families.

The analysis proceeds by measuring the wavelet moments on smoothed comoving maps of the Compton- y parameter following the definition in Sect. 10.3. The scale σ of the resulting wavelet spectrum is then converted to angular units. Because my SZ-maps are computed on a grid of 128^2 mesh points with adaptively chosen side length for each cluster, the dynamical range of the wavelet spectra always comprises approximately two decades. However, this is no fundamental limitation of this approach because the maps are featureless below the smoothing scale of $1'$ (FWHM).

10.5.2. Measurement of wavelet quantities

In order to derive the actual flux decrement or, equivalently, the decrement in antenna temperature from the line-of-sight Compton- y amplitude, its value at each pixel needs to be multiplied with the solid angle it subtends. For the conversion, a standard Λ CDM-cosmology was assumed, the parameters of which have already been given in Sect. 10.4. Thus, the pixel amplitudes were modified according to:

$$y(x) \longrightarrow y(\phi) = y(x) \cdot 4 \arctan^2 \left[\frac{g}{2w(z)} \right], \quad (10.34)$$

where $w(z)$ is the comoving distance in the model cosmology and g denotes the comoving size of a single pixel. It should be emphasised that the wavelet coefficients $\chi(\boldsymbol{\mu}, \sigma)$ are evaluated on a comoving grid, which has been adapted to the cluster size before converting the wavelet scale σ to angular units. This, however, should not pose a problem for real observations, provided the sampling scale is of the same order of magnitude as the angular scale of the finest pixels.

In order to obtain dimensionless quantities, the unit of the wavelet $\psi_\sigma(\mathbf{x})$ has been set to inverse steradians, such that the wavelet expansion coefficients $\chi(\boldsymbol{\mu}, \sigma)$ and the wavelet moments $X_q(\sigma)$ are dimensionless, irrespective of q . For numerical convenience, the pixel amplitudes in the combined SZ-maps have been multiplied with 10^{12} .

The summation in the definition of the wavelet moment $X_q(\sigma)$ in eqn. (10.4) discards the information about the position $\boldsymbol{\mu}$ at which the wavelet expansion coefficient $\chi(\boldsymbol{\mu}, \sigma)$ is evaluated. Consequently, the position of a cluster inside the observing frame does not influence the wavelet decomposition.

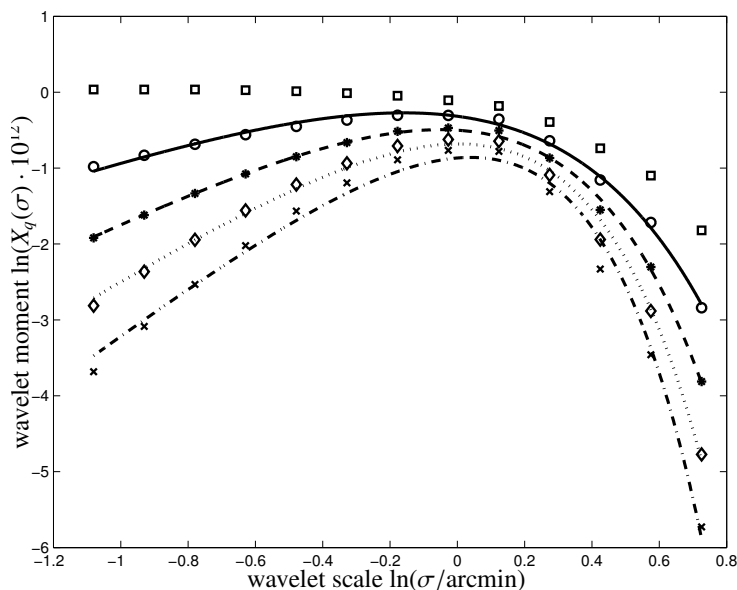


Figure 10.6.: The spectrum of wavelet moments, together with the fitting formula (10.35) for increasing wavelet moment order q : $q = 2$ (squares), $q = 3$ (circles, solid), $q = 4$ (stars, dashed), $q = 5$ (diamonds, dotted) and $q = 6$ (crosses, dash-dotted) for a single cluster. The wavelet moments $X_q(\sigma)$ followed from wavelet expansion with the *sym2*-wavelet.

10.5.3. Wavelet spectrum of SZ-cluster maps

Due to the lack of any analytical generalisation of eqn. (10.14) for $q \neq 2$, deviations of the Compton- y map from a King profile and wavelets other than the simple Mexican hat, I decided to explore phenomenological functions for describing the wavelet spectrum. The simplicity of the shape of the wavelet spectrum shown in Fig. 10.6 implies that the model function,

$$\ln X_q(\sigma) \simeq a + s \ln(\sigma/\sigma_0) - \sigma/c, \quad (10.35)$$

is able to extract all apparently contained information, i.e. the spectrum is described by means of three quantities: the amplitude a , the slope s and a break at c . The parameter σ_0 has been included in eqn. (10.35) in order to obtain a formula that is dimensionally correct, although it does not yield any new information and this specific degree of freedom is already described by the variable a .

The usage of eqn. (10.35) implicitly discards information about asphericity and effectively determines an average of the cluster's extension along its major axes. The problem would be significantly complicated by including asymmetry and considering vectorial nature of σ (see Zaroubi et al. 1998, 2001).

Because the cutoff parameter c is of great importance to my analysis, it needs to be derived reliably. Thus, the order of wavelet moments q was restricted to $q \geq 3$, because larger q -values facilitate the determination of c . From Fig. 10.6 it is obvious that an increase in q suppresses the value of $X_q(\sigma)$ at small scales σ such that the curve develops a maximum in the vicinity of c . Additionally, by the choice of large values for q , the wavelet expansion coefficients $\chi(\mu, \sigma)$ dominated by CMB noise are suppressed relative to those obtained in the central part of the cluster and consequently higher order wavelet moments $X_q(\sigma)$ provide a cleaner measurement. The range of sensible q -values is restricted by the fact that for increasing q the moment $X_q(\sigma)$ is successively dominated by the largest wavelet expansion coefficient $\chi(\mu, \sigma)$ and does no longer contain information of the structure to be analysed. In order to stabilise the fitting procedure I interpolate in between the wavelet moments $X_q(\sigma)$. This is justified because I expect a smooth variation of the wavelet spectrum according to Sect. 10.3.2.1.

10.5.4. Correlations with physical quantities

The parameters derived from the fit to the spectrum of wavelet coefficients have a physical interpretation. As shown in Sect. 10.3.2.1, the wavelet spectrum breaks at the cluster scale. Therefore, one expects a correlation between the

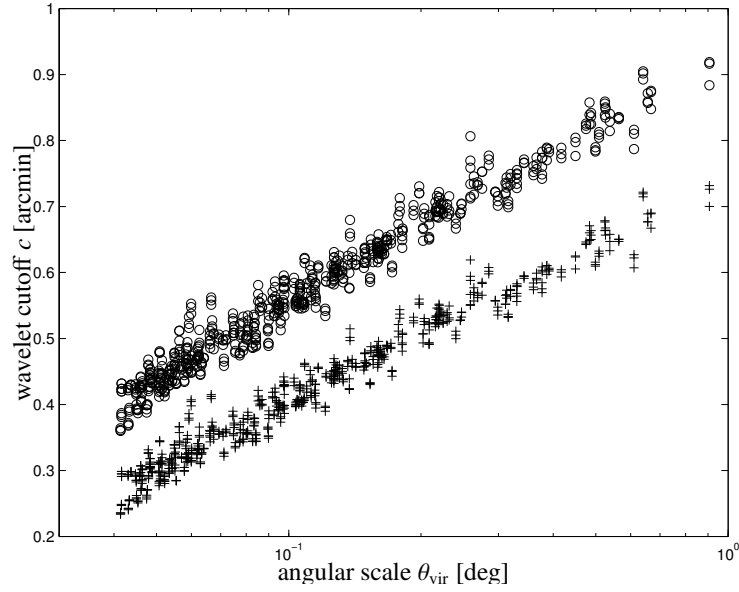


Figure 10.7.: Wavelet measured cluster size c versus angular extension θ_{vir} for increasing wavelet moment order q : $q = 3$ (circles) and $q = 6$ (crosses) without including CMB fluctuations. The c -values have been determined with the *sym2*-wavelet.

angular size of the cluster θ_{vir} and the **cutoff** c , as found in Fig. 10.7. Increasing weighting exponents q shift the regression line to smaller values of c , which can be understood by the fact that larger values of q suppress small wavelet expansion coefficients arising at the outskirts of the cluster, which in turn leads to a break in the wavelet spectrum at smaller scales.

Similarly, the **amplitude** a determined by the fit is proportional to the integrated Compton- y flux,

$$\mathcal{Y} = \int d^2\phi y(\phi) = \frac{kT_{\text{vir}}}{m_e c^2} \frac{\sigma_T}{d_A(z)^2} \frac{1 + f_H}{2} f_B \frac{M_{\text{vir}}}{m_p}, \quad (10.36)$$

as illustrated by Fig. 10.8. Here, f_b denotes the baryon fraction, f_H the hydrogen fraction, which determines the elemental composition and has been set to the primordial value of 0.76, and m_p is the proton mass. $d_A(z)$ is the angular diameter distance.

The normalisation a of the wavelet moments $X_q(\sigma)$ shows a steeper dependence on the integrated Comptonisation parameter \mathcal{Y} for larger choices of q , which is explained by the following argument: The amplitude $a(q)$ reflects the normalisation of the wavelet moments $X_q(\sigma)$. The integral in eqn. (10.4) is dominated by the largest wavelet expansion coefficient $\chi(\mu, \sigma)$, taken to the q^{th} power. On the other hand, the wavelet expansion coefficients $\chi(\mu, \sigma)$ are proportional to integrated Comptonisation \mathcal{Y} , resulting in observed relation $\ln[X_q(\sigma)] \propto a \propto q \cdot \ln(\mathcal{Y})$. In summary, Fig. 10.9 shows the wavelet spectra for three comparable clusters situated at different redshift taking instrumental smoothing into account. The figure illustrates, how the amplitude and the break of the spectrum decrease with increasing redshifts.

The influence of instrumental smoothing on the wavelet parameters can be summarised as follows: In the case of suppressed noise, the amplitude a , being a measurement of \mathcal{Y} should be still reliably measurable in contrast to e.g. isophotal flux or related quantities, despite the fact that it is systematically smaller due to the instrumental beam. The angular size, however, expressed by the cutoff c , increases with increasing smoothing, but can still serve as a measure for cluster size even in cases where the size of the instrumental beam becomes comparable to the cluster core. In addition, this behaviour is supported by Fig. 10.10, where a weak deviation from proportionality towards larger values of c is easily visible. Nevertheless, the value of c is not significantly deteriorated by the instrumental smoothing.

Finally, the **slope** s is purely a measure of instrumental smoothing: Placing the same cluster at different redshifts would result in a blurred image of the more distant one. Keeping in mind that there is a close analogy between

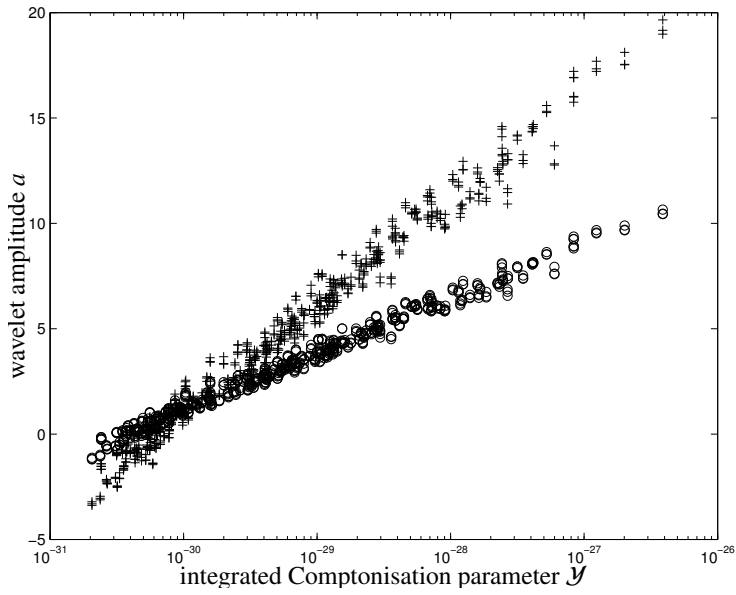


Figure 10.8.: Wavelet amplitude a as a function of integrated Comptonisation parameter \mathcal{Y} for different weighting exponents q : $q = 3$ (circles) and $q = 6$ (crosses), again without taking CMB fluctuations into account. As the analysing wavelet, the *sym2*-wavelet was chosen.

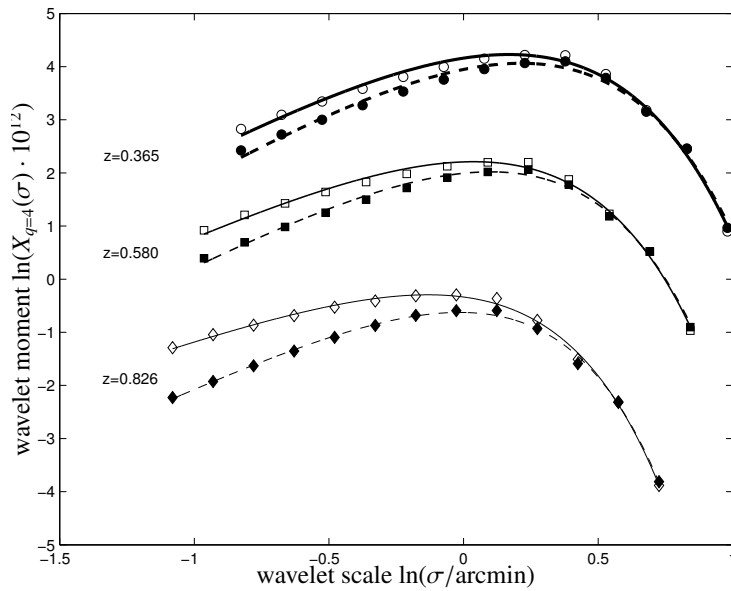


Figure 10.9.: Wavelet spectra $X_4(\sigma)$ of three clusters at redshifts $z = 0.365$ (circles, thick lines), $z = 0.580$ (squares, medium lines) and $z = 0.826$ (diamonds, thin lines), where instrumental smoothing has been ignored (open symbols, solid lines) and properly taken account of (closed symbols, dashed lines). The spectra have been derived with the *sym3*-wavelet as the analysing wavelet.

wavelet- and Fourier-transforms (as explained in Sect. 10.3.3), the wavelet moment $X_q(\sigma)$ as a function of σ can be interpreted as the variance of the wavelet-filtered field. The instrumental beam introduces an additional filtering to the Compton- y map (compare Sect. 10.3.2.4) and would cause the Fourier spectrum to drop at smaller values of the wave vector k , because the instrumental beam constitutes effectively a low-pass filter that is erasing structures smaller than its extension. Comparing clusters at different redshifts, it is clear that the drop in power happens at smaller scales in the case of the more distant cluster. Then the slope s , defined as $d \ln X_q(\sigma)/d \ln \sigma$ for $\sigma \ll r_c$, is larger in the case of an unresolved cluster compared to a resolved cluster. This measure of the influence of finite instrumental smoothing varies only by a factor of two in slope over the redshift and mass range considered here, but nevertheless serves as an indicator of cluster distance. It should be emphasised, that the s -parameter does not try to extract information from scales that are inaccessible due to instrumental smoothing. Wavelet analysis of maps that are poor in features over a certain range of scales generically results in power laws for $X_q(\sigma)$ for these scales.

10.5.5. Measurement principle

Now, it is necessary to illustrate how a measurement of the total Comptonisation \mathcal{Y} and of the angular size θ_{vir} suffices to derive a distance estimate. For that purpose, clusters are placed at unit distance and the distance dependences of the wavelet amplitude a and the the cutoff c are removed by the following formulae, since a is a logarithmic measure of flux inside an solid angle element \mathcal{Y} and c is a logarithmic measure of of angular extension θ_{vir} :

$$a_0 = a(z) + 2 \cdot \ln(d_a(z)) \quad (10.37)$$

$$c_0 = c(z) + \ln(d_a(z)). \quad (10.38)$$

By applying simple scaling arguments, one expects the ratio a_0/c_0 to be equal to 5: From the wavelet amplitude a one obtains $a_0 \propto \ln(\mathcal{Y} \cdot d_A(z)^2) \propto \ln(M_{\text{vir}} \cdot T_{\text{vir}})$. Furthermore, from the spherical collapse model follows, that $T_{\text{vir}} \propto M_{\text{vir}}^{2/3}$ (Navarro et al. 1995), which yields, together with $M_{\text{vir}} \propto r_{\text{vir}}^3$, the relation $a_0 \propto \ln(r_{\text{vir}}^5)$. Substituting $c_0 \propto \ln(r_{\text{vir}})$ gives the final result $a_0/c_0 = 5$.

Fig. 10.10 nicely illustrates how the degeneracy is broken and how a simple measurement of flux and angular extension suffices in order to derive a distance estimate: A crude fit to the distance corrected wavelet amplitude a_0 as a function of distance corrected wavelet cutoff parameter c_0 yields a slope of approximately 5.8, which corresponds well to the slope of ~ 5 expected from the theoretical consideration outlined above. If, hypothetically, the ratio a_0/c_0 was equal to 2, the measurements of flux and angular size would be completely degenerate and would not yield any distance information. This case corresponds to disks of equal surface brightness, where measurements of flux and angular size are completely degenerate and do not yield any distance information at all. It should be noted, that by adopting the usual scaling relations, one introduces a systematic error in slope that can amount to $\approx 20\%$ error.

10.5.6. Principal component analysis

In order to rate the extent to which the parameters derived in the fit to the spectrum of wavelet moments are independent, a principal component analysis (PCA, see e.g. Deeming 1964) was performed. The PCA is determining a transformation to a new orthogonal coordinate system in parameter space spanned by a , c and s , such that the variance along the first axis is maximised.

The first eigenvector of the matrix that describes the change of basis by the PCA reads $x_{\text{PCA}} = (0.65, 0.70, 0.32)$ which has been derived for the spectral parameters for $q = 3$ and with the *sym2*-wavelet as the analysing wavelet. The values similar in magnitude suggest that the variation in the data set is contained in all three parameters a , c and s .

As can be read off from table 10.1, the parameter space is tightly constrained and all three parameters are interrelated, such that the data points form a narrow ray in parameter space. This result holds irrespective of the choice of q , although the scatter increases with higher choices for q . The values in table 10.1 have been determined without considering CMB fluctuations. Given the physical interpretation of the wavelet amplitude a and the cutoff c , it is obvious that the tight correlation can be traced back to the self-similarity of clusters and the cluster scaling relations linking T_{vir} , M_{vir} and r_{vir} that follow from the spherical collapse model. The scaling relations for SZ-quantities derived by da Silva et al. (2003) support this view. This shows together with Sect. 10.5.4 and Sect. 10.5.5 that both

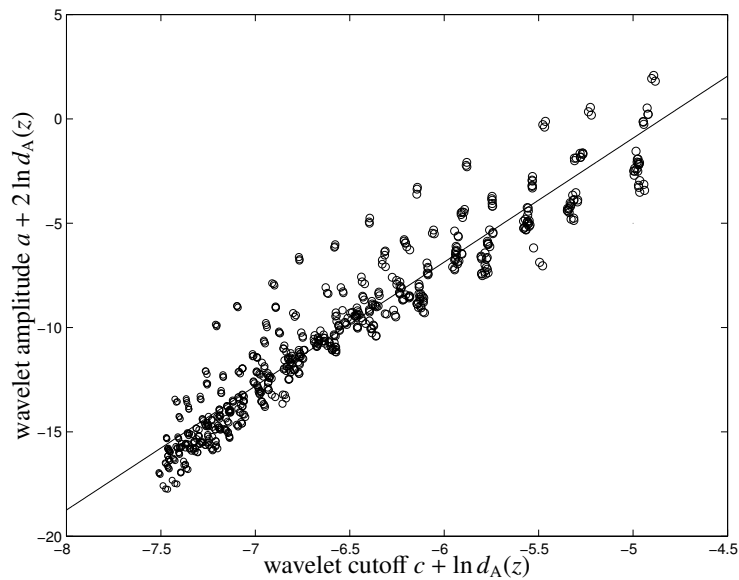


Figure 10.10.: Distance corrected wavelet amplitude $a_0 = a(z) + 2 \cdot \ln(d_A(z))$ as a function of distance corrected wavelet cutoff parameter $c_0 = c(z) + \ln(d_A(z))$. The values have been determined in fits to the wavelet spectrum $X_3(\sigma)$, that has been derived with the *sym2*-wavelet as the analysing wavelet.

	$q = 3$	$q = 4$	$q = 5$	$q = 6$
1 st principal component	95.6%	94.2%	92.8%	91.5%
2 nd principal component	2.7%	4.2%	5.5%	6.7%

Table 10.1.: Result of the PCA. The variance explained by the first and second principal component as a function of wavelet order q . Here, no CMB fluctuations were included.

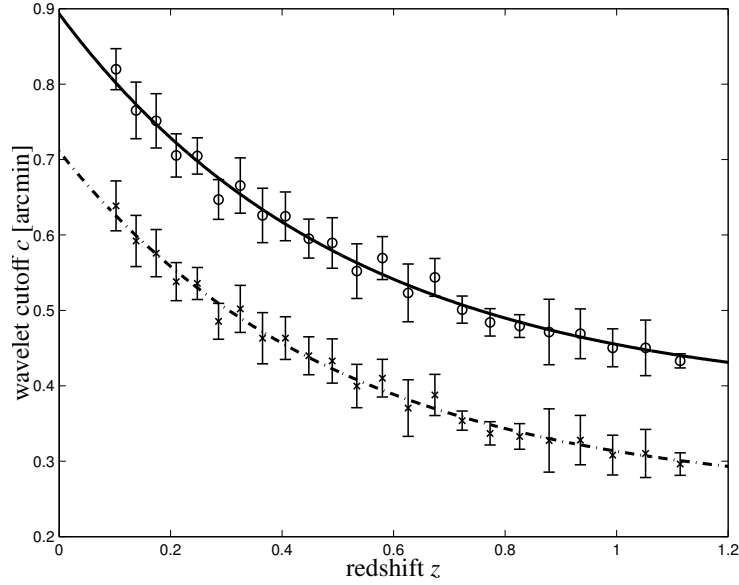


Figure 10.11.: Dependence of the wavelet cutoff parameter c on redshift z without considering CMB fluctuations for $q = 3$ (circles, solid) and $q = 6$ (crosses, dash-dotted). The analysing wavelet was the *sym2*-wavelet.

parameter	variable	$i = 1$	$i = 2$	$i = 3$
amplitude	a	10.5837	0.6475	-1.9570
cutoff [arcmin]	c	0.5124	0.5165	0.3809
slope	s	1.3423	0.4144	1.3803

Table 10.2.: Fitting values for the gauge functions defined in eqn. (10.39) for the cluster sample at hand and the *sym2*-wavelet basis. The order of the wavelet moment $X_q(\sigma)$ has been set to $q = 3$. The values have been derived without taking CMB fluctuations into account.

the cutoff c and the amplitude a are functions of M_{vir} . By only considering systems close to virialisation I thus expect a fundamental narrow ray in parameter space which can be described by a single principal component.

10.5.7. Redshift dependence of the wavelet parameters

The parameters a and c are expected to decrease with increasing redshift z , the reason for which is quite apparent: The angular diameter θ_{vir} and the integrated Comptonisation \mathcal{Y} decreases because of the increasing angular diameter distance $d_A(z)$ that enters θ_{vir} linearly and \mathcal{Y} quadratically. Furthermore, clusters accrete matter during their formation history and thus are on average more massive at later times, i.e. at smaller redshifts z (see, e.g., [Wechsler et al. 2002](#), [van den Bosch 2002](#), [Zhao et al. 2003](#)). From the physical point of view, the dependence of a and c on redshift z is far from trivial, and therefore, their functional behaviour is described by an empirical approach. Among others, the exponential function provides a good fit to the data, as illustrated by Figs. 10.11 and 10.12:

$$x(z) = x_1 \exp\left(-\frac{z}{x_2}\right) + x_3, \text{ where } x \in \{a, c, s\}. \quad (10.39)$$

The optimised parameters x_i , $i \in \{1, 2, 3\}$, for $x \in \{a, c, s\}$ in the gauge functions eqn. (10.39) are given in table 10.2 for the case $q = 3$. It should be emphasised that the parameters stated are only valid for image analysis with the *sym2*-wavelet, where the maps have been smoothed with a Gaussian kernel with $1'$ (FWHM) and the considered cluster sample, which is defined by the selection criteria laid down in Sect. 10.4.3 and the minimal mass of $5 \cdot 10^{13} M_{\odot}/h$.

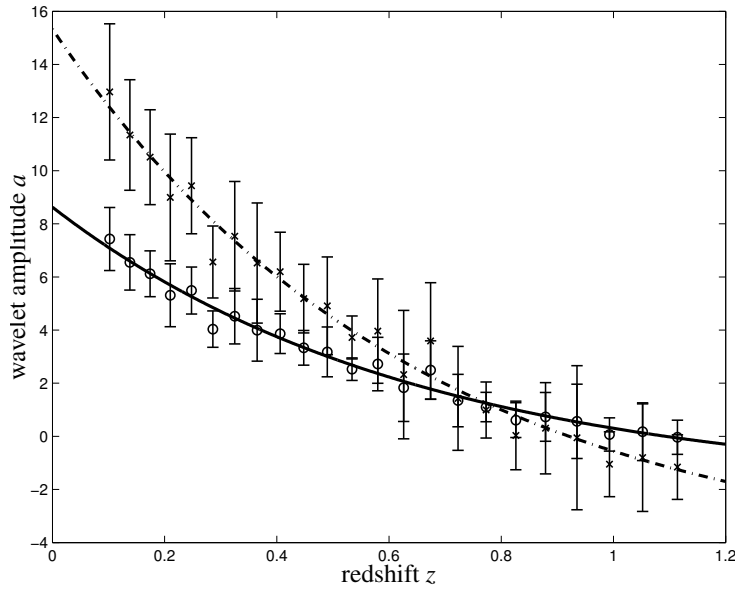


Figure 10.12.: Dependence of the wavelet amplitude parameter a on redshift z without including CMB fluctuations for $q = 3$ (circles, solid) and $q = 6$ (crosses, dash-dotted). The quantities have been determined with the *sym2*-wavelet.

10.5.8. Noise contributions and their suppression

10.5.8.1. Influence of instrumental noise

The extent to which the wavelet spectra are affected by instrumental noise is a very important issue: Even though experiments like the ACT aim at achieving noise levels as low as $\sigma_T \approx 2 - 5 \mu\text{K}$ per 3 arcmin²-pixel (depending on the channel, Kosowsky 2004), instrumental noise nevertheless impacts on the shape of the wavelet spectra. Fig. 10.13 shows the distorted wavelet spectrum for two different wavelet families on SZ-maps where uncorrelated pixel noise at a level equivalent to (a pessimistic value of) $\sigma_T = 10 \mu\text{K}$ per square arcminute has been added.

Instrumental noise can be characterised by an approximate power-law component in the spectrum of wavelet coefficients $X_q(\sigma)$. The influence of the noise on the wavelet spectrum is small and can be suppressed by either choosing large q or by employing a smoothly varying wavelet, for instance, a member of the *symlet* family instead of a peaked wavelet, such as the *coiflet*. Furthermore, the instrumental noise does not cause a significant deviation of the model parameters a , c and s once the detection of the cluster is sufficiently reliable, i.e. exceeds a value of 10σ which is the case even for the least massive clusters in my sample out to redshifts of $z = 0.8$. At even higher redshifts, wavelet analysis will be seriously impeded by instrumental noise.

10.5.8.2. Influence of CMB fluctuations

Clusters at high redshift z are characterised by their small angular scale on which the underlying CMB is represented by a smooth gradient due to Silk damping (Silk 1968). In this case the wavelet analysis produces the same results irrespective of the CMB noise owing to the distinct morphological feature of the cluster on top of the smooth CMB gradient. Once clusters at lower redshifts reach angular sizes comparable to characteristic scales of CMB fluctuations, the wavelet analysis has to be made more sophisticated. This complication in the wavelet analysis arises because wavelets are primarily suited for determining morphological features rather than solely singling out high amplitude characteristics. Because the angular scale of the clusters ranges between $10'$ and $1'$, which corresponds to multipole orders of $\ell \approx 10^3 \dots 10^4$, it suffices to consider the Silk damping tail of the angular power spectrum of the CMB. In the wavelet spectrum $X_q(\sigma)$ this translates into an additional approximate power-law component $X_q^{\text{CMB}}(\sigma)$, as can be seen from Fig. 10.14:

$$\ln X_q^{\text{CMB}}(\sigma) \approx a_{\text{CMB}} + s_{\text{CMB}} \ln \sigma. \quad (10.40)$$

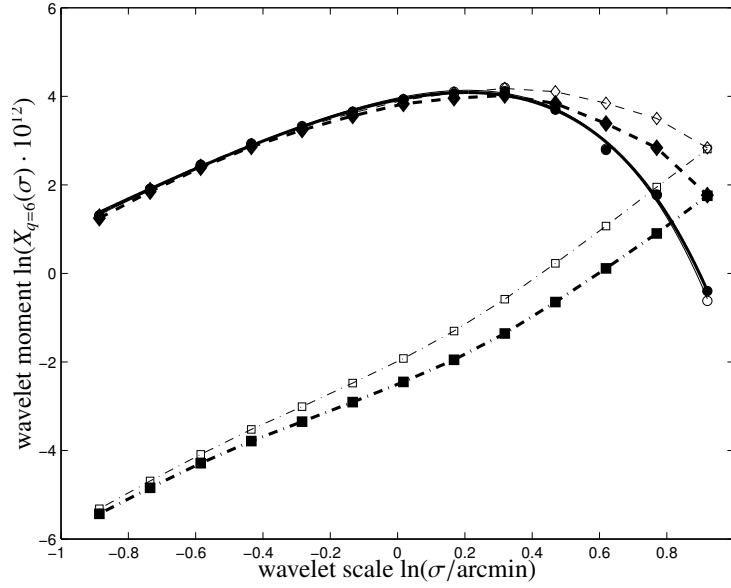


Figure 10.13.: Changes to the wavelet spectrum of a single cluster (situated at $z = 0.49$) caused by instrumental noise: unperturbed wavelet spectrum of the SZ-cluster (circles, solid), of pure instrumental noise (squares, dash-dotted) and of the combined map (diamonds, dashed). Data points were derived from simulated data and the joining line in the case of the unperturbed wavelet spectrum the result of the fitting functions described by eqn. (10.35). The order of the wavelet moment is $q = 6$. As analysing wavelets, the *sym3*-wavelet (thick lines, closed symbols) and the *coif1*-wavelet are compared (thin lines, open symbols).

This is due to the discrete sampling of the wavelet moments as well as the inherent statistics of the wavelet spectra of order q which can be interpreted as suitably weighted q -point correlation functions in Fourier analysis (compare Sect. 10.3.3).

Fig. 10.15 shows the probability distribution function $p(s_{\text{CMB}})ds_{\text{CMB}}$ of the slopes s_{CMB} following from linear fits to the wavelet moments $X_q(\sigma)$ for the range of q 's considered here. Again, the *sym2*-wavelet was chosen as the analysing wavelet. The slopes s_{CMB} are not well confined, keeping the vast range of angular scales in mind, which in turn will make it difficult to subtract the CMB-contribution to the wavelet spectrum of the combined map.

In order to disentangle the contributions from the CMB noise from those of the cluster, one may pursue different approaches: Among others, CMB fluctuations underneath the cluster can be reconstructed with spline polynomials and successively subtracted. Here, I have masked the cluster and fitted 5th-order polynomials to the remaining data points. Because the y -maps and the realisations of the CMB are to leading order combined linearly and because the CMB is a smoothly varying field, it is possible to reconstruct the CMB fluctuations from the environment of the cluster and interpolate to the cluster centre. The reconstructed CMB field can be subtracted from the initial image and by applying wavelet decomposition to the cleaned field one obtains a wavelet spectrum, from which the parameters a , c and s can be reliably derived.

An important question common to the suppression of the CMB and instrumental noise is the choice of a cluster mask region, either for reconstructing the ambient CMB fluctuations with polynomials or for reducing the contribution of pixel noise (which is proportional to the map area) to the wavelet spectrum. As soon as the cluster is detected at sufficient significance levels, it should be possible to choose the cluster mask region according to a preliminary determination of the cluster size. Choosing too large a mask region results in higher amplitudes of $X_q(\sigma)$ at large angular scales σ , but the parameters of the model function a and c are relatively insensitive to $X_q(\sigma)$ at large σ . Furthermore, it would introduce a systematic trend in measurements of a and c , which could be taken account of by altering the functions that model the redshift dependence of those parameters.

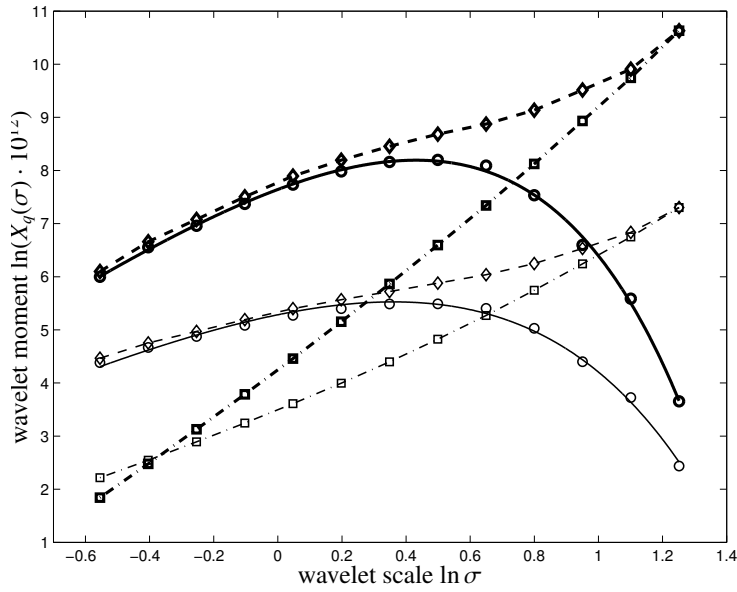


Figure 10.14.: Changes to the wavelet spectrum of a single cluster caused by the fluctuating CMB: unperturbed wavelet spectrum of the SZ-cluster (circles, solid), of the pure CMB (squares, dash-dotted) and of the combined map (diamonds, dashed). Data points were derived from simulated data and the joining line in the case of the unperturbed wavelet spectrum the result of the fitting functions described by eqn. (10.35). The order of the wavelet moment is $q = 6$ (thick) and $q = 4$ (thin). Again, the analysing wavelet is the *sym2*-wavelet.

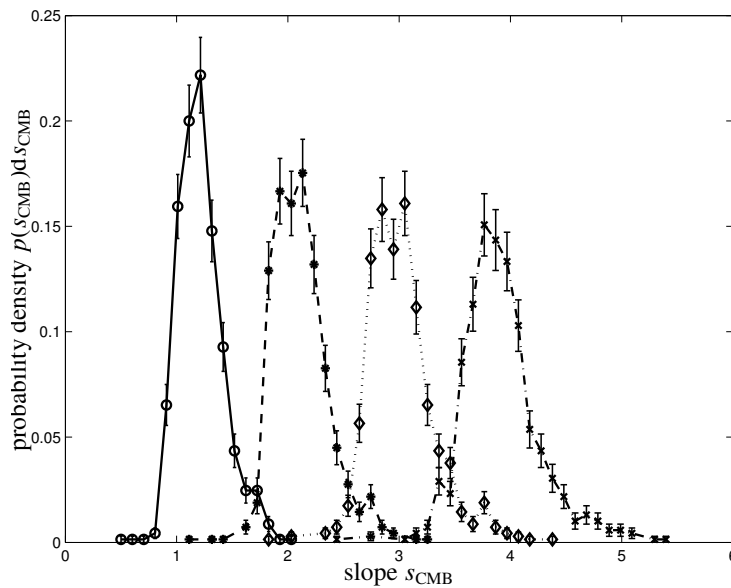


Figure 10.15.: Distributions of the power-law slopes s_{CMB} of CMB wavelet spectra as a function of wavelet moment order: $q = 3$ (circles, solid), $q = 4$ (stars, dashed), $q = 5$ (diamonds, dotted), $q = 6$ (crosses, dash-dotted). For the analysing wavelet, the *symlet sym2* was chosen.

10.5.8.3. Influence of point sources

Yet another impediment to SZ-observations are point sources such as infra-red galaxies and microwave emitting AGNs. They influence SZ-observations in two ways: Firstly, the integrated flux of microwave sources inside the instrument's beam distorts the SZ-flux modulation and diminishes the signal at SZ-decrement frequencies. Secondly, the Poisson fluctuation in the number of sources inside the beam leads to an additional noise component. While the first effect concerns the detectability of SZ-clusters, the second effect influences the wavelet analysis in a way similar to instrumental noise.

The integrated emission from unresolved infra-red galaxies make up the cosmic infra-red background (CIB) (Puget et al. 1996, Lagache & Puget 2000), the fluctuations of which are become important at frequencies above $\nu \simeq 100$ GHz (Aghanim et al. 2004). Lagache (2003) and White & Majumdar (2003) have estimated the number counts of unresolved infra-red galaxies at SZ-frequencies. In the easiest case, the sources are uncorrelated and the fluctuations obey Poissonian statistics, but the inclusion of correlations is expected to boost the fluctuations by a factor of ~ 1.7 (Song et al. 2003). According to Aghanim et al. (2004), the resulting fluctuations vary between a few 10^2 Jy/sr and 10^5 Jy/sr. A proper modelling would involve a biasing scheme for populating halos, the knowledge of the star formation history and template spectra in order to determine the K-corrections.

In AGNs, the situation is notably more complex: The spectra show a variety of functional behaviours, with spectral indices α generally ranging from -1 to -0.5, but sources with inverted spectra $\alpha > 0$ are commonplace. This variety makes it difficult to extrapolate fluxes to observing frequencies of CMB experiments. Two studies (Toffolatti et al. 1998, Sokasian et al. 2001) have estimated the fluctuations generated by radio emitting AGNs at SZ-frequencies and found them to amount to $10^3 - 10^4$ Jy/sr. However, AGNs are known to reside in high-density environments and the proper modelling would involve a biasing scheme in order to assign AGN to the dark matter halos. Apart from that, one would have to assume spectral properties from a wide range of spectral indices and AGN activity duty cycles.

Given the poor experimental constraints no attempt is made at modelling the influence of point sources on wavelet spectra. The additional noise component due to fluctuating number of point sources can be expected to influence wavelet spectra in a way similar to instrumental noise and therefore, all proposed methods of suppression are applicable to this case as well.

10.5.9. Redshift estimation

In order to assess the accuracy of the redshift measurement, a maximum likelihood estimation is performed. The likelihood function is defined as:

$$\mathcal{L}(z) = \frac{1}{(2\pi)^{3/2} \sigma_a \sigma_c \sigma_s} \exp\left(-\sum_{x \in \{a,c,s\}} \frac{1}{N} \sum_{i=1}^N \frac{(x_i - x(z))^2}{2\sigma_x^2}\right), \quad (10.41)$$

and was evaluated for each bin separately, i.e. the index i enumerates clusters within the redshift bin under consideration. $N = 30$ denotes the number of clusters within a single redshift bin. From the position of the maximum in $\mathcal{L}(z)$ the most probable redshift estimate z was derived and the accuracy of the estimate followed from the corresponded to the $1-\sigma$ confidence intervals, i.e. the accuracy is determined by the range in redshift z enclosing 68% of the estimates. The function was found to be symmetric about the maximum value and hence the mean width is stated as the estimation accuracy. Fig. 10.16 shows the estimated redshift versus the real redshift for the cluster sample derived by using all of the three parameters a , c and s . In comparison, the error bars have become larger by a factor of $\simeq 1.5$ when including the fluctuating CMB, as illustrated by Fig. 10.17. The measurement is unbiased and the error relative to $1 + z$ rises slightly with increasing redshift z .

The results for different analysing wavelets as a function of wavelet moment order q are summarised in tables 10.3 and 10.4. Clearly, the method starts to fail at redshifts exceeding $\gtrsim 1$, when the angular diameter distance $d_A(z)$ develops a plateau and does not cause clusters to appear smaller. The average attainable accuracy is stated relative to $1 + z$ in order to facilitate comparison to photometric redshifts. The accuracy slightly degrades with increasing q , which is due to suppression of small wavelet expansion coefficients especially at small scales and the resulting inaccuracy of the fitting formula eqn. (10.35) used to extract the spectral parameters a , c and s from the wavelet spectrum.

Inclusion of the CMB in order to test the applicability of determining morphological redshifts in the case of

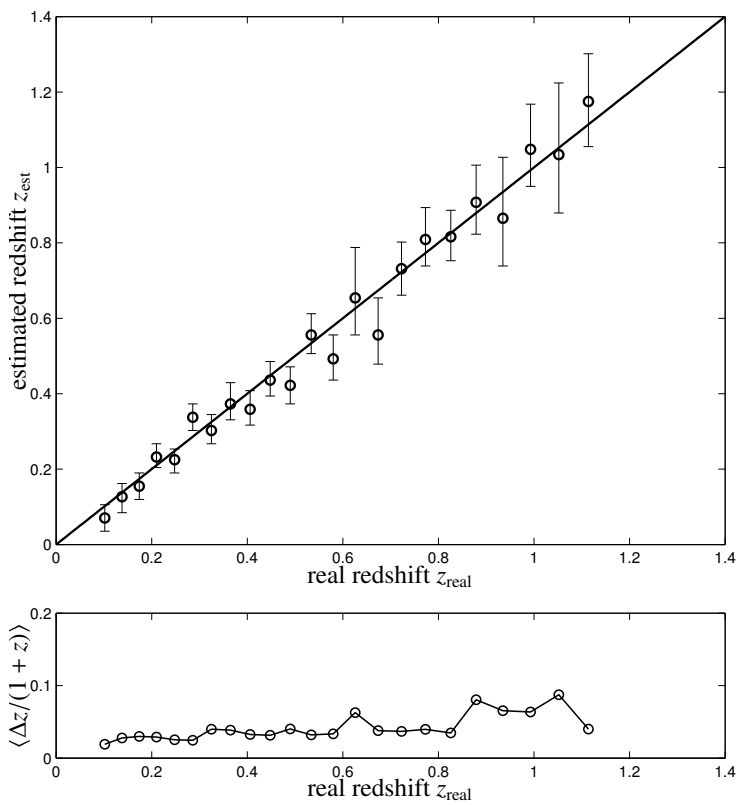


Figure 10.16: Redshift determination and error estimation from all three parameters a , c and s that followed from wavelet analysis with the *sym2*-wavelet. The upper panel shows the estimated redshift z_{est} and its error Δz and the lower panel shows the relative accuracy $\Delta z/(1+z)$, both as a function of redshift z_{real} . Here, CMB fluctuations were not taken into account. The value of the wavelet moments was set to be $q = 3$.

wavelet family	wavelet	$q = 3$	$q = 4$	$q = 5$	$q = 6$
symlet	<i>sym2</i>	4.1%	4.4%	4.7%	4.8%
symlet	<i>sym3</i>	4.3%	4.8%	5.1%	5.2%
Daubechies'	<i>db4</i>	5.2%	5.3%	5.4%	5.4%
Daubechies'	<i>db5</i>	5.5%	5.0%	4.9%	4.8%
coiflet	<i>coif1</i>	4.2%	4.4%	4.8%	5.0%
biorthogonal	<i>bior1.3</i>	5.5%	5.4%	5.4%	5.4%

Table 10.3: Averaged accuracy of the redshift-determination relative to $1+z$ based on three parameters derived from the wavelet spectrum of order q without the noise contribution from the fluctuating CMB.

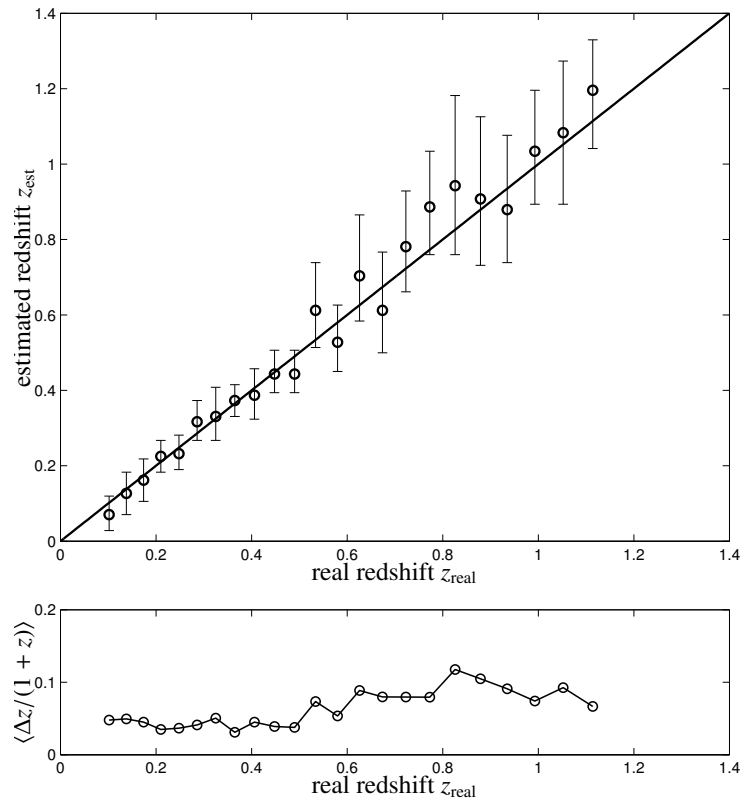


Figure 10.17.: Redshift determination and error estimation from all three parameters a , c and s resulting from wavelet decomposition of the combined maps (i.e. with CMB) using the *sym2*-wavelet. In the upper panel, the estimated redshift z_{est} and its error Δz is shown a function of real redshift z_{real} . In comparison, the relative accuracy $\Delta z / (1 + z)$ as a function of z_{real} is shown in the lower panel. Again, the order of the wavelet moments was taken to be $q = 3$.

wavelet family	wavelet	$q = 3$	$q = 4$	$q = 5$	$q = 6$
symlet	<i>sym2</i>	6.2%	6.3%	6.2%	6.3%
symlet	<i>sym3</i>	6.7%	6.5%	6.4%	7.2%
Daubechies'	<i>db4</i>	6.9%	6.8%	6.9%	6.9%
Daubechies'	<i>db5</i>	7.6%	7.4%	7.3%	7.2%
coiflet	<i>coif1</i>	6.1%	5.9%	6.0%	6.8%
biorthogonal	<i>bior1.3</i>	7.5%	7.4%	7.2%	7.3%

Table 10.4.: Averaged accuracy of the redshift-determination relative to $1 + z$ based on three parameters derived from the wavelet spectrum of order q with the noise contribution CMB caused by fluctuations in the CMB.

single-frequency interferometers results in a deterioration of the redshift estimation accuracy of a factor close to 1.5, which is caused by imperfections of the CMB removal by 5^{th} -order spline polynomials.

It should be kept in mind that the given accuracy estimates depend on the properties of the selected cluster sample. Especially the insufficient sampling of the high-mass end of the Press-Schechter function can be expected to play a significant role and leads to a systematic underestimation of the redshift accuracy.

10.6. Systematics

SZ-clusters would be self-similar and would perfectly follow scaling relations provided several requirements are fulfilled: (i) virial equilibrium ($T \propto M^{2/3}$), (ii) structural identity, expressed in equal form factors, (iii) a universal baryon fraction and (iv) the absence of heating and cooling processes. Each of these assumptions may be challenged and leads to deviations from the self-similar scaling relations. While the first two points are included in the numerical simulation and are limited by the selection criteria, they increase the scatter in the relations between virial quantities, or equally, the wavelet parameters a , c and s . Systematic trends caused by tilted scaling relations (see Sect. 10.6.1) and the formation of cool cores (formerly referred to as cooling flows) (Sect. 10.6.2) as well as the necessity of preselecting clusters (Sect. 10.6.3) need to be addressed separately.

10.6.1. Influence of tilted scaling relations

Analyses of X-ray observations carried out by [Arnaud & Evrard \(1999\)](#) and [Mohr et al. \(1999\)](#) suggest a weak trend of the clusters baryon fraction with cluster mass M and a deviation from the universal value $f_B = \Omega_b/\Omega_m$, which is due to feedback processes like galactic winds that more effectively deplete the ICM of baryons in low temperature clusters compared to high temperature clusters.

The dependence especially of the wavelet parameter a , which is a logarithmic measure of the SZ-flux \mathcal{Y} would be increased in more massive clusters and would thus increase the scatter in a of a cluster sample at a given redshift. The quoted analyses of X-ray data find the baryon fraction to show a relative variation amounting to $\simeq 10\%$ at fixed temperature, i.e. at fixed depth of the potential well for a sample of local clusters. Apart from the systematic component, that can in principle be removed, once high quality X-ray data will improve the understanding of this phenomenon and allows proper modelling, the stochastic contribution can only be constrained to be at most of equal relative influence to $\Delta\mathcal{Y}/\mathcal{Y}$ as the scatter in morphology.

The baryon fraction is estimated from X-ray observations that sample the gas at the cluster core, whereas SZ-effect will be sensitive to the gas at much larger scales. Therefore, since the observed trend is probably due the complicated hydrodynamic and feedback processes at the cluster center, the trend is expected to be much weaker on the scales probed by the SZ effect.

10.6.2. Cool cores of clusters

In order to estimate the accuracy of the method outlined above, so far I only used adiabatic hydrodynamical simulations which lack of cooling processes. Thus I need to address the influence of cool cores of clusters on our proposed

method. After an analytical investigation following Sect. 10.3.2.1 I compare clusters with and without cool cores and show how the morphological changes in cool core clusters impacts on the wavelet spectra.

10.6.2.1. Analytical wavelet transform of cool core clusters

Instead of a single King profile I assume that the SZ-emission of a cool core cluster can be described by a double King profile for reasons of analytical feasibility:

$$y(x) = y(r) = \sum_{i=1}^2 y_i \left[1 + \left(\frac{r}{r_i} \right)^2 \right]^{-1}, \quad (10.42)$$

where the second term describes the additional enhancement owing to the cool core. Deprojecting this two-dimensional profile by means of Pfrommer & Enßlin (2004) yields:

$$p_e(R) = n_e(R) k_B T_e(R) = \frac{m_e c^2}{\sigma_T} \sum_{i=1}^2 \frac{y_i}{\pi r_i} \frac{\mathcal{B}\left(\frac{1}{2}, \frac{3}{2}\right)}{\left(1 + R^2/r_i^2\right)^{3/2}}, \quad (10.43)$$

where R denotes the three-dimensional radius and $\mathcal{B}(a, b)$ denotes the β -function (Abramowitz & Stegun 1965). Thus I obtain for the ratio of the central values of the Comptonisation parameters y_i

$$\frac{y_2}{y_1} = \frac{p_2 r_2}{p_1 r_1} \sim \frac{1}{2}, \quad (10.44)$$

where I inserted typical values for cool core clusters, $p_2/p_1 \sim 3$ and $r_2/r_1 \sim 1/6$. The second order wavelet moment of cool core clusters can be obtained in analogy to the non-cool core case:

$$X_2^{\text{CF}}(\sigma) = 2\pi \int dk k^5 \exp(-k^2 \sigma^2) \left| y_1 r_1^2 K_0(kr_1) + y_2 r_2^2 K_0(kr_2) \right|^2. \quad (10.45)$$

This second order wavelet moment shows an increasing amplitude and a decreasing cutoff parameter compared to the one without a cool core.

10.6.2.2. Numerical analysis

In order to scrutinise these findings I apply the method to adiabatically simulated clusters to which I add an enhanced emission to mimic the SZ-emission of the cool core. In Fig. 10.18 the resulting spectra of wavelet moments are shown together with the fitting formula eqn. (10.35) for increasing wavelet moment order q .

It can clearly be seen in Fig. 10.18 that the enhanced emission due to the cool core yields a slightly higher amplitude of the wavelet spectrum on small scales. Extracting information from the wavelet spectrum by means of eqn. (10.35) reveals slightly higher values for the amplitude a and smaller values for the cutoff c on the percent level. However, this influence is minimised when considering finite instrumental resolution particularly for high redshift clusters. In any case, if a prominent cool core is sufficiently well resolved it could be masked and replaced by an interpolation in between the mask boundaries.

10.6.3. Wavelet analysis of unselected clusters

It is an important issue to quantify the deterioration of the wavelet method when applied to clusters of arbitrary morphologies. In merging systems, for instance, one observes a doubly peaked wavelet spectrum, where the peak at large σ reflects the angular size of the merger system itself, whereas the second peak at smaller σ corresponds to the merging objects. In these systems, the model function eqn. (10.35) does not yield a good fit to the spectrum of wavelet coefficients $X_q(\sigma)$ and hence fails to extract sensible values for the parameters a , c and s . Similarly, pronounced substructure causes deviations from the wavelet spectrum and yield additional power on scales smaller than the cluster scale. In these cases, the model function (c.f. eqn. (10.35)) does not necessarily provide a fit to the wavelet spectrum $X_q(\sigma)$ and it cannot be expected that the wavelet quantities a and c reflect cluster properties such as \mathcal{Y} .

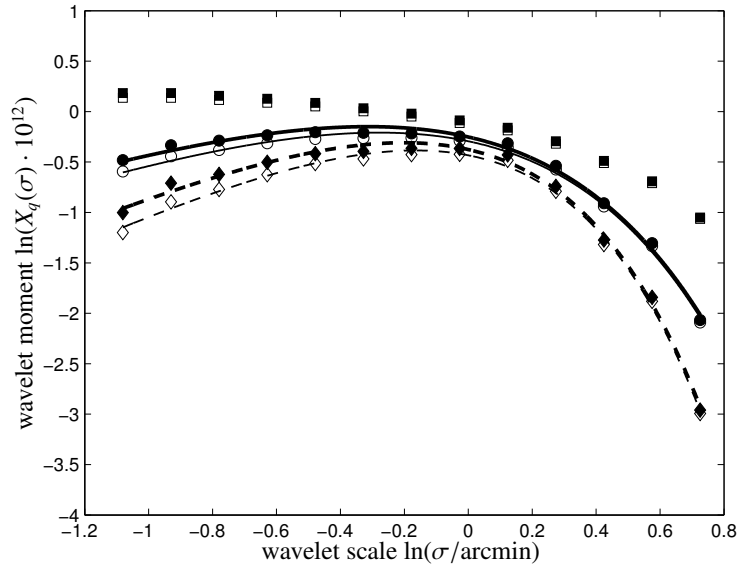


Figure 10.18.: The influence of cool cores to the spectrum of wavelet moments, together with the fitting formula (10.35) for increasing wavelet moment order q : $q = 2$ (squares), $q = 3$ (circles, solid), and $q = 4$ (diamonds, dashed) for a single cluster without instrumental smoothing. Open symbols are values derived from the simulated non-cool core cluster, whereas filled symbols denote the corresponding cool core cluster.

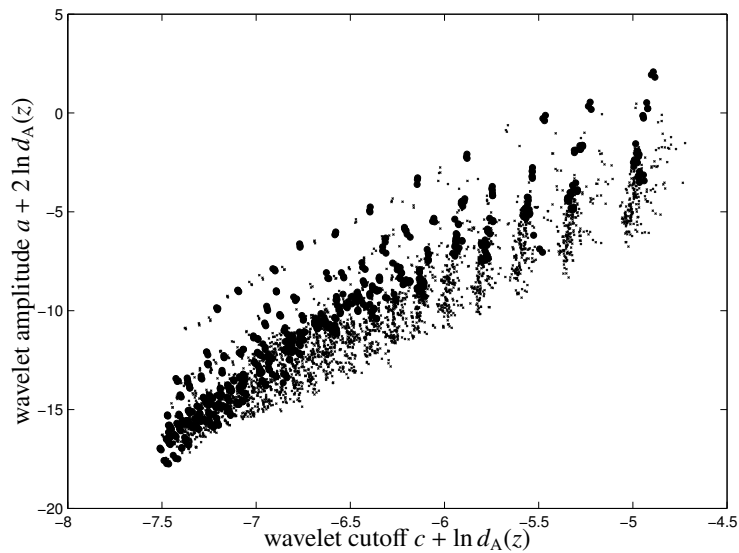


Figure 10.19.: Distance corrected wavelet amplitude $a_0 = a(z) + 2 \cdot \ln(d_A(z))$ as a function of distance corrected wavelet cutoff $c_0 = c(z) + \ln(d_A(z))$ for the selected clusters (circles) and all clusters (crosses) extracted from the simulation outputs. The wavelet moments $X_q(\sigma)$ were considered for $q = 4$ and as the analysing wavelet, the *sym3*-wavelet was employed.

In Fig. 10.19, the distance corrected wavelet amplitude $a_0 = a(z) + 2 \cdot \ln(d_A(z))$ is given as a function of distance corrected wavelet cutoff $c_0 = c(z) + \ln(d_A(z))$, for all clusters resulting from the simulation (in total 3957 maps) and, in comparison, for the selected subsample. The wavelet parameters were derived from a fit to the spectrum $X_q(\sigma)$ of order $q = 4$ with the *sym3*-wavelet as the analysing wavelet. While in Fig. 10.10 the data points follow a narrow track along $a \propto c^5$, this is not observed in Fig. 10.19. Especially for clusters at small wavelet cutoffs c , the scatter in wavelet amplitude a is doubled and data points fall below the region covered by the selected subsample. This might be hinting toward clusters exhibiting substructure, because in these cases the sizes are systematically underestimated by the fit to wavelet spectrum $X_q(\sigma)$. Furthermore, a strong scatter in cutoff c is introduced. Given these significant deteriorations that only partially can be compensated by changes in the redshift models eqn. (10.39), the redshift estimation accuracy is significantly affected.

10.7. Redshift estimation in a nutshell

This section shall provide a short summary of how to apply my method to an SZ-survey for estimating redshifts provided a temperature map of a patch on the sky with resolved images of clusters.

- Once a cluster candidate has been localised at a particular position of the map this cluster and its ambient field has to be cut out. If the number of grid points amounts below 64^2 sampling points, the mesh should be refined by interpolation in order to reach dynamical range of approximately two decades. This is important in order to provide a sufficiently broad range of scales to be probed by the wavelet decomposition.
- The wavelet spectrum of the map is obtained by wavelet transforming the map preferentially using the *symlet* basis functions (compare Sect. 10.3.1). The morphological information contained within the wavelet spectrum can be extracted by means of the model function of eqn. (10.35). In the case of single-frequency observations the ambient CMB field cannot be separated from the SZ-signal of a cluster. The method described in Sect. 10.5.8.2 might be applied in order to reconstruct the wavelet spectrum of the pure SZ-cluster signal.
- The redshift dependence of the wavelet parameters (amplitude a , cutoff c , and slope s) follows the functional form of eqn. (10.39). However, the single model parameters depend on the definitions of the particular wavelets and the details of the survey, including different sources of noise and the cluster detection criteria. The most promising way of determining the parameters of the gauge functions laid down in eqn. (10.39) would be to derive them from a training set of clusters with known (photometric) redshifts. The final redshift estimate of the cluster is most conveniently determined by means of maximum likelihood analysis, as described by eqn. (10.41).

10.8. Summary

In this chapter, a method of estimating the redshift of a cluster based on the wavelet decomposition of its resolved SZ-morphology is presented. From a fit to the spectrum of wavelet moments three spectral parameters are derived, that in turn are non-degenerate and indicative of cluster distance. These parameters are utilized, through a maximum likelihood technique, for estimating the cluster's redshift. In the maximum likelihood technique, empirical gauge functions describing the wavelet parameter's z -dependence are used.

First, the method was tested on a simple analytical case: The spectrum of Mexican-hat wavelet moments can be derived analytically for a King-profile, which is known to describe the Compton- y amplitude of clusters well. The spectrum of wavelet coefficients as a function of wavelet scale σ , exhibits a break at the cluster scale r_c and may thus serve as a measure of the cluster's size. Additionally, the asymptotic behaviour of the wavelet spectrum in the limit of $\sigma \gg r_c$ and $\sigma \ll r_c$ can be understood. The derivation of wavelet moments of order $q = 2$ is analogous to considering the Fourier power spectrum of the Compton- y map, filtered with Fourier transformed wavelet. The shape of the spectrum of wavelet moments of order $q = 2$ from the analytic calculation is consistent with one obtained by applying wavelet decomposition to simulated SZ-cluster maps.

The method was then applied to set of numerically simulated SZ-clusters with $1'$ (FWHM) resolution – comparable to the resolution of future SZ-experiments. The sample comprises 690 cluster maps distributed in 23 redshift bins, which is a comparably large cluster sample. The clusters are chosen such that they are not in a merging state

and their SZ-image is not too elongated, two criteria that favour clusters close to virialisation. Additionally, in order to simulate single-frequency observations, the cluster maps were combined with realisations of the CMB that constitute the main source of noise.

The method was tested for a range of wavelet functions (e.g., *symlet*, *coiflet*, *Daubechies*, *biorthogonal*). The average attainable accuracy in estimating redshifts is found to be almost independent of the specific functional form used, although the *symlet* basis yielded the best results. However, the method could benefit from improvements concerning the choice of the wavelet basis. For instance, one could try to construct an optimised wavelet specifically for β -profiles, that yields maximised wavelet coefficients $\chi(\mu, \sigma)$.

As expected, there is only a weak change in accuracy with respect to the order q of the chosen wavelet moment $X_q(\sigma)$. This, however, is most likely to change when applying the wavelet analysis to noisy images, because for increasing choices of q , uncorrelated noise is suppressed relative to the cluster's signal and concentrating on higher values for q should provide a more robust measurement of the set of structural parameters a , c and s . The increment of q itself is limited by numerics – this is the case when the wavelet moment $X_q(\sigma)$ is dominated by the largest wavelet expansion coefficient $\chi(\mu, \sigma)$, and does not reflect anymore the dependence on the wavelet scale σ . In this limit, the wavelet spectrum would exhibit a generic power law behaviour: $X_q(\sigma) \propto \sigma^{\gamma(q)}$ for large q . The structural parameters a , c and s were found to depend on redshift z by a simple exponential (eqn. (10.39)). The free parameters in this equation can be determined from a (relatively small) sample of SZ-cluster images with known redshift.

The accuracy of determining cluster distances has been assessed by maximum likelihood estimation. The method yields accuracies of 4–5% relative to $1+z$, which is competitive with photometric redshifts, but reaches out to larger distances. At redshifts exceeding $z \gtrsim 1$, the accuracy is expected to degrade because the angular diameter distance $d_A(z)$ starts to level off and thus sets the limit of applicability. For single frequency data, the CMB fluctuations can be removed with a simple polynomial reconstruction approach; the accuracy in the redshift estimation is then decreased to 6–7%.

In this work I have considered two major systematic effects that might degrade the accuracy of the method. The first is the varying baryon fraction with cluster mass, which has been studied only for local cluster samples. While the systematic trend could in principle be corrected for, the stochastic contribution will always add to the uncertainty of the distance determination. Another systematic is the influence of cool cores at the cluster's centre. In this case we have been able to show that the uncertainty it adds to the redshift estimate is very small, mainly because the volume occupied by the cool core region is limited to the cluster's core.

Although the result in the distance estimation is stated in terms of redshift, it should be emphasised that a specific cosmology is assumed, which is needed for converting the observables, namely the wavelet parameters, to a distance estimate. The distances following from the analysis have been expressed as redshifts because of their elementary interpretation, but the implicit assumption of an underlying cosmology should be kept in mind when comparing to e.g. photometric redshifts. For that reason, the precision of the method presented is limited by the accuracy to which the cosmological parameters are known. Apart from being a distance indicator, the redshift also plays the role of an evolutionary parameter.

Comparing this work to the pioneering paper by [Diego et al. \(2003\)](#), my expectations concerning the accuracy of morphological redshifts are even more optimistic: Without fitting β -profiles to the observational data, it is possible to describe the cluster's SZ-morphology by solely relying on wavelet decomposition. Also, I describe the spectrum of wavelet moments with a small set of structural parameters, that have a lucid physical interpretation, provide a non-degenerate distance measurement and enable redshift determination owing to their monotonic decline with redshift. The most important difference is that, the redshift dependence of the structural parameters is calibrated with the data set itself without relying on *prior* and simplifying assumptions. In spite of the small number of observables considered here, the accuracy in the redshift estimation of this method is doubled, in comparison with [Diego et al. \(2003\)](#), even for a single frequency experiment.

The results of this chapter were derived in collaboration with S. Zaroubi (Kapteyn Institute, Groningen) and C. Pfrommer (Max-Planck-Institute for Astrophysics, Garching). A resulting paper entitled Redshift estimation of clusters by wavelet decomposition of their Sunyaev-Zel'dovich morphology has been submitted to the journal Monthly Notices of the Royal Astronomical Society and is available online ([preprint astro-ph/0310613](#)).

11. Coded mask imaging of extended sources with Gaussian random fields

Abstract

A novel method for generating coded mask patterns based on Gaussian random fields (GRF) is proposed. In contrast to traditional algorithms based on cyclic difference sets, it is possible to construct mask patterns that encode a predefined point spread function (PSF). The viability of this approach and the reproducibility of the PSFs is examined, together with studies on the mean transparency, pixel-to-pixel variance and PSF deterioration due to partial shadowing. Sensitivity considerations suggest the construction of thresholded realisations of Gaussian random fields (TGRF) which were subjected to the same analyses. Special emphasis is given to ray-tracing simulations of the pattern's performance under finite photon statistics in the observation of point sources as well as of extended sources in comparison to random masks and the pattern employed in the wide field imager onboard BeppoSAX. A key result is that in contrast to traditional mask generation schemes, coded masks based on GRFs are able to identify extended sources at accessible photon statistics. Apart from simulating on-axis observations with varying levels of signal and background photon counts, partial shadowing of the mask pattern in the case of off-axis observations and the corresponding field-of-view is assessed.

11.1. Introduction

In X-ray astronomy, focusing of radiation is so far feasible only for photon energies up to about 10 keV through grazing incidence reflection. Applied in Wolter-type mirrors, this method can provide a very good angular resolution, i.e. down to $0'.5$ in the case of Chandra¹ and $4'' - 12''$ for XMM-Newton². The collecting area is maximised through the use of nested mirrors. The field-of-view (FOV) is limited by the grazing incidence condition set by the diffractive index of the mirror material to $\lesssim 1^\circ$. At energies higher than 10 keV, focusing is technologically very hard to achieve. A workaround are coded mask imagers, where a position sensitive detector records the shadow of a mask pattern cast by the sources under investigation. The arrangement of sources can be reconstructed by cross-correlating the recorded shadowgram with the mask pattern.

Coded masks have by now found a widespread use in high energy astrophysics and there is a large number of successful missions such as BeppoSAX³, currently flying instruments like INTEGRAL⁴ and HETE-2⁵, and ambitious future projects, for instance the recently launched SWIFT-satellite⁶.

In this chapter, I propose coded mask patterns based on Gaussian random fields, because they enable the construction of a coded mask device for predefined imaging characteristics, i.e. for a given PSF. The shape of the PSF can be tuned to match the anticipated source profile. A beautiful example of a naturally occurring Gaussian random field is the pattern of fluctuations in the cosmic microwave background (CMB). Analyses of WMAP data carried out among others by Cayón et al. (2001) and Komatsu et al. (2003) find the CMB consistent with Gaussian primordial fluctuations and have set upper limits on non-Gaussianity.

After a recapitulation of coded mask imaging and existing mask pattern generation schemes in Sect. 11.2, GRFs are introduced in Sect. 11.3. The feasibility of GRFs in coded mask imagers is examined in Sect. 11.4 with special

¹<http://cxc.harvard.edu/>

²<http://xmm.vilspa.esa.es/>

³<http://beppojax.gsfc.nasa.gov/beppojax/index.html>

⁴<http://astro.estec.esa.nl/SA-general/Projects/Integral/>

⁵<http://space.mit.edu/HETE/>

⁶<http://swift.gsfc.nasa.gov/>

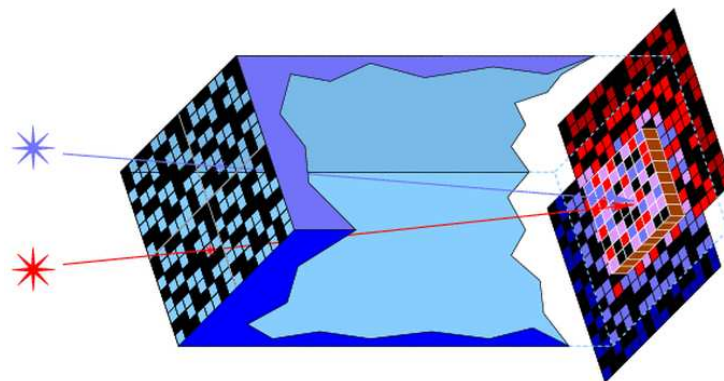


Figure 11.1.: Principle of coded mask imaging: The shadow cast by the coded mask is recorded by a position sensitive detector. The coded mask depicted is that of the IBIS instrument onboard INTEGRAL.

emphasis on the performance of GRFs in realistic scenarios, i.e. under finite photon statistics and in the observation of extended sources (Sect. 11.5). A summary of the key results in Sect. 11.6 concludes the chapter.

11.2. Coded mask imaging

Coded mask cameras observe a source by recording the shadow cast by the mask onto the detector. The mask pattern is described by the position dependent transparency $\psi(x)$. A shifted shadowgram $\psi(x - d \tan(\theta))$ is observed if the radiation incides under an angle θ with respect to the optical axis. The distance between the coded mask and the detector is denoted by d . The correlation function $a(x)$, defined as

$$a(x) = \psi(x - d \tan \theta) \otimes \psi(x) = \langle \psi(x - d \tan \theta + \lambda) \psi(\lambda) \rangle_{\lambda}, \quad (11.1)$$

peaks at $x_0 = d \tan \theta$, from which the angle of incidence $\theta = \arctan(x_0/d)$ can be inferred. The PSF $c(x)$, defined as the correlation function at normal incidence ($\theta = 0^\circ$), i.e. the auto-correlation function, reads

$$c(x) = \psi(x) \otimes \psi(x) = \langle \psi(x + \lambda) \psi(\lambda) \rangle_{\lambda}. \quad (11.2)$$

The influence of imperfections of the detector can be modelled by convolution of $\psi(x)$ with suitable kernels describing the positional detector response (see, e.g. Schäfer & Kawai 2003). Techniques for analysing coded mask data have been summarised by Skinner et al. (1987) and Caroli et al. (1987). A nice illustration of the imaging principle of coded mask cameras is given by Fig. 11.1.

Random mask patterns as used in the HETE-2 satellite (in 't Zand et al. 1994) consist of white noise. They are not ideal imagers, because their auto-correlation possess sidelobes and are not perfectly flat. Aiming at δ -like PSFs, mask patterns based on cyclic difference sets have been introduced by Gunson & Polychronopoulos (1976). As pointed out by Fenimore & Cannon (1978), these uniformly redundant arrays (URA) provide even sampling at all spatial scales. URA patterns are less susceptible to noise compared to truly random arrays and their auto-correlation function is a δ -spike with perfectly flat sidelobes in case of complete imaging. In this chapter, I propose a method for constructing coded mask pattern encoding arbitrary PSFs. While the traditional masks are optimised for the observation of point sources, the PSFs of masks based on GRFs can be adjusted to the source profile of extended sources and make the observation of extended sources such as extended structures in the Milky Way possible.

11.3. Gaussian random fields

11.3.1. Definitions

The statistical properties of a GRF are homogeneous and isotropic and the phases of different Fourier modes are mutually uncorrelated and random. A consequence of the central limit theorem is then that the amplitudes follow

a Gaussian distribution. Due to all correlations above the two-point level being either vanishing in the case of odd moments or being expressible in terms of two-point functions for even moments, the statistics of amplitude fluctuations in a GRF is completely described by its power spectrum $P(k)$ (see eqn. (11.4)).

Because the imaging characteristics of coded mask imagers are described by the PSF, which is defined to be the auto-correlation function of their mask pattern, i.e. by their power spectrum in case of isotropic PSFs, GRFs provide a tool for generating mask patterns with predefined imaging characteristics. The theory of structure formation in cosmology and the description of the cosmic microwave background makes extensive use of GRFs (c.f. Peacock 1999, Longair 1998). Their application is commonplace in generating initial conditions for simulations of cosmic structure formation and in constructing mock CMB fields for simulating sub-millimetric observations.

11.3.2. Algorithm

Starting from the PSF $c(\mathbf{x})$, the Fourier transform $C(\mathbf{k})$ is derived:

$$C(\mathbf{k}) = \mathcal{F}[c(\mathbf{x})] = \int \frac{d^2x}{(2\pi)^2} c(\mathbf{x}) \exp(-i\mathbf{k}\mathbf{x}). \quad (11.3)$$

The power spectrum $P(k)$ is defined as the Fourier-transform $C(\mathbf{k})$ of the auto-correlation function $c(\mathbf{x})$. In more than one dimension, an average of the Fourier transform $C(\mathbf{k})$ of the statistically isotropic random field $c(\mathbf{x})$ over all directions of the wave vector \mathbf{k} at fixed length $k = |\mathbf{k}|$ needs to be performed:

$$P(k) = \langle |C(\mathbf{k})| \rangle_{|\mathbf{k}|=k}. \quad (11.4)$$

All elementary waves $\exp(i\mathbf{k}\mathbf{x})$ with wave vectors in the k -space shell $[|\mathbf{k}|, |\mathbf{k} + \Delta\mathbf{k}|]$ contribute to the variance $\sigma_k^2 = P(k)$ required by the power spectrum on scale $k = |\mathbf{k}|$. In discretising, the amplitudes $\Psi(\mathbf{k})$ are set such that their quadratic sum $\sum_{\mathbf{k} \in [|\mathbf{k}|, |\mathbf{k} + \Delta\mathbf{k}|]} |\Psi(\mathbf{k})|^2$ matches σ_k^2 with the only exception $\Psi(\mathbf{k} = 0)$, which is set to zero in order to ensure a vanishing expectation value of the realisation $\psi(\mathbf{x})$. The normal modes $\exp(i\mathbf{k}\mathbf{x})$ are modified by a phase factor $\exp(2\pi i q)$, where $q \in [0, 1)$ is a uniformly distributed random number. By inverse Fourier transform, the normal modes $\Psi(\mathbf{k})$ are brought to interference which finally results in the realisation, the real part of which is denoted by $\psi(\mathbf{x})$:

$$\psi(\mathbf{x}) = \Re(\mathcal{F}^{-1}[\Psi(\mathbf{k})]) = \Re\left(\int d^2k \Psi(\mathbf{k}) \exp(i\mathbf{k}\mathbf{x} + 2\pi i q)\right). \quad (11.5)$$

Alternatively, one may require the additional symmetry $\Psi(-\mathbf{k}) = \Psi^*(\mathbf{k})$ in Fourier space (the complex conjugation is denoted by the asterisk), which forces the realisation to be purely real. The flow chart eqn. (11.6) summarises all steps:

$$\begin{array}{ccc} C(\mathbf{k}) & \xrightarrow{\langle \dots \rangle_{|\mathbf{k}|=k}} & P(k) \xrightarrow{\cdot \exp(2\pi i q)} \Psi(\mathbf{k}) \\ \mathcal{F} \uparrow & & \downarrow \mathcal{F}^{-1} \\ c(\mathbf{x}) & & \psi(\mathbf{x}). \end{array} \quad (11.6)$$

Due to the periodic boundary conditions imposed by the Fourier transform, the resulting realisations of the Gaussian random field have cyclic boundaries, which is a desirable feature for coded mask patterns. For reasons of numerical accuracy, it is strongly recommended to use shells in \mathbf{k} -space with varying thickness $\Delta\mathbf{k} \propto |\mathbf{k}|^{-1}$, such that approximately the same number of discretised modes contributes to the variance required by the power spectrum $P(k)$.

11.3.3. Choice of the PSF

Although the algorithm outlined in Sect. 11.3.2 is capable of generating random fields $\psi(\mathbf{x})$ encoding any isotropic PSF $c(\mathbf{x})$, PSFs should be shaped like Lorentzian functions $c_L(x)$ or Gaussian functions $c_G(x)$. The parameter σ_x describes the spatial extent:

$$c_L(x) = \frac{\sigma_x^2}{x^2 + \sigma_x^2}, \quad (11.7)$$

$$c_G(x) = \exp\left(-\frac{x^2}{2\sigma_x^2}\right). \quad (11.8)$$

The normalisation has been chosen such that the maximum correlation strength at $x = 0$ is set to one. In the realisation $\psi(\mathbf{x})$, the variable σ_x , that parameterises the PSF can be interpreted as a correlation length. [Skinner & Grindlay \(1993\)](#) have pursued a related idea and have suggested coded masks with two spatial scales. In contrast, the realisations considered here have an entire spectrum of length scales.

11.3.4. Scaling applied to the Gaussian random fields

If one aims at employing GRFs in coded mask imagers, the field has to be scaled such that it assumes values ranging from $\psi(\mathbf{x}) = 0$ (opaqueness) to full transparency ($\psi(\mathbf{x}) = 1$). This scaling ensures that the full dynamical range between is used and the modulation of the shadowgram as strong as possible. Hence, the sensitivity is maximised. One could think of two different linear transformations, the most intuitive being:

$$\psi(\mathbf{x}) \longrightarrow \psi^*(\mathbf{x}) = \frac{\psi(\mathbf{x}) - \min\{\psi(\mathbf{x})\}}{\max\{\psi(\mathbf{x})\} - \min\{\psi(\mathbf{x})\}}. \quad (11.9)$$

With the symmetry condition $\max\{\psi(\mathbf{x})\} = -\min\{\psi(\mathbf{x})\}$ being fulfilled, the mean transparency $\langle\psi^*(\mathbf{x})\rangle$ is equal to $1/2$: The mean $\langle\psi(\mathbf{x})\rangle = 0$ vanishes by construction, because each normal mode $\cos(\mathbf{k}\mathbf{x})$ has a vanishing expectation value. In general, the realisation $\psi(\mathbf{x})$ will not fulfill the above mentioned symmetry condition.

Instead, the scaling

$$\psi(\mathbf{x}) \longrightarrow \psi'(\mathbf{x}) = \frac{1}{2} \left[\frac{\psi(\mathbf{x})}{\max\{|\psi(\mathbf{x})|\}} + 1 \right] \quad (11.10)$$

ensures $\langle\psi'\rangle = 1/2$ and will be used in the remainder of the chapter. It should be noted that none of the above scalings strictly conserves Gaussianity, because each particular realisation is scaled by its maximal amplitude and consequently, high amplitudes do not appear any more in an ensemble of realisations.

Now that the mean transparency $\langle\psi'\rangle$ is fixed, the absolute flux from a source can be inferred from the number of measured photons. The scaling eqn. (11.9) may be taken advantage of in designing a mask that blocks a larger or smaller fraction of photons than the generic fraction of $1/2$: In anticipation of Sect. 11.4.3, in the case of a realisation of a GRF encoding a Gaussian PSF $c_G(x)$ with $\sigma_x = 8$ pixels, the probability density $p(\langle\psi^*\rangle)d\langle\psi^*\rangle$ of the mean transparency $t = \langle\psi^*\rangle$ is described by a Gaussian distribution with mean $\mu_t = 0.504 \pm 0.082$ and standard deviation $\sigma_t = 0.028 \pm 0.006$ at 95% confidence. When constructing realisations of Gaussian fields for coded mask instruments, one obtains patterns with transparencies $\langle\psi^*\rangle \in [\mu_t - \sigma_t, \mu_t + \sigma_t]$ with a probability of $\text{erf}(1/\sqrt{2}) \approx 0.6827$.

11.3.5. Gaussian random fields for circular apertures

For coded-mask experiments with a circular aperture it is possible to construct GRFs with azimuthal symmetry, in the same way as hexagonal uniformly redundant arrays (HURA) are an adaptation of the URA patterns to circular apertures ([Finger & Prince 1985](#)). Instead of constructing a GRF with plane waves as the solutions of Laplace's equation $\Delta\psi(\mathbf{x}) = (\partial_x^2 + \partial_y^2)\psi(\mathbf{x}) = 0$ in Cartesian coordinates ($\mathbf{x} = (x, y)$) with boundary conditions $\psi(\mathbf{x} = -L) = 0 = \psi(\mathbf{x} = L)$ ($2L$ denotes the pattern's side length) one would resort to solving $\Delta\psi(\mathbf{r}) = (\partial_r^2 + 1/r\partial_r + 1/r^2\partial_\phi^2)\psi(\mathbf{r}) = 0$ in polar coordinates ($\mathbf{r} = (r, \phi)$) with the boundary condition $\psi(r = R) = 0 \forall\phi$, where the radius of the aperture is denoted as R . ψ is easily found as the solution to Bessel's differential equation and reads as:

$$\psi_{\ell m}(r, \phi) = J_m[r \cdot Z_m(\ell)] \cdot \exp(im\phi), \quad (11.11)$$

where the numbers ℓ and m are only allowed to assume integer values. $Z_m(\ell)$ is the ℓ^{th} zero of the Bessel function J_m . In Fig. 11.2, three solutions are depicted for $(\ell, m) = (2, 2)$, $(\ell, m) = (2, 3)$ and $(\ell, m) = (3, 4)$. In reality, it might be cumbersome to construct a GRF on the basis of the normal modes given by eqn. (11.11) due to Bessel function's complicated orthonormality relations.

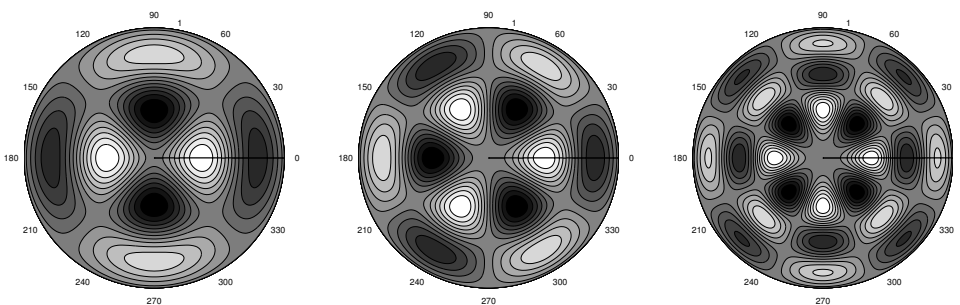


Figure 11.2.: Normal modes $\psi_{\ell m}(r, \phi)$ used for constructing GRFs for circular apertures, for $(\ell, m) = (2, 2)$ (left panel), $(\ell, m) = (2, 3)$ (centre panel) and $(\ell, m) = (3, 4)$ (right panel).

11.4. Results

In order to provide a visual impression, two GRFs encoding the above stated PSF with their auto-correlation functions are presented (Sect. 11.4.1). Subsequently, the reproducibility of the chosen PSF (Sect. 11.4.2), the pixel-to-pixel variance (Sect. 11.4.3), the Gaussianity of the distribution of pixel amplitudes (Sect. 11.4.4) and the shape of the PSF under partial shadowing (Sect. 11.4.5) are examined. Finally, thresholded GRFs are introduced and the deterioration of the PSF of such thresholded realisations (Sect. 11.4.6) is addressed.

11.4.1. Visual impression

Following the above prescription, 100 realisations of GRFs encoding Gaussian and Lorenzian PSFs of different widths σ_x were generated on a 2-dimensional square grid with 256^2 mesh cells. Figs. 11.3 and 11.4 show a realisation of the GRF and its auto-correlation function for a Gaussian and a Lorenzian PSF, respectively. In order to facilitate comparison, the widths of the PSFs have been chosen to be the same: $\sigma_x = 8$ pixels. The random fields are scaled to mean values of $1/2$ (by means of eqn. (11.10)) and the central correlation strength in the auto-correlation functions is equal to 1. The contours have a linear spacing of 0.1. The auto-correlation functions have the symmetry property that $\psi(\mathbf{x}) \otimes \psi(\mathbf{x}) = \psi(-\mathbf{x}) \otimes \psi(-\mathbf{x})$. In the derivation of auto-correlation and cross-correlation functions, the balanced correlation scheme was used. The correlation functions were derived for ideal detectors, i.e. finite position resolution or similar imperfections were neglected.

In comparing the realisations in Figs. 11.3 and 11.4 one notices the larger abundance of small scale structures in the realisation encoding the Lorenzian PSF $c_L(x)$ in comparison to the realisation derived for the Gaussian PSF $c_G(x)$. This can be explained by the fact that the power spectrum $P_L(k)$ declines $\propto \exp(-k)$ and thus much slower than the power spectrum $P_G(k) \propto \exp(-k^2)$. Both realisations have been derived with the same random seed, i.e. the relative phases are identical and one immediately recognises similar structures in $\psi_G(\mathbf{x})$ and $\psi_L(\mathbf{x})$.

11.4.2. Reproducibility of the PSF

An important issue is the reproducibility of a chosen PSF $c(x)$ in realisations generated with differing random seeds. This can be assessed by determining the auto-correlations of the scaled GRFs $\psi'(\mathbf{x})$ for all realisations within the data sample. In Fig. 11.5 the Gaussian target PSF $c_G(x)$ and the auto-correlation functions $\psi'_G(\mathbf{x}) \otimes \psi'_G(\mathbf{x})$ following from two realisations $\psi(\mathbf{x})$ are shown. The error bars denote the sample variance derived from 100 realisations of $\psi_G(\mathbf{x})$ following from different random seeds. The width of the PSF was chosen as $\sigma_x = 8\sqrt{2}$ pixels for better visibility. Fig. 11.6 shows the analogous for the Lorenzian target PSF $c_L(x)$ with $\sigma_x = 8\sqrt{2}$ pixels.

As Figs. 11.5 and 11.6 illustrate, the functional shape of the target PSF $c(x)$ can be reproduced with high reliability and the ratio of the peak-height to the correlation noise is ≈ 40 . However, there are minor imaging artefacts, namely very weak sidelobes: This is readily explained by the fact that the Fourier transform of a well localised PSF in real space is extended and affected by the cutoff at the Nyquist frequency k_{Nyquist} , which induces a $\sin(k_{\text{Nyquist}}x)/x$ -like modulation. Consequently, the sidelobes are suppressed in PSFs with large σ_x . The Lorenzian PSF is a bad choice

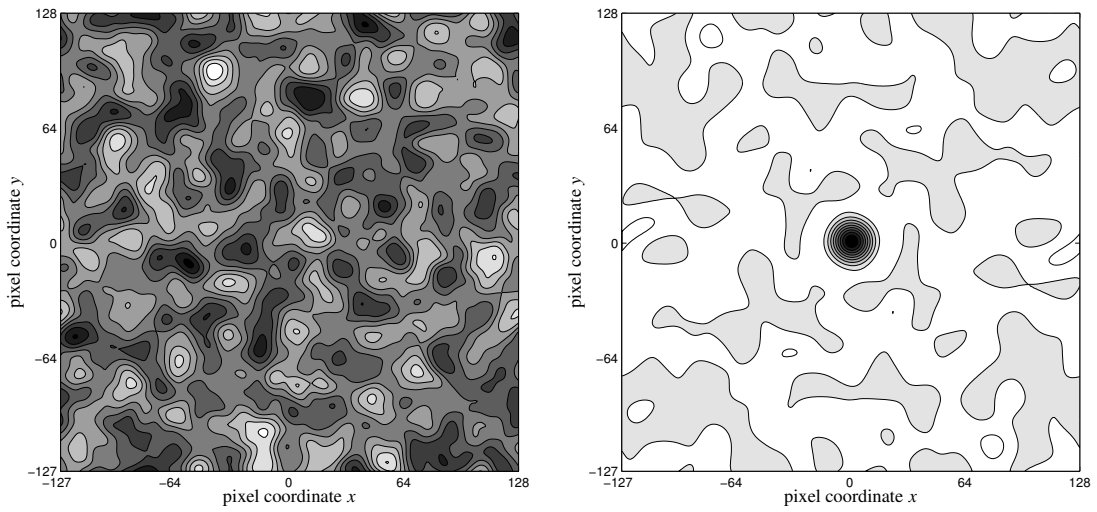


Figure 11.3.: A realisation of a GRF $\psi_G(\mathbf{x})$ (upper panel) for the Gaussian PSF $c_G(x)$ and the auto-correlation function $\psi_G(\mathbf{x}) \otimes \psi_G(\mathbf{x})$ (lower panel).

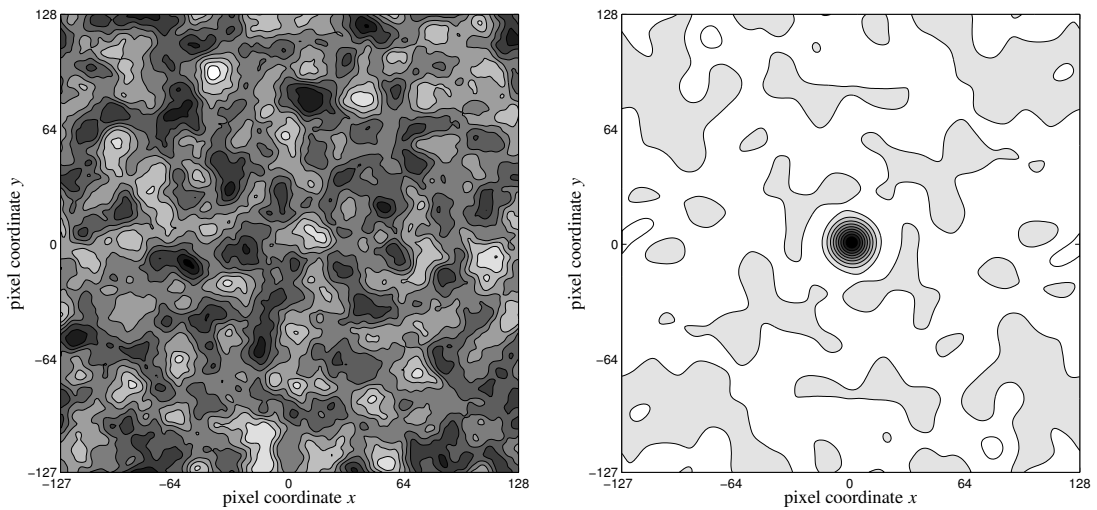


Figure 11.4.: A realisation of a GRF $\psi_L(\mathbf{x})$ (upper panel) for the Lorentzian PSF $c_L(x)$ and the auto-correlation function $\psi_L(\mathbf{x}) \otimes \psi_L(\mathbf{x})$ (lower panel).

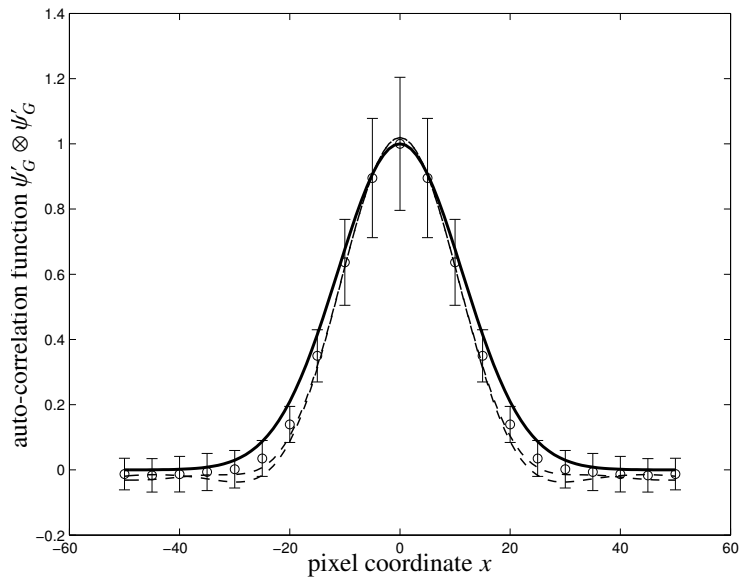


Figure 11.5: Cross section along the x -axis through the central part of the auto-correlation function $\psi'_G(x) \otimes \psi'_G(x)$ for two different realisations $\psi'_G(x)$ (dashed) and the Gaussian target curve $c_G(x)$ (solid).

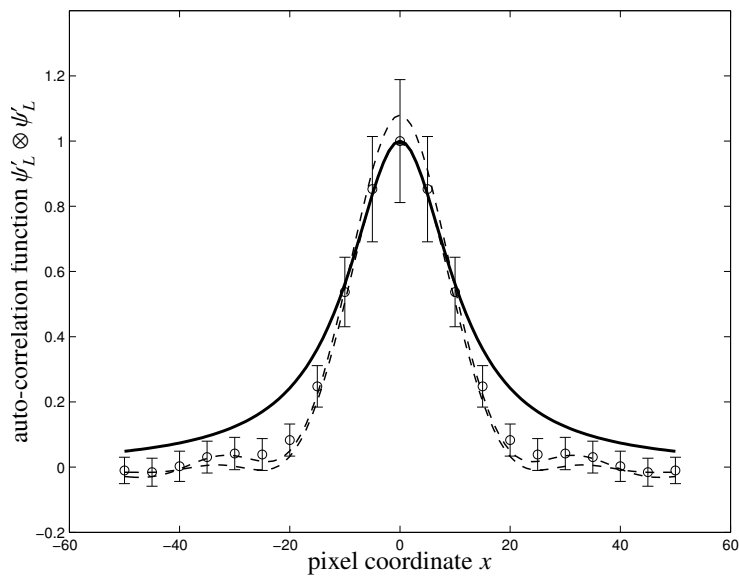


Figure 11.6: Cross section along the x -axis through the central part of the auto-correlation function $\psi'_L(x) \otimes \psi'_L(x)$ for two different realisations $\psi'_L(x)$ (dashed) and the Lorentzian target curve $c_L(x)$ (solid).

PSF width	mean transparency	variance	standard deviation
σ_x	$\langle \psi' \rangle$	$\langle \psi'^2 \rangle - \langle \psi' \rangle^2$	$\sqrt{\langle \psi'^2 \rangle - \langle \psi' \rangle^2}$
$2\sqrt{2}$	1/2	0.013 ± 0.002	0.116 ± 0.009
4	1/2	0.014 ± 0.002	0.121 ± 0.010
$4\sqrt{2}$	1/2	0.016 ± 0.003	0.128 ± 0.012
8	1/2	0.018 ± 0.003	0.135 ± 0.013

Table 11.1.: The mean transparencies $\langle \psi' \rangle$, the variance $\langle \psi'^2 \rangle - \langle \psi' \rangle^2$ and the standard deviation $\sqrt{\langle \psi'^2 \rangle - \langle \psi' \rangle^2}$ together with their respective uncertainties (1σ) for a set of GRFs encoding Gaussian PSFs with differing width σ_x .

in comparison to the Gaussian PSF, because its Fourier transform $C(k) \propto \exp(-k)$ decays slower and is consequently more affected by the cutoff at k_{Nyquist} . Interpreting σ_x as the correlation length of the GRF, it is clear that in the limit of very narrow PSFs σ_x assumes very small values, i.e. the amplitudes $\psi(\mathbf{x})$ for neighbouring pixels start losing their correlation. This, however, does not correspond to white noise masks because the amplitude distribution is still Gaussian (c.f. Sect. 11.4.4) and not bimodal, as in the case of white noise masks. Due to the high confidence with which a chosen PSF is reproduced, the number of realisations to be examined is very small. On the contrary, relying on truly random patterns, the number of necessary realisations with the accompanying tests may be very high: For HETE-2, where such a random pattern is used, 10^5 realisations had to be generated that were subjected to certain boundary conditions (see in 't Zand et al. 1994).

11.4.3. Pixel-to-pixel variance

In sensitivity considerations carried out by in 't Zand et al. (1994) for purely random masks, i.e. masks consisting of either transparent ($\psi'(\mathbf{x}) = 1$) or opaque ($\psi'(\mathbf{x}) = 0$) pixels, optimised mean transparency $\langle \psi' \rangle$ and standard deviation $\sqrt{\langle \psi'^2 \rangle - \langle \psi' \rangle^2}$ are derived to be equal to 1/2. In that way, the variance and therefore the modulation of the signal is maximised. For the GRFs considered here, the variance and hence the modulation of the shadowgram is noticeably smaller. In Table 11.1, the mean transparencies $\langle \psi' \rangle$, the variance $\langle \psi'^2 \rangle - \langle \psi' \rangle^2$ and the standard deviation $\sqrt{\langle \psi'^2 \rangle - \langle \psi' \rangle^2}$ together with their respective uncertainties for a set of GRFs encoding Gaussian PSFs with differing width σ_x are summarised.

One would expect that with increasing PSF width σ_x the variance decreases, which would be explained by the fact that the variance is given by a weighted integration over the power spectrum $P(k)$. For increased position resolution, i.e. a narrow PSF $c(x)$, a wide power spectrum $P(k)$ is needed, which in turn would lead to a high variance.

This simple argument however, does not straightforwardly apply to the scaled realisations at hand: As laid down in eqn. (11.10), the field $\psi(\mathbf{x})$ is modified by a factor depending on the maximal value $|\psi(\mathbf{x})|$ of the particular realisation. The occurrence of a high amplitude is following a Gaussian distribution with variance $\propto \int d^2k P(k)$. This means, that in the case of narrow PSFs $c(x)$, i.e. for wide power spectra $P(k)$, the field $\psi(\mathbf{x})$ is more likely to assume large amplitudes (compare Cartwright & Longuet-Higgins 1956). The latter effect is of great importance and causes the surprising result that the measured variances in $\psi'(\mathbf{x})$ are larger for extended PSFs.

Comparing coded masks based on GRFs with purely random fields, the modulation of the shadowgram decreases by a factor $\sim 3 \dots 4$. Therefore, the sensitivity is expected to be weaker. While the above consideration is only valid for the observation of point sources, sensitivity is most likely to be gained in the observation of extended sources. For those sources, it is possible to adjust the PSF to the expected source intensity profile. In this case, modulations below the scale of the object to be observed are discarded - this corresponds to applying Wiener filtering to the recorded shadowgram prior to source reconstruction.

11.4.4. Distribution of the pixel amplitudes

As Fig. 11.7 illustrates, the pixel amplitudes $\psi(\mathbf{x})$ follow a Gaussian distribution, irrespective of the encoded PSF,

$$p(\psi') d\psi' = \frac{1}{\sqrt{2\pi}\sigma_\psi} \exp\left(-\frac{(\psi' - \mu_\psi)^2}{2\sigma_\psi^2}\right) d\psi', \quad (11.12)$$

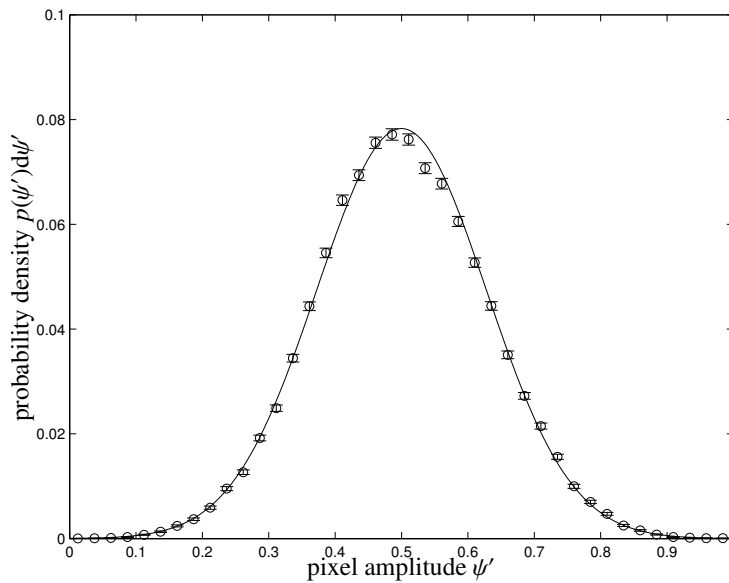


Figure 11.7.: Probability density $p(\psi')d\psi'$ of the pixel amplitudes $\psi'(\mathbf{x})$ (circles) and the best-fitting Gaussian for a particular realisation of a GRF. The error bars are Poissonian errors.

as a consequence of the central limit theorem (see [Kendall & Stuart \(1958\)](#)). The mean and variance of that particular realisation have been determined to be $\mu_\psi = 0.5000 \pm 0.001$ and $\sigma_\psi = 0.1277 \pm 0.0007$ at 95% confidence. For illustrative purposes, a Gaussian PSF with $\sigma_x = 2\sqrt{2}$ pixels has been chosen.

Again, it should be emphasised that the scaling eqn. (11.10), while being reasonable from the physical point of view, is not conserving Gaussianity. This is for the application at hand not a serious limitation, because the variance of the distribution $p(\psi')d\psi'$ is small compared to 1.

11.4.5. Partial shadowing

It is interesting to see how partial shadowing affects shape and amplitude of the auto-correlation function. If a source is observed at large off-axis angles, the shadowgram cast by the coded mask onto the detector is incomplete and reconstruction artefacts emerge in the correlation function. In order to examine the extent to which the PSF suffers from partial shadowing, the amplitudes $\psi_G(\mathbf{x})$ in a margin amounting to a fraction of 25%, 50% and 75% of the total area have been set to zero and the cross-correlation function $\psi_G(\mathbf{x}) \otimes \psi_G^{shadow}(\mathbf{x})$ has been determined with the full coded mask.

As Fig. 11.8 shows for a Gaussian PSF with $\sigma_x = 8$ pixels, the PSF drops in central amplitude according the unshadowed area, but otherwise its shape remains unaltered. A second observation is that the amplitude of the sidelobes is unaffected by the partial shadowing.

The reconstructed PSF $\psi'_G(\mathbf{x}) \otimes \psi_G^{shadow}(\mathbf{x})$ for the case of radiation from a source situated at large angles away from the optical axis, where only 1/32 of the mask has been imaged onto the detector is depicted in Fig. 11.9. Even though a tiny part of the mask amounting to $\approx 3\%$ has been imaged, the correlation peak is clearly recognisable and its peak value is a factor ≈ 4 above the correlation noise.

11.4.6. Thresholded realisations

Due to possible technical complications in attempting to build a coded mask pattern based on a GRF with quasi-continuous opaqueness, thresholded realisations are considered. A second argument in favour of thresholded realisations would be their achromatic properties, because the mask has to be constructed from the field $\psi'(\mathbf{x})$ for a specific photon distribution in order to assure the maximal modulation of the shadowgram cast onto the detector. Yet another argument in favour of thresholded realisations of GRFs is their better sensitivity, because they imprint a

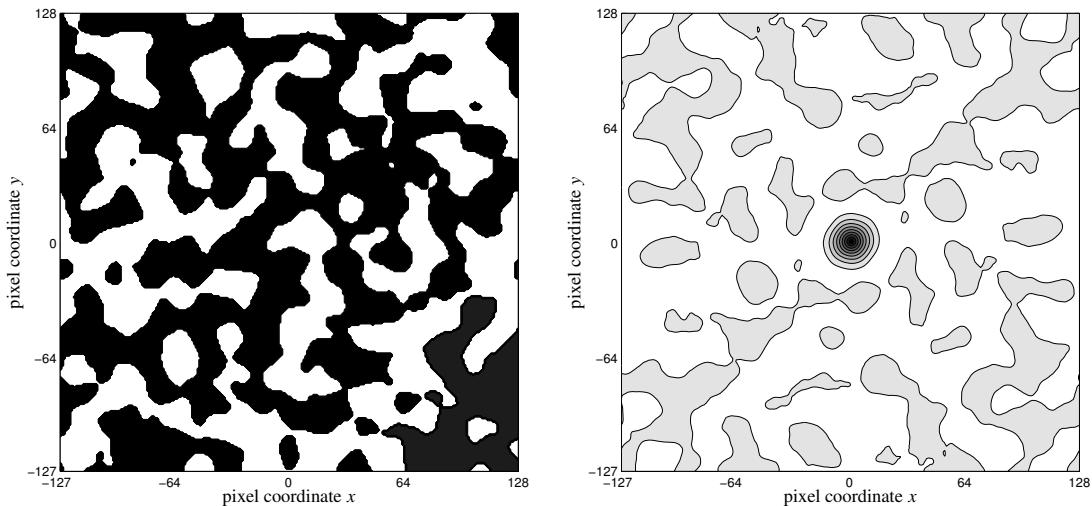


Figure 11.10.: A thresholded realisation $\psi_G^{(t)}(\mathbf{x})$ of a GRF $\psi_G(\mathbf{x})$ (upper panel) for the Gaussian PSF $c_G(x)$ and the auto-correlation function $\psi_G^{(t)}(\mathbf{x}) \otimes \psi_G^{(t)}(\mathbf{x})$ (lower panel).

stronger modulation of the shadowgram compared to smoothly varying GRFs.

In thresholded realisations, mask elements are taken to be transparent, if the value $\psi(\mathbf{x})$ of the realisation is greater than zero, conversely, for values $\psi(\mathbf{x}) < 0$ the mask element is set to be opaque. An example for a thresholded realisation of a GRF and its PSF is given in Fig. 11.10.

An important issue is the degradation of the PSF $\psi_G^{(t)}(\mathbf{x}) \otimes \psi_G^{(t)}(\mathbf{x})$ imposed by the thresholding. As Fig. 11.11 illustrates, the resulting auto-correlation function is pointy and its kurtosis is larger than zero (leptokurtic). This results from the fact that small scale power is added by the thresholding: In order to construct a step transition, more small-scale Fourier modes are needed, which leads to an additive power law contribution $\propto k^{-2}$ in the power spectrum $P(k)$, such that the power spectrum acquires Lorentzian wings. The point spread function $\psi_G^{(t)}(\mathbf{x}) \otimes \psi_G^{(t)}(\mathbf{x})$, being the inverse Fourier transform of $P(k)$, can then be approximated by two decaying branches of an exponential, which readily explains the pointiness. The target Gaussian PSF $c_G(x)$ with $\sigma_x = 8\sqrt{2}$ pixels is shown for comparison. Again, the error of the auto-correlation function is estimated by determining the sample variance in 100 realisations.

The size distribution of the patches as a function of threshold value can be described by means of the Press-Schechter theory well known in cosmology. [Press & Schechter \(1974\)](#), [Bond et al. \(1991\)](#) and [Mo & White \(2002\)](#) provide the mathematical foundation.

11.5. Ray-tracing simulations including finite photon statistics

Extensive ray-tracing simulations were performed describing the imaging of point sources with a finite number of photons (Sect. 11.5.1), and the attainable sensitivity in such an observation was assessed (Sect. 11.5.2). The analogous was carried out for the observation of extended sources (Sect. 11.5.3). Finally, the size of the field-of-view in the case of GRFs compared to traditional masks is examined (Sect. 11.5.4). In the following, coded mask patterns based on Gaussian random fields are compared to purely random mask patterns and the mask pattern used in the WFI-instrument onboard *BeppoSAX*.

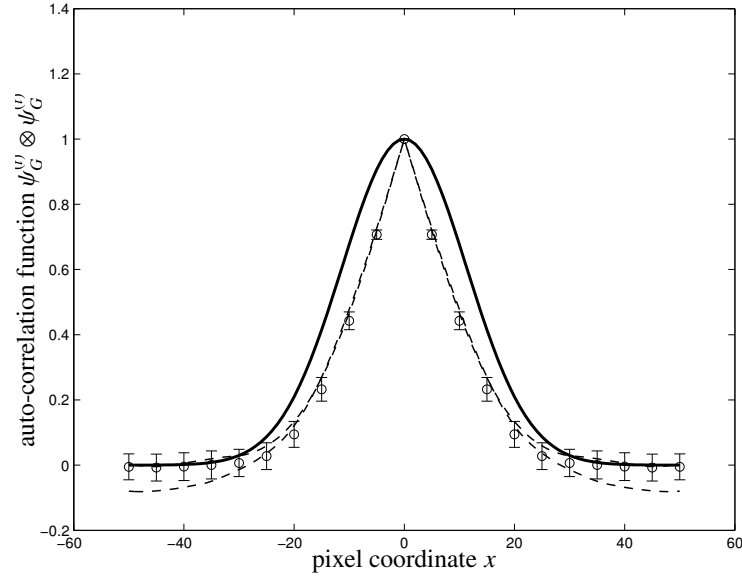


Figure 11.11.: Deterioration of the auto-correlation function $\psi_G^{(i)}(x) \otimes \psi_G^{(i)}(x)$ from two thresholded realisations $\psi_G^{(i)}(x)$ (dashed) in comparison to the initial Gaussian PSF $c_G(x)$ (solid).

11.5.1. Simulation setup

In the following, the performance of the coded mask is examined as a function of photon statistics. The statistical significance σ of a simulated observation is defined to be

$$\sigma = \frac{N_{\text{source}}}{\sqrt{N_{\text{bg}}}}, \quad (11.13)$$

where N_{source} and N_{bg} denote the source and background count rates, respectively. Here it should be emphasised, that σ , N_{source} and N_{bg} always refer to the number of actually detected photons which makes a difference when considering the coded mask employed in BeppoSAX's WFI instrument, in which the average transparency is not equal to $1/2$.

Observations were simulated by randomly choosing $2N_{\text{source}}$ homogeneously distributed photon impact positions \mathbf{x} across the mask face. In order to emulate the random process of photons penetrating the mask, a homogeneously distributed random number r from the interval $r \in [0 \dots 1]$ was drawn for each photon, and compared to the value $\psi(\mathbf{x})$ of the GRF at the same position \mathbf{x} . In the case $r > \psi(\mathbf{x})$ the photon was assumed to be able to penetrate the mask, whereas in the case $r \leq \psi(\mathbf{x})$ the photon was taken to be absorbed by the mask. For BeppoSAX's mask pattern, which has an average transparency of $1/3$, a total number of $3N_{\text{source}}$ photons was simulated.

For the background, which was assumed to be homogeneous, N_{bg} photon impact positions were determined and the count rates in the corresponding pixels were increased accordingly. Background count rates were fixed to a value of $N_{\text{bg}} = 10^4$ photons, which are typical for an instrument like WFI in a 100 second exposure.

The resulting field $\psi^{(\text{sim})}$ containing the number of photons that struck a certain pixel was then correlated with the original mask pattern ψ , again using balanced correlation. In the next step, the highest peak was localised in the correlated data field $\psi^{(\text{sim})} \otimes \psi$ and its significance Σ was determined by comparing the peak height $a_{\text{max}} = \max\{\psi^{(\text{sim})} \otimes \psi\}$ to the level of fluctuations $\sigma_{\psi}^2 = \langle (\psi^{(\text{sim})} \otimes \psi)^2 \rangle$ in the field. If the peak had a significance $\Sigma = a_{\text{max}}/\sigma_{\psi}$ exceeding 3 and was located at a position which deviated less than half a PSF width from the nominal position, the simulated detection was taken to be successful. A particular realisation of a Gaussian random field was exposed to 100 simulated photon distributions from which the detection probability p (i.e. the occurrence of a $\geq 3\sigma_{\psi}$ -peak located at the correct position) and the false detection probability q (i.e. the occurrence of a $\geq 3\sigma_{\psi}$ -peak at a wrong position) was derived. The sample variance in comparing 100 realisations of Gaussian random fields was used to derive errors on p and q . For the purpose of this work, the detector efficiency and position response were assumed

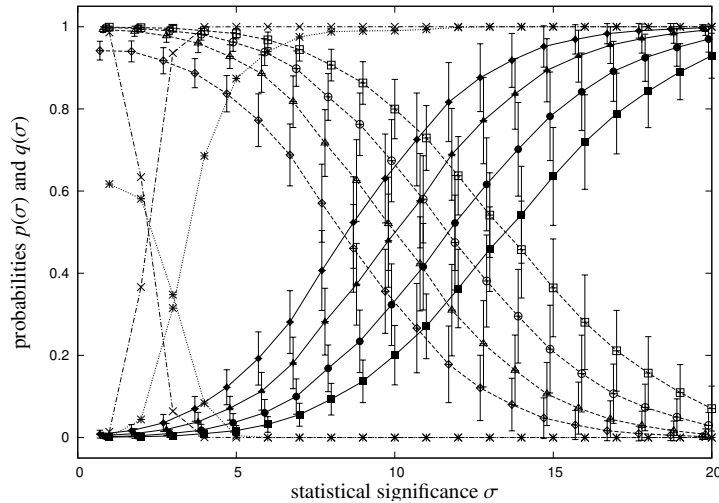


Figure 11.12.: Point source sensitivity in on-axis observations of a set of GRFs: The detection probability $p(\sigma)$ (solid lines, closed symbols) and the false detection probability $q(\sigma)$ (dashed lines, open symbols) are plotted as functions of statistical significance σ for PSF widths $\sigma_x = 2$ (squares), $\sigma_x = 2\sqrt{2}$ (circles), $\sigma_x = 4$ (triangles) and $\sigma_x = 4\sqrt{2}$ (diamonds), in comparison to purely random masks (dotted line, stars) and BeppoSAX-WFI pattern (dash-dotted line, crosses). In contrast to the ensemble of GRFs it is not possible to state an ensemble variance for $p(\sigma)$ and $q(\sigma)$ in the case of BeppoSAX's pattern. The data points have been slightly displaced for better visibility.

to be ideal.

11.5.2. Point source sensitivity of a set of Gaussian random fields

Fig. 11.12 shows the detection probability p and the false detection probability q as a function of photon statistics, expressed in terms of statistical significance σ for GRFs, a purely random mask and BeppoSAX's URA pattern. The source was assumed to lie on the optical axis, i.e. the mask pattern is imaged completely onto the detector. Common to all mask patterns is the fact that p rises with statistical significance, and that q drops accordingly. But while reliable observations can be done using the BeppoSAX-pattern or random patterns even at low photon statistics of $2 - 3\sigma$, the patterns based on GRFs require high photon fluxes. For them, observations are feasible starting from $\approx 9\sigma$. The reason why GRFs are less sensitive to the traditional mask pattern is the fact that they imprint a weaker modulation of the shadowgram. Furthermore, one immediately notices the trend that the patterns are more sensitive for wider PSF widths due to the increase in variance of the mask pattern with increasing PSF width. Thus, position resolution is traded for sensitivity.

Fig. 11.13 shows the analogous results for an off-axis observation in which only half of the mask pattern has been imaged onto the detector. The result corresponds to the findings for the case of normal incidence, but $p(\sigma)$ and $q(\sigma)$ are shifted to higher values of σ , which is due to the fact, that only half of the photons actually reach the detector and that the reconstruction has to cope with the decreased signal. Again, one attains higher sensitivities for wider PSFs in the case of patterns based on GRFs.

Common to all figures is the fact, that the curves $p(\sigma)$ and $q(\sigma)$ are not adding up to one, which is caused by the combined criterion where apart from the correct peak position a minimal peak height above the correlation background is required, which is often not fulfilled in the cases of low photon statistics.

11.5.3. Sensitivity in observations of extended sources

In addition, suitable simulations were carried out in order to assess the performance of GRFs in the observation of extended sources, such as supernova remnants, structures in the Milky Way and clusters of galaxies. Typical sizes of those sources range between arcminutes and a degree. For simplicity, the source was assumed to be described by a Gaussian profile with extension $\sigma_{\text{profile}} = 2$ pixels. The shadowgram recorded in observations of extended sources

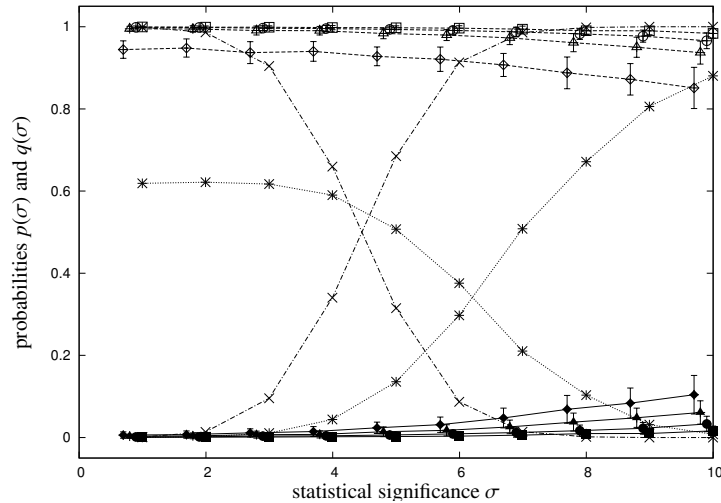


Figure 11.13: Point source sensitivity in off-axis observations (50% obscuration) of a set of GRFs: The detection probability $p(\sigma)$ (solid lines, closed symbols) and the false detection probability $q(\sigma)$ (dashed lines, open symbols) are given for PSF widths $\sigma_x = 2$ (squares), $\sigma_x = 2\sqrt{2}$ (circles), $\sigma_x = 4$ (triangles) and $\sigma_x = 4\sqrt{2}$ (diamonds), in comparison to purely random masks (dotted line, stars) and BeppoSAX's WFI pattern (dash-dotted line, crosses).

are superpositions of slightly displaced point source shadowgrams, where the relative intensities follow from the source profile. Consequently, the imaging of extended sources is simulated by convolving the mask pattern with the source profile prior to the ray-tracing. Despite that, the image reconstruction has been carried out with the unconvolved mask pattern.

Fig. 11.14 gives the dependence of the detection probability p and the corresponding q on the photon counting statistic σ . In the observation of extended sources, the patterns based on GRFs are superior to the traditional approaches: While reliable detections can be achieved starting from $\sigma \gtrsim 10$ (for $\sigma_x = 4\sqrt{2}$) up to $\sigma \gtrsim 20$ (for $\sigma_x = 2$), the performance of the traditional masks is notably worse. At the examined levels of photons statistics, the detection probability p stays close to zero and shows but a shallow increase with σ in the case of BeppoSAX's URA pattern.

The good performance of the GRFs, and their decreasing performance with correlation length, i.e. PSF width σ_x is of course to be traced back to the fact, that mask patterns with large structures are less affected by the convolution with the source profile than mask patterns exhibiting small structures; in the extreme case of random masks or BeppoSAX's pattern, the structures are washed out and consequently, the modulation of the shadowgram is very weak. This can be circumvented, however, by tuning the angular size of a mask pixel to match the angular size of the source to be observed.

11.5.4. Field-of-view in the observation of point sources

Now, the size of the field-of-view, i.e. the minimal fraction of the mask pattern required to be imaged onto the detector in order to yield a significant detection peak is investigated. For that purpose, the point source detection probability p and the false detection probability q are considered to be functions of the obscuration Q , which is defined as the fraction of the mask area imaged onto the detector. The number of background photons was kept fixed to be $N_{\text{bg}} = 10^4$, while the number of source photons N_{source} was diminished by this factor of Q prior to the ray-tracing. Their number was fixed to yield a significance of $\sigma = 20$ for $Q = 1$, i.e. for the case of complete imaging. The background photons were assumed to be homogeneously distributed. The simulation and the derivation of the values for $p(Q)$ and $q(Q)$ were carried out in complete analogy to Sect. 11.5.2.

The results are depicted in Fig. 11.15: While the traditional patterns show a good performance and have a high detection probability $p(Q)$ for values of $Q \gtrsim 0.1$ (BeppoSAX's pattern) and $Q \gtrsim 0.2$ (random mask), the GRFs fall behind significantly in performance. Imaging is only possible in the cases where a fraction of at least $Q = 0.5 \dots 0.6$

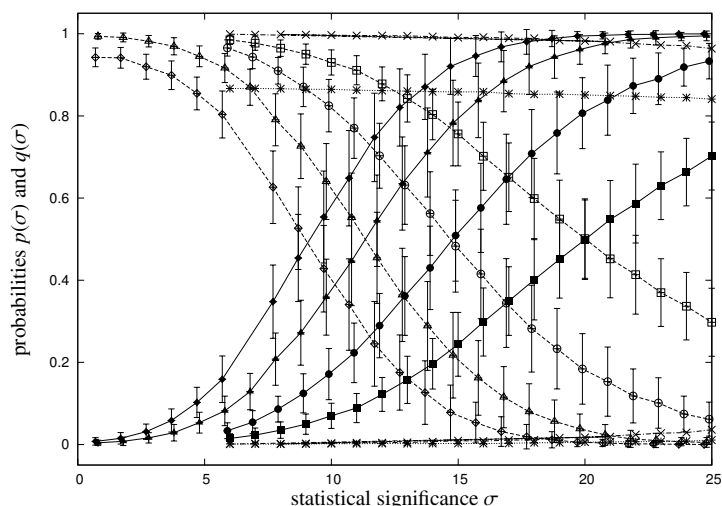


Figure 11.14.: Sensitivity in on-axis observations of extended sources of a set of GRFs: The detection probability $p(\sigma)$ (solid lines, closed symbols) are given along the false detection probability $q(\sigma)$ (dashed lines, open symbols) for PSF widths of $\sigma_x = 2$ (squares), $\sigma_x = 2\sqrt{2}$ (circles), $\sigma_x = 4$ (triangles) and $\sigma_x = 4\sqrt{2}$ (diamonds), in comparison to purely random masks (dotted line, stars) and BeppoSAX's WFI pattern (dash-dotted line, crosses).

of the mask has been imaged onto the detector, resulting in a decrease of the field-of-view of about a factor of 3...5, which renders the usage of GRFs very unlikely in survey missions. Again, the GRF patterns encoding wide PSFs are more sensitive and yield larger fields-of-view than GRFs with narrow PSFs.

11.6. Summary and outlook

In this article, a new algorithm for generating coded masks is presented that allows the construction of a mask with defined imaging properties, i.e. point spread functions.

- The viability of constructing a coded mask for a predefined PSF as a realisation of a GRF has been shown. For realisations generated with differing random seeds, the shape of the PSF is reproducible with high accuracy. Due to the reproducibility of the PSF, the parameter space is greatly reduced and the necessity of running extensive Monte-Carlo simulations is alleviated.
- The generation of 2-dimensional URA patterns requires the number of pixels in each direction to be incommensurable, i.e. they are not allowed to have a common divisor. While twin prime numbers exist, mask patterns generated that way are almost, but not quite square (Miyamoto 1977, Proctor et al. 1979). Coded masks based on GRFs may have any side length and any ratio of side lengths. Additionally, sizes chosen equal to 2^n , $n \in \mathbb{N}$ enable the usage of fast Fourier transforms. Realisations of GRFs have cyclic boundary conditions which is a desirable feature for coded mask imagers.
- The average transparency of coded mask patterns based on scaled GRFs is equal to 1/2, irrespective of the PSF they encode. The pixel amplitudes of a realisation are Gaussianly distributed as a consequence of the central limit theorem. The pixel-to-pixel variance, however, is smaller in the case of GRFs compared to purely random fields, which results in a weaker modulation of the shadowgram and hence the sensitivity is expected to be smaller. The variance shows the trend of decreasing with increasing PSF width, which is caused by the scaling with the maximal values of the realisation.
- Coded masks based on GRFs are chromatic in contrast to purely random fields: The mask pattern has to be designed for a specific spectral distribution of photons due to semi-transparent mask elements. Any mismatch in the photon spectrum of a source under observation would result in a less pronounced modulation of the

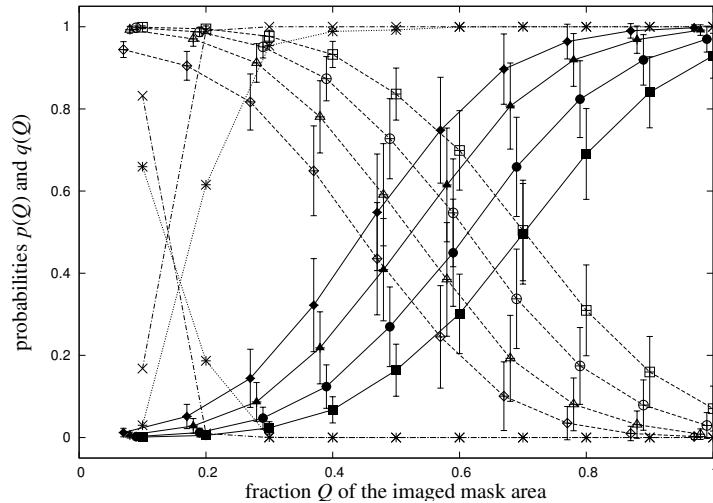


Figure 11.15.: Decrease of the field-of-view: The source detection probability $p(Q)$ (solid lines, closed symbols) and the false detection probability $q(Q)$ (dashed lines, open symbols) as functions of the obscuration Q are shown for a set of Gaussian random fields for varying PSF width: $\sigma_x = 2$ (squares), $\sigma_x = 2\sqrt{2}$ (circles), $\sigma_x = 4$ (triangles) and $\sigma_x = 4\sqrt{2}$ (diamonds). In comparison, a purely random mask (dotted line, stars) and BeppoSAX's WFI pattern (dash-dotted line, crosses) are considered.

shadowgram, which in turn affects the sensitivity of the coded mask imager. A possible workaround is the usage of thresholded Gaussian random fields, that show pointy auto-correlation functions in contrast to smooth target PSFs. Another advantage is their enhanced sensitivity due to the stronger modulation of the shadowgram. The properties of thresholded realisations, however, show a large sample variance which requires selections with suitable criteria after construction.

- Ray-tracing simulations including finite photons statistics and background noise show, that the sensitivity of GRFs falls behind that of purely random masks and URA patterns like the one employed in BeppoSAX by a factor of $2 \dots 3$ in the observation of *point sources*, depending on PSF width. For GRFs, the sensitivity was found to depend exponentially on PSF width, one is trading sensitivity for position resolution.
- The sensitivity of patterns based on GRFs is significantly better in the observation of *extended sources* because their comparably large structures are less affected by the convolution with the source profile than traditional masks that possess pronounced structures on small scales.
- Finally, the size of the field-of-view of GRFs in comparison to traditional masks is examined. It is found that reliable imaging can only performed with GRFs, if a large fraction of the mask is imaged onto the detector. In contrast, purely random masks and especially BeppoSAX's URA pattern enable imaging at large off-axis angles. Comparing the resulting fields-of-view for the preset number of photons shows, that the field-of-view of patterns based on GRFs are smaller by a factor of $3 \dots 5$ (depending on PSF width).

Although the shortcomings of Gaussian random fields with respect to point source sensitivity, chromaticity and localisation accuracy make their usage in observing point sources doubtful, they may find application in observations of extended sources, while simultaneously providing a moderate performance in the observation of point sources. Coded mask patterns on the basis of GRFs may be aesthetically pleasing because they utilise an abstract cosmological concept for a technological application.

A paper entitled *Coded mask imaging of extended sources with Gaussian random fields* which summarises the contents of this chapter has been submitted to the journal *Monthly Notices of the Royal Astronomical Society* and is available online ([preprint astro-ph/0407286](https://arxiv.org/abs/1904.07286)).

12. Gravitational Lensing

12.1. Introduction

Gravitational light deflection (Einstein 1911, 1916, 1936) has evolved since its first observational confirmation during a solar eclipse in 1919 (Dyson et al. 1920) which was a grand confirmation of Einstein's theory of relativity, to a sound tool in astronomy and cosmology. Of special interest to this thesis is the gravitational light deflection on the cosmological large scale structure which can be observed by tiny distortions of images of distant galaxies. In this chapter, the theory of gravitational light deflection is developed (Sect. 12.2), with special emphasis on gravitational light deflection of the large scale structure. In Sect. 12.3, a code is described, that can perform ray-tracing studies of gravitational light deflection on numerical simulations of cosmic structure formation.

12.2. Gravitational light deflection

12.2.1. Light deflection from Fermat's principle

The equation for the propagation of light through arbitrary space times is given by the geodesic equation (Misner et al. 1973). The Minkowski metric of special relativity is assumed to be weakly perturbed by the gravitational potential Φ . In this case, the line element ds reads:

$$(ds)^2 = \left(1 + \frac{2}{c^2}\Phi\right)c^2 dt^2 - \left(1 - \frac{2}{c^2}\Phi\right)d\mathbf{x}^2 \quad (12.1)$$

For a geodesic, the line element ds vanishes:

$$ds = 0 \longrightarrow \left(1 + \frac{2}{c^2}\Phi\right)d^2 t = \left(1 - \frac{2}{c^2}\Phi\right)d\mathbf{x}^2. \quad (12.2)$$

From this, an effective index of refraction n_{eff} can be derived:

$$\frac{|\mathbf{dx}|}{dt} = c' = \frac{c}{n_{\text{eff}}} \text{ with } n_{\text{eff}} \equiv 1 - \frac{2\Phi}{c^2} > 1, \quad (12.3)$$

i.e. light travels slower in potential wells. This immediately gives the time delay of a light ray transversing a gravitational field, commonly referred to as the Shapiro delay:

$$dt = \left|\frac{d\mathbf{x}}{c'}\right| = n_{\text{eff}} \frac{|\mathbf{dx}|}{c} \longrightarrow \Delta t = -\frac{2}{c^3} \int |\mathbf{dx}| \Phi \quad (12.4)$$

The photon trajectory can be parameterised by $\mathbf{x}(s)$ in terms of an affine parameter s , chosen such that $|\mathbf{dx}/ds| = 1$, with the initial point \mathbf{x}_i and the final point \mathbf{x}_f . The local tangent to the photon trajectory is defined by $\mathbf{e} \equiv d\mathbf{x}/ds$. Fermat's principle now states that the path actually taken by the photon minimises the run time $\int n_{\text{eff}} d|\mathbf{x}|$:

$$\delta \int_{\mathbf{x}_i}^{\mathbf{x}_f} ds \sqrt{\frac{d\mathbf{x}^2}{ds^2}} n_{\text{eff}}(\mathbf{x}(s)) = 0 \quad (12.5)$$

Carrying out the variation for the specific choice of s yields:

$$\nabla n - \mathbf{e}(\mathbf{e}\nabla n) - \frac{d\mathbf{e}}{ds}n = 0 \longrightarrow \frac{d\mathbf{e}}{ds} = \frac{\nabla_{\perp} n}{n} = \nabla_{\perp} \ln n \simeq -\nabla_{\perp} \left(\frac{2\Phi}{c^2}\right) \quad (12.6)$$

Here, the perpendicular gradient is defined by $\nabla_{\perp} \equiv \nabla - \mathbf{e}(\mathbf{e}\nabla)$. The deflection angle α is easily obtained as difference between the initial and final tangents:

$$\frac{d\mathbf{e}}{ds} = -\frac{2}{c^2}\nabla_{\perp}\Phi \longrightarrow \hat{\alpha} = \mathbf{e}_f - \mathbf{e}_i = \frac{2}{c^2} \int ds \nabla_{\perp}\Phi \quad (12.7)$$

In cosmological applications, the deflection angle $\hat{\alpha}$ is very small (below 1', such that the integration can be carried out along a straight line in the neighbourhood of the deflecting mass instead of the lensing geodesic, which corresponds to the Born approximation in atomic and nuclear physics. Hence, the change of direction of a light ray is taken to happen instantaneously and the distribution of masses giving rise to a gravitational deflection can be considered to be collapsed onto a surface mass density $\kappa(\theta)$. The lensing potential $\psi(\theta)$, which replaces the gravitational potential Φ in this limit, can be obtained by solving the two-dimensional Laplace equation $\Delta\psi(\theta) = 2\kappa(\theta)$, where the natural logarithm is now the Green-function for the Laplacian, and the deflection angle is given by $\alpha(\theta) = \nabla\psi(\theta)$:

$$\psi(\theta) = \frac{1}{\pi} \int d^2\theta' \kappa(\theta') \ln|\theta - \theta'| \quad \text{with } \kappa(\theta) = \left(\frac{c^2}{4\pi G} \frac{D_s}{D_d D_{ds}} \right)^{-1} \int dz \rho(\xi, z). \quad (12.8)$$

12.2.2. Cosmological weak lensing

12.2.2.1. Imaging by a cosmological lens: the lens equation

The lens equation can be read off from Fig. 12.1:

$$\boldsymbol{\eta} = \frac{D_s}{D_d} \boldsymbol{\xi} - D_{ds} \hat{\alpha}(\boldsymbol{\xi}), \quad (12.9)$$

where the D 's denote the angular diameter distances. Introducing angular variables $\boldsymbol{\eta} = D_s \boldsymbol{\beta}$ and $\boldsymbol{\xi} = D_d \boldsymbol{\theta}$ yields the lens equation

$$\boldsymbol{\beta} = \boldsymbol{\theta} - \frac{D_{ds}}{D_s} \hat{\alpha}(\boldsymbol{\theta}) \equiv \boldsymbol{\theta} - \boldsymbol{\alpha}, \quad (12.10)$$

i.e. a source at true position $\boldsymbol{\theta}$ can be seen by an observer at position $\boldsymbol{\theta}$. The reduced deflection angle $\boldsymbol{\alpha}$ is given by the gradient $\nabla_{\perp}\psi$ of the lensing potential ψ . The distortion of galaxy images is given by the Jacobian of the optical mapping:

$$\mathbf{J} = \frac{\partial \boldsymbol{\beta}}{\partial \boldsymbol{\theta}} = \left(\delta_{ij} - \frac{\partial^2 \psi(\boldsymbol{\theta})}{\partial \theta_i \partial \theta_j} \right) = \begin{pmatrix} 1 - \kappa - \gamma_1 & -\gamma_2 \\ -\gamma_2 & 1 - \kappa + \gamma_1 \end{pmatrix} \quad (12.11)$$

with the convergence κ and the two components of shear γ_1 and γ_2 , which manifest themselves in the distortion of galaxy images.

12.2.2.2. Weak lensing observables

The shape of (elliptical) galaxies can be described by the complex ellipticity,

$$\epsilon \equiv \frac{Q_{xx} - Q_{yy} + 2iQ_{xy}}{Q_{xx} + Q_{yy} + 2\sqrt{Q_{xx}Q_{yy} - Q_{xy}^2}}, \quad (12.12)$$

which is built from the second moments Q_{ij} of the brightness distribution $I(\boldsymbol{\theta})$, centered on $\bar{\boldsymbol{\theta}}$,

$$Q_{ij} = \frac{\int d^2\theta I(\boldsymbol{\theta})(\theta_i - \bar{\theta}_i)(\theta_j - \bar{\theta}_j)}{\int d^2\theta I(\boldsymbol{\theta})}, \quad (12.13)$$

with $(i, j) \in \{x, y\}$. Gravitational lensing distorts the apparent shape of background galaxies. The transformation between the (complex) source ellipticity ϵ' and the image ellipticity ϵ is given by:

$$\epsilon = \frac{\epsilon' + g}{1 + g^* \epsilon'} \quad \text{for } |g| \leq 1 \quad \text{and} \quad \epsilon = \frac{1 + (\epsilon')^* g}{(\epsilon')^* - g^*} \quad \text{for } |g| > 1. \quad (12.14)$$

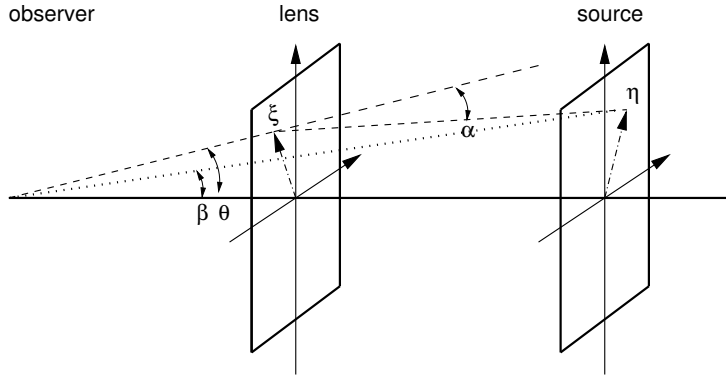


Figure 12.1.: Geometry of a gravitational lensing system. The distance to the lens is denoted by D_d , the distance to the source by D_s , and the distance from the lens to the source by D_{ds} .

with the reduced shear g , being of the order $g \approx 10^{-2}$ in typical weak lensing applications:

$$g(\boldsymbol{\theta}) = \frac{\gamma(\boldsymbol{\theta})}{1 - \kappa(\boldsymbol{\theta})}. \quad (12.15)$$

12.2.3. Applications of weak lensing in cosmology

12.2.3.1. Inversion of shear maps

A primary application of weak lensing data is the reconstruction of cluster mass maps. The distortion of images of background galaxies can be used to determine the tidal gravitational field of a cluster. The original algorithm by [Kaiser & Squires \(1993\)](#) has been improved and extended by a number of authors, most notably by [Schneider & Seitz \(1995\)](#) and [Seitz & Schneider \(1995, 1996, 1997\)](#). The shear field $\gamma(\boldsymbol{\theta})$ can be obtained by convolution of the surface mass density $\kappa(\boldsymbol{\theta})$ with the kernel \mathcal{D} :

$$\gamma(\boldsymbol{\theta}) = \frac{1}{\pi} \int d^2\theta' \mathcal{D}(\boldsymbol{\theta} - \boldsymbol{\theta}') \kappa(\boldsymbol{\theta}') \quad \text{with} \quad \mathcal{D}(\boldsymbol{\theta}) = \frac{\theta_2^2 - \theta_1^2 - 2i\theta_1\theta_2}{|\boldsymbol{\theta}|^4} = -\frac{1}{(\theta_1 - i\theta_2)^2} \quad (12.16)$$

This equation can be inverted in Fourier space, which yields a convolution relation linking the shear field to the surface mass density up to an overall additive constant κ_0 . Complications that arise include boundary artifacts, violation of the weak lensing assumption and random distribution of lensed galaxies which causes additional shot noise to error estimators.

12.2.3.2. Cosmic shear

The weak distortion of the images of background galaxies due to lensing on the large-scale structure is commonly referred to as cosmic shear. It has been discovered almost simultaneously by several groups ([Bacon et al. 2000](#), [Kaiser 2000](#), [van Waerbeke et al. 2000](#), [Wittman et al. 2000](#)). From the angular 2-point correlation function $C_\kappa(\ell)$ of a weak lensing quantity, e.g. the weak lensing convergence κ , the normalisation σ_8 of the dark matter power spectrum $P_\delta(k)$ can be determined with Limber's equation ([Bartelmann & Schneider 2001](#)):

$$C_\kappa(\ell) = \frac{9H_0^4 \Omega_M^2}{4c^4} \int_0^{w_H} dw \frac{\bar{W}^2(w)}{a^2(w)} P_\delta\left(\frac{\ell}{f_K(w)}, w\right), \quad \text{with} \quad \bar{W}(w) = \int_w^{w_H} dw' G(w') \frac{f_K(w' - w)}{f_K(w')}. \quad (12.17)$$

In this equation, $G(w)$ denotes the distance distribution of the background sources to be imaged, w_H is the horizon size out to which the integration dw along the line-of-sight is extended, and $f_K(w)$ takes care of the geometry of the universe.

12.3. Ray-tracing simulations on the large-scale structure

12.3.1. A ray-tracing code for cosmological n -body simulations: `leica.c`

For ray-tracing studies on cosmological density fields, one needs to solve the transport equation numerically in an efficient way:

$$\frac{d^2}{dw^2}\mathbf{x} + K\mathbf{x} = -\frac{2}{c^2}\nabla_{\perp}\Phi(\mathbf{x}), \quad (12.18)$$

where \mathbf{x} is the position of the light ray, w the comoving distance to the observer, K the spatial curvature and Φ the gravitational potential. This is reached by discretising the density field into so-called lens planes along the radial comoving variable w (Schneider et al. 1992, Jain et al. 2000). In this approximation, the smooth lensing geodesic is replaced by a series of straight lines and the Born approximation is used for determining the deflection on each lens plane. The matter content $\delta(\mathbf{x})$ in each slice of thickness Δw at distance w_i is projected onto the lens planes perpendicular to w to yield the surface mass density $\delta_i^{\text{proj}}(\mathbf{x}, w_i)$:

$$\delta_i^{\text{proj}}(\mathbf{x}, w_i) = \int_{w_i - \frac{\Delta w}{2}}^{w_i + \frac{\Delta w}{2}} dw \delta(\mathbf{x}). \longrightarrow \Delta\psi_i(\mathbf{x}) = \frac{8\pi G}{3c^2} \delta_i^{\text{proj}}(\mathbf{x}) \quad (12.19)$$

From the projected overdensity field $\delta_i^{\text{proj}}(\mathbf{x})$, the lensing potential $\psi_i(\mathbf{x})$ is most conveniently obtained by solving Laplace's equation in Fourier space.

The (angular) position θ_i of the light ray on the plane i can be determined from the angle θ_{i-1} and the perpendicular gradient of the lensing potential on the plane $i-1$:

$$\theta_i = \theta_{i-1} - \frac{f_K(w_i - w_{i-1})}{a(w_{i-1})f_K(w_i)} \nabla_{\perp}\psi_{i-1} \text{ with the initial angle } \theta_0 \quad (12.20)$$

The gradient has to be evaluated at the spatial position of the ray on the $(i-1)^{\text{th}}$ plane, i.e. at $\mathbf{x}_{i-1} = f_K(w_{i-1})\theta_{i-1}$. In this equation, $f_K(w)$ is the angular diameter distance, which is defined as:

$$f_K(w) = \begin{cases} \frac{1}{\sqrt{K}} \sin(\sqrt{K}w) & , \Omega_K > 0, \text{ spherical,} \\ w & , \Omega_K = 0, \text{ flat,} \\ \frac{1}{\sqrt{|K|}} \sinh(\sqrt{|K|}w) & , \Omega_K < 0, \text{ hyperbolic.} \end{cases} \quad (12.21)$$

K denotes the curvature of spatial hypersurfaces, $\Omega_K = \Omega_M + \Omega_{\Lambda} - 1$ and $K = (H_0/c)^2\Omega_K$. The shear of light rays is evaluated by computing the evolution of Jacobian matrix \mathbf{J} on each lens plane i :

$$\mathbf{J}_i = \mathbf{J}_{i-1} - \frac{f_K(w_{i-1})f_K(w_i - w_{i-1})}{a(w_{i-1})f_K(w_i)} \mathbf{U}_{i-1} \cdot \mathbf{J}_{i-1} \text{ with circular initial beams, } \mathbf{J}_0 = \begin{pmatrix} 1 & 0 \\ 0 & 1 \end{pmatrix} \quad (12.22)$$

The quantity analogous to the lensing potential gradient $\nabla_{\perp}\psi(\mathbf{x})$ is the tidal matrix \mathbf{U} , which contains the second derivatives of the gravitational potential:

$$\mathbf{U}_i = \begin{pmatrix} \frac{\partial^2\psi_i}{\partial x^2} & \frac{\partial^2\psi_i}{\partial x\partial y} \\ \frac{\partial^2\psi_i}{\partial y\partial x} & \frac{\partial^2\psi_i}{\partial y^2} \end{pmatrix} \quad (12.23)$$

The final Jacobi-matrix \mathbf{J} can be easily decomposed via

$$\mathbf{J} = \mathbf{J}_n = \begin{pmatrix} 1 - \kappa - \gamma_1 & -\gamma_2 + \omega \\ -\gamma_2 - \omega & 1 - \kappa + \gamma_1 \end{pmatrix}, \quad (12.24)$$

to yield the convergence κ , the two components of the shear $\gamma_{1,2}$ to form $\gamma = \sqrt{\gamma_1^2 + \gamma_2^2}$ and the rotation of the light bundle ω . From the inverse determinant of \mathbf{J} , the magnification $\mu = (\det\mathbf{J})^{-1}$ can be determined. As explained in Sect. 12.2.2.2, the distortion of galaxy images, which is described by their ellipticity ϵ and phase angle φ , can be derived from the reduced shear g .

12.3.2. Features

- The code can compute weak lensing geodesics in arbitrary cosmologies, which are described in terms of the fluid densities Ω_M , Ω_K , Ω_Q and Ω_Λ with their respective equation of state.
- Since `leica.c` works in comoving coordinates, it is especially suited for weak lensing studies modelled on cosmological n -body simulations, that are commonly carried out in the Lagrangian frame of reference.
- `leica.c` determines not only the shear field γ , but determines the actual change of galaxy ellipticities imprinted on the natural distribution of phase angles (which are uniformly distributed) and ellipticities ϵ ,

$$p(\epsilon)d\epsilon = \frac{1}{\sqrt{2\pi}\sigma_\epsilon} \exp\left(-\frac{\epsilon^2}{2\sigma_\epsilon^2}\right) d\epsilon, \quad (12.25)$$

which follow a Gaussian distribution with $\sigma_\epsilon \simeq 0.2$. From this data, it can determine tangential ellipticities relative to the centre of an aperture and derive aperture mass measures (Kaiser 1995, Schneider & Bartelmann 1997) with the most common radial weighting functions.

- The code takes account of the distribution $p(z)dz$ of faint blue galaxies in redshift z (Ellis 1997) that are commonly selected in weak lensing surveys; and determines target redshifts for each ray from a suitably transformed Γ -distribution,

$$p(z)dz = \left[\frac{1}{\beta} \Gamma\left(\frac{3}{\beta}\right) \right]^{-1} z^2 \exp(-z^\beta) dz \quad (12.26)$$

with $\beta = \frac{3}{2}$ and mean redshift $\langle z \rangle = \Gamma(4/\beta)/\Gamma(3/\beta) = 3/2$.

- It can carry out line-of-sight integrations of scalar quantities along the weak lensing geodesics, while simultaneously taking care of the change in solid angle due to the focusing and defocusing effect of overdensities and underdense regions, respectively. The change in solid angle is equal to the lensing magnification $\mu^{-1} = \det \mathbf{J}$, where \mathbf{J} is the Jacobian of the weak lensing mapping.
- `leica.c` can deal with gravitomagnetic corrections to weak lensing. Furthermore, it can determine line-of-sight integrations of the divergence $\text{div}_\perp \mathbf{A} = dA_x/dx + dA_y/dy$ of the gravitomagnetic field \mathbf{A} for the Rees-Sciama effect and of $\text{rot}_\perp \mathbf{A} = dA_y/dx - dA_x/dy$ for the gravitational Faraday rotation (see Chapter 13).
- The code features several improvements with respect to interpolation and numerical derivatives compared to the code by Hamana & Mellier (2001), using bilinear interpolations and derivatives computed using the mean of the left and right differential quotients. It outperforms the code by Hamana & Mellier (2001) in speed reaching up to 10^6 rays per minute on a 1.1 GHz G4 processor. For extensive lensing studies, an OpenMP¹ parallelised version is being written.

Examples of convergence fields $\kappa(\theta)$ and shear fields $\gamma(\theta)$ derived with the `leica.c` code for a cosmological n -body simulation are given in Fig. 12.2. The output density field was projected onto $N = 30$ lens planes, ranging in redshift from $z = 0.016$ out to $z = 1.421$ with comoving spacing of $\Delta w = 100$ Mpc. The lensing potential was determined on a Cartesian grid with 1024^2 mesh points. Target redshifts have been drawn independently for each ray from the generic distribution. A detailed view of the two shear components $\gamma_1(\theta)$ and $\gamma_2(\theta)$ is shown in Fig. 12.3. In this case, a single lens plane at $z = 0.016$ was imaged by rays with identical target redshifts of $z = 0.1$. The +- and \times -shaped shear pattern induced by the clusters can clearly be seen. The functionality of the code has been verified by tests on analytical cluster profiles, where the outputs are close (relative deviation $\lesssim 10^{-3}$) to theoretical expectations.

12.4. Summary and conclusion

A primary field of application will be ray-tracing studies of the Rees-Sciama effect (see Chapter 13) and the investigation of weak lensing properties of filaments. *For the visualisation, Francesco Pace (ITA, Heidelberg) provided mass sheets from a cosmological n-body simulation carried out with GADGET.*

¹<http://www.openmp.org>

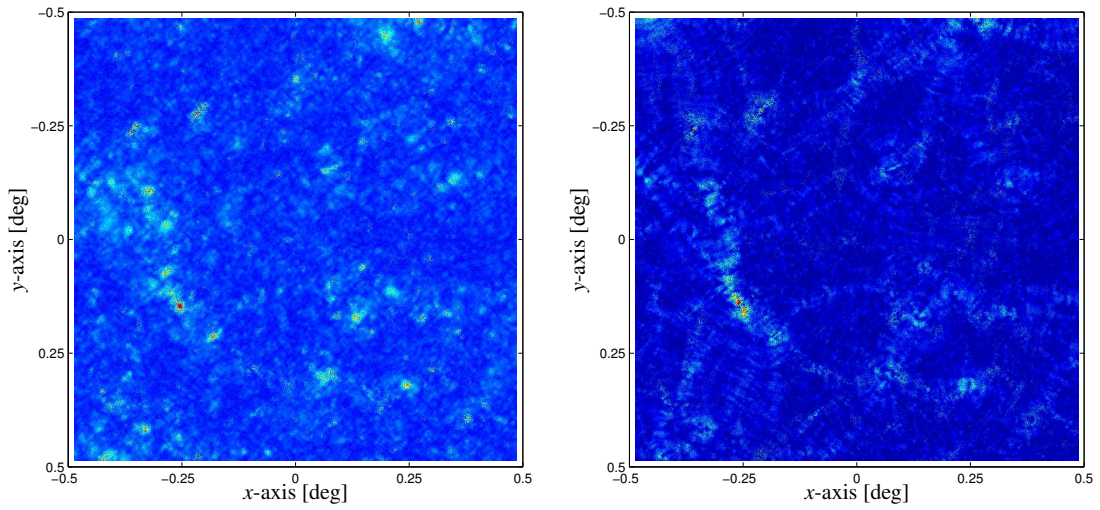


Figure 12.2.: Weak lensing convergence $\kappa(\boldsymbol{\theta})$ (left panel) and reduced shear $g(\boldsymbol{\theta})$ (right panel) in linear shading. The end points of rays are drawn from the generic redshift distribution of faint blue galaxies.

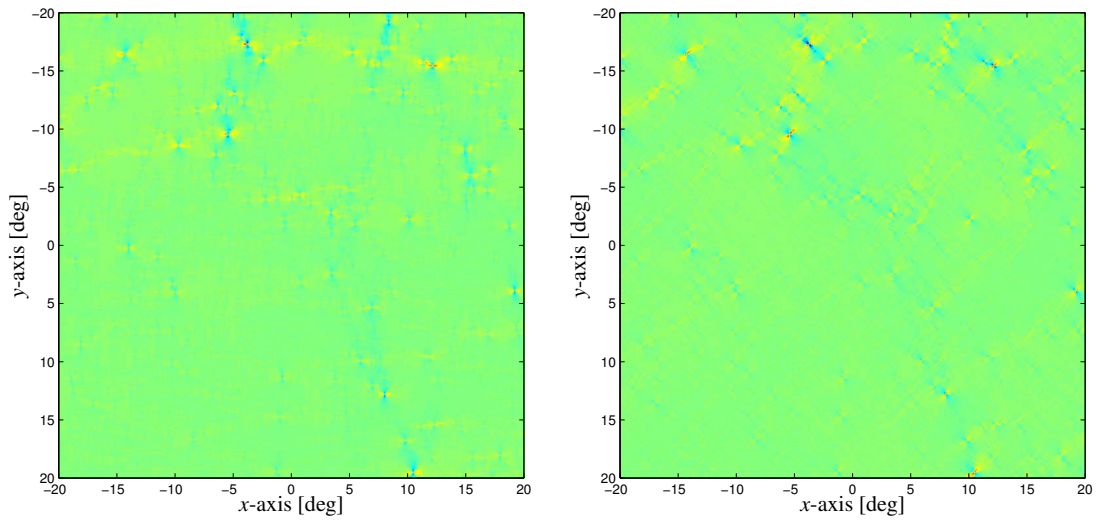


Figure 12.3.: Weak lensing shear fields $\gamma_1(\boldsymbol{\theta}) = \gamma_+(\boldsymbol{\theta})$ (left panel) and $\gamma_2(\boldsymbol{\theta}) = \gamma_\times(\boldsymbol{\theta})$ (right panel) in linear shading, for a single lens plane at $z = 0.016$ (corresponding to $w = 50$ Mpc) and with all target redshifts fixed to $z = 0.1$.

13. Gravitomagnetic lensing and the integrated Sachs-Wolfe/Rees-Sciama effect

Abstract

Dark matter currents in the large-scale structure give rise to gravitomagnetic terms in the metric, which affect the light propagation. Corrections to the weak lensing power spectrum due to these gravitomagnetic potentials are evaluated by perturbation theory. A connection between gravitomagnetic lensing and the integrated Sachs-Wolfe (iSW) effect is drawn, which can be described by a line-of-sight integration over the divergence of the gravitomagnetic vector potential. This allows the power spectrum of the iSW-effect to be derived within the framework of the same formalism as derived for gravitomagnetic lensing and reduces the iSW-effect to a second order lensing phenomenon. The three-dimensional power spectra are projected by means of a generalised Limber-equation to yield the angular power spectra. While gravitomagnetic corrections to the weak lensing spectrum are negligible at observationally accessible scales, the angular power spectrum of the iSW-effect should be detectable as a correction to the CMB spectrum up to multipoles of $\ell \simeq 100$ with the PLANCK-satellite.

13.1. Introduction

Cosmological weak lensing (Bartelmann & Schneider 2001) has evolved to be a valuable tool in cosmology. Weak lensing surveys have contributed significantly to the determination of the dark matter power spectrum and to the estimation of its amplitude σ_8 (Schneider et al. 1998, van Waerbeke et al. 2000) by the measurement of cosmic shear and have enabled the reconstruction of the dark matter distribution in rich clusters of galaxies (e.g. Kaiser & Squires 1993, Seitz et al. 1996, Ménard et al. 2003).

So far, only static matter distributions have been considered but from the solution to Maxwell's equations in the framework of general relativity it follows that gravitomagnetic potentials generated by moving masses should alter the predictions for light deflection (Schneider et al. 1992). While gravitomagnetic corrections to lensing are small, being of order v/c , where v is the velocity of the deflecting mass, they may contribute to the weak cosmological lensing: The cluster peculiar velocities following from a cosmological N -body simulation like the Hubble-volume simulation (Colberg et al. 2000, Jenkins et al. 2001) are well described by a Gaussian distribution with zero mean and a standard deviation of $\sigma_v \simeq 300$ km/s, which is a fraction of 10^{-3} of the speed of light. Thus, relativistic effects influence the lensing signal appreciably in $\lesssim 1\%$ of all clusters. In filaments (Colberg et al. 2004) where matter is funneled towards the clusters, velocities are even higher: Infall velocities up to a few 10^3 km/s have been measured.

The integrated Sachs-Wolfe (iSW) effect, or Rees-Sciama (RS) effect (Sachs & Wolfe 1967, Rees & Sciama 1968) arises if CMB photons encounter time-varying gravitational potentials on their passage from the last-scattering surface to the observer. When transversing time-varying potentials, the energy gains and losses a CMB photon experiences in entering and leaving potential wells do not cancel exactly. In this way, one expects a net blueshift of CMB photons in forming voids and a net redshift in matter-accreting clusters of galaxies.

The iSW/RS effect has been studied theoretically in individual objects (Martínez-González et al. 1990) and can be used for the investigation of cluster mergers (Rubiño-Martín et al. 2004). More importantly, it is sensitive to mapping the large-scale structure as it highlights the sites of active structure formation (Kaiser 1982, Martínez-González & Sanz 1990, Martínez-González et al. 1992, 1994, Seljak 1996b). Furthermore, the iSW-effect may turn out to be a powerful probe for dark energy's influence on structure formation (Crittenden & Turok 1996), when combined with other tracers of structure. A numerical approach has been undertaken by Tuluie & Laguna (1995a,b), who followed photons through a cosmological n -body simulation and carried out the line-of-sight integration numerically.

The aim of this paper is to determine the corrections to the power spectra of weak lensing quantities caused by gravitomagnetic terms and to derive the iSW power spectrum, both by applying perturbation theory. In comparison

to preceding treatments by Seljak (1996b) and Cooray (2002), the novel approach taken to determine the iSW power spectrum is by relating it to the gravitomagnetic terms in considered in lensing. Gravitomagnetic corrections to lensing have indeed been observed by Fomalont & Kopeikin (2003) in imaging radio waves from a quasar on Jupiter, which is an outstanding achievement in VLBI astrometry. Gravitomagnetic corrections to lensing in the large-scale structure would only be detectable by their n -point statistics or by topological measures like Minkowski functionals, that would be especially sensitive to the effect's intrinsic non-Gaussianity. Concerning the iSW-effect, there are a quite a few reports on its detection in WMAP data in cross correlation with various populations of tracer objects (Afshordi et al. 2004, Fosalba et al. 2003, Boughn & Crittenden 2004, Nolta et al. 2004, Hirata et al. 2004), but so far it has not been possible to derive values for single multipoles based on CMB data alone.

The paper is structured as follows: After a compilation of key formulae and the derivation of Limber's equation for vector fields in Sect. 13.2, the power spectrum of weak gravitational lensing is considered and the correction terms due to gravitomagnetic potentials are worked out by perturbation theory in Sect. 13.3. Then, the iSW-effect is related to gravitomagnetic lensing and its power spectrum is subsequently derived in a perturbative approach in Sect. 13.4. The results are summarised in Sect. 13.5.

13.2. Key formulae

The assumed cosmological model is the standard Λ CDM cosmology, which has recently been supported by observations of the WMAP satellite¹ (Spergel et al. 2003). Parameter values have been chosen as $\Omega_M = 0.3$, $\Omega_\Lambda = 0.7$, $H_0 = 100 h \text{ km s}^{-1} \text{ Mpc}^{-1}$ with $h = 0.7$, $\Omega_B = 0.04$, $n_s = 1$ and $\sigma_8 = 0.9$.

13.2.1. Structure formation

The cosmic density field ρ given in terms of the dimensionless density perturbation $\delta = (\rho - \langle\rho\rangle)/\langle\rho\rangle$, where $\langle\rho\rangle$ is the average density of matter. The 2-point correlation properties of the overdensity field δ are described by the power spectrum $P(k)$:

$$\langle\delta(\mathbf{k})\delta^*(\mathbf{k}')\rangle = (2\pi)^3\delta_D(\mathbf{k} - \mathbf{k}')P(k), \text{ where} \quad (13.1)$$

$$\delta(\mathbf{k}) = \int \frac{d^3x}{(2\pi)^3}\delta(\mathbf{x})\exp(-i\mathbf{k}\mathbf{x}) \quad (13.2)$$

is the Fourier transform of the overdensity field δ . The normalisation of the power spectrum $P(k)$ is given by the parameter σ_8 , i.e. the variance of δ on scales of $R = 8 \text{ Mpc}/h$:

$$\sigma_R^2 = \frac{1}{2\pi^2} \int_0^\infty dk k^2 W^2(kR)P(k). \quad (13.3)$$

Here, W is a window function of top-hat shape, the Fourier-transform of which is given by:

$$W(x) = \frac{3}{x^3} [\sin(x) - x \cos(x)] = \frac{3}{x} J_1(x). \quad (13.4)$$

The shape of the power spectrum $P(k) \propto k^{n_s} \cdot T^2(k)$ is well approximated by the transfer functions $T(k)$ suggested by Bardeen et al. (1986). They read in case of adiabatic initial conditions:

$$T(q) = \frac{\ln(1 + 2.34q)}{2.34q} \left[1 + 3.89q + (16.1q)^2 + (5.46q)^3 + (6.71q)^4 \right]^{-\frac{1}{4}} \quad (13.5)$$

The wave vector k is commonly divided by the shape parameter Γ introduced by Efstathiou et al. (1992) for CDM models and extended to models with $\Omega_M \neq 1$ by Sugiyama (1995):

$$q = \frac{k/\text{Mpc}^{-1}h}{\Gamma} \text{ with } \Gamma = \Omega_M h \exp\left(-\Omega_B \cdot \left[1 + \frac{\sqrt{2}h}{\Omega_M}\right]\right). \quad (13.6)$$

¹<http://map.gsfc.nasa.gov/>

In linear structure formation, each Fourier-mode grows independently and at the same rate. The time dependence of the overdensity field δ can be described by the growth function $D(a)$:

$$\delta(a) = \delta_0 D(a) \text{ with } D(a) = a \frac{d'(a)}{d'(1)}. \quad (13.7)$$

The shape of $d'(a)$ is well approximated by the formula suggested by [Carroll et al. \(1992\)](#):

$$d'(a) = \frac{5}{2} \Omega_M(a) \left[\Omega_M^{4/7}(a) - \Omega_\Lambda(a) + \left(1 + \frac{\Omega_M(a)}{2} \right) \left(1 + \frac{\Omega_\Lambda(a)}{70} \right) \right]^{-1}. \quad (13.8)$$

13.2.2. Dark matter currents

The continuity equation $\dot{\rho} = -\text{div}(\rho\mathbf{v})$ requires the existence of large-scale coherent matter streams $\mathbf{j} = \rho\mathbf{v}$ superimposed on the Hubble flow due to the formation of structure. In Fourier space, the relation between density and velocity reads in the Eulerian frame:

$$\mathbf{v}(\mathbf{k}) = -iaH(a)f(\Omega) \frac{\mathbf{k}}{k^2} \delta(\mathbf{k}) = -i\dot{a}f(\Omega) \frac{\mathbf{k}}{k^2} \delta(\mathbf{k}). \quad (13.9)$$

The $1/k$ -dependence causes cosmological velocities to come predominantly from perturbations on larger scales in comparison to those that dominate the density field. $H(a) = d \ln(a)/dt$ is Hubble's function. The function f describes the dependence of the equation of continuity on cosmic time and is a function of the mass density Ω_M ([Peebles 1980](#), [Lahav et al. 1991](#)):

$$f(\Omega) = \frac{d \ln \delta}{d \ln a} = \frac{d \ln D(a)}{d \ln a} \simeq \Omega_M(a)^{0.6} \quad (13.10)$$

In analogy to eqn. (13.7), time evolution of of dark matter current velocities in the comoving frame is described by $G(a)$,

$$G(a) = \frac{g'(a)}{g'(1)} \text{ with } g'(a) \equiv H(a)f(\Omega). \quad (13.11)$$

The theory of peculiar velocity fields is reviewed in detail in [Dekel \(1994\)](#) and [Strauss & Willick \(1995\)](#).

In general, the effects considered here are sensitive to density weighted velocities. The Fourier transform of vector fields $\mathbf{q}(\mathbf{x}) = \delta(\mathbf{x})\mathbf{v}(\mathbf{x})$ can be derived with the convolution theorem:

$$\mathbf{q}(\mathbf{k}) = \int \frac{d^3x}{(2\pi)^3} \mathbf{q}(\mathbf{x}) \exp(-i\mathbf{k}\mathbf{x}) = \frac{1}{2} \int \frac{d^3p}{(2\pi)^3} [\mathbf{v}(\mathbf{p})\delta(\mathbf{k}-\mathbf{p}) + \mathbf{v}(\mathbf{k}-\mathbf{p})\delta(\mathbf{p})], \quad (13.12)$$

where the integrand has been symmetrised in eqn. (13.12).

13.2.3. Limber's equation for vector fields

For the derivation of the angular power spectrum of the gravitomagnetic corrections to weak cosmological lensing or that of the iSW-effect, a variant of Limber's equation is necessary that is able to deal with projections of vector fields $\mathbf{q}(\mathbf{x})$ instead of scalar fields. The derivation presented here is generalised from [Vishniac \(1987\)](#). Consider a vector field $\mathbf{q}(\mathbf{x})$ and its Fourier transform $\mathbf{q}(\mathbf{k})$:

$$\mathbf{q}(\mathbf{x}) = \int d^3k \mathbf{q}(\mathbf{k}) \exp(i\mathbf{k}\mathbf{x}) \quad (13.13)$$

Any effect κ in question is assumed to measure a projection of $\mathbf{q}(\mathbf{x})$ on the line-of-sight, where \mathbf{e} is a unit tangent vector on the photon geodesic. $W(w)$ is a general weighing function dependent on the comoving distance w which describes its redshift dependence and is later to be replaced by e.g. the lensing efficiency function:

$$\kappa = \int_0^{w_{\max}} dw W(w) [\mathbf{e} \cdot \mathbf{q}] = \int_0^{w_{\max}} dw W(w) [\mathbf{e} \cdot \mathbf{q}(\mathbf{k})] \int d^3k \exp(i\mathbf{k}\mathbf{x}) \quad (13.14)$$

The decomposition of the projected field $\kappa(\boldsymbol{\theta})$ into spherical harmonics $Y_{\ell m}(\boldsymbol{\theta})$ is:

$$\kappa(\boldsymbol{\theta}) = \sum_{\ell=0}^{\infty} \sum_{m=-\ell}^{+\ell} \kappa_{\ell m} Y_{\ell m}(\boldsymbol{\theta}) \leftrightarrow \kappa_{\ell m} = \int_{4\pi} d\Omega \kappa(\boldsymbol{\theta}) Y_{\ell m}^*(\boldsymbol{\theta}) \text{ with} \quad (13.15)$$

$$Y_{\ell m}(\boldsymbol{\theta}) = \sqrt{\frac{2\ell+1}{4\pi}} \sqrt{\frac{(\ell-|m|)!}{(\ell+|m|)!}} P_{\ell m}(\cos\theta) \exp(im\phi). \quad (13.16)$$

In the random phase approximation, one obtains for the variance $\langle |\kappa_{\ell m}|^2 \rangle$ of $\kappa(\boldsymbol{\theta})$ in two directions \mathbf{e}_1 and \mathbf{e}_2 :

$$\langle |\kappa_{\ell m}|^2 \rangle = \int_0^{w_{\max}} dw_1 W(w_1) \int_{4\pi} d\Omega_1 Y_{\ell m}(\boldsymbol{\theta}_1) \int_0^{w_{\max}} dw_2 W(w_2) \int_{4\pi} d\Omega_2 Y_{\ell m}^*(\boldsymbol{\theta}_2) \int d^3k \exp(ik\mathbf{e}_1 w_1) \exp(-ik\mathbf{e}_2 w_2) \langle [\mathbf{e}_1 \mathbf{q}(\mathbf{k})] [\mathbf{e}_2 \mathbf{q}^*(\mathbf{k})] \rangle. \quad (13.17)$$

According to the cosmological principle, there is no preferred orientation, which allows to replace $\langle |\kappa_{\ell m}|^2 \rangle$ with its average value over all m for a given ℓ :

$$C_{\kappa}(\ell) = \frac{1}{2\ell+1} \sum_{m=-\ell}^{+\ell} \langle |\kappa_{\ell m}|^2 \rangle. \quad (13.18)$$

The vector field $\mathbf{q}(\mathbf{k})$ can be separated into components parallel and perpendicular to the line-of-sight \mathbf{e} :

$$\mathbf{q} = \mathbf{q}_{\parallel} + \mathbf{q}_{\perp} \text{ with } \mathbf{q}_{\parallel} = \mathbf{e} \cdot (\mathbf{q} \cdot \mathbf{e}) \text{ and } \mathbf{q}_{\perp} = \mathbf{q} - \mathbf{q}_{\parallel} = \mathbf{e} \times (\mathbf{q} \times \mathbf{e}). \quad (13.19)$$

For the projections $\mathbf{e} \cdot \mathbf{q}_{\perp} = 0$ and $\mathbf{e} \times \mathbf{q}_{\parallel} = 0$ are valid. Eqn. (13.17) is further simplified by choosing the coordinate system in a way that the z -coordinate is parallel to the wave vector, $\mathbf{e}_z \parallel \mathbf{k}$. Introducing spherical coordinates (θ, ϕ) and putting $x = \cos\theta$ on obtains:

$$\mathbf{q}_{\parallel} \frac{\mathbf{k}}{k} = x \mathbf{q}_{\parallel} \text{ and } \mathbf{q}_{\perp} \frac{\mathbf{k}}{k} = \sqrt{1-x^2} \exp(-i\phi) \mathbf{q}_{\perp} \quad (13.20)$$

Furthermore, with $\exp(ik\mathbf{e}w) = \exp(ikxw)$, the expression for the correlator is separated into:

$$\langle \mathbf{q}(\mathbf{k}) \mathbf{q}^*(\mathbf{k}) \rangle = x_1 x_2 \langle \mathbf{q}_{\parallel}(\mathbf{k}) \mathbf{q}_{\parallel}^*(\mathbf{k}) \rangle + \sqrt{1-x_1^2} e^{-i\phi_1} \sqrt{1-x_2^2} e^{i\phi_2} \langle \mathbf{q}_{\perp}(\mathbf{k}) \mathbf{q}_{\perp}^*(\mathbf{k}) \rangle. \quad (13.21)$$

With these simplifications, the integrals over the azimuthal angles ϕ_1 and ϕ_2 can be carried out. Inserting the orthonormality relation $\int_0^{2\pi} d\phi \exp[i(n-m)\phi] = 2\pi \delta_{mn}$ reduces the summation over m to a single term, which is $m=0$ for the components parallel to the line-of-sight and $|m|=1$ for the components perpendicular to the line-of-sight. The final expression for the power spectrum $C_{\kappa}(\ell)$ is now split into the two orthogonal projections:

$$C_{\kappa}(\ell) = C_{\kappa}^{\parallel}(\ell) + C_{\kappa}^{\perp}(\ell). \quad (13.22)$$

13.2.3.1. Components parallel to the line-of-sight $C_{\kappa}^{\parallel}(\ell)$

For the power spectrum $C_{\kappa}^{\parallel}(\ell)$ of the components of \mathbf{q}_{\parallel} parallel to the line-of-sight, one obtains:

$$C_{\kappa}^{\parallel}(\ell) = 4\pi \int dk k^2 \int_0^{w_{\max}} dw_1 W(w_1) \int_0^{w_{\max}} dw_2 W(w_2) \int_{-1}^{+1} dx_1 \exp(ikx_1 w_1) \int_{-1}^{+1} dx_2 \exp(-ikx_2 w_2) [x_1 P_{\ell 0}(x_1) x_2 P_{\ell 0}(x_2)] \langle \mathbf{q}_{\parallel}(\mathbf{k}, w_1) \mathbf{q}_{\parallel}^*(\mathbf{k}, w_2) \rangle. \quad (13.23)$$

The dx_1 - and dx_2 -integrations can be performed by taking advantage of the connection between Bessel functions and Legendre polynomials (Watson 1952, Abramowitz & Stegun 1965):

$$J_{\ell}(z) = \frac{1}{2i^{\ell}} \int_{-1}^{+1} dx P_{\ell}(x) \exp(izx), \quad (13.24)$$

which can be generalised to give:

$$\int_{-1}^{+1} dx x^n P_{\ell}(x) \exp(izx) = \frac{1}{i^n} \frac{d^n}{dz^n} J_{\ell}(z). \quad (13.25)$$

Inserting formula (13.25) for $n=1$ yields the final result:

$$C_{\kappa}^{\parallel}(\ell) = 2\pi \int dk \int_0^{w_{\max}} dw_1 W(w_1) \int_0^{w_{\max}} dw_2 W(w_2) \left[\frac{d}{dw_1} J_{\ell}(kw_1) \right] \left[\frac{d}{dw_2} J_{\ell}(kw_2) \right] \langle \mathbf{q}_{\parallel}(\mathbf{k}, w_1) \mathbf{q}_{\parallel}^*(\mathbf{k}, w_2) \rangle. \quad (13.26)$$

13.2.3.2. Components perpendicular to the line-of-sight $C_{\kappa}^{\perp}(\ell)$

After reducing the summation to $|m| = 1$, the power spectrum $C_{\kappa}^{\perp}(\ell)$ of the components of \mathbf{q}_{\perp} perpendicular to the line-of-sight reads:

$$C_{\kappa}^{\perp}(\ell) = \frac{4\pi}{2\ell(\ell+1)} \int dk k^2 \int_0^{w_{\max}} dw_1 W(w_1) \int_0^{w_{\max}} dw_2 W(w_2) \int_{-1}^{+1} dx_1 \exp(ikx_1 w_1) \int_{+1}^{+1} dx_2 \exp(-ikx_2 w_2) \left[\sqrt{1-x_1^2} P_{\ell 1}(x_1) \sqrt{1-x_2^2} P_{\ell 1}(x_2) \right] \langle q_{\perp}(\mathbf{k}, w_1) q_{\perp}^*(\mathbf{k}, w_2) \rangle. \quad (13.27)$$

The integration over the polar angles x_1 and x_2 is slightly more complicated than the previous case. Inserting the definition of the associated Legendre polynomials $P_{\ell m}$ for $m = 1$ gives another factor of $\sqrt{1-x^2}$:

$$P_{\ell m}(x) = (-1)^m (1-x^2)^{\frac{m}{2}} \frac{d^m P_{\ell}(x)}{dx^m} \rightarrow P_{\ell 1}(x) = -\sqrt{1-x^2} \frac{dP_{\ell}(x)}{dx}. \quad (13.28)$$

The derivative of the Legendre polynomial can be replaced via

$$(1-x^2) \frac{d}{dx} P_{\ell}(x) = \ell [P_{\ell-1}(x) - x P_{\ell}(x)], \quad (13.29)$$

and the integration be carried out by inserting relation (13.25). Then, the two Bessel functions can be combined by using the Bessel function's derivative relation:

$$\frac{d}{dz} [z^{\ell} J_{\ell}(z)] = z^{\ell} J_{\ell-1}(z) \rightarrow \frac{J_{\ell}(z)}{z} = \frac{1}{\ell} \left[J_{\ell-1} - \frac{d}{dz} J_{\ell}(z) \right], \quad (13.30)$$

which yields the formula:

$$\int_{-1}^{+1} dx \sqrt{1-x^2} P_{\ell 1}(x) \exp(izx) = \ell(\ell+1) \frac{J_{\ell}(z)}{z}. \quad (13.31)$$

This relation allows the final result to be written as:

$$C_{\kappa}^{\perp}(\ell) = 2\pi\ell(\ell+1) \int dk \int_0^{w_{\max}} dw_1 W(w_1) \int_0^{w_{\max}} dw_2 W(w_2) \left[\frac{J_{\ell}(kw_1)}{w_1} \frac{J_{\ell}(kw_2)}{w_2} \right] \langle q_{\perp}(\mathbf{k}, w_1) q_{\perp}^*(\mathbf{k}, w_2) \rangle. \quad (13.32)$$

13.3. Gravitomagnetic lensing

13.3.1. Definitions

Light propagation through a slowly moving perfect fluid can be described by an effective refractive index n_{eff} (Schneider et al. 1992):

$$n_{\text{eff}} = 1 - \frac{2}{c^2} \Phi + \frac{4}{c^3} \mathbf{A} \cdot \mathbf{e}, \quad (13.33)$$

where Φ is the scalar potential and \mathbf{A} are the gravitomagnetic vector potentials. \mathbf{e} denotes a unit tangent vector along the photon geodesic. In this approximation, the metric takes account of the matter density ρ and the matter current densities $\mathbf{j} = \rho\mathbf{v}$ (i.e. terms of order v/c), but neglects the stresses $T_{ij} = \rho v_i v_j + p \delta_{ij}$. The smallness of these terms (being of order v^2/c^2) makes them unobservable, but they would be sensitive to the velocity tensor $v_i v_j$, i.e. to shear flows, velocity dispersions and turbulence.

In the near zone of a system of slowly moving bodies the retardation can be neglected; in this case the expressions for Φ and \mathbf{A} are given as solutions to Laplace's equation:

$$\Delta\Phi(\mathbf{r}) = 4\pi G\rho(\mathbf{r}) \quad \leftrightarrow \quad \Phi(\mathbf{r}) = -G \int d^3 r' \frac{\rho(\mathbf{r}')}{|\mathbf{r} - \mathbf{r}'|} \quad (13.34)$$

$$\Delta\mathbf{A}(\mathbf{r}) = 4\pi G\mathbf{j}(\mathbf{r}) \quad \leftrightarrow \quad \mathbf{A}(\mathbf{r}) = -G \int d^3 r' \frac{\mathbf{j}(\mathbf{r}')}{|\mathbf{r} - \mathbf{r}'|}. \quad (13.35)$$

The dark matter flux \mathbf{j} is defined as the momentum density $\mathbf{j} \equiv \rho\mathbf{v}$.

An expression for $d\mathbf{e}/dw$, i.e. the change in propagation direction, follows from the variational principle $\delta \int ds n_{\text{eff}} = 0$. s denotes an affine parameter. The deflection angle α , being defined as $\alpha = \mathbf{e}_{\text{initial}} - \mathbf{e}_{\text{final}}$ can be obtained by integration:

$$\alpha = \frac{2}{c^2} \int ds \nabla_{\perp} \Phi - \frac{4}{c^3} \int ds \mathbf{e} \times \text{rot} \mathbf{A}. \quad (13.36)$$

The derivative perpendicular to the line-of-sight is defined via $\nabla_{\perp} \Phi \equiv \nabla \Phi - \mathbf{e}(\mathbf{e} \cdot \nabla \Phi)$. The first contribution to α in eqn. (13.36) corresponds to the attraction \mathbf{g} towards the deflecting mass via $\mathbf{g} = -\nabla \Phi$. The microscopic picture of photon interaction with a gravitomagnetic field is illustrated in Appendix F.

The second term, however, is due to the gravitomagnetic fields generated by the matter current densities \mathbf{j} . This contribution is related to the dragging of inertial frames which gives rise to the precession of orbiting spinning tops in the particular case of rotation of the field-generating body (Lense-Thirring precession, to be measured by Gravity Probe B²). This formalism has been applied to various astrophysical systems, namely by Ibanez (1983) to gravitational light deflection of a rotating galaxy and by Sereno (2003), who considered light deflection on rotating stars. Furthermore, corrections to the deflection angle in galactic microlensing due to moving lenses have been evaluated by Heyrovsky (2004).

13.3.2. Gravitomagnetic lensing by the large-scale structure

Adopting the Born-approximation, which states that the gravitational light deflection is weak such that the integral in eqn. (13.36) can be evaluated along a straight line instead of the photon geodesic itself, it can be seen that gravitational lensing is insensitive to derivatives of the potentials along the line-of-sight. Working out the deflection angles α and the tidal matrix $\psi_{ij} = \partial\alpha_i/\partial x_j$ while neglecting derivatives along the line-of-sight yields formulae analogous to the case of static lensing, but with the gravitational potential Φ replaced by $\Phi - \frac{2}{c} A_{\parallel}$. Thus, the sources of gravitational light deflection are the matter distribution δ and the component of the matter flux j_{\parallel} parallel to the line-of-sight. The gravitational light deflection is stronger, if an object is moving towards the observer, because the photon stays in the interaction potential for a longer period of time, and vice versa.

With the source term $\delta + \frac{2}{c} j_{\parallel}$, one obtains for the lensing convergence κ up to the comoving distance w :

$$\kappa(\theta, w) = \frac{3H_0^2 \Omega_0}{2c^2} \int_0^w dw' \frac{f_K(w') f_K(w_{\text{max}} - w')}{f_K(w_{\text{max}}) a(w')} \left(\delta + \frac{2}{c} j_{\parallel} \right). \quad (13.37)$$

where $f_K(w) = w$, if spatial hypersurfaces are flat, which is the case for $\Omega_M + \Omega_{\Lambda} = 1$. The redshift distribution of lensed population of background sources such as faint blue galaxies is described by the distribution $p(z)dz$, being recast in comoving distance, $Z(w)dw = p(z)dz$. Then, the average influence $\bar{Z}(w)$ of the lever arms of the optical path for a given configuration of source and lens is given by:

$$\bar{Z}(w) = \int_w^{w_{\text{max}}} dw' Z(w') \frac{f_K(w' - w)}{f_K(w')}. \quad (13.38)$$

In this work, I assume the generic distribution in redshift z for faint blue galaxies (c.f. Ellis 1997),

$$p(z)dz = p_0 z^2 \exp(-z^{\beta}) \text{ with } \frac{1}{p_0} = \frac{1}{\beta} \Gamma\left(\frac{3}{\beta}\right). \quad (13.39)$$

with mean redshift $\langle z \rangle = \Gamma(4/\beta)/\Gamma(3/\beta) \simeq 1.5$ and most likely redshift $z_{\text{max}} = (2/\beta)^{1/\beta} \simeq 1.21$ for $\beta = 3/2$. For the average convergence $\bar{\kappa}$, the final result reads:

$$\bar{\kappa}(\theta) = \int_0^{w_{\text{max}}} dw Z(w) \kappa(\theta, w) = \frac{3H_0^2 \Omega_0}{2c^2} \int_0^{w_{\text{max}}} dw \bar{Z}(w) \frac{f_K(w)}{a(w)} \left(\delta + \frac{2}{c} j_{\parallel} \right).$$

For $\bar{Z}(w)$, the phenomenological fitting formula

$$\bar{Z}(w) \simeq Z_0 \exp\left(-\frac{1}{1 - [\log(w/w_0)]^b}\right), \quad (13.40)$$

²<http://www.gravityprobeb.com>

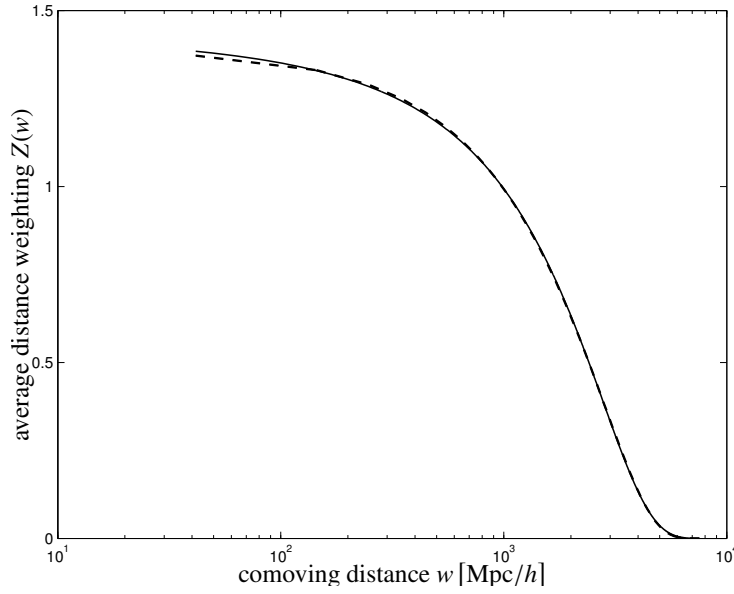


Figure 13.1.: The redshift weighting function $\bar{Z}(w)$ (c.f. eqn. (13.38), rendered as a dashed line), and the fitting formula (13.40) (solid line) in comparison. The maximum relative deviation between the properly evaluated function and the fitting formula is $\lesssim 3\%$.

with $Z_0 = 1.441$, $b = 3.186$ and $w_0 = 2314$ Mpc/h is used, which yields excellent agreement with the properly evaluated function, as shown by Fig. 13.1. The fitting formula alleviates the need of numerically carrying out the integration in eqn. (13.38) when projecting the dark matter power spectrum.

13.3.3. Perturbative treatment

When considering gravitomagnetic corrections to gravitational lensing, the source term δ of static lensing has to be replaced by $q_{\parallel} = (1 + \frac{2}{c}v_{\parallel})\delta$. It should be emphasised, that the fluctuations in a weak lensing shear field are predominantly caused by modes in k -space, that are propagating perpendicularly to the line-of-sight (Blandford et al. 1991). Evaluating the correlator $\langle q_{\perp}(\mathbf{k}, w_1)q_{\perp}^*(\mathbf{k}, w_2) \rangle$ yields apart from the dominating 2-point term,

$$\langle q_{\perp}(\mathbf{k}, w_1)q_{\perp}(\mathbf{k}, w_2) \rangle_{2\text{pt}} = D(w_1)D(w_2)\langle \delta(\mathbf{k})\delta^*(\mathbf{k}) \rangle, \quad (13.41)$$

contributions of 3- and 4-point terms. The 2-point term stated in eqn. (13.41) is of order unity and is the basis of the conventional theory of static gravitational lensing. In the perturbative treatment, the coupling of \mathbf{k} -modes in nonlinear structure growth is neglected, integrations are implicitly taken to be restricted to quasi-linear scales.

13.3.3.1. 3-point term

The 3-point term $\langle q_{\perp}(\mathbf{k}, w_1)q_{\perp}^*(\mathbf{k}, w_2) \rangle_{3\text{pt}}$ consists of four contributions and is of order v/c compared to the 2-point term (c.f. eqn. (13.41)):

$$\langle q_{\perp}(\mathbf{k}, w_1)q_{\perp}^*(\mathbf{k}, w_2) \rangle_{3\text{pt}} = \frac{1}{c} \int \frac{d^3p}{(2\pi)^3} \left\{ \begin{aligned} &\langle \delta(-\mathbf{k}, w_1)v_{\perp}(\mathbf{p}, w_2)\delta(\mathbf{k}-\mathbf{p}, w_2) \rangle + \langle \delta(-\mathbf{k}, w_1)v_{\perp}(\mathbf{k}-\mathbf{p}, w_2)\delta(\mathbf{p}, w_2) \rangle + \\ &\langle \delta(\mathbf{k}, w_2)v_{\perp}(-\mathbf{p}, w_1)\delta(\mathbf{p}-\mathbf{k}, w_1) \rangle + \langle \delta(\mathbf{k}, w_2)v_{\perp}(\mathbf{p}-\mathbf{k}, w_1)\delta(-\mathbf{p}, w_1) \rangle \end{aligned} \right\} \quad (13.42)$$

Here, the relations $\delta^*(\mathbf{k}) = \delta(-\mathbf{k})$ and $v^*(\mathbf{k}) = v(-\mathbf{k})$ were inserted, which hold for real fields. By using this fact, the condition $\sum_i \mathbf{k}_i = \mathbf{0}$ is fulfilled which allows the 3-point correlators in eqn. (13.42) to be reduced to products of

2-point correlators by virtue of the formulae derived in Appendix E. This yields four terms of the type $\langle v_\perp \delta \rangle \langle \delta \delta \rangle / c$ and two contributions $\langle v_\perp \delta \rangle^2 / c^2$ of second order.

The correlation function can then be projected onto a plane perpendicular to wave vector \mathbf{k} : The component of the velocity in the celestial plane is given by $\mathbf{v}_\perp = \mathbf{k} \times (\mathbf{v} \times \mathbf{k}) / k^2$ and hence $v_\perp = v \sin \theta = v \sqrt{1 - x^2}$, with $x = \cos \theta$, where θ is the angle of separation between \mathbf{p} and \mathbf{k} . In doing this, the contributions of the type $\langle v_\perp \delta \rangle^2 / c^2$ vanish because they contain a multiplicative term $\langle \delta(\mathbf{k}) \nu(\mathbf{k}) \rangle$, which is a vector field collinear to \mathbf{k} . The remaining terms can be combined to give:

$$(2\pi)^3 \langle q_\perp(\mathbf{k}, w_1) q_\perp^*(\mathbf{k}, w_2) \rangle_{3\text{pt}} = \frac{4\pi}{c} D(w_1) D(w_2) [g'(w_1) + g'(w_2)]$$

$$\int p^2 dp \int_{-1}^{+1} dx \sqrt{1 - x^2} \left\{ P(|\mathbf{p}|) P(|\mathbf{p} - \mathbf{k}|) M(\mathbf{p}, \mathbf{p} - \mathbf{k}) \left[\frac{1}{|\mathbf{p}|} + \frac{p}{|\mathbf{p} - \mathbf{k}|^2} \right] \right.$$

$$\left. + P(|\mathbf{k}|) \left[M(\mathbf{k}, -\mathbf{p}) \frac{P(|\mathbf{p}|)}{|\mathbf{p}|} + M(\mathbf{k}, \mathbf{p} - \mathbf{k}) \frac{p}{|\mathbf{p} - \mathbf{k}|^2} P(|\mathbf{p} - \mathbf{k}|) \right] \right\} \quad (13.43)$$

In the integrand of eqn. (13.43), the replacement $|\mathbf{p} - \mathbf{k}|^2 = k^2 - 2kpx + p^2$ can be inserted. Additionally, the time evolution of the velocity-density cross correlation function,

$$\langle v_\perp(\mathbf{k}, w_1) \delta^*(\mathbf{k}, w_2) \rangle = g'(w_1) D(w_2) \langle v_\perp(\mathbf{k}) \delta^*(\mathbf{k}) \rangle, \quad (13.44)$$

was inserted. The function $M(\mathbf{p}, \mathbf{p}')$ is defined as:

$$M(\mathbf{p}, \mathbf{p}') = \frac{10}{7} + \frac{\mathbf{p}\mathbf{p}'}{pp'} \left(\frac{p}{p'} + \frac{p'}{p} \right) + \frac{4}{7} \left(\frac{\mathbf{p}\mathbf{p}'}{pp'} \right)^2. \quad (13.45)$$

It should be emphasised, that this 3-point correlator does not take account of the evolution of non-Gaussian features in the correlation function $\langle \delta(\mathbf{k}_1) \delta(\mathbf{k}_2) \delta(\mathbf{k}_3) \rangle$ and their influence on lensing determined by [Jain & Seljak \(1997\)](#), [Bernardeau \(1997\)](#) and [Takada & Jain \(2003a,b\)](#), which strongly affects weak lensing quantities on small angular scales. A detailed derivation of this 3-point correlation function is given in Appendix E.

13.3.3.2. 4-point term

The last contribution to the weak lensing power spectrum evoked by gravitomagnetic corrections is the 4-point term $\langle q_\perp(\mathbf{k}, w_1) q_\perp^*(\mathbf{k}, w_2) \rangle_{4\text{pt}}$, which is of order v^2/c^2 and thus strongly suppressed. The derivation of the term is easy prey: It can be done in complete analogy to that of the Ostriker-Vishniac effect ([Ostriker & Vishniac 1986](#), [Vishniac 1987](#)), where any optical depth depending on redshift needs to be replaced by the appropriate weighting function (c.f. Sect. 13.4.6) and conversions from dark matter densities into baryonic densities are to be discarded.

The derivation evolves cross-terms between the velocity and density fields, perhaps the most elegant way of reducing it to a sum of 2-point correlations is given by [Ma & Fry \(2002\)](#), using a result from [Monin & Yaglom \(1965a,b\)](#):

$$(2\pi)^3 \langle q_i(\mathbf{k}) q_j^*(\mathbf{k}) \rangle_{4\text{pt}} \equiv P_{qq}^{ij}(|\mathbf{k}|) \simeq$$

$$\frac{4}{c^2} \int \frac{d^3 p}{(2\pi)^3} \int \frac{d^3 p'}{(2\pi)^3} (2\pi)^3 \delta_D(\mathbf{k} - \mathbf{p} - \mathbf{p}') \times \left[\frac{\mathbf{p}^i}{|\mathbf{p}^i|} \frac{\mathbf{p}^j}{|\mathbf{p}^j|} P_{vv}(|\mathbf{p}|) P_{\delta\delta}(|\mathbf{p}'|) + \frac{\mathbf{p}^i}{|\mathbf{p}^i|} \frac{\mathbf{p}'^j}{|\mathbf{p}'^j|} P_{\delta v}(|\mathbf{p}|) P_{\delta v}(|\mathbf{p}'|) \right],$$

where the irreducible 4-point correlation $P_{\delta v \delta v}(\mathbf{k})$ has been neglected.

Following [Ma & Fry \(2002\)](#), the projection to be carried out is $(2\pi)^3 \langle q_\perp(\mathbf{k}) q_\perp^*(\mathbf{k}) \rangle_{4\text{pt}} = 2 \sum_{ij} \mathbf{e}_i \mathbf{e}_j P_{qq}^{ij}(|\mathbf{k}|)$, where \mathbf{e}_i and \mathbf{e}_j are unit vectors along the lines-of-sight. The expression for $P_{qq}^{ij}(|\mathbf{k}|)$ is given by eqn. (13.3.3.2). In neglecting the irreducible 4-point term one obtains:

$$(2\pi)^3 \langle q_\perp(\mathbf{k}) q_\perp^*(\mathbf{k}) \rangle_{4\text{pt}} = \frac{1}{c^2} \int \frac{d^3 p}{(2\pi)^3} \left\{ (1 - x^2) P_{\delta\delta}(|\mathbf{k} - \mathbf{p}|) P_{vv}(|\mathbf{p}|) - \frac{(1 - x^2)p}{|\mathbf{k} - \mathbf{p}|} P_{\delta v}(|\mathbf{k} - \mathbf{p}|) P_{\delta v}(|\mathbf{p}|) \right\} \quad (13.47)$$

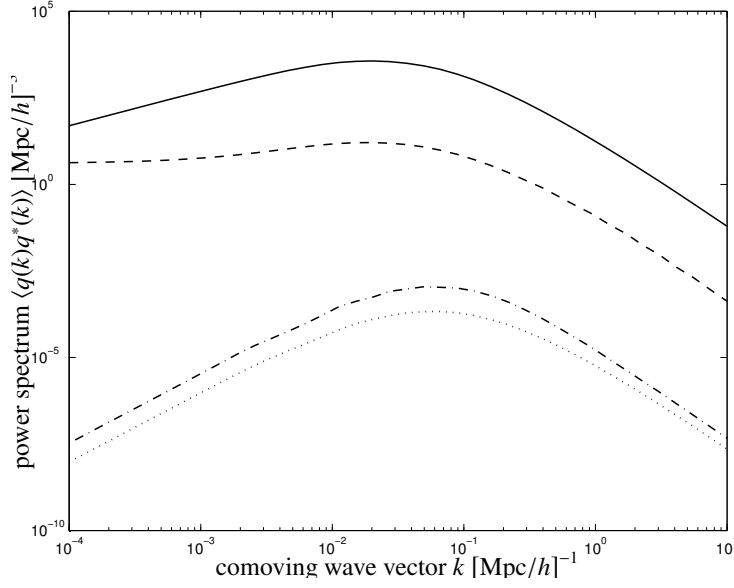


Figure 13.2.: Three-dimensional power spectrum $\langle q_{\perp}(\mathbf{k})q_{\perp}^*(\mathbf{k}) \rangle$ including dark matter currents perpendicular to the line-of-sight, split up into the 2-point contribution (solid line), the 3-point contribution (dashed line) and the 4-point contribution (dash-dotted line). Additionally, the 4-point term of the currents parallel to the line-of-sight $\langle q_{\parallel}(\mathbf{k})q_{\parallel}^*(\mathbf{k}) \rangle$ is drawn (dotted line). The power spectra are given for the present epoch, i.e. $a = 1$ and $z = 0$.

Inserting the time-evolution of the density-velocity and velocity-velocity cross correlation terms,

$$\langle v_{\perp}(\mathbf{k}, w_1)v_{\perp}^*(\mathbf{k}, w_2) \rangle = g'(w_1)g'(w_2)\langle v_{\perp}(\mathbf{k})v_{\perp}^*(\mathbf{k}) \rangle, \quad (13.48)$$

$$\langle v_{\perp}(\mathbf{k}, w_1)\delta^*(\mathbf{k}, w_2) \rangle = g'(w_1)D(w_2)\langle v_{\perp}(\mathbf{k})\delta^*(\mathbf{k}) \rangle, \quad (13.49)$$

yields the final result:

$$(2\pi)^3 \langle q_{\perp}(\mathbf{k}, w_1)q_{\perp}^*(\mathbf{k}, w_2) \rangle_{4\text{pt}} = \frac{8\pi}{c^2} D(w_1)D(w_2)g'(w_1)g'(w_2) \int dp \int_{-1}^{+1} dx P(|\mathbf{k}-\mathbf{p}|)P(|\mathbf{p}|) \frac{k(1-x^2)(k-2xp)}{k^2-2xkp+p^2}. \quad (13.50)$$

13.3.4. Corrections to the power spectrum

The three-dimensional power spectra $\langle q_{\perp}(\mathbf{k})q_{\perp}^*(\mathbf{k}) \rangle$ of the matter currents parallel to the line-of-sight is shown in Fig. 13.2 for the various n -point contributions. Compared to the dominating 2-point term, the 3-point term is smaller by more than two orders of magnitude on small scales, but it becomes important on large spatial scales beyond 1 Gpc where it levels out. On these large scales, however, limitations due to cosmic variance and insufficient sampling due to galactic foregrounds cast doubt on its detectability. The leveling on large spatial scales of the 3-point term is due to the fact, that for small k all powers in p in eqn. (13.43) add up to zero, which results in a flat curve for $\langle q_{\perp}(\mathbf{k})q_{\perp}^*(\mathbf{k}) \rangle_{3\text{pt}}$. In comparison to the 3-point term, the 4-point term is smaller by another three orders of magnitude, but in shape it very much resembles the 2-point term and its influence on the weak lensing power spectrum is safely negligible.

13.3.5. Projected lensing power spectra

The final expression for $\langle q_{\perp}(\mathbf{k})q_{\perp}^*(\mathbf{k}) \rangle$ can be projected by means of eqn. (13.32) to yield the angular power spectrum of any lensing quantity, for example the convergence κ . The distance weighting function to be employed can be read off from eqn. (13.40):

$$W_{\perp}(w) = \frac{3H_0^2\Omega_0}{2c^2} \frac{f_K(w)}{a(w)} \int_w^{w_{\max}} dw' Z(w') \frac{f_K(w'-w)}{f_K(w')}. \quad (13.51)$$

By substituting $y = kw$, the distance weighting $W_L(w)$ can be combined with the time evolution of the correlators to yield the functions

$$\varphi_\ell(k)_{2\text{pt}} = \left[\int_0^{y_{\text{max}}} dy W_L\left(\frac{y}{k}\right) \frac{J_\ell(y)}{y} D(y) \right]^2, \quad (13.52)$$

$$\varphi_\ell(k)_{3\text{pt}} = \int_0^{y_{\text{max}}} dy W_L\left(\frac{y}{k}\right) \frac{J_\ell(y)}{y} D(y) G(y) \int_0^{y_{\text{max}}} dy W_L\left(\frac{y}{k}\right) \frac{J_\ell(y)}{y} D(y), \quad (13.53)$$

$$\varphi_\ell(k)_{4\text{pt}} = \left[\int_0^{y_{\text{max}}} dy W_L\left(\frac{y}{k}\right) \frac{J_\ell(y)}{y} D(y) G(y) \right]^2, \quad (13.54)$$

which carry out the projection of the 3-dimensional power spectrum $\langle q_\perp(k) q_\perp^*(k) \rangle$ to the angular power spectrum $C_\kappa(\ell)$ by convolution:

$$C_\kappa(\ell) = 2\pi\ell(\ell + 1) \int dk \langle q_\perp(k) q_\perp^*(k) \rangle \times \varphi_\ell(k), \quad (13.55)$$

where the associativity of the time-evolution enables the 3-fold integration in eqn. (13.32) to be reduced to a 2-fold integration. Numerical issues connected to the integration of J_ℓ -weighted functions are discussed in Appendix D.

The functions $\varphi_\ell(k)_{2\text{pt}}$, $\varphi_\ell(k)_{3\text{pt}}$ and $\varphi_\ell(k)_{4\text{pt}}$ are shown in Fig. 13.3. Clearly, the fluctuations on a certain angular scale described by the angular power spectrum $C(\ell)$ are dominated by spatial fluctuations with a certain wave vector k , which leads the peak of the function $\varphi_\ell(k)$ to shift with increasing ℓ . The projection kernels $\varphi_\ell(k)$ for the different n -point correlation functions show the common feature of rising fast at small k , but their decays at large k vary appreciably, because the increasing influence of the time evolution of the velocities $G(w)$ makes the functions to drop faster with increasing values of k . In this way, the observed asymptotic behaviour is $\varphi_\ell(k_{2\text{pt}}) \propto k^{-2}$ for the 2-point projector, but the $\varphi_\ell(k_{3\text{pt}})$ and $\varphi_\ell(k_{4\text{pt}})$ exhibit faster decays that are not described by a mere power law. Evaluating the functions (13.52), (13.53) and (13.54) requires accurate numerical integration over $J_\ell(y)$ -weighted integrands, which rapidly oscillate at large values of y . Details of this numerical integration are explained in Appendix D.

The angular power spectrum of the weak lensing convergence $C_\kappa(\ell)$ and its corrections due to gravitomagnetic terms is depicted in Fig. 13.4. Even at the largest angular scales considered here, the function $\varphi_\ell(k)$ peaks at values of k at which the corrections of the 3-point term are negligible. The detection of corrections to the weak lensing power spectrum due to gravitomagnetic terms requires the measurement of weak lensing shear on very large angular scales, which is beyond feasibility with current technology. On large angular scales, cosmic variance additionally limits the observability of gravitomagnetic lensing.

13.4. Integrated Sachs-Wolfe effect

13.4.1. Definitions

The growth of structure imprints additional anisotropies on the cosmic microwave background (CMB) by the time variation of the gravitational potentials along the propagation path of a CMB photon. This effect is called the integrated Sachs-Wolfe (iSW) effect in the regime of linear structure formation (Sachs & Wolfe 1967, Hu & Sugiyama 1994) and Rees-Sciama effect (Rees & Sciama 1968, Seljak 1996b, Cooray 2002) if the density perturbations grow nonlinearly. The perturbations ΔT of the sky temperature T can be written as:

$$\tau \equiv \frac{\Delta T}{T} = -\frac{2}{c^3} \int dw \frac{\partial \Phi}{\partial \eta}, \quad (13.56)$$

where $\partial \Phi / \partial \eta$ is the derivative of the gravitational potentials with respect to conformal time η . Similar to gravitomagnetic lensing discussed in Sect. 13.3.1 (c.f. eqns. (13.33) and (13.36)), the effect is of the order $1/c^3$.

13.4.2. Connection to the gravitomagnetic potentials

Using the definition of $\Phi(\mathbf{r})$ and the equation of continuity, $\dot{\rho} + \text{div} \mathbf{j}$, where $\mathbf{j} = \rho \mathbf{v}$ is the matter current density, one obtains for the time derivative of Φ :

$$\frac{\partial}{\partial \eta} \Phi(\mathbf{r}, \eta) = -G \int d^3 r' \frac{\dot{\rho}(\mathbf{r}')}{|\mathbf{r} - \mathbf{r}'|} = G \int d^3 r' \frac{\nabla' \cdot \mathbf{j}(\mathbf{r}')}{|\mathbf{r} - \mathbf{r}'|}. \quad (13.57)$$

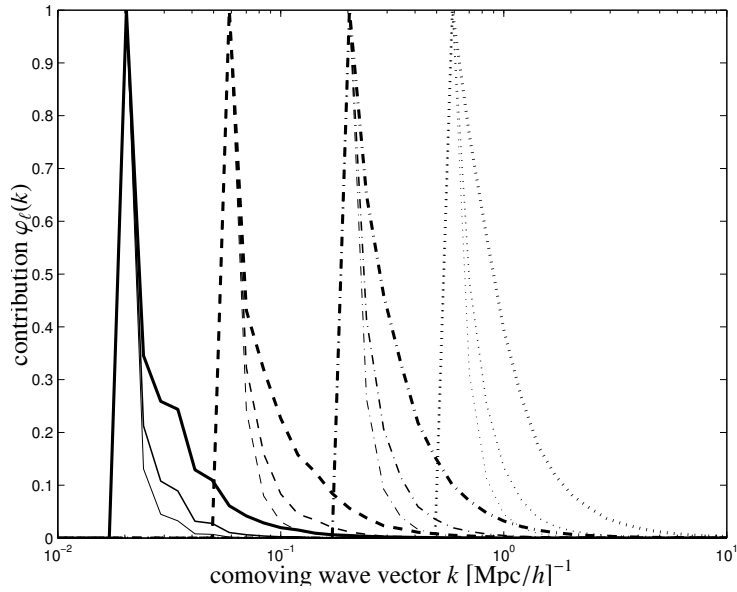


Figure 13.3: Contribution $\varphi_\ell(k)$ of the 2-point terms (thick lines), 3-point terms (medium lines) and 4-point terms (thin lines) to the angular power spectrum $C_\kappa(\ell)$ of the weak lensing convergence κ as a function of wave vector k , for $\ell = 100$ (solid line), $\ell = 300$ (dashed line), $\ell = 1000$ (dash-dotted line) and $\ell = 3000$ (dotted line). The curves are normalised to unity.

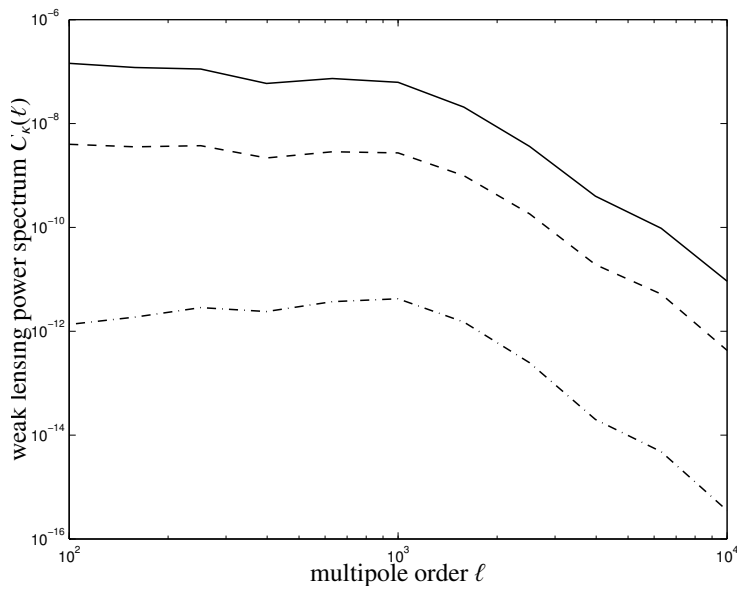


Figure 13.4: Angular power spectrum $C_\kappa(\ell)$ of the weak lensing convergence κ and its correction due to gravitomagnetic potentials. The contributions from the 2-point term (solid line), the 3-point term (dashed line) and the 4-point term (dash-dotted line) are given separately.

Integration by parts with respect to d^3r' yields:

$$G \int d^3r' \frac{\nabla' \cdot \mathbf{j}(\mathbf{r}')}{|\mathbf{r} - \mathbf{r}'|} = -G \int d^3r' \mathbf{j}(\mathbf{r}') \cdot \nabla' \frac{1}{|\mathbf{r} - \mathbf{r}'|}. \quad (13.58)$$

With the identity

$$\nabla' \frac{1}{|\mathbf{r} - \mathbf{r}'|} = -\nabla \frac{1}{|\mathbf{r} - \mathbf{r}'|}, \quad (13.59)$$

the derivative with respect to the primed coordinate can be replaced by a derivative with respect to the unprimed one. In the last steps, the ∇ -operator can be drawn in front of the integral and the definition of \mathbf{A} (c.f. eqn. (13.35)) be inserted to yield:

$$G \int d^3r' \mathbf{j}(\mathbf{r}') \cdot \nabla \frac{1}{|\mathbf{r} - \mathbf{r}'|} = -\nabla \cdot \left(-G \int d^3r' \frac{\mathbf{j}(\mathbf{r}')}{|\mathbf{r} - \mathbf{r}'|} \right) = -\text{div} \mathbf{A}. \quad (13.60)$$

Thus, the final result reads:

$$\frac{\partial}{\partial \eta} \Phi(\mathbf{r}, t) = -\text{div} \mathbf{A} \rightarrow \tau = \frac{2}{c^3} \int dw \text{div} \mathbf{A}. \quad (13.61)$$

Eqn. (13.61) has a lucid interpretation: The formation of objects such as clusters of galaxies requires the matter fluxes \mathbf{j} to converge and to accumulate matter ($\dot{\rho} > 0$). Consequently, potential wells deepen and give rise to the iSW-effect in regions where $\text{div} \mathbf{A}$ does not vanish. The iSW-effect measures the rate of change of a potential with respect to conformal time, or equivalently, the divergence of the vector potential \mathbf{A} , which is proportional to the accretion rate in the Lagrangian frame. The microscopic picture of gravitomagnetic interaction of a photon is developed in Appendix. F.

13.4.3. Putting the Sachs-Wolfe effect in a cosmological context

In order to relate the statistical properties of the iSW temperature fluctuations $\tau(\boldsymbol{\theta})$ to those of the matter streams $\mathbf{j}(\mathbf{r})$, the auxiliary vector field $\boldsymbol{\chi}(\boldsymbol{\theta})$ is introduced, which is defined as the negative gradient of the iSW temperature fluctuation $\tau(\boldsymbol{\theta})$:

$$\boldsymbol{\chi}(\boldsymbol{\theta}) \equiv -\nabla \tau(\boldsymbol{\theta}), \quad (13.62)$$

i.e. $\boldsymbol{\chi}(\boldsymbol{\theta})$ points along the steepest descent in temperature from hot to cold patches in an iSW field. Inserting eqn. (13.61) into the defining equation for $\boldsymbol{\chi}(\boldsymbol{\theta})$ and converting the derivation with respect to the angular variable $\boldsymbol{\theta}$ into a derivation with respect to the comoving variable \mathbf{r} by using $\nabla_{\boldsymbol{\theta}} = f_K(w) \nabla$, enables interchanging integration and differentiation:

$$\boldsymbol{\chi}(\boldsymbol{\theta}) = \frac{2}{c^3} \int dw f_K(w) \nabla (\text{div} \mathbf{A}) = \frac{2}{c^3} \int dw f_K(w) \Delta \mathbf{A}. \quad (13.63)$$

Additionally, the replacement $\nabla (\text{div} \mathbf{A}) = \Delta \mathbf{A}$ is inserted, which is valid if $\text{rot rot} \mathbf{A} = \mathbf{0}$. This is fulfilled in vorticity-free velocity fields, $\text{rot} \mathbf{j} = \mathbf{0}$. In linear theory, initial vorticity perturbations are damped and after a sufficiently long time, the linear velocity field should be completely irrotational. Even in the regime of quasi- or nonlinear structure formation, Kelvin's circulation theorem forces the flow to remain irrotational and described by a velocity potential until dissipative processes on smallest scales give rise to vortical flows.

Inserting Laplace's equation in the comoving frame, $\Delta \mathbf{A} = 4\pi G a^2 \langle \rho \rangle (\delta \mathbf{v})$ with the source term $\mathbf{j} = \delta \mathbf{v}$, allows to replace Newton's constant G and the ambient mass density $\langle \rho \rangle$ by using $\rho_{\text{crit}} = 3H_0^2 / (8\pi G)$, $\langle \rho \rangle_0 = \Omega_0 \rho_{\text{crit}}$ and $\langle \rho \rangle = \langle \rho \rangle_0 / a^3$:

$$\boldsymbol{\chi}(\boldsymbol{\theta}) = \frac{2}{c^3} \int dw f_K(w) \frac{4\pi G \langle \rho \rangle}{a} \mathbf{j} = \frac{3H_0^2 \Omega_0}{c^2} \int dw \frac{f_K(w)}{a(w)} \frac{\mathbf{j}}{c}. \quad (13.64)$$

The structural similarity of eqn. (13.64) with the weak lensing convergence eqn. (13.40) is striking.

Now, the 2-point correlation of the iSW temperature gradient field $\boldsymbol{\chi}(\boldsymbol{\theta})$ is related to the matter flux density $\mathbf{j}(\mathbf{r})$. For the derivation of the correlation function $C_{\tau}(\ell)$ of the temperature field $\tau(\boldsymbol{\theta})$ itself, one rewrites eqn. (13.62) in Fourier space, yielding:

$$\boldsymbol{\chi}(\boldsymbol{\theta}) = \int d^2\ell \boldsymbol{\chi}(\ell) \exp(i\ell \cdot \boldsymbol{\theta}) \rightarrow \boldsymbol{\chi}(\ell) = i\ell \tau(\ell) \quad (13.65)$$

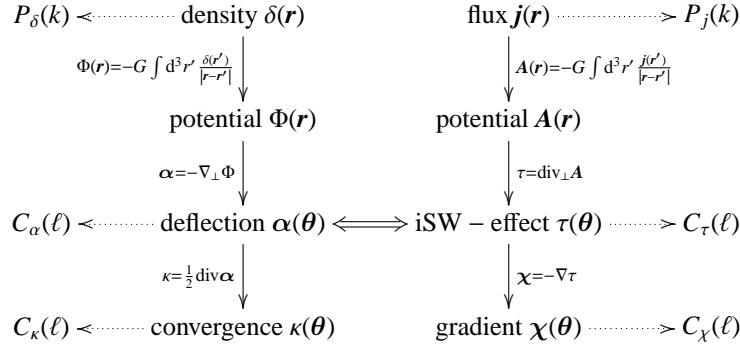


Figure 13.5.: Flow chart with correspondent quantities in gravitational lensing (left column) and the integrated Sachs-Wolfe effect (right column). The quantity analogous to the iSW temperature fluctuation $\tau(\theta)$ in weak gravitational lensing is the deflection angle $\alpha(\theta)$.

The expansion into Fourier modes rather than spherical harmonics is permissible, because τ is expected to show fluctuations on small angular scales, so that τ can be considered on a plane locally tangential to the celestial sphere. Squaring immediately gives:

$$C_\chi(\ell) = \ell^2 C_\tau(\ell) \simeq \ell(\ell + 1) C_\tau(\ell), \quad (13.66)$$

where the last step is a valid approximation for small angular scales. The complementarity of gravitational lensing and the iSW-effect and the lensing counterparts of iSW quantities are illustrated in the flow chart Fig. 13.5.

The validity of the assumption of vorticity-free flows used in the derivation above could in principle be tested by measuring the gravitational Faraday rotation, i.e. the rotation of the plane of polarisation of a photon transversing a gravitational field. This signature unique to vortical matter streams, although it is likely to be a very small effect on e.g. galactic scales. The theory of gravitational Faraday rotation is developed in papers by Piran & Safier (1985), Nouri-Zonoz (1999) and Sereno (2004).

13.4.4. Perturbative treatment

In the following, I adopt the approximation that the rate of change of a potential is constant during the photon passage and that the accretion geometry does not change significantly. In this approximation, the component dA_z/dz of $\text{div}A$ is cancelled by the integration in eqn. (13.61) and makes the iSW effect to measure the components of $\text{div}A$ perpendicular to the line-of-sight, i.e. $\tau \propto \text{div}_\perp A = dA_x/dx + dA_y/dy$. Consequently, the matter fluxes $\mathbf{q}_\perp(\mathbf{x}) = \mathbf{j}_\perp(\mathbf{x})/c = \delta(\mathbf{x})\mathbf{v}_\perp(\mathbf{x})/c$ perpendicular to the line-of-sight primarily give rise to the iSW-effect. Accordingly, the fluctuations in the CMB due to the Rees-Sciama effect, being sensitive to the components of the matter flux perpendicular to the line-of-sight, are dominated by the components of k -modes parallel to the line of sight.

Power spectra of the form $\langle q_{\parallel}(\mathbf{k}) q_{\parallel}^*(\mathbf{k}) \rangle$ have been considered by many authors in the derivation of the Ostriker-Vishniac effect (e.g. Vishniac 1987, Jaffe & Kamionkowski 1998). In order to obtain the projection onto the line-of-sight, $(2\pi)^3 \langle q_{\parallel}(\mathbf{k}) q_{\parallel}^*(\mathbf{k}) \rangle_{4\text{pt}} = \sum_{ij} \frac{k^i}{|k^i|} \frac{k^j}{|k^j|} P_{qq}^{ij}(|\mathbf{k}|)$, has to be carried out, which can be interpreted as the quadratic form $\hat{\mathbf{k}}^T \tilde{P} \hat{\mathbf{k}}$ with a unit vector $\hat{\mathbf{k}}$ and the matrix $\tilde{P} = P_{qq}^{ij}$ (compare eqn. 13.3.3.2). The matrix \tilde{P} introducing the scalar product $\hat{\mathbf{k}}^T \tilde{P} \hat{\mathbf{k}}$ is positive definite, due to the reality of the density and velocity fields.

$$(2\pi)^3 \langle q_{\parallel}(\mathbf{k}) q_{\parallel}^*(\mathbf{k}) \rangle_{4\text{pt}} = \frac{4}{c^2} \int \frac{d^3 p}{(2\pi)^3} x^2 P_{\delta\delta}(|\mathbf{k}-\mathbf{p}|) P_{vv}(|\mathbf{p}|) + \frac{(k-p_x)x}{|\mathbf{k}-\mathbf{p}|} P_{\delta v}(|\mathbf{k}-\mathbf{p}|) P_{\delta v}(|\mathbf{p}|) \quad (13.67)$$

The scalar product \mathbf{pk} is again equal to pkx , where x is the cosine of the angle of separation. Inserting the velocity-density and velocity-velocity cross correlation functions with their proper time evolution,

$$\langle v_{\parallel}(\mathbf{k}, w_1) \delta^*(\mathbf{k}, w_2) \rangle = g'(w_1) D(w_2) \langle v_{\parallel}(\mathbf{k}) \delta^*(\mathbf{k}) \rangle, \quad (13.68)$$

$$\langle v_{\parallel}(\mathbf{k}, w_1) v_{\parallel}^*(\mathbf{k}, w_2) \rangle = g'(w_1) g'(w_2) \langle v_{\parallel}(\mathbf{k}) v_{\parallel}^*(\mathbf{k}) \rangle, \quad (13.69)$$

yields the final result:

$$(2\pi)^3 \langle q_{\parallel}(\mathbf{k}, w_1) q_{\parallel}(\mathbf{k}, w_2) \rangle_{4\text{pt}} = D(w_1) D(w_2) g'(w_1) g'(w_2) \frac{2\pi}{c^2} \int dp \int_{-1}^{+1} dx P(|\mathbf{k} - \mathbf{p}|) P(|\mathbf{p}|) \frac{kx(kx - 2px^2 + p)}{k^2 - 2xkp + p^2}. \quad (13.70)$$

13.4.5. Power spectrum of dark matter currents

The three-dimensional power spectrum $\langle q_{\parallel}(\mathbf{k}) q_{\parallel}^*(\mathbf{k}) \rangle$ of the matter currents perpendicular to the line-of-sight is given in Fig. 13.2. Its amplitude is by a factor of 4 smaller than the power spectrum $\langle q_{\perp}(\mathbf{k}) q_{\perp}^*(\mathbf{k}) \rangle$, because the iSW-effect measures the streams δv in contrast to gravitomagnetic lensing, where the source terms read $(1 + 2\nu/c)\delta$. Despite the fact that different projections are considered, the shape and asymptotic forms of $\langle q_{\parallel}(\mathbf{k}) q_{\parallel}^*(\mathbf{k}) \rangle$ and $\langle q_{\perp}(\mathbf{k}) q_{\perp}^*(\mathbf{k}) \rangle$ are very similar.

13.4.6. integrated Sachs-Wolfe angular power spectrum

Fig. 13.7 shows the angular power spectra $C_{\tau}(\ell)$ of the iSW-effect $\tau(\boldsymbol{\theta})$ and $C_{\chi}(\ell)$ of the iSW temperature gradient $\chi(\boldsymbol{\theta})$ which have been obtained by applying the projection formula (13.26) to the spectrum $\langle q_{\parallel}(\mathbf{k}) q_{\parallel}^*(\mathbf{k}) \rangle$ with the weighing function

$$W_{\text{iSW}}(w) = \frac{3H_0^2 \Omega_0}{c^2} \frac{f_K(w)}{a(w)}, \quad (13.71)$$

which can be read off from eqn. (13.64). The redshift-weightings and the time-evolution of the density and velocity fields can be combined, which yields the function (13.72) after substituting $y = kw$,

$$\psi_{\ell}(k)_{4\text{pt}} = \left[\int_0^{y_{\text{max}}} dy W_{\text{iSW}} \left(\frac{y}{k} \right) \frac{dJ_{\ell}(y)}{dy} D(y) G(y) \right]^2 \quad (13.72)$$

which mediates between the 3-dimensional power spectrum $\langle q_{\parallel}(k) q_{\parallel}^*(k) \rangle$ and the angular power spectrum $C_{\tau}(\ell)$ by convolution:

$$C_{\tau}(\ell) = 2\pi \int dk \langle q_{\parallel}(k) q_{\parallel}^*(k) \rangle \times \psi_{\ell}(k). \quad (13.73)$$

Again, the 3-fold integration in eqn. (13.26) is reduced to a 2-fold integration. The shape of the function $\psi_{\ell}(k)$ is depicted in Fig. 13.6 for various values of ℓ . In contrast to the function $\varphi_{\ell}(k)$ used in the projection of the lensing power spectra, the function $\psi_{\ell}(k)$ is symmetric about its peak, which is caused by the replacement of $J_{\ell}(y)/y$ with the derivative $dJ_{\ell}(y)/dy$. The fast variability is again due to the strong influence of the velocity time evolution $G(y)$. Details concerning numerics of the integration in eqn. 13.72 which involves a rapidly oscillating function are discussed in Appendix D.

The angular power spectrum $C_{\tau}(\ell)$ of the iSW temperature fluctuations $\tau(\boldsymbol{\theta})$ along with the primary CMB fluctuations and the limiting PLANCK-sensitivity is depicted in Fig. 13.7. The angular power spectrum has an amplitude of $\simeq 3 \times 10^{-11} \text{ K}^2$ at small ℓ and shows but little variation with the multipole order ℓ . The amplitude agrees well with the result from Seljak (1996b), but the decline of the power spectrum on large angular scales could not be confirmed, which is due to the fact that for large angles, the Bessel functions $J_{\ell}(x)$ are a poor approximation to the Legendre polynomials $P_{\ell}(x)$. The position of the peak in the projection kernel $\psi_{\ell}(k)$ suggests that on the largest scales considered here, the angular spectrum $C_{\tau}(\ell)$ is dominated by fluctuations at the maximum of $P(k)$ on scales at $k^{-1} \simeq 10 \text{ Mpc}$. With increasing multipole order ℓ , the peak in $\psi_{\ell}(k)$ shifts only slowly towards higher values of k , which explains the small variation of $C_{\chi}(\ell) = \ell(\ell + 1)C_{\tau}(\ell)$.

The channel averaged PLANCK-sensitivity is described by (Knox 1995, Tegmark & Efstathiou 1996):

$$C_{\text{noise}}(\ell) = \frac{4\pi\sigma^2}{N_{\text{pix}}} \exp\left[\theta_b^2 \ell(\ell + 1)\right], \quad (13.74)$$

where $N_{\text{pix}} \simeq 5.03 \times 10^7$ is the number of pixels and θ_b the FWHM extension of the PLANCK-beam. For the average amplitude of the noise σ_{eff} per solid angle subtended by a single pixel I use the quadratic harmonic mean over all six HFI-channels:

$$\frac{1}{\sigma_{\text{eff}}^2} = \sum_{i=1}^6 \frac{1}{\sigma_i^2} \longrightarrow \sigma_{\text{eff}} = 13.42 \mu\text{K}. \quad (13.75)$$

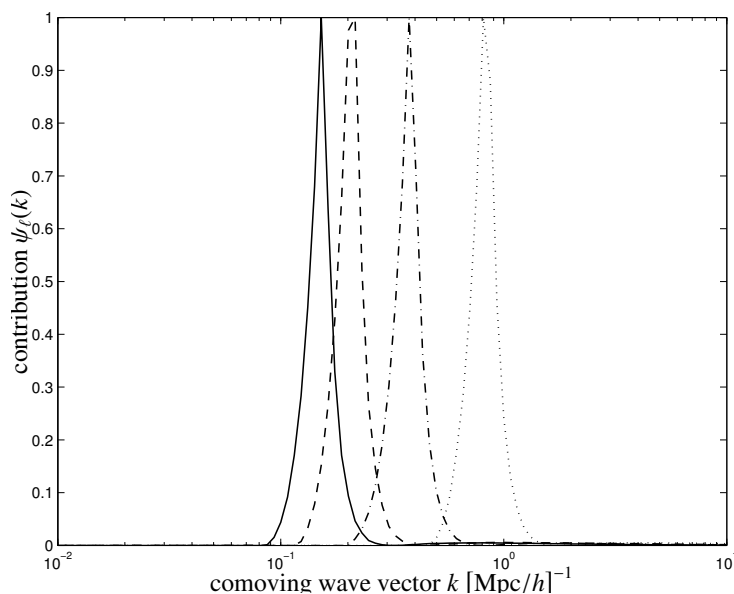


Figure 13.6.: Contribution $\psi_\ell(k)$ of the 4-point term to the angular power spectrum $C_\tau(\ell)$ of the iSW temperature fluctuations τ as a function of wave vector k , for $\ell = 100$ (solid line), $\ell = 300$ (dashed line), $\ell = 1000$ (dash-dotted line) and $\ell = 3000$ (dotted line). The curves have been normalised to a peak value of unity.

The sensitivity considerations suggest that the iSW-effect is well above the noise level of the combined PLANCK *HFI*-channels, so that the power spectrum of $C_\tau(\ell)$ should be observable for angular scales $\ell \lesssim 200$ as a contribution to the primary CMB fluctuations $C_{\text{CMB}}(\ell)$, which in Fig. 13.7 have been computed using the CMBfast code by [Seljak & Zaldarriaga \(1996\)](#).

13.5. Summary

The scope of this paper is to derive the corrections to the power spectrum of weak gravitational lensing due to gravitomagnetic terms in the metric by perturbation theory. Within the same formalism, the power spectrum of the iSW-effect can be determined as well.

- The iSW-effect and gravitomagnetic lensing measure the evolution of velocities and densities in the large-scale structure and are sensitive to the cosmological parameters Ω_M and σ_8 . Applied to single objects like clusters, where the above described formalism equally applies, the iSW-effect would allow to measure the cosmological evolution of merger rates and dark matter accretion strengths ([van den Bosch 2002](#), [Wechsler et al. 2002](#), [Zhao et al. 2003](#)).
- Gravitomagnetic lensing would test general relativity on the largest scales (Mpc - Gpc) to second order, and could help decide in favour of or against other metric theories of gravity. It should be emphasised that in the current theoretical description of structure formation or in current numerical simulations the motion of bodies is described by classical mechanics, i.e. instantaneous propagation of potentials and no relativistic increase of inertial mass with velocity, but the interaction of light with matter should be treated in the framework of the post-Newtonian limits of general relativity.
- Gravitomagnetic terms influence the weak lensing power spectrum most notably on large spatial and angular scales, which are difficult to access experimentally. Furthermore, cosmic variance and galactic foregrounds prevent accurate measurements on the scales in question, i.e. $\gtrsim \text{Gpc}/h$ and above. The small gravitomagnetic corrections could be amplified by cross correlation with the kinetic Sunyaev-Zel'dovich effect ([Sunyaev & Zel'dovich 1972](#)), once future CMB telescopes will provide accurate measurements of line-of-sight velocities

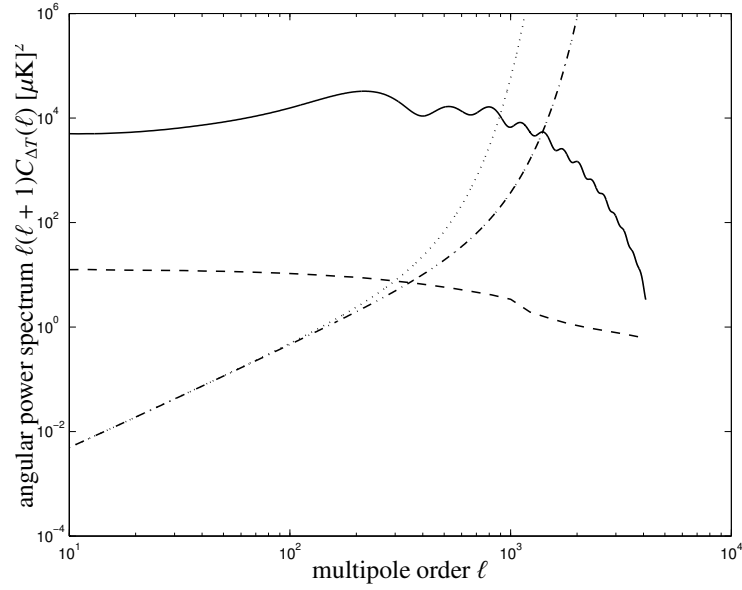


Figure 13.7.: Angular power spectrum $C_{\Delta T}(\ell) = T_{\text{CMB}}^2 C_{\tau}(\ell)$ of the iSW temperature fluctuations $\tau(\theta)$ (dashed line). The CMB power spectrum $C_{\text{CMB}}(\ell)$ for the Λ CDM cosmology (solid line) and the limiting PLANCK-sensitivities $C_{\text{noise}}(\ell)$ for angular resolutions $\Delta\theta = 5:0$ (dash-dotted line) and $\Delta\theta = 9:1$ (dotted line) are depicted for comparison.

or with the velocity information from optical galaxy surveys. For current weak lensing surveys, gravitomagnetic corrections to cosmic shear do not play a significant role.

- The iSW-effect is described by a line-of-sight integration over the divergence of the gravitomagnetic potentials. By this argument, the iSW-effect is reduced to a second order lensing effect. Every iSW quantity has a correspondence in weak gravitational lensing and the derivation of the power spectrum $C_{\tau}(\ell)$ proceeds in complete analogy to that of any weak lensing quantity, for instance that of the convergence $C_{\kappa}(\ell)$. The most important difference of the derivation presented here to the ones carried out by [Seljak \(1996b\)](#) or [Cooray \(2002\)](#) is that my derivation explicitly pays tribute to the lensing nature of the iSW-effect.
- Gravitomagnetic lensing and the iSW-effect are complementary in measuring the matter flows parallel and perpendicular to the line-of-sight. The picture emerging is that (subject to the approximations made) in gravitational light deflection (including the gravitomagnetic term A_z), the photon's \mathbf{k} -vector is rotated but its normalisation is conserved. Contrarily, the components of \mathbf{A} transverse to the line-of-sight change the normalisation of the \mathbf{k} -vector, i.e. the photon's energy, but leave the direction of \mathbf{k} invariant.
- Both effects, gravitomagnetic lensing and the iSW-effect, are achromatic which makes them only accessible by their n -point statistics. Furthermore, the iSW-effect needs to be separated from other achromatic CMB structures such as the kinetic Sunyaev-Zel'dovich effect and the Ostriker-Vishniac effect. The derivation predicts iSW temperature fluctuations of $\Delta T = \tau T_{\text{CMB}} \simeq 5.4 \mu\text{K}$ on large angular scales, which is within reach of future CMB experiments like the European PLANCK-mission.
- The gradient $\chi(\theta)$ of the iSW temperature fluctuation field $\tau(\theta)$ should directly map regions of large matter flows, e.g. filaments and clusters with high peculiar velocities, but it can be expected to be very susceptible to noise due to the differentiation required in obtaining $\chi(\theta)$ from $\tau(\theta)$, which is reflected by the fact that ratio of the angular power spectra $C_{\chi}(\ell)/C_{\tau}(\ell)$ is proportional to $\ell(\ell+1)$.

The verification of the theoretical approach by a ray-tracing simulation of photons through a cosmological n -body simulation will be the subject of future research. The non-Gaussian features the iSW-effect and gravitational lensing exhibit and the mode-coupling in nonlinear structure growth are unaccessible to perturbation theory and are important on small scales. The novel approach to the iSW-effect presented here should allow a much improved

precision in the numerical treatment, because inaccuracies in interpolating the scalar potential's time derivative $\partial\Phi/\partial\eta$ for each integration time step and in integrating a rapidly oscillating function inherent the direct approach (e.g. [Tuluie & Laguna 1995a,b](#)) are alleviated.

The results of this chapter were derived in collaboration with M. Bartelmann (ITA, Heidelberg). A resulting paper entitled Gravitational lensing in the second post-Newtonian approximation: Gravitomagnetic potentials and the integrated Sachs-Wolfe effect will be submitted to the journal Monthly Notices of the Royal Astronomical Society.

14. Summary and outlook

The main subject of this thesis is the simulation of observations of cluster of galaxies for the European PLANCK-satellite. PLANCK will be able to detect clusters of galaxies by their thermal Sunyaev-Zel'dovich signature in sub-millimetric data and will open a new observational window for investigating structure growth and baryonic physics inside clusters of galaxies. In Chapter 5, I present all-sky maps of the thermal and kinetic Sunyaev-Zel'dovich effects which was constructed from numerical data by combining template clusters extracted from a high-resolution hydrodynamical simulation and a cluster catalogue following from a large-volume dark matter simulation. By construction, the map correctly shows the clustering properties on large spatial scales, deviation from canonical scaling relations and asymmetric and non-analytic temperature and density profiles of the individual clusters of galaxies. In the kinetic Sunyaev-Zel'dovich map, the peculiar velocities correspond to the local density field. The comparison to estimates of the Sunyaev-Zel'dovich signal strengths following from virial arguments showed that the number of clusters detectable with PLANCK is likely to be overestimated.

These maps were combined with various Galactic and ecliptic foregrounds. Specifically, I considered synchrotron radiation, free-free emission, infrared emission by thermal dust, line transition produced in rotational transitions of carbon monoxide molecules and the thermal radiation of planets and asteroids of the Solar system. I combined the Sunyaev-Zel'dovich maps with these foreground maps and with a realisation of the fluctuating CMB while taking care of the different spectral properties of the respective emission components and convolved the individual spectra with PLANCK's frequency response functions. The maps were successively convolved with PLANCK's respective point-spread functions, yielding antenna temperature maps for all nine PLANCK channels. In order to simulate the finite sensitivity of PLANCK's receivers, I generated noise maps that incorporate the spatial highly-non uniform exposure pattern due to PLANCK's scanning strategy, which were successively added. In Chapter 6 I describe the simulation in detail and investigate the complicated cross- and autocorrelation properties which have special relevance to filtering and component separation.

In Chapter 7, I describe an approach how the weak Sunyaev-Zel'dovich signal can be amplified and extracted by matched and scale-adaptive filtering. These filter schemes are particularly appealing because they are based on a variational principle. The algorithms require filter kernels to minimise the variance of a data set with the condition that the amplitude of the filtered field is an unbiased estimator of the underlying signal and that the amplitude of the filtered field is maximal if the spatial scale of the filter corresponds to the spatial extension of the signal. These filtering schemes were extended to multifrequency observations and to spherical topologies. In collaboration with C. Pfommer I could derive formulae that yield filter kernels for a given signal profile, for a specific spectral behaviour of the signal, and for the angular cross- and autocorrelation function of the spurious components. I derived filter kernels numerically for the simulated PLANCK antenna temperature maps and verified their functionality.

The characterisation of the PLANCK Sunyaev-Zel'dovich cluster sample is the subject of Chapter 8. It was shown that the SZ-cluster sample derived in this work, which contains 6×10^3 entries above 3σ does not live up to the high expectations claimed by analytic estimates. But the SZ-sample was shown to be clean and not to contain spurious detections on a significant level. The redshift range probed by PLANCK is restricted to redshifts smaller than $z < 0.8$, which is due to the highly structured noise on small scales. The sample was analysed in detail and the distributions of mass, redshift and detection significance are given. The spatial distribution was demonstrated to be spatially non-uniform on a significant level, irrespective of the filtering scheme, which is due to the improper removal of long-wavelength modes. The linearity of the filters was proved and position accuracies were demonstrated to be too coarse for direct follow-up studies in the X-ray band or in optical wavelengths.

The SZ-cluster catalogue of PLANCK will exceed classic X-ray catalogues with respect to number of detections and will complement our view of the baryonic processes inside clusters of galaxies. Furthermore, aspects of structure formation ranging from dark energy parameters, especially the dark energy density Ω_Q , its equation of state parameter w_Q , the shape of the power spectrum on Mpc scales and its normalisation σ_8 will be a highlight application of PLANCK's SZ sample. The simulation presented here surpasses in detail every simulation of

SZ observations with PLANCK carried out so far and covers all important aspects of cluster physics, foreground contamination, observation and instrumental imperfections, filtering and peak extraction.

In a supplementary project aiming at PLANCK data analysis algorithms I worked out a new pixel numbering scheme for the HEALPix tessellation commonly used in analyses of CMB data. A core quantity in many CMB data analysis tasks is the pairwise pixel covariance matrix. Common pixel numbering schemes face the difficulty that the covariance matrix does not have a simple shape and is difficult to access algorithmically and numerically. Basic matrix manipulations like inversion and computation of the determinant are very difficult to carry out, keeping the vast number of pixels of current and future CMB experiments in mind. In Chapter 9, I propose to use a pixel numbering based on a fractal, self-similar Peano-Hilbert curve that runs through all pixels on the sphere. If pixels were numbered successively along this curve, the pairwise pixel covariance matrix would assume a band-diagonal shape if correlations on large angular separations are neglected. For band diagonal matrices, fast and efficient algorithms for computing e.g. determinants and inverses exist. I tested the locality of the spherical Peano-Hilbert curve and investigated the shape of the covariance matrix for typical shapes of the correlation function and found its properties with respect to locality to be superior to the two existing pixel numbering schemes. It is planned to add the Peano-numbering to the HEALPix software package.

Aiming at future high-resolution CMB observations I analysed the morphology of simulated SZ-maps of clusters of galaxies with wavelets. It was found that the spectrum of wavelet coefficients can be described with elementary functions that have certain characteristics which are non-degenerate indicators of redshift. These morphological redshifts will be particularly useful for future SZ surveys that are expected to detect thousands of clusters in order to select targets for e.g. X-ray follow up observations. A detailed analysis in Chapter 10 examined the redshift estimation based on wavelet decomposition and found the relative accuracy in the distance estimation to be accurate to a few percent out to redshifts of unity. Adding noise contributions such as instrumental noise at reasonable levels and CMB fluctuations in order to simulate monochromatic observations proved the method to be very robust. Other complications like finite instrumental resolution, cool cores of clusters and systematic deviations from the universal baryon fraction that significantly alter the SZ-morphology of a cluster or impact on the SZ-scaling relations were shown to be controllable. Morphological redshift estimators will be of particular use for dedicated high-yield SZ observatories in order to select targets for optical or X-ray follow-up observations.

The statistical description of the CMB based on Gaussian random fields led to an unexpected application of this cosmological key concept to X-ray and γ -ray imaging in high energy astronomy. Imaging of highly energetic radiation by refractive or reflective optics is far from easy. Imaging at these high photon energies is commonly achieved by coded mask imaging, where the shadow cast of a mask consisting of randomly placed open elements is registered by a position sensitive detector. By using correlation techniques, it is possible to reconstruct the distribution of sources inside the field-of-view from the shadowgram, which is a superposition of the intensity distributions imaged by each individual pinhole. In Chapter 11, I propose to use Gaussian random fields as coded mask patterns, because they can be constructed to encode a specific functional shape of the point-spread function. I investigated the properties of Gaussian random fields in coded mask imagers in extensive photon ray-tracing studies and found the Gaussian random fields to perform well in the observation of extended sources which are inaccessible to traditional coded mask instruments and to yield a moderate performance in the observation of point sources.

Apart from the interaction of photons with the electrons of the intra-cluster medium I studied their gravitational interaction with clusters of galaxies and with the cosmic large-scale structure in Chapter 13. I was able to explain the integrated Sachs-Wolfe/Rees-Sciama effect, which predicts a frequency shift of photons transversing time-variable gravitational wells to be a second-order gravitational lensing effect emerging in the post-Newtonian expansion of general relativity. In this approximation, the Rees-Sciama effect measures the divergence of the gravitomagnetic vector potential integrated along the line-of-sight. By using this access, I could show interesting analogies between gravitational lensing quantities and Rees-Sciama quantities and point out many analogies in the respective formulae. I derived the angular autocorrelation function of the Rees-Sciama temperature fluctuations in the quasilinear regime in perturbation theory by using the gravitomagnetic formalism. The angular power spectrum was found to be detectable by PLANCK as a correction to the primordial CMB power spectrum at low multipoles. The Rees-Sciama effect on these scales will be an important diagnostic for dark matter clustering as it probes the transition from the linear into the nonlinear regime of structure formation.

By using the same tools, I addressed gravitomagnetic corrections to weak gravitational lensing of the large scale structure arising due to large-scale matter streams. The corrections evolved three- and four-point correlators of the density and velocity fields with their respective time evolution, which were reduced to products of two-point functions by perturbation theory in the limit of quasilinear growth. As in the case of the Rees-Sciama effect, I derived

a projection formula analogous to Limber's equation that is able to deal with vectorial fields in order to compute the angular power spectra from the three dimensional correlation functions. The corrections to weak lensing quantities were shown to be important on large spatial and angular scales, which are difficult to access observationally. For current weak lensing surveys, gravitomagnetic corrections play only a minor role.

In Chapter 12 I describe a code that I implemented for studying weak lensing on simulated cosmological density fields. This code computes the deflection and shear a light ray experiences when transversing a cosmological volume and has a number of improvements over competing ray-tracing codes with respect to functionality, performance and accuracy. It will certainly be interesting to investigate the Rees-Sciama effect and gravitomagnetic corrections to weak gravitational lensing on n -body simulations of cosmic structure formation and to access the fully nonlinear growth of structure where interesting non-Gaussian features in the density field evolve and Fourier modes of the density field are coupled, which is inaccessible to perturbation theory. The code is extended to derive the Rees-Sciama signal as a line-of-sight integration of the divergence of the gravitomagnetic vector potential, which is likely to have computational advantages over the traditional, direct approach. Furthermore, the code can compute the gravitational Faraday rotation, i.e. the rotation of the plane of polarisation due to vortical matter streams which evolve in the late phase of structure formation due to dissipative processes.

Now that physical cosmology has reached the stage at which the parameters governing the Hubble expansion and the geometry of the homogeneous universe are determined on the percent level, the Λ CDM paradigm of gravitational structure growth needs to be tested. The interaction of photons with the emerging large-scale structure by various mechanisms is able to shed light on the shape of the dark matter power spectrum $P(k)$, its normalisation σ_8 and the parameters describing dark energy, which starts to influence structure growth only in recent cosmic history. Among the most promising observational channels are the thermal Sunyaev-Zel'dovich effect and the Rees-Sciama effect, which were shown to be detectable by PLANCK and which will be particularly useful to break remaining degeneracies between cosmological parameters, to yield important constraints on the parameters and mechanism of structure growth and halo formation.

A. Numerical evaluation of SPH-projections

SPH (*smooth particle hydrodynamics*, originally developed by [Lucy 1977](#), [Gingold & Monaghan 1977](#), [Monaghan 1992](#), for solving hydrodynamical problems in stellar models) approximates continuous density fields by discrete distributions of point particles. In contrast to algorithms that solve the hydrodynamical equations on grids, SPH has the benefit of adapting its resolution to the local density, i.e. dense regions are well sampled by a large number of particles and vice versa. In the SPH formalism, continuous fields $A(\mathbf{x})$ (e.g the hydrodynamical quantities) are represented by their values A_i at discrete particle positions $\mathbf{r}_i = (x_i, y_i, z_i)$ with local spatial resolution h_i . This smoothing length h_i is adaptive and is chosen to be the distance of the N^{th} closest particle, where $N \simeq 30$.

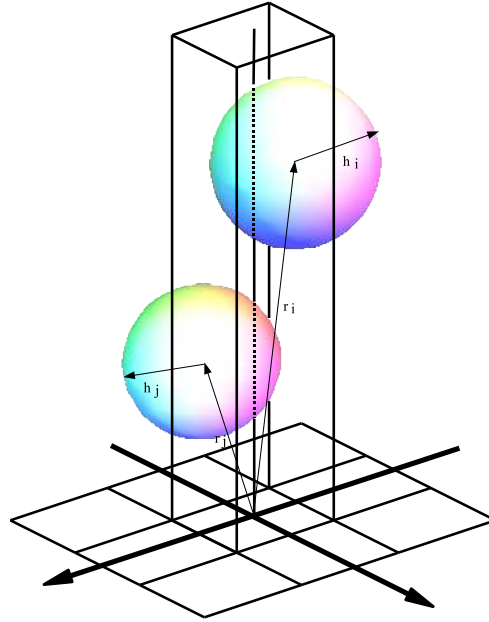


Figure A.1.: Derivation of line-of-sight quantities from an SPH-simulation.

In order to construct Cartesian maps $a(\mathbf{x})$ of line-of-sight integrated quantities from (cosmological) SPH simulations, one needs to employ an interpolation scheme. The line-of-sight integration of any quantity $A(\mathbf{x})$ at the pixel at position $\mathbf{x} = (x, y, z)$ is determined as the average of integration of all lines-of-sight passing through the pixel, which is equal to the volume integral of the kernel-weighted quantity A_i above a given pixel divided by the pixel area (compare Fig. [A.1](#)):

$$a(\mathbf{x}) = \frac{1}{g^2} \sum_i h_i^3 \left[\int_{x-g/2}^{x+g/2} dx_i \int_{y-g/2}^{y+g/2} dy_i \int_{-h_i}^{h_i} dz_i \mathcal{K}\left(\frac{r}{h_i}\right) \cdot A_i \right] \text{ with } r = \sqrt{(x_i - x)^2 + (y_i - y)^2 + z_i^2}, \quad (\text{A.1})$$

where the summation is extended over all particles of the simulation. g denotes the mesh size of the underlying Cartesian grid. The function \mathcal{K} is the spherically symmetric cubic spline kernel suggested by [Monaghan & Lattanzio](#)

(1985), which is commonly used in SPH simulations:

$$\mathcal{K}(u) = \frac{8}{\pi} \cdot \begin{cases} 1 - 6u^2 + 6u^3, & 0 \leq u \leq 1/2 \\ 2(1 - u)^3 & , 1/2 < u \leq 1 \\ 0 & , u > 1 \end{cases} \quad \text{with } u = r/h_i. \quad (\text{A.2})$$

The fact that the kernel \mathcal{K} is defined on a compact support $u \in [0 \dots 1]$ greatly reduces the computational effort. The dz -integration of this cubic spline kernel can be carried out analytically, while taking care of the piecewise definition of \mathcal{K} . This yields for the outer region, $1/2 \leq \rho \leq 1$, where $\rho^2 \equiv x^2 + y^2$:

$$\int_0^{\sqrt{\frac{1}{4}-\rho^2}} dz \mathcal{K}\left(\sqrt{\rho^2 + z^2}\right) = \frac{21\rho^2 \sqrt{1-\rho^2}}{4} - \frac{3\sqrt{1-\rho^2}}{2} - \frac{3}{4}\rho^4 \ln(\sqrt{1-\rho^2} + 1) + 2(1-\rho^2)^{\frac{3}{2}} - \quad (\text{A.3}) \\ 3\rho^2 \ln(\sqrt{1-\rho^2} + 1) + \frac{3}{2}\rho^2 \ln(\rho^2) + \frac{3}{8}\rho^4 \ln(\rho^2),$$

and for the inner region, $0 < \rho \leq 1/2$:

$$\int_{\sqrt{\frac{1}{4}-\rho^2}}^{\sqrt{1-\rho^2}} dz \mathcal{K}\left(\sqrt{\rho^2 + z^2}\right) = \frac{\sqrt{1-4\rho^2}}{8} - \frac{13\rho^2 \sqrt{1-4\rho^2}}{4} - 3\rho^4 \ln(2) + 3\rho^4 \ln(\sqrt{1-4\rho^2} + 1) - \quad (\text{A.4}) \\ \frac{9}{8}\rho^4 \ln(\rho^2) + \frac{21\rho^2 \sqrt{1-\rho^2}}{4} - \frac{3\sqrt{1-\rho^2}}{2} - \frac{3}{4}\rho^4 \ln(\sqrt{1-\rho^2} + 1) + \\ 2(1-\rho^2)^{\frac{3}{2}} - 3\rho^2 \ln(\sqrt{1-\rho^2} + 1) - 3\rho^2 \ln(2) + 3\rho^2 \ln(\sqrt{1-4\rho^2} + 1).$$

The dx - and dy -integrations need to be carried out numerically: For this task, Gauss-quadrature with a moderate number of sampling points (typically five sampling points in one dimension) has proven to yield results that recover the normalisation of the kernel with an accuracy of $\approx 10^{-5}$. The performance is around 10^6 particles per minute on a 1.1 GHz G4 processor.

Another choice for the SPH-kernel that is continuous in the unit interval is the function:

$$\mathcal{K}(u) = \mathcal{K}_0 \exp\left(-\frac{1}{1-u^2}\right) \quad \text{with } \mathcal{K}_0 \approx 2.267116739, \quad (\text{A.5})$$

but for this function one would need to carry out the dz -integration numerically as well, which would be too time consuming. By chance coincidence, this function yields an excellent fit to the weak lensing radial weighting function (see Sect. 13.3.2).

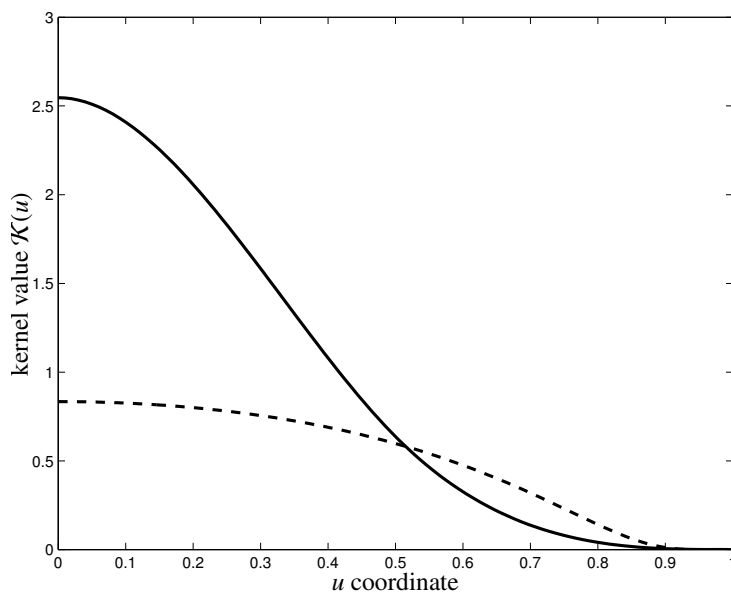


Figure A.2.: The cubic spline SPH-kernel (eqn. (A.2), solid line) and the alternative kernel (eqn. (A.5), dashed line).

B. Derivation of spherical matched and scale-adaptive filter kernels

This appendix presents the derivation of optimised filters for single frequency all-sky observations and serves as a detailed supplement to Chapter. 7, where optimised filters for multi-frequency observations were derived.

B.1. Assumptions and definitions

In order to construct filters, I consider an all-sky map of the detected scalar field $s(\boldsymbol{\theta})$

$$s(\boldsymbol{\theta}) = y(|\boldsymbol{\theta} - \boldsymbol{\theta}_0|) + n(\boldsymbol{\theta}), \quad (\text{B.1})$$

where $\boldsymbol{\theta} = (\vartheta, \varphi)$ denotes a two-dimensional vector on the sphere and $\boldsymbol{\theta}_0$ is the source location. The first term of the right-hand side represents the amplitude of the sources to be detected, while the second term corresponds to the generalised noise present in the map which is composed of any detected features other than the desired signal including for instance instrumental noise. The statistical properties of the noise are assumed to be characterised by its power spectrum $\langle n_{\ell m} n_{\ell' m'}^* \rangle = C_\ell \delta_{\ell\ell'} \delta_{mm'}$. In order to sketch the construction of the optimised filter, I assume an individual cluster situated at the North pole ($\boldsymbol{\theta}_0 = \boldsymbol{\theta}$) with a characteristic angular SZ-signal $y(\boldsymbol{\theta} = |\boldsymbol{\theta}|) = A\tau(\boldsymbol{\theta})$, separating the amplitude A from the profile $\tau(\boldsymbol{\theta})$.

I adapt the following convention for the expansion of the field $a(\boldsymbol{\theta})$ into spherical harmonics $Y_\ell^m(\boldsymbol{\theta})$ and its expansion coefficients $a_{\ell m}$,

$$a(\boldsymbol{\theta}) = \sum_{\ell=0}^{\infty} \sum_{m=-\ell}^{+\ell} a_{\ell m} Y_\ell^m(\boldsymbol{\theta}) \text{ and } a_{\ell m} = \int d\Omega a(\boldsymbol{\theta}) Y_\ell^m(\boldsymbol{\theta})^*, \quad (\text{B.2})$$

where the asterisk denotes the complex conjugate and $d\Omega = d(\cos \vartheta) d\varphi$ denotes the differential solid angle element. The background $n_\nu(\boldsymbol{\theta})$ is assumed to be a homogeneous and isotropic random field with vanishing mean, which is characterised by the power spectrum C_ℓ defined by

$$\langle n_{\ell m} n_{\ell' m'}^* \rangle = C_\ell \delta_{\ell\ell'} \delta_{mm'}, \quad \text{with } \langle n(\boldsymbol{\theta}) \rangle = 0. \quad (\text{B.3})$$

$n_{\ell m}$ denote the spherical harmonics expansion coefficients of $n(\boldsymbol{\theta})$, $\delta_{\ell\ell'}$ is the Kronecker symbol, and $\langle \rangle$ corresponds to an ensemble average. Assuming ergodicity of the field under consideration allows taking spatial averages over sufficiently large areas $\Omega = O(4\pi)$ instead of performing the ensemble average.

B.2. Convolution theorem on the sphere

Filtering a scalar field on the sphere with an arbitrary, asymmetric kernel requires the specification of the convolution path as well as the orientation of the filter kernel at each position on the sphere in order to apply any convolution algorithm (Wandelt & Górski 2001). Because of the simplifying restriction to axially symmetric filter kernels, I give the theorem for the convolution of two functions, one of which is assumed to be axially symmetric. The filtered field $u(\boldsymbol{\beta})$ is obtained by convolution of the axially symmetric filter function $\psi(\boldsymbol{\theta})$ with the scalar field on the sphere $s(\boldsymbol{\theta})$,

$$u(\boldsymbol{\beta}) = \int d\Omega s(\boldsymbol{\theta}) \psi(|\boldsymbol{\theta} - \boldsymbol{\beta}|). \quad (\text{B.4})$$

Expansion of these two scalar fields into spherical harmonics yields

$$s(\boldsymbol{\theta}) = \sum_{\ell=0}^{\infty} \sum_{m=-\ell}^{+\ell} s_{\ell m} Y_{\ell}^m(\boldsymbol{\theta}), \text{ and } \psi(\boldsymbol{\theta}) = \sum_{\ell=0}^{\infty} \sum_{m=-\ell}^{+\ell} \psi_{\ell m} Y_{\ell}^m(\boldsymbol{\theta}) = \sum_{\ell=0}^{\infty} \sqrt{\frac{2\ell+1}{4\pi}} \psi_{\ell 0} P_{\ell}(\cos \theta). \quad (\text{B.5})$$

The last step assumes axial symmetry. In this case, only modes with $m = 0$ are contributing. For proceeding, the addition theorem for Legendre polynomials $P_{\ell}(x)$ (Arfken & Weber 1995) is used in substituting $\gamma = |\boldsymbol{\theta} - \boldsymbol{\beta}|$:

$$P_{\ell}(\cos \gamma) = \frac{4\pi}{2\ell+1} \sum_{m=-\ell}^{+\ell} Y_{\ell}^m(\boldsymbol{\theta}) Y_{\ell}^{m*}(\boldsymbol{\beta}). \quad (\text{B.6})$$

Combining these equations and applying the completeness relation yields the convolution relation for an axially symmetric filter kernel,

$$u(\boldsymbol{\beta}) = \sum_{\ell=0}^{\infty} \sum_{m=-\ell}^{+\ell} u_{\ell m} Y_{\ell}^m(\boldsymbol{\beta}), \text{ with } u_{\ell m} = \sqrt{\frac{4\pi}{2\ell+1}} s_{\ell m} \psi_{\ell 0}. \quad (\text{B.7})$$

B.3. Concepts of optimised filtering on the sphere

The idea of optimised matched filters was proposed by Tegmark & de Oliveira-Costa (1998), and generalised to scale-adaptive filters by Sanz et al. (2001) for a flat topology. The construction of a axially symmetric optimised filter function $\psi(\theta)$ for the amplification and detection of signal profiles differing only in size but not in shape implies a family of filters $\psi(\theta/R)$ introducing a scaling parameter R . Decomposing the family of filter functions $\psi(\theta/R)$ into spherical harmonics yields

$$\psi\left(\frac{\theta}{R}\right) = R^2 \sum_{\ell=0}^{\infty} \sqrt{\frac{2\ell+1}{4\pi}} \psi_{\ell 0}(R) P_{\ell}(\cos \theta), \quad (\text{B.8})$$

$$\psi_{\ell 0}(R) = \frac{1}{R^2} \int d^2\theta \sqrt{\frac{2\ell+1}{4\pi}} \psi\left(\frac{\theta}{R}\right) P_{\ell}(\cos \theta), \quad (\text{B.9})$$

while allowing for central symmetry of the filter function. For a particular choice of R the filtered field $u(R, \boldsymbol{\beta})$ is obtained by convolution (c.f. Appendix. B.2):

$$u(R, \boldsymbol{\beta}) = \sum_{\ell=0}^{\infty} \sum_{m=-\ell}^{+\ell} u_{\ell m} Y_{\ell}^m(\boldsymbol{\beta}), \text{ and } u_{\ell m} = \sqrt{\frac{4\pi}{2\ell+1}} s_{\ell m} \psi_{\ell 0}(R). \quad (\text{B.10})$$

Taking into account the vanishing expectation value of the noise $\langle n_{\nu}(\boldsymbol{\theta}) \rangle = 0$, the expectation value of the filtered field at the North pole $\boldsymbol{\beta} = \boldsymbol{\theta}$ is given by

$$\langle u(R, \boldsymbol{\theta}) \rangle = A \sum_{\ell=0}^{\infty} \tau_{\ell 0} \psi_{\ell 0}(R). \quad (\text{B.11})$$

Assuming that the power spectrum of the signal is negligible compared to the noise power spectrum, which is certainly the case in noise-dominated CMB measurements, the variance of the filtered field is given by

$$\sigma_u^2(R) = \langle [u(R, \boldsymbol{\beta}) - \langle u(R, \boldsymbol{\beta}) \rangle]^2 \rangle = \sum_{\ell=0}^{\infty} C_{\ell} \psi_{\ell 0}^2(R). \quad (\text{B.12})$$

While the optimised *matched filter* in the case of single frequency observations is defined to obey the first two of the following conditions, the optimised *scale-adaptive filter* is required to obey all three conditions:

1. The filtered field $u(R, \boldsymbol{\theta})$ is an unbiased estimator of the source amplitude A at the true source position, i.e. $\langle u(R, \boldsymbol{\theta}) \rangle = A$.

2. The variance of $u(R, \beta)$ has a minimum at the scale R ensuring that the filtered field is an efficient estimator.
3. The expectation value of the filtered field at the source position has an extremum with respect to the scale R , implying

$$\frac{\partial}{\partial R} \langle u(R, \boldsymbol{\theta}) \rangle = 0. \quad (\text{B.13})$$

B.3.1. Matched filter

In order to derive the matched filter, constraint (1) can be rewritten yielding

$$\sum_{\ell=0}^{\infty} \tau_{\ell 0} \psi_{\ell 0} = 1. \quad (\text{B.14})$$

Performing functional variation (with respect to the filter function ψ) of $\sigma_u^2(R)$ while incorporating the constraint (B.14) through a Lagrangian multiplier yields the spherical matched filter:

$$\psi_{\ell 0} = \alpha \frac{\tau_{\ell 0}}{C_{\ell}}, \quad \text{where} \quad \alpha^{-1} = \sum_{\ell=0}^{\infty} \frac{\tau_{\ell 0}^2}{C_{\ell}}. \quad (\text{B.15})$$

In any realistic application, the power spectrum C_{ℓ} can be estimated from the observed data provided the power spectrum of the signal is negligible. The quantities α , $\tau_{\ell 0}$, and thus the filter kernel $\psi_{\ell 0}$ can be straightforwardly computed for any model source profile $\tau(\theta)$.

B.3.2. Scale-adaptive filter

The next step consists of reformulating constraint (3) in order to find a convenient representation for the application of functional variation. The expansion coefficient of the family of filter functions $\psi(\theta/R)$ of eqn. (B.8) can be rewritten yielding

$$\psi_{\ell 0}(R) = \frac{1}{R^2} \int d^2\theta \psi\left(\frac{\theta}{R}\right) Y_{\ell}^0(\theta) = \int d^2\beta \psi(\beta) Y_{\ell}^0(R\beta), \quad (\text{B.16})$$

where $\beta \equiv \theta/R$. In general, this substitution is *not* valid, because $d^2\theta = \sin\theta d\theta d\phi$. In the case of localised source profiles, the angle θ is small for non-vanishing values of ψ justifying the approximation $\sin\theta \approx \theta$. The same argument also applies for the boundaries of integration. With the aid of eqn. (B.11), condition (B.13) reads

$$\frac{\partial}{\partial R} \langle u(R, \boldsymbol{\theta}) \rangle = \sum_{\ell=0}^{\infty} \tau_{\ell 0} \frac{\partial \psi_{\ell 0}(R)}{\partial R} = 0. \quad (\text{B.17})$$

Using eqn. (B.16), the derivative now acts on the Legendre polynomial P_{ℓ} ,

$$\sum_{\ell=0}^{\infty} \sqrt{\frac{2\ell+1}{4\pi}} \tau_{\ell 0} \int d^2\beta \psi(\beta) P'_{\ell}(\cos R\beta) \beta \sin R\beta = 0. \quad (\text{B.18})$$

Using the derivative relation of the Legendre polynomials (Arfken & Weber 1995),

$$P'_{\ell}(x) = \frac{\ell+1}{1-x^2} [x P_{\ell}(x) - P_{\ell+1}(x)], \quad (\text{B.19})$$

one obtains

$$\sum_{\ell=0}^{\infty} \sqrt{\frac{2\ell+1}{4\pi}} (\ell+1) \tau_{\ell 0} \int d^2\beta \psi(\beta) \frac{R\beta}{\sin R\beta} \times [\cos R\beta P_{\ell}(\cos R\beta) - P_{\ell+1}(\cos R\beta)] = 0. \quad (\text{B.20})$$

In this case, the angle θ is small for non-vanishing values of ψ justifying the approximations $\sin R\beta \approx R\beta$ and $\cos R\beta \approx 1$. Substituting back, $d^2\beta = d^2\theta/R^2$, introducing $x \equiv \cos\theta = \cos R\beta$, and inserting the inversion of eqn. (B.16), namely

$$\psi(\beta) = \sum_{\ell'=0}^{\infty} \psi_{\ell' 0}(R) Y_{\ell' 0}^0(R\beta), \quad (\text{B.21})$$

one arrives at

$$\sum_{\ell', \ell=0}^{\infty} \sqrt{\frac{2\ell+1}{4\pi}} \sqrt{\frac{2\ell'+1}{4\pi}} (\ell+1) \tau_{\ell 0} \psi_{\ell' 0}(R) \times \frac{2\pi}{R^2} \int dx P_{\ell'}(x) [P_{\ell}(x) - P_{\ell+1}(x)] = 0. \quad (\text{B.22})$$

Applying the orthogonality relation for the Legendre polynomials,

$$\int_{-1}^{+1} dx P_{\ell}(x) P_{\ell'}(x) = \frac{2}{2\ell+1} \delta_{\ell\ell'}, \quad (\text{B.23})$$

and using the small angle approximation in the second term of eqn. (B.22) with the same argument as given above, yields the final result

$$\sum_{\ell=0}^{\infty} \psi_{\ell 0}(R) [\tau_{\ell 0} + \ell(\tau_{\ell 0} - \tau_{\ell-1,0})] = 0. \quad (\text{B.24})$$

Replacing the differential quotient with the corresponding derivative is a valid approximation for $\ell \gg 1$. Thus, eqn. (B.24) can be recast in shorthand notation yielding

$$\sum_{\ell=0}^{\infty} \psi_{\ell 0}(R) \tau_{\ell 0} \left[2 + \frac{d \ln \tau_{\ell 0}}{d \ln \ell} \right] = 0. \quad (\text{B.25})$$

This result could have been obtained independently by attaching the tangential plane to the North pole and applying Fourier decomposition of the filter function ψ and the source profile τ . For that reason, it is not surprising that the functional form of this condition on the sphere agrees with that obtained by [Sanz et al. \(2001\)](#) for a flat topology in two dimensions. The becomes invalid for large angular scales, because then the multipoles are of comparable or larger size than any reasonable tangential plane, thus eqn. (B.24) is an important generalisation of eqn. (B.25) valid for Fourier decompositions.

Performing functional variation (with respect to the filter function ψ) of $\sigma_u^2(R)$ while interlacing the constraints (B.14) and (B.25) through a pair of Lagrangian multipliers yields the spherical scale-adaptive filter,

$$\psi_{\ell 0} = \frac{\tau_{\ell 0}}{C_{\ell} \Delta} \left[2b + c - (2a + b) \frac{d \ln \tau_{\ell 0}}{d \ln \ell} \right], \quad (\text{B.26})$$

$$\Delta = ac - b^2, \quad (\text{B.27})$$

$$a = \sum_{\ell=0}^{\infty} \frac{\tau_{\ell 0}^2}{C_{\ell}}, \quad (\text{B.28})$$

$$b = \sum_{\ell=0}^{\infty} \frac{\tau_{\ell 0}}{C_{\ell}} \frac{d\tau_{\ell 0}}{d\ell}, \quad (\text{B.29})$$

$$c = \sum_{\ell=0}^{\infty} C_{\ell}^{-1} \left(\frac{d\tau_{\ell 0}}{d \ln \ell} \right)^2. \quad (\text{B.30})$$

As before in the case of the matched filter, the power spectrum C_{ℓ} can be derived from observed data provided the power spectrum of the signal is negligible. Assuming a model source profile $\tau(\theta)$, the quantities $\tau_{\ell 0}$, a , b , c , and finally $\psi_{\ell 0}$ can be computed in a straightforward way. The derivative of $\tau_{\ell 0}$ with respect to the multipole order ℓ is a shorthand notation of the differential quotient in eqn. (B.24).

C. Integration of Legendre- P_ℓ weighted functions

For the derivation of filter kernels (see Chapter 7), the Legendre-transform of a β -profile $p(\theta)$ is needed:

$$p_{\ell 0} = 2\pi \int_0^\pi \sin \theta d\theta p(\theta) \sqrt{\frac{2\ell+1}{4\pi}} P_\ell(\cos \theta) = 2\pi \sum_{i=0}^{N-1} \int_{z_i}^{z_{i+1}} \sin \theta d\theta p(\theta) \sqrt{\frac{2\ell+1}{4\pi}} P_\ell(\cos \theta), \quad (\text{C.1})$$

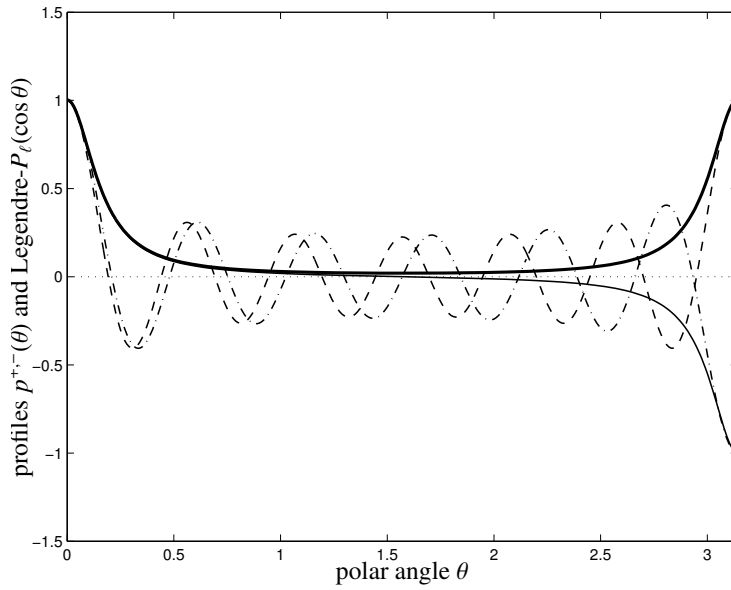


Figure C.1.: The symmetric function $p^+(\theta)$ (thick solid line) and its antisymmetric counterpart $p^-(\theta)$ (thin solid line), along with the even Legendre polynomial $P_{\ell=12}(\cos \theta)$ (dashed line) and the odd polynomial $P_{\ell=11}(\cos \theta)$ (dash-dotted line).

As in the case of Bessel functions (Appendix D), the integrand is rapidly oscillating such that it is favourable to split up the integration. Here, z_i denotes the i^{th} zero of the Legendre polynomial $P_\ell(\cos \theta)$ with the integration boundaries, $z_0 = \cos \theta_i = 1$ and $z_N = \cos \theta_f = -1$. The integration can be accelerated by using the symmetry properties of the Legendre polynomials $P_\ell(\theta)$: $P_\ell(\theta) = P_\ell(-\theta)$ for even ℓ and $P_\ell(\theta) = -P_\ell(-\theta)$ for odd ℓ . This suggests to form a symmetric and an antisymmetric combination,

$$p^+(\theta) = \frac{1}{2} [p(\theta) + p(\pi - \theta)], \quad \text{and} \quad p^-(\theta) = \frac{1}{2} [p(\theta) - p(\pi - \theta)], \quad \text{respectively.} \quad (\text{C.2})$$

Carrying out the integration while inserting the symmetry relations, one obtains for the non-zero contributions:

$$p_{\ell m} = \begin{cases} p_{\ell 0}^+ = 2\pi \int_0^{\pi/2} \sin \theta d\theta p^+(\theta) \sqrt{\frac{2\ell+1}{4\pi}} P_\ell(\cos \theta), \ell \text{ even} \\ p_{\ell 0}^- = 2\pi \int_0^{\pi/2} \sin \theta d\theta p^-(\theta) \sqrt{\frac{2\ell+1}{4\pi}} P_\ell(\cos \theta), \ell \text{ odd} \end{cases} \quad (\text{C.3})$$

which are depicted in Fig. C.1. In this way, the integrand is always even and hence the integration range can be reduced to $[0 \dots \pi/2]$ instead of $[0 \dots \pi]$. Consequently, the integrand needs to be evaluated on half as many

sampling points, or, the numerical accuracy can be increased by distributing the initial number of sampling points in an interval of half the initial size.

D. Integration of Bessel- J_ℓ weighted functions

D.1. Approximation formulae

In Chapter 13, numerical integrations over J_ℓ -weighted functions need to be carried out. Complications arise because of the large values of ℓ considered, which causes the integrands to oscillate rapidly, and because of the large range in the integration variable. The latter property of the integral requires many evaluations of the Bessel- J_ℓ functions and their derivatives, which can be sped up by using the following two approximations:

$$J_\ell(x) = \begin{cases} \frac{1}{2^{\ell} \ell!} x^\ell & , x \ll 1, \\ \sqrt{\frac{2}{\pi x}} \cos\left(x - \frac{\pi}{4}(2\ell + 1)\right) & , x \gg 1 \end{cases} \quad (\text{D.1})$$

$$\frac{d}{dx} J_\ell(x) = \begin{cases} \frac{1}{2^{\ell} (\ell-1)!} x^{\ell-1} & , x \ll 1, \\ -\sqrt{\frac{2}{\pi x}} \left[\frac{1}{x} \cos\left(x - \frac{\pi}{4}(2\ell + 1)\right) + \sin\left(x - \frac{\pi}{4}(2\ell + 1)\right) \right] & , x \gg 1 \end{cases} \quad (\text{D.2})$$

These approximations, which are depicted in Fig. D.1, yield excellent fits to the Bessel function.

In the range where the the Bessel functions $J_\ell(x)$ and their derivatives $dJ_\ell(x)/dx$ need to be properly evaluated, an excerpt taken from the `CMBfast` code written by Seljak & Zaldarriaga (1996) was used. Their description expresses Bessel functions as series of cot- and sec-functions (as derived in the excellent book by Watson 1952), and uses the recurrence relation of Bessel functions only up to order $\ell = 5$. The derivative can be determined via

$$\frac{d}{dx} [x^\ell J_\ell(x)] = x^\ell J_{\ell-1}(x) \longrightarrow \frac{d}{dx} J_\ell(x) = J_{\ell-1}(x) - \frac{\ell}{x} J_\ell(x). \quad (\text{D.3})$$

Standard descriptions based on spline interpolations fail to deliver the required numerical accuracy at high order ℓ , especially when considering the derivative $dJ_\ell(x)/dx$.

D.2. Numerical integration

When integrating rapidly oscillating functions $g(x)J_\ell(x)$, it is advisable to split up the numerical integration:

$$\int_{x_i}^{x_f} dx g(x)J_\ell(x) = \sum_{i=0}^{N-1} \int_{z_i}^{z_{i+1}} dx g(x)J_\ell(x), \quad (\text{D.4})$$

where z_i denotes the i^{th} zero of the Bessel function $J_\ell(x)$ and, naturally, $z_0 = x_i$ and $z_N = x_f$. The zeros of the Bessel- $J_\ell(x)$ function have to be evaluated numerically for small x (for instance, by bisection), and coincide with the zeros of the approximating cos-function for large x .

In the case of the derivative $dJ_\ell(x)/dx$, integration by parts is not feasible because the function $g(x)$ to be integrated is only given numerically and determining the derivative by differencing is likely to pick up noise. The determination of the zeros of $dJ_\ell(x)/dx$ can only be carried out numerically, even for large arguments x , but one can take advantage of the fact that a zero of $dJ_\ell(x)/dx$ is always located between two successive zeros of $J_\ell(x)$, which serve as starting values for the bisection. Further numerical accuracy can be gained if two successive cycles are differenced before adding up all contributions. For the numerical integration in between the zeros, Gaussian quadrature or Romberg integration have proven to be reliable.

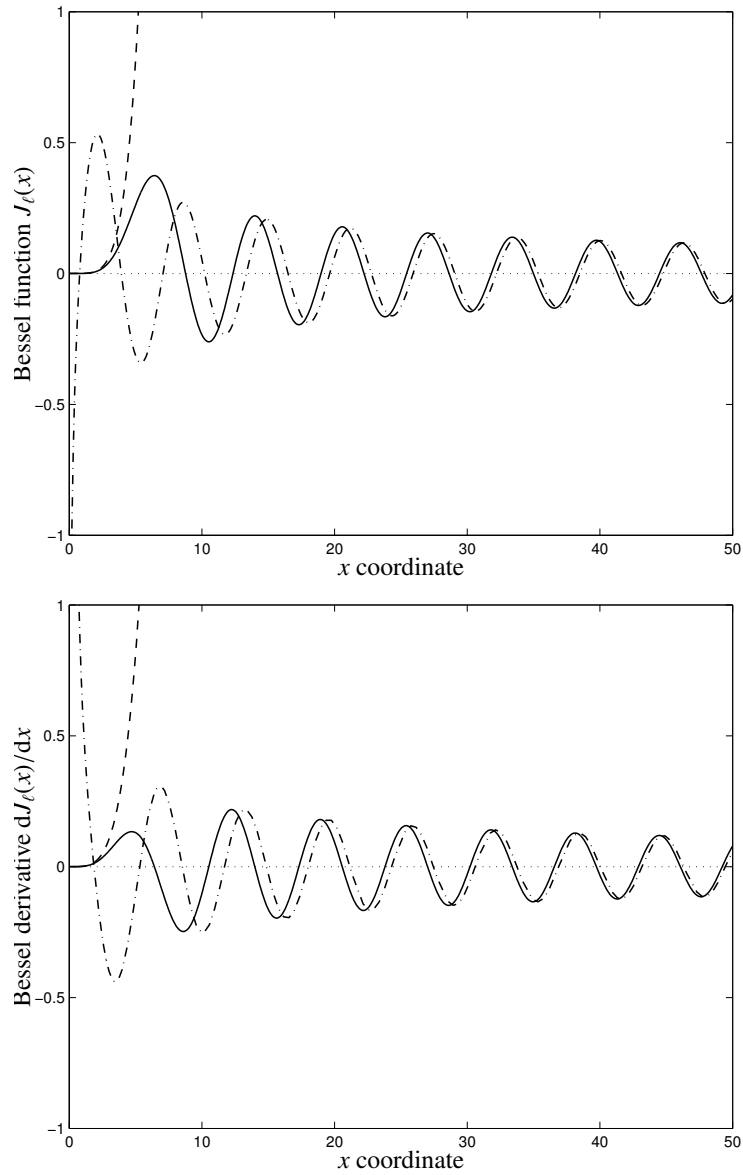


Figure D.1.: The Bessel function $J_\ell(x)$ (upper panel) and its derivative $dJ_\ell(x)/dx$ (lower panel) for $\ell = 5$ (solid line) and the approximations used for small x (dashed line) and large x (dash-dotted line).

E. Decomposition of mixed 3-point correlators of density and velocity fields

The determination of corrections to the 2-point correlation function of gravitational lensing including gravitomagnetic terms (as carried out in Chapter 13) requires the computation of 3-point and 4-point correlators. In this appendix, it is shown how the 3-point correlation function can be reduced to products of 2-point correlators by means of perturbation theory. In order to evaluate the 3-point correlation function $\langle \delta(\mathbf{k}_1)v(\mathbf{k}_2)\delta(\mathbf{k}_3) \rangle$ in perturbation theory, the density- and velocity fields are decomposed into linear terms $\delta^{(1)}, v^{(1)}$ and small perturbations $\delta^{(2)}, v^{(2)}$:

$$\delta(\mathbf{k}) = \delta^{(1)}(\mathbf{k}) + \delta^{(2)}(\mathbf{k}) \quad \text{and} \quad v(\mathbf{k}) = v^{(1)}(\mathbf{k}) + v^{(2)}(\mathbf{k}). \quad (\text{E.1})$$

As shown by Fry (1984), the second order density perturbation can be written as:

$$\delta^{(2)}(\mathbf{k}) = \int \frac{d^3 p}{(2\pi)^3} \int \frac{d^3 p'}{(2\pi)^3} (2\pi)^3 \delta_D(\mathbf{p} + \mathbf{p}' - \mathbf{k}) M(\mathbf{p}, \mathbf{p}') \delta(\mathbf{p}) \delta(\mathbf{p}') = \int \frac{d^3 p}{(2\pi)^3} M(\mathbf{p}, \mathbf{k} - \mathbf{p}) \delta^{(1)}(\mathbf{p}) \delta^{(1)}(\mathbf{k} - \mathbf{p}), \quad (\text{E.2})$$

with the function $M(\mathbf{p}, \mathbf{p}')$ being defined as:

$$M(\mathbf{p}, \mathbf{p}') = \frac{10}{7} + \frac{\mathbf{p}\mathbf{p}'}{pp'} \left(\frac{p}{p'} + \frac{p'}{p} \right) + \frac{4}{7} \left(\frac{\mathbf{p}\mathbf{p}'}{pp'} \right)^2. \quad (\text{E.3})$$

Clearly, the function M is symmetric, $M(\mathbf{p}, \mathbf{p}') = M(\mathbf{p}', \mathbf{p})$ and has the properties that $M(-\mathbf{p}, -\mathbf{p}') = M(\mathbf{p}, \mathbf{p}')$ and $M(-\mathbf{p}, \mathbf{p}') = M(\mathbf{p}, -\mathbf{p}')$. For the first order perturbation of the velocity field, one obtains:

$$v^{(2)}(\mathbf{k}) = -iH(a)f(\Omega) \frac{\mathbf{k}}{k^2} \delta^{(2)}(\mathbf{k}). \quad (\text{E.4})$$

The 3-point correlation function $\langle \delta(\mathbf{k}_1)v(\mathbf{k}_2)\delta(\mathbf{k}_3) \rangle$ can now be expanded to yield to second order:

$$\langle \delta(\mathbf{k}_1)v(\mathbf{k}_2)\delta(\mathbf{k}_3) \rangle \simeq \langle \delta^{(1)}(\mathbf{k}_1)v^{(1)}(\mathbf{k}_2)\delta^{(2)}(\mathbf{k}_3) \rangle + \langle \delta^{(1)}(\mathbf{k}_1)v^{(2)}(\mathbf{k}_2)\delta^{(1)}(\mathbf{k}_3) \rangle + \langle \delta^{(2)}(\mathbf{k}_1)v^{(1)}(\mathbf{k}_2)\delta^{(1)}(\mathbf{k}_3) \rangle \quad (\text{E.5})$$

with the first order term $\langle \delta^{(1)}(\mathbf{k}_1)v^{(1)}(\mathbf{k}_1)\delta^{(1)}(\mathbf{k}_1) \rangle$ vanishing due to $v^{(1)}(\mathbf{k}) \propto \delta^{(1)}(\mathbf{k})$ for truly Gaussian random fields. If the perturbation is contained in the density field δ , inserting eqn. (E.2) into the correlator yields:

$$\langle \delta^{(1)}(\mathbf{k}_1)v^{(1)}(\mathbf{k}_2)\delta^{(2)}(\mathbf{k}_3) \rangle = \int \frac{d^3 p}{(2\pi)^3} \int \frac{d^3 p'}{(2\pi)^3} (2\pi)^3 \delta_D(\mathbf{p} + \mathbf{p}' - \mathbf{k}_3) M(\mathbf{p}, \mathbf{p}') \langle \delta(\mathbf{k}_1) \delta(\mathbf{p}) \rangle \langle \delta(\mathbf{p}') v(\mathbf{k}_2) \rangle. \quad (\text{E.6})$$

Similarly, if the perturbation is the velocity-field v , one obtains:

$$\langle \delta^{(1)}(\mathbf{k}_1)v^{(2)}(\mathbf{k}_2)\delta^{(1)}(\mathbf{k}_3) \rangle = \int \frac{d^3 p}{(2\pi)^3} \int \frac{d^3 p'}{(2\pi)^3} (2\pi)^3 \delta_D(\mathbf{p} + \mathbf{p}' - \mathbf{k}_2) M(\mathbf{p}, \mathbf{p}') \langle \delta(\mathbf{k}_1) v(\mathbf{p}) \rangle \langle v(\mathbf{p}') \delta(\mathbf{k}_3) \rangle. \quad (\text{E.7})$$

Collecting these results for the mixed 3-point correlator of density and velocity fields in question yields for the first order expansion of $\langle \delta(\mathbf{k}_1)v(\mathbf{k}_2)\delta(\mathbf{k}_3) \rangle$ in perturbation theory:

$$\langle \delta^{(1)}(\mathbf{k}_1)v^{(1)}(\mathbf{k}_2)\delta^{(2)}(\mathbf{k}_3) \rangle = M(\mathbf{k}_1, \mathbf{k}_2) P_{\delta\delta}(|\mathbf{k}_1|) P_{\delta v}(|\mathbf{k}_2|), \quad (\text{E.8})$$

$$\langle \delta^{(1)}(\mathbf{k}_1)v^{(2)}(\mathbf{k}_2)\delta^{(1)}(\mathbf{k}_3) \rangle = M(\mathbf{k}_1, \mathbf{k}_3) P_{\delta v}(|\mathbf{k}_1|) P_{\delta v}(|\mathbf{k}_3|), \quad (\text{E.9})$$

$$\langle \delta^{(2)}(\mathbf{k}_1)v^{(1)}(\mathbf{k}_2)\delta^{(1)}(\mathbf{k}_3) \rangle = M(\mathbf{k}_2, \mathbf{k}_3) P_{\delta\delta}(|\mathbf{k}_2|) P_{\delta v}(|\mathbf{k}_3|), \quad (\text{E.10})$$

if the condition $\sum_{i=1}^3 \mathbf{k}_i = \mathbf{0}$ is fulfilled. Hence, in first order perturbation theory, the 3-point correlation function can be decomposed into products of the density-density and density-velocity correlation functions, which are of the order v/c (eqns. E.8 and E.10), and into the square of the density-velocity cross correlation, which is of order v^2/c^2 (eqn. E.9).

F. Propagation of photons through gravitomagnetic fields

This appendix provides a detailed derivation of the action of gravitomagnetic potentials on photons and serves as a supplement to Chapter 13. The microscopic picture of photon propagation in the presence of general gravitational fields has been the subject of many treatises, e.g. (Misner et al. 1973, d’Inverno 1992, Pyne & Birkinshaw 1993, Frittelli 2003), but this appendix summarises the main results in a condensed form that has been implemented in Chapter 13.

The metric g_{ab} is assumed to be weakly perturbed by γ_{ab} on a Minkowski background η_{ab} :

$$(ds)^2 = g_{ab}dx^a dx^b = (\eta_{ab} + \gamma_{ab})dx^a dx^b = (1 + 2\Phi)c^2 dt^2 - 8c \mathbf{A} \cdot d\mathbf{x} dt - (1 - 2\Phi)d\mathbf{x} \cdot d\mathbf{x}. \quad (\text{F.1})$$

The scalar potential Φ and the gravitomagnetic vector potential \mathbf{A} are given in the slow motion, near-zone approximation as solutions to Poisson’s equation with matter density ρ and matter current density $\mathbf{j} = \rho\mathbf{v}$:

$$\Delta\Phi(\mathbf{x}, t) = 4\pi G\rho(\mathbf{x}, t) \quad \longrightarrow \quad \Phi(\mathbf{x}, t) = -G \int \frac{\rho(\mathbf{x}', t)}{|\mathbf{x} - \mathbf{x}'|} d^3x', \quad (\text{F.2})$$

$$\Delta\mathbf{A}(\mathbf{x}, t) = 4\pi G\mathbf{j}(\mathbf{x}, t) \quad \longrightarrow \quad \mathbf{A}(\mathbf{x}, t) = -G \int \frac{\mathbf{j}(\mathbf{x}', t)}{|\mathbf{x} - \mathbf{x}'|} d^3x'. \quad (\text{F.3})$$

The photon trajectory is described by $x^a(s)$. At each point the tangent is given by $u^a = dx^a/ds = (u^0, \mathbf{u})$. The path shall be parametrised by the Euclidean arc length $d\ell^2 = d\mathbf{x} \cdot d\mathbf{x}$, in this case the photon trajectory can be written as $x^a(\ell) = (t(\ell), \mathbf{x}(\ell))$ with tangent $u^0 = dt/d\ell$ and $\mathbf{e} = d\mathbf{x}/d\ell$, which is normalised by $\mathbf{e}^2 = 1$. Using these coordinates, the condition that the photon’s wave-vector needs to be situated on the forward light cone (the null condition) reads:

$$u^a u_a = 0 \quad \longrightarrow \quad (1 + 2\Phi)c^2(u^0)^2 + 8c \mathbf{e} \cdot \mathbf{A} u^0 - (1 - 2\Phi) = 0. \quad (\text{F.4})$$

Hence, if the photon transverses a potential it experiences a frequency shift, whose approximate value is given by the time-component of u :

$$cu^0 = 1 - 2(\Phi - 2\mathbf{e} \cdot \mathbf{A}/c). \quad (\text{F.5})$$

In this equation, the gravitomagnetic correction to lensing can be read off, which replaces the gravitational scalar potential Φ by $\Phi - \frac{2}{c}\mathbf{A}_{\parallel}$. For the spatial part, the equation of geodesic transport,

$$\frac{d}{d\ell}u^a + \Gamma_{bc}^a u^b u^c - \mu a^0 = 0 \quad (\text{F.6})$$

has to be solved. μ denotes a free parameter, reflecting the freedom in choice of the parametrisation. For the spatial components u^i , the geodesic equation reads:

$$\frac{d}{d\ell}u^i + \Gamma_{00}^i (u^0)^2 + 2\Gamma_{0j}^i u^j u^0 + \Gamma_{jk}^i u^j u^k - \mu a^0 = 0 \quad (\text{F.7})$$

For weak perturbations γ_{ab} , the Christoffel-symbols Γ_{bc}^a can be linearised:

$$\Gamma_{bc}^a = \frac{1}{2}\eta^{cd} [h_{ad,b} + h_{bd,a} - h_{ab,d}] \quad (\text{F.8})$$

With the above defined potentials Φ and \mathbf{A} and the ansatz (F.1) for the metric one derives the expressions:

$$\Gamma_{00}^i = 4c\dot{A}^i + c^2\Phi_{,i}, \quad (\text{F.9})$$

$$\Gamma_{0j}^i = 2c [A_{i,j} - A_{j,i}] - \delta_{ij}\dot{\Phi}, \text{ and} \quad (\text{F.10})$$

$$\Gamma_{jk}^i = \delta_{jk}\Phi_{,i} - \delta_{ik}\Phi_{,j} - \delta_{ij}\Phi_{,k}, \quad (\text{F.11})$$

where $_{,i} \equiv \partial/\partial x^i$ and $\dot{} \equiv \partial/\partial t$. By ignoring $\dot{\mathbf{A}}$ and setting $\dot{\Phi} = A_{i,i} = \text{div}\mathbf{A}$, which follows from the continuity equation $\dot{\rho} + c \text{div}\mathbf{j} = 0$, one obtains:

$$\frac{d}{d\ell} u^i = c^2 \Phi_{,i} (u^0)^2 + 2 \left[2c(A_{i,j} - A_{j,i}) - \delta_{ij} A_{i,i} \right] u^j u^0. \quad (\text{F.12})$$

With the replacement $u^j [A_{i,j} - A_{j,i}] = -[\text{erot}\mathbf{A}]_i$, the final expression for the tangent is derived:

$$\frac{d}{d\ell} \mathbf{e} = 2\nabla\Phi - 4\mathbf{e} \text{rot}\mathbf{A} - (2\mathbf{e} \nabla\Phi + \mu) \mathbf{e}. \quad (\text{F.13})$$

In gravitational lensing, the norm of the wave-vector \mathbf{e} is conserved, $e^2 = \text{const}$, hence $\frac{1}{2} \frac{\partial}{\partial \ell} e^2 = \mathbf{e} \cdot \frac{\partial}{\partial \ell} \mathbf{e} = 0$. After multiplying eqn (F.13) with \mathbf{e} , the left side can be set to zero and the resulting equation solved for μ . Re-inserting μ in eqn. (F.13) gives:

$$\frac{\partial}{\partial \ell} \mathbf{e} = -2 [\nabla\Phi - \mathbf{e}(\mathbf{e}\nabla\Phi) - 2\mathbf{u} \times \text{rot}\mathbf{A}] = -2 [\nabla_{\perp}\Phi - 2\mathbf{u} \times \text{rot}\mathbf{A}]. \quad (\text{F.14})$$

In the last step, the perpendicular gradient $\nabla_{\perp} \equiv \nabla - \mathbf{e}(\mathbf{e}\nabla)$ has been inserted. This equation is an expression for the change of direction of a photon transversing a gravitomagnetic field. For the change in wavelength λ , its relation to the affine parameter μ derived by [Pyne & Birkinshaw \(1993\)](#) can be used:

$$\frac{d}{d\ell} \ln \lambda = \mu, \quad (\text{F.15})$$

which immediately yields the formula for the integrated Sachs-Wolfe/Rees-Sciama effect:

$$\frac{\Delta\lambda}{\lambda} = \frac{\lambda_{\text{obs}} - \lambda_{\text{source}}}{\lambda_{\text{source}}} = -2 \int_{\text{source}}^{\text{obs}} d\ell \frac{\partial}{\partial t} \Phi = 2 \int_{\text{source}}^{\text{obs}} d\ell \text{div}\mathbf{A}. \quad (\text{F.16})$$

Bibliography

- Abell G. O., Corwin H. G., Olowin R. P., 1989, *ApJS*, 70, 1
- Abramowitz M., Stegun I. A., 1965, *Handbook of mathematical functions*. Dover Books on Advanced Mathematics, New York: Dover
- Afshordi N., Loh Y., Strauss M. A., 2004, *Phys. Rev. D*, 69, 083524
- Aghanim N., de Luca A., Bouchet F. R., Gispert R., Puget J. L., 1997, *A&A*, 325, 9
- Aghanim N., Górski K. M., Puget J.-L., 2001, *A&A*, 374, 1
- Aghanim N., Hansen S. H., Lagache G., 2004, *astro-ph/0402571*
- Arfken G. B., Weber H. J., 1995, *Materials and Manufacturing Processes*
- Arnaud M., Evrard A. E., 1999, *MNRAS*, 305, 631
- Böhringer H., Schuecker P., Guzzo L., Collins C. A., Voges W., Cruddace R. G., Ortiz-Gil A., Chincarini G., De Grandi S., Edge A. C., MacGillivray H. T., Neumann D. M., Schindler S., Shaver P., 2004, *A&A*, 425, 367
- Bacon D. J., Refregier A. R., Ellis R. S., 2000, *MNRAS*, 318, 625
- Bardeen J. M., Bond J. R., Kaiser N., Szalay A. S., 1986, *ApJ*, 304, 15
- Bartelmann M., 2001, *A&A*, 370, 754
- Bartelmann M., Schneider P., 2001, *Physics Reports*, 340, 291
- Basu K., Hernández-Monteagudo C., Sunyaev R. A., 2004, *A&A*, 416, 447
- Bennett C. L., Fixsen D. J., Hinshaw G., Mather J. C., Moseley S. H., Wright E. L., Eplee R. E., Gales J., Hewagama T., Isaacman R. B., Shafer R. A., Turpie K., 1994, *ApJ*, 434, 587
- Bennett C. L., Halpern M., Hinshaw G., et al. 2003, *ApJS*, 148, 1
- Bennett C. L., Halpern M., Hinshaw G., Jarosik N., 2003, *ApJ*, submitted, *astro-ph/0302207*
- Bennett C. L., Hill R. S., Hinshaw G., Nolte M. R., Odegard N., Page L., Spergel D. N., Weiland J. L., Wright E. L., Halpern M., Jarosik N., Kogut A., Limon M., Meyer S. S., Tucker G. S., Wollack E., 2003, *ApJS*, 148, 97
- Bernardeau F., 1997, *A&A*, 324, 15
- Bersanelli M., Mandolesi N., 2000, *Astrophysical Letters Communications*, 37, 171
- Bertschinger E., Dekel A., 1989, *ApJL*, 336, L5
- Bertschinger E., Dekel A., 1991, in *Astronomical Society of the Pacific Conference Series Mapping Large-Scale Flows in Three Dimensions: Method*. pp 67–+
- Birkinshaw M., 1999, *Phys. Rep.*, 310, 98
- Blandford R. D., Saust A. B., Brainerd T. G., Villumsen J. V., 1991, *MNRAS*, 251, 600

- Bond J. R., Cole S., Efstathiou G., Kaiser N., 1991, *ApJ*, 379, 440
- Bond J. R., Efstathiou G., Tegmark M., 1997, *MNRAS*, 291, L33
- Bond J. R., Kofman L., Pogosyan D., 1996, *Nature*, 380, 603
- Bouchet F. R., Gispert R., 1999, *New Astronomy*, 4, 443
- Bouchet F. R., Prunet S., Sethi S. K., 1999, *MNRAS*, 302, 663
- Boughn S., Crittenden R., 2004, *Nature*, 427, 45
- Boulanger F., 1990, in *IAU Symp. 139: The Galactic and Extragalactic Background Radiation Infrared emission at high galactic latitude*. pp 139–148
- Broadhurst T., Takada M., Umetsu K., Kong X., Arimoto N., Chiba M., Futamase T., 2004, *ArXiv Astrophysics e-prints*
- Bryan G. L., Norman M. L., 1998, *ApJ*, 495, 80
- Carlstrom J. E., Holder G. P., Reese E. D., 2002, *ARA&A*, 40, 643
- Caroli E., Stephen J. B., di Cocco G., Natalucci L., Spizzichino A., 1987, *Space Science Reviews*, 45, 349
- Carroll S. M., Press W. H., Turner E. L., 1992, *ARA&A*, 30, 499
- Cartwright D. E., Longuet-Higgins M. S., 1956, *Proc. R. Soc. Lond*, p. 212
- Cavaliere A., 1980, in *NATO ASIC Proc. 60: X-Ray Astronomy Models of X-ray emission from clusters of galaxies*. pp 217–237
- Cavaliere A., Fusco-Femiano R., 1978, *A&A*, 70, 677
- Cayón L., Sanz J. L., Barreiro R. B., Martínez-González E., Vielva P., Toffolatti L., Silk J., Diego J. M., Argüeso F., 2000, *MNRAS*, 315, 757
- Cayón L., Sanz J. L., Martínez-González E., Banday A. J., Argüeso F., Gallegos J. E., Górski K. M., Hinshaw G., 2001, *MNRAS*, 326, 1243
- Colberg J. M., Krughoff K. S., Connolly A. J., 2004, *ArXiv Astrophysics e-prints*
- Colberg J. M., White S. D. M., MacFarland T. J., Jenkins A., Pearce F. R., Frenk C. S., Thomas P. A., Couchman H. M. P., 2000, *MNRAS*, 313, 229
- Colberg J. M., White S. D. M., Yoshida N., MacFarland T. J., Jenkins A., Frenk C. S., Pearce F. R., Evrard A. E., Couchman H. M. P., Efstathiou G., Peacock J. A., Thomas P. A., *The Virgo Consortium 2000*, *MNRAS*, 319, 209
- Cole S., Efstathiou G., 1989, *MNRAS*, 239, 195
- Cole S., Kaiser N., 1989, *MNRAS*, 237, 1127
- Cooray A., 2002, *Phys. Rev. D*, 65, 083518
- Coulson D., Crittenden R. G., Turok N. G., 1994, *Physical Review Letters*, 73, 2390
- Cremonese G., Marzari F., Burigana C., Maris M., 2002, *New Astronomy*, 7, 483
- Crittenden R. G., Turok N., 1996, *Physical Review Letters*, 76, 575
- da Silva A. C., Kay S. T., Liddle A. R., Thomas P. A., 2003, *astro-ph/0308074*
- da Silva A. C., Kay S. T., Liddle A. R., Thomas P. A., Pearce F. R., Barbosa D., 2001, *ApJL*, 561, L15
- Dame T. M., Hartmann D., Thaddeus P., 1996, *Bulletin of the American Astronomical Society*, 28, 1362

- Dame T. M., Hartmann D., Thaddeus P., 2001, *ApJ*, 547, 792
- Daubechies I., Bates B. J., 1993, *Acoustical Society of America Journal*, 93, 1671
- Deeming T. J., 1964, *MNRAS*, 127, 493
- Dekel A., 1994, *ARA&A*, 32, 371
- Dekel A., Bertschinger E., 1991, in *Astronomical Society of the Pacific Conference Series Mapping Large-Scale Flows in Three Dimensions: Application*. pp 83–+
- Delabrouille J., Melin J.-B., Bartlett J. G., 2002, in *ASP Conf. Ser. 257: AMiBA 2001: High-Z Clusters, Missing Baryons, and CMB Polarization Simulations of Sunyaev-Zel'dovich Maps and Their Applications*. pp 81–097
- Dennis J. M., 2003, in *Proceedings of Workshop on Massively Parallel Processing at IPDPS'03. Nice, France Partitioning with Space-Filling Curves on the Cubed-Sphere*. p. 537
- Dicke R. H., Peebles P. J. E., Roll P. G., Wilkinson D. T., 1965, *ApJ*, 142, 414
- Diego J. M., Mohr J., Silk J., Bryan G., 2003, *MNRAS*, 341, 599
- Diego J. M., Vielva P., Martínez-González E., Silk J., Sanz J. L., 2002, *MNRAS*, 336, 1351
- d'Inverno R., 1992, *Introducing Einstein's Relativity*. Oxford University Press, Oxford 1992
- Dodelson S., Gates E., Stebbins A., 1996, *ApJ*, 467, 10
- Doré O., Teyssier R., Bouchet F. R., Vibert D., Prunet S., 2001, *A&A*, 374, 358
- Doran M., Wetterich C., 2003, *Nuclear Physics B Proceedings Supplements*, 124, 57
- Dressler A., 1980, *ApJ*, 236, 351
- Dressler A., 2004, *American Astronomical Society Meeting Abstracts*, 204,
- Dyson F. W., Eddington A. S., Davidson C. R., 1920, *Mem. R. Astron. Soc.*, 62, 291
- Efstathiou G., 2004, *MNRAS*, 349, 603
- Efstathiou G., Bond J. R., 1999, *MNRAS*, 304, 75
- Efstathiou G., Bond J. R., White S. D. M., 1992, *MNRAS*, 258, 1P
- Einstein A., 1911, *Annalen der Physik*, 35, 898
- Einstein A., 1916, *Annalen der Physik*, 49, 769
- Einstein A., 1936, *Science*, 84, 506
- Eke V. R., Cole S., Frenk C. S., 1996, *MNRAS*, 282, 263
- Eke V. R., Cole S., Frenk C. S., Patrick Henry J., 1998, *MNRAS*, 298, 1145
- Ellis R. S., 1997, *ARA&A*, 35, 389
- Enßlin T. A., Kaiser C. R., 2000, *A&A*, 360, 417
- Evrard A. E., MacFarland T. J., Couchman H. M. P., Colberg J. M., Yoshida N., White S. D. M., Jenkins A., Frenk C. S., Pearce F. R., Peacock J. A., Thomas P. A., 2002, *ApJ*, 573, 7
- Fabricant D., Lecar M., Gorenstein P., 1980, *ApJ*, 241, 552
- Falgarone E., Puget J.-L., Perault M., 1992, *A&A*, 257, 715

- Fenimore E. E., Cannon T. M., 1978, *Appl. Opt.*, 17, 337
- Finger M. H., Prince T. A., 1985, NASA. Goddard Space Flight Center 19th Intern. Cosmic Ray Conf., Vol. 3 p 295-298 (SEE N85-34862 23-93), 3, 295
- Finkbeiner D. P., 2003, *ApJS*, 146, 407
- Finkbeiner D. P., Davis M., Schlegel D. J., 1999, *ApJ*, 524, 867
- Finkbeiner D. P., Davis M., Schlegel D. J., 2000, *ApJ*, 544, 81
- Fixsen D. J., Cheng E. S., Gales J. M., Mather J. C., Shafer R. A., Wright E. L., 1996, *ApJ*, 473, 576
- Fomalont E. B., Kopeikin S. M., 2003, *ApJ*, 598, 704
- Fosalba P., Gaztañaga E., Castander F. J., 2003, *ApJL*, 597, L89
- Franceschini A., Andreani P., 1995, *ApJL*, 440, L5
- Freedman W. L., Madore B. F., Gibson B. K., Ferrarese L., Kelson D. D., Sakai S., Mould J. R., Kennicutt R. C., Ford H. C., Graham J. A., Huchra J. P., Hughes S. M. G., Illingworth G. D., Macri L. M., Stetson P. B., 2001, *ApJ*, 553, 47
- Friedmann A., 1922, *Z. Phys.*, 10, 377
- Friedmann A., 1924, *Z. Phys.*, 32, 326
- Frittelli S., 2003, *MNRAS*, 340, 457
- Fry J. N., 1984, *ApJL*, 277, L5
- Górski K. M., Banday A. J., Hivon E., Wandelt B. D., 2002, in *ASP Conf. Ser. 281: Astronomical Data Analysis Software and Systems XI HEALPix — a Framework for High Resolution, Fast Analysis on the Sphere.* pp 107–+
- Geisbüsch J., Kneissl R., Hobson M., 2004, *astro-ph/0406190*
- Giardino G., Banday A. J., Górski K. M., Bennett K., Jonas J. L., Tauber J., 2002, *A&A*, 387, 82
- Gingold R. A., Monaghan J. J., 1977, *MNRAS*, 181, 375
- Giovannini M., 2004, *astro-ph/0412601*
- Goldin A. B., Kowitt M. S., Cheng E. S., Cottingham D. A., Fixsen D. J., Inman C. A., Meyer S. S., Puchalla J. L., Ruhl J. E., Silverberg R. F., 1997, *ApJL*, 488, L161+
- Gorski K. M., Hivon E., Banday A. J., Wandelt B. D., Hansen F. K., Reinecke M., Bartelman M., 2004, *ArXiv Astrophysics e-prints*
- Gradshteyn I. S., Ryzhik I. M., 1994, *Table of integrals, series and products.* New York: Academic Press, |c1994, 5th ed. completely reset, edited by Jeffrey, Alan
- Griffin M. J., Ade P. A. R., Orton G. S., Robson E. I., Gear W. K., Nolt I. G., Radostitz J. V., 1986, *Icarus*, 65, 244
- Gunson J., Polychronopoulos B., 1976, *MNRAS*, 177, 485
- Haehnelt M. G., 1997, in *Microwave Background Anisotropies: Cobras/Samba and measurements of the Sunyaev-Zel'dovich effect.* pp 413–+
- Haiman Z., Mohr J. J., Holder G. P., 2001, *ApJ*, 553, 545
- Halverson N. W., Leitch E. M., Pryke C., Kovac J., Carlstrom J. E., Holzzapfel W. L., Dragovan M., Cartwright J. K., Mason B. S., Padin S., Pearson T. J., Readhead A. C. S., Shepherd M. C., 2002, *ApJ*, 568, 38

- Hamana T., Bartelmann M., Yoshida N., Pfrommer C., 2004, MNRAS, pp 672–+
- Hamana T., Mellier Y., 2001, MNRAS, 327, 169
- Harrison E. R., 1970, Phys. Rev. D, 1, 2726
- Haslam C. G. T., Klein U., Salter C. J., Stoffel H., Wilson W. E., Cleary M. N., Cooke D. J., Thomasson P., 1981, A&A, 100, 209
- Haslam C. G. T., Stoffel H., Salter C. J., Wilson W. E., 1982, A&A Suppl. Ser., 47, 1
- Hauser M. G., Arendt R. G., Kelsall T., Dwek E., Odegard N., Weiland J. L., Freudenreich H. T., Reach W. T., Silverberg R. F., Moseley S. H., Pei Y. C., Lubin P., Mather J. C., Shafer R. A., Smoot G. F., Weiss R., Wilkinson D. T., Wright E. L., 1998, ApJ, 508, 25
- Henry J. P., 2000, ApJ, 534, 565
- Herranz D., Sanz J. L., Hobson M. P., Barreiro R. B., Diego J. M., Martínez-González E., Lasenby A. N., 2002, MNRAS, 336, 1057
- Heyrovsky D., 2004, ArXiv Astrophysics e-prints
- Hinshaw G., Spergel D. N., Verde L., Hill R. S., Meyer S. S., Barnes C., Bennett C. L., Halpern M., Jarosik N., Kogut A., Komatsu E., Limon M., Page L., Tucker G. S., Weiland J. L., Wollack E., Wright E. L., 2003, ApJS, 148, 135
- Hirata C. M., Padmanabhan N., Seljak U., Schlegel D., Brinkmann J., 2004, ArXiv Astrophysics e-prints
- Hivon E., Wandelt B. D., Gorski K. M., 1998, in Evolution of Large-Scale Structure: From Recombination to Garching Cosmic Microwave Background Anisotropy Power Spectrum Statistics for High Precision Cosmology
- Hobson M. P., Barreiro R. B., Toffolatti L., Lasenby A. N., Sanz J., Jones A. W., Bouchet F. R., 1999, MNRAS, 306, 232
- Hobson M. P., Jones A. W., Lasenby A. N., Bouchet F. R., 1998, MNRAS, 300, 1
- Hobson M. P., McLachlan C., 2003, MNRAS, 338, 765
- Hogg D. W., 1999, astro-ph/9905116
- Hu W., 2000a, ArXiv Astrophysics e-prints
- Hu W., 2000b, Phys. Rev. D, 62, 43007
- Hu W., Sugiyama N., 1994, Phys. Rev. D, 50, 627
- Hu W. T., 1995, Ph.D. Thesis
- Ibanez J., 1983, A&A, 124, 175
- in 't Zand J. J. M., Fenimore E. E., Kawai N., Yoshida A., Matsuoka M., Yamauchi M., 1994, Presented at the Imaging in High Energy Astronomy Conference, Capri (Italy), 26-30 Sep. 1994, 95, 22436
- in 't Zand J. J. M., Heise J., Jager R., 1994, A&A, 288, 665
- Jaffe A. H., Kamionkowski M., 1998, Phys. Rev. D, 58, 043001
- Jain B., Seljak U., 1997, ApJ, 484, 560
- Jain B., Seljak U., White S., 2000, ApJ, 530, 547
- Jenkins A., Frenk C. S., White S. D. M., Colberg J. M., Cole S., Evrard A. E., Couchman H. M. P., Yoshida N., 2001, MNRAS, 321, 372

- Kaiser N., 1982, MNRAS, 198, 1033
- Kaiser N., 1986, MNRAS, 222, 323
- Kaiser N., 1995, ApJL, 439, L1
- Kaiser N., 2000, ApJ, 537, 555
- Kaiser N., Squires G., 1993, ApJ, 404, 441
- Kay S. T., Liddle A. R., Thomas P. A., 2001, MNRAS, 325, 835
- Keihanen E., Kurki-Suonio H., Poutanen T., 2004, ArXiv Astrophysics e-prints
- Kendall M. G., Stuart A., 1958, The Advanced Theory of Statistics. Publisher: Griffin
- Kibble T. W. B., 1976, Journal of Physics A Mathematical General, 9, 1387
- Knox L., 1995, Phys. Rev. D, 52, 4307
- Komatsu E., Kogut A., Nolta M., Bennett C. L., Halpern M., Hinshaw G., Jarosik N., Limon M., Meyer S. S., Page L., Spergel D. N., Tucker G. S., Verde L., Wollack E., Wright E. L., 2003, ApJ, submitted, astro-ph/0302223
- Kosowsky A., 2004, astro-ph/0402234
- Lagache G., 2003, A&A, 405, 813
- Lagache G., Puget J. L., 2000, A&A, 355, 17
- Lagerros J. S. V., 1996a, A&A, 310, 1011
- Lagerros J. S. V., 1996b, A&A, 315, 625
- Lagerros J. S. V., 1997, A&A, 325, 1226
- Lagerros J. S. V., 1998, A&A, 332, 1123
- Lahav O., Rees M. J., Lilje P. B., Primack J. R., 1991, MNRAS, 251, 128
- Lamarre J. M., Puget J. L., Bouchet F., 2003, New Astronomy Review, 47, 1017
- Landau L. D., Lifshitz E. M., 1975, The classical theory of fields. Course of theoretical physics - Pergamon International Library of Science, Technology, Engineering and Social Studies, Oxford: Pergamon Press, 1975, 4th rev.engl.ed.
- Leinert C., Ábrahám P., Acosta-Pulido J., Lemke D., Siebenmorgen R., 2002, A&A, 393, 1073
- Lewis A., Challinor A., Lasenby A., 2000, ApJ, 538, 473
- Lloyd-Davies E. J., Ponman T. J., Cannon D. B., 2000, MNRAS, 315, 689
- Longair M. S., 1998, Galaxy formation. Publisher: Springer
- Lucy L. B., 1977, AJ, 82, 1013
- Ménard B., Erben T., Mellier Y., 2003, in Matter and Energy in Clusters of Galaxies, ASP Conference Proceedings, Vol. 301. Held 23-27 April 2002 at National Central University, Chung-Li, Taiwan. Edited by Stuart Bowyer and Chong-Yuan Hwang. San Francisco: Astronomical Society of the Pacific, 2003. ISBN: 1-58381-149-4, p.537
- Weak Lensing Study of Abell 2029. pp 537–+
- Müller T. G., 2001, Planetary and Space Science, 49, 787
- Müller T. G., Lagerros J. S. V., 1998, A&A, 338, 340

- Müller T. G., Lagerros J. S. V., 1999, AAS/Division for Planetary Sciences Meeting, 31, 0
- Müller T. G., Lagerros J. S. V., 2002, A&A, 381, 324
- Ma C., Fry J. N., 2002, Physical Review Letters, 88, 211301
- Maino D., Burigana C., Maltoni M., Wandelt B. D., Górski K. M., Malaspina M., Bersanelli M., Mandolesi N., Banday A. J., Hivon E., 1999, A&A Suppl. Ser., 140, 383
- Maino D., Farusi A., Baccigalupi C., Perrotta F., Banday A. J., Bedini L., Burigana C., De Zotti G., Górski K. M., Salerno E., 2002, MNRAS, 334, 53
- Mandolesi N., Bersanelli M., Cesarsky C., Danese L., Efstathiou G., Griffin M., Lamarre J. M., Norgaard-Nielsen H. U., Pace O., Puget J. L., Raisanen A., Smoot G. F., Tauber J., Volonte S., 1995, Planetary and Space Science, 43, 1459
- Martínez-González E., Sanz J. L., 1990, MNRAS, 247, 473
- Martínez-González E., Sanz J. L., Silk J., 1990, ApJL, 355, L5
- Martínez-González E., Sanz J. L., Silk J., 1992, Phys. Rev. D, 46, 4193
- Martínez-González E., Sanz J. L., Silk J., 1994, ApJ, 436, 1
- Mather J. C., Fixsen D. J., Shafer R. A., Mosier C., Wilkinson D. T., 1999, ApJ, 512, 511
- Mathiesen B. F., Evrard A. E., 2001, ApJ, 546, 100
- Misner C. W., Thorne K. S., Wheeler J. A., 1973, Gravitation. W.H. Freeman and Co., San Francisco, 1973
- Miville-Deschenes M., Lagache G., 2004, ArXiv Astrophysics e-prints
- Miyamoto S., 1977, Space Science Instrumentation, 3, 473
- Mo H. J., White S. D. M., 2002, MNRAS, 336, 112
- Mohr J. J., Mathiesen B., Evrard A. E., 1999, ApJ, 517, 627
- Monaghan J. J., 1992, ARA&A, 30, 543
- Monaghan J. J., Lattanzio J. C., 1985, A&A, 149, 135
- Monin A. S., Yaglom A. M., 1965a, Statistical Fluid Mechanics: Mechanics of Turbulence (Volume 1). The MIT Press
- Monin A. S., Yaglom A. M., 1965b, Statistical Fluid Mechanics: Mechanics of Turbulence (Volume 2). The MIT Press
- Moore P., 2000, The data book of astronomy. The data book of astronomy, Bristol: Institute of Physics Publishing (IOPP), 2000, 529 p. ISBN 0750306203
- Moscardini L., Bartelmann M., Matarrese S., Andreani P., 2002, MNRAS, 335, 984
- Muzy J. F., Bacry E., Arneodo A., 1993, PRE, 47, 875
- Myers A. D., Shanks T., Outram P. J., Frith W. J., Wolfendale A. W., 2004, MNRAS, 347, L67
- Nagai D., Kravtsov A. V., Kosowsky A., 2003, ApJ, 587, 524
- Natoli P., de Gasperis G., Gheller C., Vittorio N., 2001, A&A, 372, 346
- Navarro J. F., Frenk C. S., White S. D. M., 1995, MNRAS, 275, 720
- Navarro J. F., Frenk C. S., White S. D. M., 1996, ApJ, 462, 563

- Navarro J. F., Hayashi E., Power C., Jenkins A. R., Frenk C. S., White S. D. M., Springel V., Stadel J., Quinn T. R., 2004, *MNRAS*, 349, 1039
- Neugebauer G., Miinch G., Kieffer H., Chase S. C., Miner E., 1971, *AJ*, 76, 719
- Nolta M. R., Wright E. L., Page L., Bennett C. L., Halpern M., Hinshaw G., Jarosik N., Kogut A., Limon M., Meyer S. S., Spergel D. N., Tucker G. S., Wollack E., 2004, *ApJ*, 608, 10
- Nouri-Zonoz M., 1999, *Phys. Rev. D*, 60, 024013
- Ostriker J. P., Vishniac E. T., 1986, *ApJL*, 306, L51
- Peacock J. A., 1999, *Cosmological physics*. Publisher: Cambridge University Press
- Peebles P. J. E., 1980, *The large-scale structure of the universe*. Research supported by the National Science Foundation. Princeton, N.J., Princeton University Press, 1980. 435 p.
- Peebles P. J. E., Yu J. T., 1970, *ApJ*, 162, 815
- Penzias A. A., Wilson R. W., 1965, *ApJ*, 142, 419
- Persi F. M., Spergel D. N., Cen R., Ostriker J. P., 1995, *ApJ*, 442, 1
- Pfrommer C., Enßlin T. A., 2004, *A&A*, 413, 17
- Pierpaoli E., Anthoine S., Huffenberger K., Daubechies I., . 2004, *ArXiv Astrophysics e-prints*
- Piran T., Safier P. N., 1985, *Nature*, 318, 271
- Pratt G. W., Arnaud M., 2002, *A&A*, 394, 375
- Press W. H., Schechter P., 1974, *ApJ*, 187, 425
- Proctor R. J., Skinner G. K., Willmore A. P., 1979, *MNRAS*, 187, 633
- Puget J. L., 1998a, in *Abstracts of the 19th Texas Symposium on Relativistic Astrophysics and Cosmology*, held in Paris, France, Dec. 14-18, 1998. Eds.: J. Paul, T. Montmerle, and E. Aubourg (CEA Saclay), meeting abstract. *Cosmology in the I.R.*
- Puget J. L., 1998b, *Highlights in Astronomy*, 11, 1142
- Puget J.-L., Abergel A., Bernard J.-P., Boulanger F., Burton W. B., Desert F.-X., Hartmann D., 1996, *A&A*, 308, L5+
- Puy D., Grenacher L., Jetzer P., Signore M., 2000, *A&A*, 363, 415
- Pyne T., Birkinshaw M., 1993, *ApJ*, 415, 459
- Ratra B., Peebles P. J. E., 1988, *Phys. Rev. D*, 37, 3406
- Reach W. T., Morris P., Boulanger F., Okumura K., 2003a, *Icarus*, 164, 384
- Reach W. T., Morris P., Boulanger F., Okumura K., 2003b, *astro-ph/0304289*
- Rees M. J., Sciama D. W., 1968, *Nature*, 217, 511
- Refregier A., Komatsu E., Spergel D. N., Pen U., 2000, *Phys. Rev. D*, 61, 123001
- Rephaeli Y., 1995, *ARA&A*, 33, 541
- Rubiño-Martín J. A., Hernández-Monteagudo C., Enßlin T. A., 2004, *A&A*, 419, 439
- Sachs R. K., Wolfe A. M., 1967, *ApJ*, 147, 73

- Sanz J. L., Herranz D., Martínez-González E., 2001, *ApJ*, 552, 484
- Sarazin C. L., 1986, *Reviews of Modern Physics*, 58, 1
- Sazonov S. Y., Sunyaev R. A., 1998, *Astronomy Letters*, 24, 553
- Sazonov S. Y., Sunyaev R. A., 2000, *A&A*, 354, L53
- Scaramella R., Cen R., Ostriker J. P., 1993, *ApJ*, 416, 399
- Schäfer B. M., Kawai N., 2003, *Nucl. Instr. Meth. A*, 500, 263
- Schechter P., 1976, *ApJ*, 203, 297
- Schlegel D. J., Finkbeiner D. P., Davis M., 1997, *Bulletin of the American Astronomical Society*, 29, 1354
- Schlegel D. J., Finkbeiner D. P., Davis M., 1998, *ApJ*, 500, 525
- Schneider P., Bartelmann M., 1997, *MNRAS*, 286, 696
- Schneider P., Ehlers J., Falco E. E., 1992, *Gravitational Lenses*. Springer-Verlag Berlin Heidelberg New York.
- Schneider P., Seitz C., 1995, *A&A*, 294, 411
- Schneider P., van Waerbeke L., Jain B., Kruse G., 1998, *MNRAS*, 296, 873
- Seitz C., Kneib J.-P., Schneider P., Seitz S., 1996, *A&A*, 314, 707
- Seitz C., Schneider P., 1995, *A&A*, 297, 287
- Seitz C., Schneider P., 1997, *A&A*, 318, 687
- Seitz S., Schneider P., 1996, *A&A*, 305, 383
- Seljak U., 1994, *ApJ*, 436, 509
- Seljak U., 1996a, *ApJ*, 463, 1
- Seljak U., 1996b, *ApJ*, 460, 549
- Seljak U., Burwell J., Pen U., 2001, *Phys. Rev. D*, 63, 063001
- Seljak U., Zaldarriaga M., 1996, *ApJ*, 469, 437
- Sereno M., 2003, *MNRAS*, 344, 942
- Sereno M., 2004, *Phys. Rev. D*, 69, 087501
- Shapiro S. L., Teukolsky S. A., 1983, *Black holes, white dwarfs, and neutron stars - The physics of compact objects*. Wiley, New York, 1983
- Sheth R. K., Tormen G., 1999, *MNRAS*, 308, 119
- Silk J., 1968, *ApJ*, 151, 459
- Skinner G. K., Grindlay J. E., 1993, *A&A*, 276, 673
- Skinner G. K., Ponman T. J., Hammersley A. P., Eyles C. J., 1987, *A&A Suppl.*, 136, 337
- Sokasian A., Gawiser E., Smoot G. F., 2001, *ApJ*, 562, 88
- Song Y., Cooray A., Knox L., Zaldarriaga M., 2003, *ApJ*, 590, 664

- Spergel D. N., Verde L., Peiris H. V., Komatsu E., Nolte M. R., Bennett C. L., Halpern M., Hinshaw G., Jarosik N., Kogut A., Limon M., Meyer S. S., Page L., Tucker G. S., Weiland J. L., Wollack E., Wright E. L., 2003, *ApJ*, submitted, astro-ph/0302209
- Springel V., Hernquist L., 2002, *MNRAS*, 333, 649
- Springel V., Yoshida N., White S. D. M., 2001, *New Astronomy*, 6, 79
- Steinhardt P. J., 1996, *APS Meeting Abstracts*, pp 103–+
- Stöhr F., 1999, *High Resolution Simulations of Underdense Regions*, Diploma Thesis, Munich: Technical University
- Stöhr F., White S. D. M., Springel V., Tormen G., Yoshida N., 2003, *MNRAS*, 345, 1313
- Stolyarov V., Hobson M. P., Ashdown M. A. J., Lasenby A. N., 2002, *MNRAS*, 336, 97
- Strauss M. A., Willick J. A., 1995, *Physics Reports*, 261, 271
- Strukov I. A., Brukhanov A. A., Skulachev D. P., Sazhin M. V., 1992a, *Pis ma Astronomicheskii Zhurnal*, 18, 387
- Strukov I. A., Brukhanov A. A., Skulachev D. P., Sazhin M. V., 1992b, *MNRAS*, 258, 37P
- Sugiyama N., 1995, *ApJS*, 100, 281
- Sunyaev R. A., Zel'dovich I. B., 1972, *Comments Astrophys. Space Phys.*, 4, 173
- Sunyaev R. A., Zel'dovich I. B., 1980, *ARA&A*, 18, 537
- Tagger M., Falgarone E., Shukurov A., 1995, *A&A*, 299, 940
- Takada M., Jain B., 2003a, *MNRAS*, 340, 580
- Takada M., Jain B., 2003b, *MNRAS*, 344, 857
- Tauber J. A., 2000, in *IAU Symposium The Planck Mission*
- Tegmark M., de Oliveira-Costa A., 1998, *ApJL*, 500, L83+
- Tegmark M., Efstathiou G., 1996, *MNRAS*, 281, 1297
- Toffolatti L., Argueso Gomez F., de Zotti G., Mazzei P., Franceschini A., Danese L., Burigana C., 1998, *MNRAS*, 297, 117
- Tuluie R., Laguna P., 1995a, in *Seventeenth Texas Symposium on Relativistic Astrophysics and Cosmology Chasing CMB Photons through the Nonlinear Universe..* pp 692–+
- Tuluie R., Laguna P., 1995b, *ApJL*, 445, L73
- Valls-Gabaud D., 1998, *PASA*, 15, 111
- van den Bosch F. C., 2002, *MNRAS*, 331, 98
- van Waerbeke L., Mellier Y., Erben T., Cuillandre J. C., Bernardeau F., Maoli R., Bertin E., Mc Cracken H. J., Le Fèvre O., Fort B., Dantel-Fort M., Jain B., Schneider P., 2000, *A&A*, 358, 30
- Vielva P., Barreiro R. B., Hobson M. P., Martínez-González E., Lasenby A. N., Sanz J. L., Toffolatti L., 2001, *MNRAS*, 328, 1
- Vielva P., Martínez-González E., Cayón L., Diego J. M., Sanz J. L., Toffolatti L., 2001, *MNRAS*, 326, 181
- Villa F., Sandri M., Bersanelli M., Butler R. C., Mandolesi N., Mennella A., Marti-Canales J., Tauber J., 2003, astro-ph/0304137

- Vishniac E. T., 1987, *ApJ*, 322, 597
- Wandelt B. D., Górski K. M., 2001, *Phys. Rev. D*, 63, 123002
- Watson G. N., 1952, *A treatise on the theory of Bessel functions*. Cambridge University Press, Cambridge, 1952
- Wechsler R. H., Bullock J. S., Primack J. R., Kravtsov A. V., Dekel A., 2002, *ApJ*, 568, 52
- Weinberg S., 1972, *Gravitation and cosmology: Principles and applications of the general theory of relativity*. New York: Wiley, 1972
- Wetterich C., 1988, *Nuclear Physics B*, 302, 645
- Wetterich C., 1995, *A&A*, 301, 321
- White M., 2003, *ApJ*, 597, 650
- White M., Hernquist L., Springel V., 2002, *ApJ*, 579, 16
- White M., Majumdar S., 2003, [astro-ph/0308464](https://arxiv.org/abs/astro-ph/0308464)
- White M., Scott D., Silk J., 1994, *ARA&A*, 32, 319
- White S. D. M., Davis M., Efstathiou G., Frenk C. S., 1987, *Nature*, 330, 451
- White S. D. M., Narayan R., 1987, *MNRAS*, 229, 103
- White S. D. M., Rees M. J., 1978, *MNRAS*, 183, 341
- Wittman D. M., Tyson J. A., Kirkman D., Dell'Antonio I., Bernstein G., 2000, *Nature*, 405, 143
- Wright E. L., 1976, *ApJ*, 210, 250
- Wright E. L., 1979, *ApJ*, 232, 348
- Wright E. L., Bennett C. L., Gorski K., Hinshaw G., Smoot G. F., 1996, *ApJL*, 464, L21+
- Yoshida N., Springel V., White S. D. M., Tormen G., 2000, *ApJL*, 544, L87
- Yvon D., Mayet F., 2004, [astro-ph/0401505](https://arxiv.org/abs/astro-ph/0401505)
- Zaldarriaga M., Spergel D. N., Seljak U., 1997, *ApJ*, 488, 1
- Zaroubi S., Squires G., de Gasperis G., Evrard A. E., Hoffman Y., Silk J., 2001, *ApJ*, 561, 600
- Zaroubi S., Squires G., Hoffman Y., Silk J., 1998, *ApJL*, 500, L87+
- Zeldovich Y. B., 1972, *MNRAS*, 160, 1P
- Zhao D. H., Mo H. J., Jing Y. P., Börner G., 2003, *MNRAS*, 339, 12

Acknowledgements

Es ist mir ein besonderes Anliegen, mich bei allen zu bedanken, die zum Gelingen meiner Dissertation beigetragen haben:

Zuallererst möchte ich meinem Betreuer Prof. Dr. Matthias Bartelmann für seine Unterstützung und seine Hilfsbereitschaft danken. Ich habe von seinem Wissen sehr profitiert. Matthias hat in mir Begeisterung für die Kosmologie geweckt und ich hätte mir keinen besseren Lehrer wünschen können.

Ich danke Prof. Dr. Simon White dafür, daß er mir die Möglichkeit gegeben hat, in seiner Arbeitsgruppe am MPA zu promovieren. Auf seine Initiative hin habe ich mich mit der Beobachtung von Galaxienclustern mit PLANCK beschäftigt. Seine Einsicht und sein Verständnis astrophysikalischer Probleme haben mich oft beeindruckt und ich hoffe, daß ich von Simon viel gelernt habe.

Dr. Torsten Enßlin danke ich für seine Unterstützung und seine Förderung meiner Arbeit für PLANCK. Den Mitgliedern der PLANCK-Gruppe, insbesondere Dr. Reinhard Hell und Dr. Martin Reinecke, gebührt Dank für die reibungslose Zusammenarbeit. Ihrer Hilfe ist es zu verdanken, daß ich schnell Zugang zur PLANCK-Software fand. Martin hat durch seine Verbesserung der Software einige der Rechnungen erst durchführbar gemacht und hat auf meine Vorschläge hin viele Änderungen in die Software eingebaut.

Die Zusammenarbeit mit Christoph Pfrommer hat einen großen Teil dieser Arbeit geprägt, und ich hoffe, dass er von meiner Mitarbeit ebenso profitieren konnte wie ich von ihm. Sein mathematisches Können hat viel zu der Konstruktion der Filterfunktionen beigetragen, ebenso seine Forderungen nach mehr Präzision in der numerischen Umsetzung. Ich danke Christoph für die vielen Diskussionen, durch die wir voneinander einiges an Physik gelernt haben.

Dr. Saleem Zaroubi danke ich für die gute Zusammenarbeit in dem Wavelet-Projekt und für die vielen Empfehlungsschreiben, die er verfasst hat. Dr. Volker Springel und Dr. Klaus Dolag danke ich für die Bereitstellung von SPH-Simulationsdaten.

Viele Studenten und Postdocs haben durch ihre offene und aufgeschlossene Art zu der Atmosphäre am MPA beigetragen. Vor allem Harry Dimmelmeier, Carlos Hernández-Monteagudo, Martin Jubelgas, Francisco Kitaura, Anja von der Linden, Andreas Marek, Brice Ménard, Martin Obergaulinger, Pierre Ocvirk, Roland Oechslin, Fritz Röpke, Greg Rudnick, Leo Scheck, Corina Vogt, André Waelkens und Stefano Zibetti danke ich für die vielen Diskussionen.

Den Systemadministratoren danke ich für die exzellente Betreuung der Computer. Maria Depner und Cornelia Rickl standen mir bei organisatorischen und verwaltungstechnischen Problemen bei und konnten mir immer weiterhelfen.

Zuletzt danke ich meinen Eltern für ihre Unterstützung, die mein Studium und meine Promotion überhaupt erst ermöglichte.

Publications

1. B.M. Schäfer, C. Pfrommer, S. Zaroubi:
Redshift estimation of clusters by wavelet decomposition of their Sunyaev-Zel'dovich morphology
[preprint astro-ph/0310613](#), submitted to MNRAS, 21.Oct.2003
2. B.M. Schäfer, C. Pfrommer, M. Bartelmann, V. Springel, L. Hernquist:
Detecting Sunyaev-Zel'dovich clusters with PLANCK:
I. Construction of all-sky thermal and kinetic SZ-maps
[preprint astro-ph/0407089](#), submitted to MNRAS, 05.Jul.2004
3. B.M. Schäfer, C. Pfrommer, R.M. Hell, M. Bartelmann:
Detecting Sunyaev-Zel'dovich clusters with PLANCK:
II. Foreground components and optimised filtering schemes
[preprint astro-ph/0407090](#), submitted to MNRAS, 05.Jul.2004
4. B.M. Schäfer, C. Pfrommer, M. Bartelmann:
Detecting Sunyaev-Zel'dovich clusters with PLANCK:
III. Properties of the SZ-cluster sample
in preparation, to be submitted to MNRAS
5. B.M. Schäfer:
Coded mask imaging of extended sources with Gaussian random fields
[preprint astro-ph/0407286](#), submitted to MNRAS, 14.Jul.2004
6. B.M. Schäfer, M. Bartelmann:
Gravitational lensing the the second post-Newtonian approximation:
Gravitomagnetic potentials and the integrated Sachs-Wolfe effect
in preparation, to be submitted to MNRAS

Curriculum Vitae

personal data

name: Björn Malte Schäfer

address: Max-Planck-Institut für Astrophysik, Karl-Schwarzschild-Straße 1, 85741 Garching

birth: 22.Feb.1975 in Zweibrücken/Germany

nationality: German citizenship

education

Grundschule Contwig (1981 - 1985)

Herzog-Wolfgang-Gymnasium Zweibrücken (1985 - 1988)

Helmholtz-Gymnasium Zweibrücken (1988 - 1994)

Abitur at Helmholtz-Gymnasium Zweibrücken (Jun.1994)

academic record

study of physics at Ruprecht-Karls-Universität Heidelberg/Germany (Sep.1994 - Jun.2000)

Vordiplom in physics, Universität Heidelberg (Jun.1996)

stay at the University of Edinburgh/Scotland (Sep.1996 - Jun.1997)

participation in DESY's summer student programme, Hamburg/Germany (Jul.1997 - Aug.1997)

participation in GSI's summer student programme, Darmstadt/Germany (Jun.1998 - Aug.1998)

diploma thesis at Max-Planck-Institut für Kernphysik, Heidelberg/Germany (Jun.1999 - Jun.2000)

Diplom in physics, Universität Heidelberg (Jun.2000)

internship at RIKEN (Institute of Physical and Chemical Research), Tokyo/Japan (Nov.2000 - Nov.2001)

PhD student at Max-Planck-Institut für Astrophysik, Garching/Germany (Jan.2002 - Jan.2005)

fellowships

stipend by Studienstiftung des Deutschen Volkes (Jul.1997 - May.2000)

stipend by Studienstiftung des Deutschen Volkes in support of the internship at RIKEN (Nov.2000 - Nov.2001)

